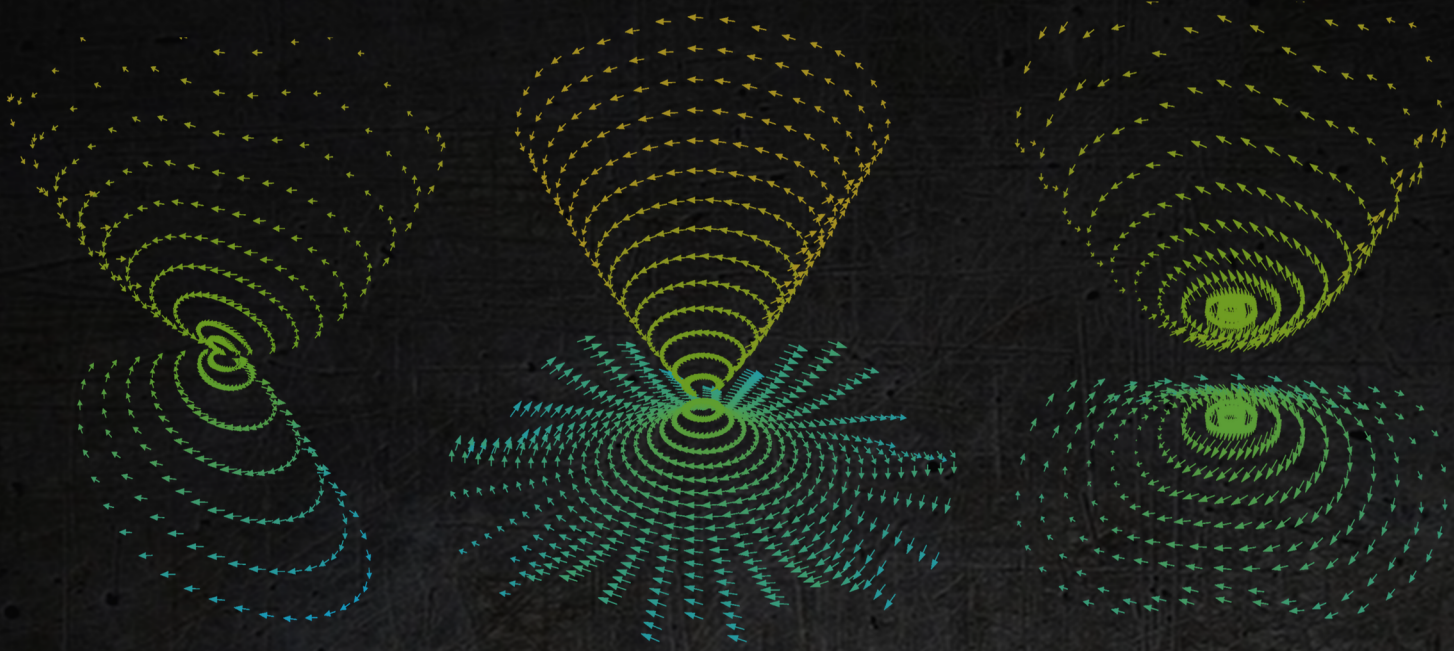

Low dimensional effects in Topological Insulators

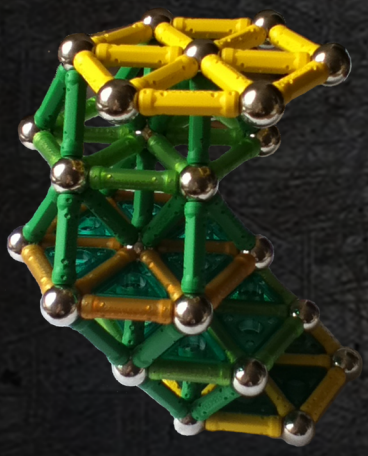

Hugo Aramberri

Madrid - 2015

Instituto de Ciencia de Materiales de Madrid

UNIVERSIDAD AUTONOMA DE MADRID

CSIC
Consejo Superior de Investigaciones Científicas

LOW DIMENSIONAL EFFECTS IN TOPOLOGICAL INSULATORS

HUGO ARAMBERRI DEL VIGO

Thesis supervised by M. CARMEN MUÑOZ

and thutorised by JUAN JOSÉ PALACIOS

In partial fulfillment of the requirements for the degree of Doctor in Physics at

Departamento de Física de la Materia Condensada
Facultad de Ciencias
Universidad Autónoma de Madrid

Instituto de Ciencia de Materiales de Madrid – CSIC. 2015–2016

Hugo Aramberri del Vigo: *Low Dimensional Effects in Topological Insulators*

ABSTRACT

Topological insulators are a new quantum state of matter that can not be described in terms of an order parameter in the traditional Ginzburg–Landau theory, but rather by a topological invariant. They host topologically protected surface states with outstanding novel electronic properties such as forbidden backscattering. Topological insulators represent a new generation of materials with potential applications in the fields of low power electronics, spintronics and topological quantum computation, and from the theoretical point of view they pose many interesting problems and provide a realistic framework in which long–sought particles (i.e. Majorana fermions or magnetic monopoles) and phases of matter (i.e. the quantum spin Hall effect, the quantum anomalous Hall effect or topological exciton condensates) can be realised. In this thesis we analyse low dimensional effects in two– and three–dimensional time–reversal symmetry protected topological insulators by means of *ab initio* calculations and employing the BHZ analytical model. The topological order is invetigated in bulk Bi_2Te_3, Sb_2Te_3, Bi_2Se_3 and Sb_2Se_3, for which topologically protected surface states arise in thin film geometry. Strain–induced topological phase transitions are predicted and characterised for the four compounds, and we present their corresponding phase diagrams. A Sb_2Te_3/Bi_2Te_3 heterojunction is investigated, showing the conditions under which it can host switchable topologically protected interface states. Moreover, different types of common stacking defects are calculated, among which inter–quintuple layer basal twin domain boundaries are found to be the most energetically favourable. We show how particular arrangements of such defects induce self–doping in the topologically protected Dirac Cones, and we indicate how the doping can be tuned in sign and magnitude by unravelling the charge doping mechanism. We additionally address the effects of magnetic impurities in Bi_2Se_3. The magnetic order of Cr–dopants is analysed and we show that Cr–doped Bi_2Se_3 thin films exhibit an exchange–coupling induced gap in the surface states and can host the quantum anomalous Hall effect phase. Furthermore, atom thin Cr overlayers on Bi_2Se_3 undergo a double spin reorientation transition as the thickness of the Cr films increases stepwise from 1 to 3 monolayers. The flip in the direction of the magnetisation comes along with a double gap opening transition that in turn affects the spin texture of the surface states, which undergoes a double skyrmion to meron transition. Finally, we describe the BHZ model for two–dimensional topological insulators including the effect of a perpendicular magnetic field. Two different AC spin current sources are proposed, one that works in the absence of external magnetic fields, and one that works in the quantum Hall regime and can be fabricated with present–day technology. The viability of the latter is discussed with realistic band dispersion diagrams for HgTe/CdTe and InAs/GaSb quantum wells.

RESUMEN

Los aislantes topológicos (ATs) son una nueva fase cuántica de la materia que no puede ser descrita mediante un parámetro de orden de acuerdo con la clasificación tradicional de Ginzburg–Landau. Por el contrario, los ATs se pueden describir por un invariante topológico, y albergan estados de superficie topológicamente protegidos con propiedades electrónicas excepcionales, entre las que destaca el *backscattering* prohibido. Los ATs son una nueva generación de materiales con posibles aplicaciones en los campos de la electrónica de bajo consumo, la espintrónica o la computación topológica cuántica, y desde un punto de vista teórico plantean interesantes retos y nos proveen de un marco realista en el que se pueden manifestar partículas (fermiones de Majorana o monopolos magnéticos) y fases de la materia (espín–Hall cuántico, Hall cuántico anómalo o condensado de excitones topológico) exóticas. En esta tesis utilizamos cálculos de *primeros principios* y el modelo analítico BHZ para investigar efectos de baja dimensionalidad en ATs bi- y tridimensionales protegidos por simetría de inversión temporal. Estudiamos el orden topológico de los materiales Bi_2Te_3, Sb_2Te_3, Bi_2Se_3 y Sb_2Se_3 en volumen, en cuyas láminas delgadas aparecen estados de superficie topológicos. Predecimos y caracterizamos transiciones de fase topológicas debidas a deformaciones para los cuatro compuestos, y mostramos sus diagramas de fases correspondientes. Investigamos una intercara de Sb_2Te_3/Bi_2Te_3 e indicamos bajo qué condiciones puede albergar estados de intercara topológicos conmutables. Además, calculamos distintos tipos de defectos de apilamiento, de los que las fronteras de dominios gemelos (*twin boundaries*) entre capas quíntuples son las más favorables energéticamente. Mostramos cómo ciertas configuraciones de dichos defectos inducen un dopaje intrínseco en los conos de Dirac, e indicamos cómo ajustar el signo y magnitud de este dopaje a través de la descripción del proceso físico que lo origina. También estudiamos los efectos de impurezas magnéticas sustitucionales en Bi_2Se_3. Analizamos el orden magnético de impurezas de Cr y mostramos que éstas abren un gap en los estados de superficie de láminas delgadas de Bi_2Se_3, lo que permite que este sistema albergue la fase efecto Hall anómalo cuántico. Recubriendo Bi_2Se_3 con láminas de tamaño atómico de Cr se observa una doble transición de espín en las capas de Cr según se aumenta escalonadamente el grosor del recubrimiento de una a tres monocapas. El cambio de dirección en la imanación origina una doble transición de apertura del gap de los estados de superficie, que a su vez induce una doble transición en la textura de espín de *skyrmión* a *merón*. Por último describimos el modelo BHZ para ATs bidimensionales, incluyendo el efecto de un campo magnético perpendicular. Proponemos dos dispositivos que generan corrientes alternas de espín, uno que no requiere de campos magnéticos externos y otro para una fase de efecto Hall cuántico que puede ser fabricado con la tecnología actual. La viabilidad de este último se analiza en términos de diagramas de bandas realistas para pozos cuánticos de HgTe/CdTe e InAs/GaSb.

ACKNOWLEDGMENTS / AGRADECIMIENTOS

Esta tesis sólo ha sido posible gracias a M. Carmen Muñoz, que me dio en primer lugar la oportunidad de embarcarme en este proyecto y trabajar con ella. Gracias por todo. También quiero agradecer a Juan José Palacios por su labor como tutor de esta tesis.

A Jorge Cerdá le agradezco que además de aguantarme muchas tardes en su despacho haya sido de mucho apoyo, y no solo a nivel científico.

I will also be forever grateful to Markus Büttiker and Balázs Ujfalussy for giving me the opportunity of working with them in Geneva and Budapest respectively, and for their kind hospitality.

Agradezco asímismo a la red académica i2basque, al Centro de Supercomputación de Galicia (CESGA) y a la Red Española de Supercomputación (RES) por facilitarme recursos de cálculo para el desarrollo de esta tesis.

No me gustaría hacer esta sección muy larga ni melosa, dirán algunos que es por eso de que soy del norte, pero quiero agradecer aquí también a mi gran compañero de fatigas, Juanmi, que tantas horas buenas me ha hecho pasar en el despacho, así como a Hernán, Marzia, Yurena, Armando, Valen, Sara[2], Marisa y María. A otros que me han aguantado mis chistes en las comidas como Jon, Willy, Ana, Alba, Héctor, Javi C., Marina, Manolo, Nacho, Javi M., y uno sin el cual el ICMM tal y como lo conocemos se vendría abajo en cuestion de semanas, Juanma.

And thanks to the great people that made my life easier and much nicer during my two stays in Geneva: Pierre, Patrick, David Das., Johan, Christian, Konrad, Christoph, Jian, Ermis, David Dav. and many others.

Por supuesto, también quiero agradecer especialmente a mis padres, que siempre han empujado en la buena dirección para que este proyecto llegue a buen puerto, y a mi hermano Mario que me ha aguantado en toda esta etapa en Madrid.

Y a Laura, que siempre ha estado ahí en los malos y buenos momentos desde el principio de esta tesis, y que espero siga estando en muchísimos más por venir.

CONTENTS

LIST OF FIGURES

LIST OF TABLES

ACRONYMS

2D	two–dimensional
2DEG	two–dimensional electron gas
2HEG	two–dimensional hole gas
3D	three–dimensional
AC	alternate current
AF	antiferromagnetic
bcc	body–centred cubic
BHZ	Bernevig, Hughes and Zhang
BIA	bulk inversion asymmetry
BZ	Brilluoin zone
CB	conduction band
CBM	conduction band minimum
DC	Dirac cone
DFE	defect formation energy
DFT	Density Functional Theory
DM	dipole moment
DOS	density of states
DP	Dirac point
DZ	double–ζ
ESS	electron–like surface state
fcc	face–centred cubic
FM	ferromagnetic
GGA	generalised gradient approximation
hcp	hexagonal close–packed
HSS	hole–like surface state

KS Kohn–Sham

LDA local density approximation

LDOS local density of states

MAE magnetic anisotropy energy

ML monolayer

MM magnetic moment

NI normal insulator

n.n. nearest neighbours

n.n.n. next nearest neighbours

PAO pseudo–atomic orbital

PAW projector augmented wave

PBE Perdew, Burke and Ernzerhof

PDOS projected density of states

PP pseudopotential

QAHE quantum anomalous Hall effect

QH quantum Hall

QHE quantum Hall effect

QL quintuple layer

QPC quantum point contact

QSHE quantum spin Hall effect

QW quantum well

RKKY Ruderman-Kittel-Kasuya-Yosida

SD stacking defect

SF stacking fault

SIA structure inversion asymmetry

SIESTA Spanish Initiative for Electronic Simulations with Thousands of Atoms

SOC spin–orbit coupling

SP spontaneous polarisation

SZ simple–ζ

TB basal twin domain boundary

TI topological insulator

TIS topologically protected interface state

TKKN Thouless, Kohmoto, Nightingale and den Nijs

TPT topological phase transition

TRIM time–reversal invariant momenta

TRS time–reversal symmetry

TSS topologically protected surface state

VB valence band

VBM valence band maximum

vdW van der Waals

VASP Vienna *ab–initio* Simulation Package

1 INTRODUCTION

1.1 INTRODUCTION

Topological insulators (TIs) are a new quantum state of matter recently predicted and observed. Until the 1980's, every known phase of a condensed matter system could be described by an order parameter and its symmetry transformations, according to the well established Ginzburg–Landau theory [1]. For instance, a solid can be understood as a system in which full rotational and translational symmetries are broken, and only some discrete number of them remain in a crystal; magnetic phases break the continuous spin rotational symmetry and superconductors break phase rotation symmetry. During the 80's, the quantum Hall effect (QHE) was first observed and described [2]. This effect takes place in two–dimensional electron or hole gases (for instance in semiconductor heterojunctions) subject to a perpendicular magnetic field and gives rise to a non–conventional phase of matter. From a semiclassical point of view, the magnetic field causes the electrons to move in circular cyclotron orbits with a decreasing radius for an increasing magnetic field. At high enough magnetic fields, the bulk electrons describe closed circular orbits, while the electrons at the edges follow skipping orbits along the edges, leading to the formation of continuous edge states. While the bulk electrons become localised, turning the system into an insulator, the edge electrons move along the one–dimensional channels at the edges with a *quantised* conductance of e^2/h per channel. This quantum phase of matter is characterised by a generic insulating phase, being time–reversal the only broken symmetry in the system, and no meaningful order parameter can be found to describe this state. Nevertheless, quantum Hall (QH) systems with different number of conducting edge channels do correspond to distinct phases of matter, and they cannot be adiabatically connected without going through a QH plateau, i.e., without closing the gap of the insulating bulk. Moreover, the quantisation of the conductance at the edges is astonishingly *robust* against disorder in the sample, in the sense that irregularities or impurities in the bulk of the material or the edges do not alter the value of the conductance for the electronic transport through the edge states. Even in highly disordered QH systems the conductance takes only integer values of the conductance quantum, and so the QHE is said to be immune to Anderson localisation.

The characterisation of the QH states was proposed to be directly related to the number of edge channels. Thouless, Kohmoto, Nightingale and den Nijs (TKKN) connected the conductance of a QH system to the calculation of its Chern number [3], which does not vary under smooth variations of the Hamiltonian. The TKKN index of the QHE is thus a *topological* invariant of a given phase, in the same sense that the number of holes of a surface (genus) is a topological invariant of a given manifold, according to the Gauss–Bonnet theorem.

The QHE picture described above already grasps the main hallmarks of topological phases of matter:

(i) They are not described by a local order parameter, but rather by a topological invariant that can only be computed in insulating systems.

(ii) This phase is robust against perturbations as long as the bulk band gap is maintained.

(iii) At a boundary with a system characterised by a different value of the topological invariant, surface or edge states develop.

The classification of the QHE as a topological phase revolutionised the field of Condensed Matter physics, both from a theoretical point of view, since it required a different description of the phases of matter and new tools from the mathematical field of topology, and from an experimental point of view, being the robustness of the quantised conductance a milestone in condensed matter physics that was recognised with the Physics Nobel price in 1985 and has established an unbeaten electrical resistance standard in metrology. Nevertheless, for more than 20 years no other topological phases of matter were identified except for the fractional QHE, which was first observed only 2 years after the QHE. It was not until 2005 that Kane and Mele proposed the so–called quantum spin Hall effect (QSHE) to occur in graphene [4], which basically consists of two copies of the QHE with opposite spin and propagation direction of the edge channels. This kind of topological phase would be robust against disorder, while time–reversal symmetry (TRS) would still be fulfiled and no external magnetic filed would be required. Almost at that same time, Bernevig, Hughes and Zhang independently proposed a model Hamiltonian that describes a two–dimensional QSHE [5], analogous to Kane and Mele's proposal, that could be probed in HgTe/CdTe quantum wells. Soon after these theoretical predictions, the quantised conductance of a QSHE system was first measured [6], and the field of TIs began to attract a lot of attention of the condensed matter community. By 2009 three stoichiometric compounds were predicted to be three–dimensional topological insulators [7] with larger gaps than the HgTe/CdTe wells, and that had been long–known for their outstanding thermoelectric properties. The topological surface state was measured in a $Bi_{1-x}Sb_x$ alloy [8] and Bi_2Se_3 [9] in 2008 and 2009 respectively, and a great amount of TI candidates have been proposed since. In the last five years new kinds of topological phases have been identified, such as topological crystalline insulators [10] or topological superconductors [11] , and a new playground for theoreticians and experimentalists related to TIs has just emerged: Weyl physics in condensed matter systems [12]. Interestingly, the concepts derived for Bloch electrons in a crystal were rapidly adapted to photons in a photonic crystal, and several astonishing experiments were carried out, being one of the most beautiful and powerful experimental demonstrations of the existence of backscattering–immune topological edge states (for photons) described in Ref. [13]. This proves that the novel concepts derived in the field of TIs are applicable in different fields of Physics.

1.2 MOTIVATION

The rapidly emerging field of TIs is interesting not only because of the great deal of attention that has attracted in the last decade, but mainly because it requires concepts from many different fields to explain the behaviour of this kind of materials. Traditional condensed matter physics can only account for some of their properties, while ideas from the mathematical field of topology and quantum field theory become essential for a full description and understanding of TIs. A wide range of exotic phenomena related to TIs have been predicted to occur. Just to name some examples: topological excitons can condensate in a TI thin film [14], a physical realisation of Majorana fermions can arise at a superconductor-TI interface [15, 16], a topological magneto–electric effect that naturally couples the magnetisation in a TI to the electric field (or the magnetic field to its polarisation) though an axion–like term in Maxwell's equations is also expected in three–dimensional (3D) TIs [17, 18], and the realisation of the quantum anomalous Hall effect (QAHE) [19] has recently been observed in Cr-doped 3D TIs [20]. Moreover, the edge states in two–dimensional (2D) TIs and surface states in their 3D counterparts are immune to backscattering, leading to disipationless transport for the former and much more efficient electronic transport for the latter, which could effectively reduce the amount of power dissipated in electronic circuits by means of the Joule effect. And most importantly, the spin–polarisation of these boundary states can be used as another information channel in circuits. Therefore, TIs have also caused a stir in the spintronics community, which looks for candidate materials in which efficient spin manipulation can be achieved and utilised. In this thesis we will study the behaviour of 2D and 3D TIs under different kinds of perturbations: stress, defect–induced electric polarisations, metallic impurities and external magnetic fields. We will focus on the Bi_2Se_3 family of compounds, since they represent the most interesting 3D TI materials up to date for their big bulk band gaps (compared to other TIs with even narrower gaps), and on HgTe/CdTe and InAs/GaSb quantum wells in the 2D realm. Low–dimensional effects make the topological character of this systems patent via surfaces, edges or interfaces, since the bulk–to–boundary correspondence [21] applies at any boundary between two topological phases.

This thesis is structured as follows: first we will describe the main theoretical methods employed along this work (Chapter 2), the only exception being the Bernevig, Hughes and Zhang (BHZ) model used in Chapter 7 and described therein. Then, we will characterise the ideal, defect–free bulks and surfaces of the four 3D TIs analysed in this thesis in Chapter 3. In Chapter 4 we will address the effects of uniaxial and biaxial strain in the Bi_2Se_3 family of compounds, and we will propose a system in which topological interfacial states develop and topological phase transitions can be probed. Chapter 5 is devoted to stacking defects in Bi_2Se_3 and their influence on the electronic structure and particularly on the topological surface state. The study of 3D TIs is completed with the investigation of the effect of magnetic impurities and atom thin metallic overlayers on such systems in Chapter 6. Next, the BHZ Hamiltonian is described and employed to describe 2D TIs in Chapter 7. Two different experimental setups are proposed to generate AC pure spin

currents. Last, some global remarks on the results and a summary of the thesis can be found in Chapter 8.

2

METHODS

2.1 INTRODUCTION

In this chapter we will describe the main methods used in this thesis work. All the calculations of electronic band structure, density of states (DOS) and projected density of states (PDOS), ionic relaxations, spin texture, charge density and potential profiles were carried out at the *ab initio* level within the Density Functional Theory (DFT) framework, being the only exception the results shown in Chapter 7, in which an effective $k \cdot p$ Hamiltonian is derived and employed. DFT is a very powerful method for calculating the electronic properties of a system. It was originally derived by the Nobel laureates Kohn and Sham in the mid 60s. This theory is based on the assumption that every physical property of an interacting particle system can be expressed as a functional of the electron density of the electronic ground state $\rho_0(\boldsymbol{r})$, instead of the more complex total wave function of the whole system. Among its many triumphs, DFT can be spotlighted for accurately predicting atomic geometries, electronic and magnetic properties as well as thermal and mechanical behaviour of countless systems, including crystals, surfaces, molecules, heterostructures, etc. A wide variety of DFT codes are available nowadays, and in a modern computer small systems can be calculated with great accuracy within minutes. As computer technology has rapidly developed in the last decades, the calculation of more complex systems, which in the recent past was unthinkable or extremely demanding, has become accessible and given many fruitful results.

2.2 DFT FORMALISM

Quantum Mechanics allows us to derive any physical property of any system once the Hamiltonian is known. For an isolated system of atoms, and in the absence of any external fields, the total, non–relativistic Hamiltonian of such a system will in general have the form:

$$\begin{aligned} H_{Tot} &= -\sum_{i=1}^{N} \frac{1}{2m} \nabla_i^2 - \sum_{i=1}^{M} \frac{1}{2M_I} \nabla_I^2 \\ &\quad - \sum_{i=1}^{N} \sum_{I=1}^{M} \frac{Z_I}{r_{iI}} + \sum_{i=1}^{N} \sum_{j>i}^{N} \frac{1}{r_{ij}} + \sum_{I=1}^{M} \sum_{J>I}^{M} \frac{Z_I Z_J}{R_{IJ}} \\ &= \widetilde{T}_e + \widetilde{T}_I + \widetilde{V}_{iI} + \widetilde{V}_{ee} + \widetilde{V}_{IJ} \end{aligned} \tag{1}$$

where m is the electron mass, M_I and Z_I the mass and atomic number of the I-th nucleus respectively. N (M) the total number of electrons (nuclei) and r_{iI}, r_{ij}, and R_{IJ} the distances between the i-th electron and the I-th nucleus, the i-th and j-th electrons and the I-th and J-th nuclei respectively. The first two terms, $\widetilde{T}_e$ and $\widetilde{T}_I$, account for the kinetic energy of the electrons and nuclei of the system respectively. The remaining three terms describe

the Coulomb interaction between electrons and nuclei, $\widetilde{V}_{iI}$, electrons and electrons, $\widetilde{V}_{ee}$, and nuclei and nuclei, $\widetilde{V}_{IJ}$.

During the very first years of Quantum Mechanics, Born and Oppenheimer introduced a first approximation to this problem that is now named after them [22]: as the electron mass is more than 1800 times smaller than the mass of the smallest possible nucleus, we can consider the electrons to move in a system with fixed nuclei, and, therefore, decouple the electronic and nuclear problems. The all–electron Hamiltonian (H_{ae}) now reads:

$$H_{ae} = \widetilde{T}_e + \widetilde{V}_{iI} + \widetilde{V}_{ee} \tag{2}$$

Although the problem is now considerably simpler, we still have to solve a $3N$ eigenvalue problem of N coupled electrons. The presence of one electron generates an electrostatic potential in the whole space and hence influences all the remaining electrons. Hartree introduced in 1928 another simplification to deal with this problem: we can consider each electron to feel the mean electrostatic field generated by all the remaining $N-1$ electrons, so that we can approximate the electron–electron interaction by:

$$\widetilde{V}_{ee} \sim \widetilde{V}_H(\boldsymbol{r}) = \sum_{j \neq i}^{N} \int \Psi_j^*(\boldsymbol{r}') \frac{1}{|\boldsymbol{r} - \boldsymbol{r}'|} \Psi_j(\boldsymbol{r}') d\boldsymbol{r}' \tag{3}$$

This single-electron approximation allows us to write down an independent equation for each monoelectronic state $\Psi_i(\boldsymbol{r})$:

$$[\widetilde{T}_e + \widetilde{V}_{iI}(\boldsymbol{r}) + \widetilde{V}_H(\boldsymbol{r})]\Psi_i(\boldsymbol{r}) = \varepsilon_i \Psi_i(\boldsymbol{r}) \tag{4}$$

where ε_i is the energy eigenvalue of $\Psi_i(\boldsymbol{r})$. The all-electron wavefunction, $\boldsymbol{\Phi}_{ae}$, becomes now the product of independent single-electron states:

$$\boldsymbol{\Phi}_{ae}(\boldsymbol{r}_1, \boldsymbol{r}_2, ..., \boldsymbol{r}_N) = \psi_1(\boldsymbol{r}_1)\psi_2(\boldsymbol{r}_2)...\psi_N(\boldsymbol{r}_N) \tag{5}$$

Despite this approximation making the problem now solvable, we are losing much of the rich physics described by Quantum Mechanics. In particular, the fermionic character of the electrons dictates that the total wavefunction of the electronic system must be antisymmetric under the exchange of indistinguishable electrons. This may be fulfiled by substituting the resulting all–electron wavefunction that solves H_{ae} by a Slater determinant, leading to the so–called Hartree–Fock approximation. [23] Still, the electron-electron correlation is also partially lost.

Both the exchange potential and the correlation potential are not known exactly *a priori*, but we may write the exact Hamiltonian within the independent electron approximation as:

$$H_{ae} = \widetilde{T}_e + \widetilde{V}_{iI} + \widetilde{V}_H + \widetilde{V}_X + \widetilde{V}_C \tag{6}$$

As the last two terms can not in general be analytically expressed, they are typically written as a single term called exchange–correlation potential, $\widetilde{V}_{XC} = \widetilde{V}_X + \widetilde{V}_C$, which accounts for the energy difference between the real system and the non–interacting and non–fermionic system. In Subsection 2.2.2 we will present a detailed description of the conventional approaches to calculate the term $\widetilde{V}_{XC}$.

2.2.1 *The DFT*

In 1964, Hohenberg and Kohn proposed an alternative way to solve the electronic Hamiltonian as written in Eq. 6. By considering every physical property of the system as a functional of the electronic density $\rho(\boldsymbol{r})$, instead of the electronic wavefunction Φ_{ae}, they were able to write a monoelectronic Schrödinger equation equivalent to the original electronic problem that can be solved iteratively. The energy of the system will now depend on the electron density in the following way:

$$E[\rho] = T_e[\rho] + \int \rho(\boldsymbol{r}) V_{eI}(\boldsymbol{r}) d\boldsymbol{r} + \frac{1}{2} \int\int \frac{\rho(\boldsymbol{r})\rho(\boldsymbol{r}')}{|\boldsymbol{r} - \boldsymbol{r}'|} d\boldsymbol{r} d\boldsymbol{r}' + E_{XC}[\rho] \quad (7)$$

This expression is called the Kohn-Sham functional of the total energy of the electron system. By making use of the concepts of calculus of variations, we may minimise $E[\rho]$ with respect to $\rho(\boldsymbol{r})$, leading to the independent electron Kohn-Sham equations:

$$[\widetilde{T}_e + \widetilde{V}_{iI} + \widetilde{V}_H + \widetilde{V}_{XC}]\psi_i^{KS} = \varepsilon_i^{KS}\psi_i^{KS} \quad (8)$$

being the Kohn-Sham Hamiltonian

$$\widetilde{h}^{KS} = \widetilde{T}_e + \widetilde{V}_{iI} + \widetilde{V}_H + \widetilde{V}_{XC} \quad (9)$$

ψ_i^{KS} the Kohn–Sham (KS) orbitals and ε_i^{KS} the eigenvalues of $\widetilde{h}^{KS}$. Under this form, we can now solve the electronic problem (assuming we have an expression for $\widetilde{V}_{XC}$ which will be addressed below) via the variational method. By minimising the energy as a functional of the density, we will get a solution for the ground state of the system. It is important to note that this approach is valid for the ground state only, so the excited states of the system will be described poorly. The other main limitation of the DFT is the fact that the KS orbitals are only auxiliary functions and do not correspond to the actual wavefunctions of the real system (note, for example, that they are not antisymmetric under the exchange of indistinguishable electrons). Nevertheless, the electron density derived from the KS orbitals *does* have a physical meaning, and can be obtained as

$$\rho(\boldsymbol{r}) = \sum_i n_i |\psi_i^{KS}(\boldsymbol{r})|^2 \quad (10)$$

where $n_i = 2/(E^{(\varepsilon_i - E_F)k_B T} + 1)$ is the occupation of the i-th KS state at temperature T, given by the Fermi-Dirac distribution. The KS equations 8 can be solved self-consistently to obtain the eigenvalues and eigenfunctions of the system. The procedure is the following:

(i) An initial electron density $\rho(\boldsymbol{r})$ is proposed

(ii) The operator $\widetilde{h}^{KS}$ is constructed from the initial $\rho(\boldsymbol{r})$

(iii) The differential equations 8 are solved

(iv) A new $\rho(\boldsymbol{r})$ is obtained from the solution

(v) The process is repeated until the difference between the initial and final $\rho(\boldsymbol{r})$'s is smaller than a given tolerance value. When this condition is met, we have arrived at a self-consistent solution for the electronic problem.

In practice, the resulting $\rho(\boldsymbol{r})$ is not used directly as the input for the next iteration, as it has been found to be much more efficient to change it slightly, and there are several algorithms that implement different kinds of mixings (with the $\rho(\boldsymbol{r})$ obtained in the previous steps) that help to solve the self–consistent problem much faster.

2.2.2 *The Exchange–Correlation functional*

The last two terms in the all–electron Hamiltonian of Eq. 6 have not yet been properly expressed. The exchange term accounts for the antisymmetric character of the total wavefunction, and an analytic expression can not be obtained but for a handful of systems. For a homogeneous electron gas, the exact analytical expression is known with the form

$$\widetilde{V}_X[\rho] = -\frac{3}{4}\Big(\frac{3}{\pi}\Big)^{1/3}\int \rho(\boldsymbol{r})^{4/3}d\boldsymbol{r} \tag{11}$$

Regarding the correlation term, there is no analytical expression for it and only its low and high density limits are known, corresponding to infinitely weak and infinitely strong correlation. As both the exchange potential and the correlation potential terms comprise unsolved fundamental problems, they are usually written as a single term, $\widetilde{V}_{XC}$, known as exchange–correlation potential, which is parametrised in terms of the exchange–correlation energy density of a homogeneous electron gas, ε_{XC}^{hom}. The simplest approach is to consider the effect of $\widetilde{V}_{XC}$ to be purely local, thus depending only on the electron density at $\boldsymbol{r}$. This approximation is called local density approximation (LDA), and the exchange–correlation energy at a point $\boldsymbol{r}$ can now be written as:

$$E_{XC}^{LDA}[\rho(\boldsymbol{r})] = \int \varepsilon_{XC}^{hom}(\rho(\boldsymbol{r}))\rho(\boldsymbol{r})d\boldsymbol{r} \tag{12}$$

The exchange–correlation potential will thus be:

$$\widetilde{V}_{XC}(\boldsymbol{r}) = \frac{\delta E_{XC}[\rho(\boldsymbol{r})]}{\delta\rho(\boldsymbol{r})} = \frac{\partial[\rho(\boldsymbol{r})\varepsilon_{XC}^{hom}(\boldsymbol{r})]}{\partial\rho(\boldsymbol{r})} = \varepsilon_{XC}^{hom}(\boldsymbol{r}) + \rho(\boldsymbol{r})\frac{\delta\varepsilon_{XC}^{hom}(\rho(\boldsymbol{r}))}{\delta\rho(\boldsymbol{r})} \tag{13}$$

In DFT codes E_{XC} is usually parametrised as a function of $\rho(\boldsymbol{r})$ for simplicity. We have used the Ceperly and Alder [24, 25] parametrisation both for Vienna *ab–initio* Simulation Package (VASP) and SIESTA-GREEN LDA calculations.

The exchange–correlation functional in the LDA approximation is purely local, as it is completely determined by the value of $\rho(\boldsymbol{r})$ at every point in space. In real systems $\rho(\boldsymbol{r})$ is not homogeneous even at scales of the order of 10 Å. To solve this issue, a first order correction can be included to E_{XC} by taking into account the dependence of ε_{XC}^{hom} with the gradient of $\rho(\boldsymbol{r})$, $\boldsymbol{\nabla}\rho(\boldsymbol{r})$. This leads to the generalised gradient approximation (GGA) [26, 27, 28], in which the exchange–correlation functional will be written as:

$$E_{XC}^{GGA}[\rho(\boldsymbol{r})] = \int \varepsilon_{XC}^{hom}(\rho(\boldsymbol{r}), \boldsymbol{\nabla}\rho(\boldsymbol{r}))\rho(\boldsymbol{r})d\boldsymbol{r} \tag{14}$$

where $\varepsilon_{XC}^{hom}(\rho(\boldsymbol{r}), \boldsymbol{\nabla}\rho(\boldsymbol{r}))$ is an analytic function for which there are several possible parametrisations. For the GGA calculations carried out in this thesis

	C	Se	Te	Bi	Sb
C_6	1.75	12.64	31.74	80.00	38.44
R_0	1.452	1.771	1.892	2.000	1.881

Table 1: Parameters used for the vdW method of Grimme as implemented in VASP. C_6 is given in $Jnm^{-6}mol^{-1}$ and R_0 in Å. In VASP, a cut-off radius for pair interactions, R_{cut}, is needed. We fixed it at 30 Å while the dimensionless scaling parameters were set to s_6=0.75 and d=20.0.

we always employed the nowadays most widely used functional of Perdew, Burke and Ernzerhof (PBE) [27].

2.2.3 *van der Waals Functional*

For the most extensively studied systems in this work, van der Waals (vdW) forces play a crucial role in determining the correct crystal structure. This is due to the fact that the inter-quintuple layer interaction in Bismuth dichalcogenides is mainly of the vdW type. For this reason, we make use of the semi–empirical pair–potential approach developed by Grimme [29] (DFT-D2) for VASP calculations, and a similar approach by Ortmann *et al.* [30] was employed in SIESTA-GREEN calculations. In both cases, a pairwise attractive potential, $\sum \varepsilon_{vdW}^{ij}$, is added to the total energy functional, where the summation is over all atomic pairs in the system. In Grimme's method it has the form

$$\varepsilon_{vdW}^{ij} = -s_6 \frac{C_6^{ij}}{R_{ij}^6} f_{ij} \tag{15}$$

where s_6 is a global, dimensionless scaling parameter, C_6^{ij} denotes the dispersion coefficient for the atom pair $\{i, j\}$, R_{ij} is the distance between the atoms in the pair, and $f_{ij} = (1 + e^{-d(R_{ij}/R_r - 1)})^{-1}$ is a Fermi damping function in which d is an empirically obtained scaling parameter and R_r is the sum of the atomic vdW radii R_0. Ortmann and collaborator's proposal is essentially equivalent but for the choice of the damping function, which they set to be $f_{ij} = (1 - e^{-d(R_{ij}^n)})$, with $n = 8$ (for $n < 7$, ε_{vdW}^{ij} diverges at $R_{ij} = 0$). The specific atomic parameters used along this thesis are listed in Table 1

The vdW correction to the energy does not affect the electronic structure, as it is not a functional of the electronic density $\rho(\boldsymbol{r})$, but it is essential for accurately determining the ionic configuration.

2.2.4 *Pseudopotentials*

Most of the interesting physics in a solid are determined by the valence electrons of the atoms, and not by the internal electrons. The chemical bonds among atoms always involve the outer–most electron shells, leaving the core electrons almost unaltered. With the aim of reducing the enormous computational effort of describing very accurately the most internal levels, we substitute the true atomic potentials with the so–called pseudopotentials (PPs), which will have, in general, the following properties:

(i) The core electrons remain unmodified upon the chemical bonding.

(ii) The valence electrons will feel an effective potential due to the core region

(iii) The core is determined by a fixed core radius (r_c) for every element.

(iv) The strong oscillations within (r_c) due to orthogonality among valence and core orbitals will be suppressed by replacing the true wavefunctions by smooth, non–oscillating pseudowavefunctions.

In summary, the pseudowavefunctions will be identical to the real wavefunctions for any $r > r_c$, being the innermost wavefunctions replaced by smoother, non–oscillating pseudowavefunctions that effectively reproduce the atomic potential outside r_c. By using PPs instead of the all–electron potential, the core electrons do not have to be addressed separately in the solution of the system, therefore the size of the matrices that have to be treated numerically (and thus the computational effort) is drastically reduced. Different approaches may now be taken to determine the exact form of the pseudopotential. One of the usual additional constraints requires the PPs to have the same integrated density inside r_c as the all–electron wavefunction, leading to the so–called norm–conserving PPs [31, 32, 33, 34]. In particular, the norm–conserving PPs derived by Troullier and Martins [31] were used in this thesis in the calculations carried out with the SIESTA-GREEN package [35, 36]. Norm–conserving PPs do not pose a great advantage when dealing with the elements of the first row of the periodic table nor with some transition metals, in the sense that they are not much smoother than the all–electron wavefunctions due to this additional restriction. To circumvent this issue, Vanderbilt proposed to relax this constriction for the PPs in the early 90s, leading to the creation of the so–called ultrasoft PPs. [37] The full electronic density is added back before the normalisation of the total wavefunction. This kind of PPs allows for good convergence with much smaller basis sets in, for example, plane-wave based DFT codes such as VASP.

2.2.5 *Spin–Orbit Coupling*

The spin–orbit coupling (SOC) is a relativistic effect that couples the spin of the electrons to their angular momentum. Expanding the four–component Dirac equation in a power series of $(mc)^{-2}$ [38], we get a first order term (second order in mc) of the form:

$$H_{SOC} = \frac{\hbar}{4m^2c^2}\Big(\boldsymbol{\nabla} V^{KS}(\boldsymbol{r}) \times \boldsymbol{p}\Big) \cdot \boldsymbol{\sigma} \tag{16}$$

where $V^{KS} = E - T$ is the Kohn–Sham potential and $\boldsymbol{p}$ the momentum operator and $\boldsymbol{\sigma}$ is the vector of Pauli spin matrices $\boldsymbol{\sigma} = (\sigma_x, \sigma_y, \sigma_z)$. In order to be able to compute the SOC term, and because its effect is only large in the surroundings of the nuclei, $V^{KS}(\boldsymbol{r})$ is assumed spherical and approximated by $V_0^{KS}(r)$, so we can rewrite Eq. 16 as:

$$H_{SOC} = \frac{\hbar}{4m^2c^2}\frac{1}{r}\frac{\partial V_0^{KS}(r)}{\partial r}\boldsymbol{L} \cdot \boldsymbol{\sigma} \tag{17}$$

where $\boldsymbol{L}$ is the angular momentum operator. This effect can be understood semi–classically as the interaction between the spin magnetic moment of the electron and the magnetic field generated by the (charged) nucleus rotating around the electron (in the electron's reference frame). Spin and orbital momenta are now coupled and S_z and L_z are no longer good quantum numbers. Instead, the *total* angular momentum $\boldsymbol{J} = \boldsymbol{L} + \boldsymbol{S}$ can be used, as $\boldsymbol{J}$ and J_z do commute with the Hamiltonian. In the VASP package, the SOC can be included in the total Hamiltonian $H_{Tot} = H_{DFT} + H_{SOC}$ and thus calculated self–consistently. The matrix elements of H_{Tot} are computed by using the atomic all–electron orbitals, determined for the atoms within a scalar–relativistic approximation [39]. In the SIESTA-GREEN package, the SOC is included self–consistently in the KS equations following the method described in Refs. [40, 36]. In this approximation the effect of SOC is directly included at the PP level by constructing fully–relativistic PPs. This is achieved by solving the Dirac equation for isolated atoms. The fully–relativistic (pseudo–)potential will be of the form:

$$\widetilde{V}_{FR} = \sum_{l,J_\pm} V_{l,J_\pm}(r)\widetilde{P}_{l,J_\pm} \tag{18}$$

where $J_\pm = l \pm 1/2$, being $J_\pm(J_\pm + 1)$ the eigenvalue of the total angular momentum operator $\boldsymbol{J}^2$, $V_{l,J_\pm}(r)$ is the radial part of the (pseudo–)potential, and the projector $\widetilde{P}_{l,J_\pm}$ expands the $(2J + 1)$ degenerate subspace of $\boldsymbol{J}^2$:

$$\widetilde{P}_{l,J_\pm} = \sum_{m_J=-(l\pm1/2)}^{l\pm1/2} |lJ_\pm, m_J\rangle\langle lJ_\pm, m_J| \tag{19}$$

The explicit expressions for $|lJ_\pm, m_J\rangle$ can be obtained in terms of the spherical harmonics through the Clebsch-Gordan coefficients $C^l_{J,m_J;m,\sigma}$:

$$|lJ, m_J\rangle = \begin{pmatrix} C^l_{J,m_J;m_J-1/2,\uparrow}|l, m_J - 1/2;\uparrow\rangle \\ C^l_{J,m_J;m_J+1/2,\downarrow}|l, m_J + 1/2;\downarrow\rangle \end{pmatrix} \tag{20}$$

It is clear that the (pseudo–)wavefunctions have to be expressed as spinors, so the basis for solving the KS equations including H_{SOC} must now be doubled to account for the spin degree of freedom. The local spin–resolved density $\rho(\boldsymbol{r})$ becomes a (2×2) matrix of the form:

$$\rho(\boldsymbol{r}) = \begin{pmatrix} \rho_{\uparrow\uparrow}(\boldsymbol{r}) & \rho_{\uparrow\downarrow}(\boldsymbol{r}) \\ \rho_{\downarrow\uparrow}(\boldsymbol{r}) & \rho_{\downarrow\downarrow}(\boldsymbol{r}) \end{pmatrix} \tag{21}$$

where the subindices indicate the spin (up or down). The magnetic moment density $\boldsymbol{m}(\boldsymbol{r})$ can thus be obtained as:

$$\boldsymbol{m}(\boldsymbol{r}) = Tr[\rho(\boldsymbol{r})\boldsymbol{\sigma}] \tag{22}$$

being the explicit form of the $\boldsymbol{m}(\boldsymbol{r}) = (m_x, m_y, m_z)$ components:

$$\begin{aligned} m_x(\boldsymbol{r}) = &\quad \rho_{\uparrow\downarrow}(\boldsymbol{r}) + \rho_{\downarrow\uparrow}(\boldsymbol{r}) \\ m_y(\boldsymbol{r}) = &\quad i(\rho_{\uparrow\downarrow}(\boldsymbol{r}) - \rho_{\downarrow\uparrow}(\boldsymbol{r})) \\ m_z(\boldsymbol{r}) = &\quad \rho_{\uparrow\uparrow}(\boldsymbol{r}) - \rho_{\downarrow\downarrow}(\boldsymbol{r}) \end{aligned} \tag{23}$$

2.2.6 *SIESTA-GREEN*

SIESTA stands for Spanish Initiative for Electronic Simulations with Thousands of Atoms. The name SIESTA is used both for denoting the numerical method developed by Soler and collaborators [35] and the DFT code that implements it. In this thesis we have made use of SIESTA through the SIESTA-GREEN package developed by Cerdá and Cuadrado [41], which additionally includes the possibility of incorporating SOC self–consistently [36] and can calculate the system's Green function. In the SIESTA code the KS equations are solved in an atomic orbital basis set. The Kohn-Sham wavefunctions $\Psi_i^{KS,m,\sigma}(\boldsymbol{r})$ are therefore written as:

$$\Psi_i^{KS,m,\sigma}(\boldsymbol{r}) = \sum_{\mu} c_{\mu,i}^{m,\sigma} \phi_\mu(\boldsymbol{r}) \tag{24}$$

where $\phi_\mu(\boldsymbol{r})$ is an atomic orbital, σ denotes the spin component, m stands for the other relevant quantum numbers (band index and/or k–point for instance), and $c_{\mu,i}^{m,\sigma} = \langle \phi_\mu | \Psi_i \rangle$ The eigenstates will be obtained by solving

$$\hat{h}^{KS,\sigma} \Psi_i^{KS,\sigma}(\boldsymbol{r}) = \epsilon_i^{KS,\sigma} \Psi_i^{KS,\sigma}(\boldsymbol{r}) \tag{25}$$

and the resulting density matrix will be

$$\rho_{\mu\nu}^{\sigma} = \sum_i n_i c_{i\nu}^{\sigma} c_{\mu i}^{\sigma} \tag{26}$$

SIESTA employs as the basis set localised numerical orbitals which are obtained by solving the Schrödinger equation for the isolated atom within the PP approximation. Atomic orbitals extend to infinity, but as they decay rapidly for large r, a confinement energy is set so that the extension of the numerical orbitals becomes finite. The resulting wavefunctions are named pseudo–atomic orbitals (PAOs) and will be constituted by a radial function times a spherical harmonic, just like the hydrogen–like atoms:

$$\phi_{nlm}(\boldsymbol{r}_I) = \chi_{nl}(r_I) Y_{lm}(\hat{\boldsymbol{r}}_I) \tag{27}$$

where n, l and m denote the principal, angular moment and magnetic quantum numbers respectively, $\boldsymbol{r}_I = \boldsymbol{r} - \boldsymbol{R}_I$ corresponds to the position of the orbital with respect to the atomic position $\boldsymbol{R}_I$, and $\chi_{nl}(r_I)$ describes the radial part of the orbital. It is crucial to decide the number of orbitals taken into consideration in each calculation. The simplest approach will be to use one PAO for every occupied atomic orbital in the ground state of the corresponding atoms, which in this context is called simple–ζ (SZ) approximation, and this approach works well for isolated atoms. Nevertheless, for molecules and solids, increasing the basis set leads to better results. This can be done in two ways: we may use more than one PAO to describe each of the atomic

orbitals in the system, and we may also include unoccupied orbitals with higher angular momentum. The second PAO for each orbital is constructed by polarising the l-shell in the case of partially occupied orbitals, which effectively generates a shell of orbital momentum $l+1$ and identical principal quantum number n. All the elements (Bi, Se, Sb, Te, Cr, Au) that constitute the systems studied in this thesis have been described in a *spd* orbital basis with confinement energies of 100 meV, where the s and p orbitals are of the double–ζ (DZ) polarised type following the *splitnorm* scheme with a fixed value of 0.15 [35]. The d orbitals used are of the SZ type for Bi, Se, Sb and Te, since they are completely filled in the isolated atoms and chemically inactive, and of the same DZ type as the s and p orbitals for Cr and Au.

2.2.7 *VASP*

The Vienna *ab initio* Simulation Package (VASP) is a widely used DFT code developed by Hafner, Kresse and collaborators [42, 43]. It solves the KS equations in a basis of plane waves, as opposed to SIESTA, in which the basis is composed of atomic orbitals. The wave function at each k–point can be expanded in a Fourier series:

$$\Psi^{KS}_{n,\boldsymbol{k}}(\boldsymbol{r}) = \sum_{\boldsymbol{g}} b_{n,\boldsymbol{k},\boldsymbol{g}} e^{i(\boldsymbol{g}+\boldsymbol{k})\cdot\boldsymbol{r}} \tag{28}$$

where $b_{n,\boldsymbol{k},\boldsymbol{g}}$ is a complex coefficient. The series is infinite in principle, but the terms become small for large $|\boldsymbol{g}+\boldsymbol{k}|$, so we can set a plane–wave cut–off $|\boldsymbol{g}+\boldsymbol{k}| < G_{\mathrm{cut-off}}$ that truncates the basis set. The cut–off is not known *a priori* and has to be converged for every specific system. The value of the cut–off is usually given in units of energy, being the conversion to the cut–off in plane waves $\frac{\hbar^2}{2m_e}|\boldsymbol{g}+\boldsymbol{k}|^2 < E_{\mathrm{cut-off}}$. We chose the projector augmented wave (PAW) method for the PPs in all our VASP calculations, developed by Blöchl [44], by which the all–electron wavefunctions $|\Psi_{ae,n}\rangle$ are mapped into pseudowavefunctions $|\Psi_{ps,n}\rangle$ by the following linear transformation:

$$|\Psi_{ae,n}\rangle = |\Psi_{ps,n}\rangle + \sum_i (|\phi_{ae,i}\rangle - |\phi_{ps,i}\rangle)\langle p_i|\Psi_{ps,n}\rangle \tag{29}$$

where the index i includes the atomic site $\boldsymbol{R}$, angular momentum quantum numbers l, m and momentum k, $\phi_{ae,i}$ are the all–electron partial waves and $\phi_{ps,i}$ are the pseudo–partial waves which are equivalent to $\phi_{ae,i}$ outside the core radius, and projector functions p_i belong to the dual space of the pseudo partial waves [45]:

$$\langle p_i|\phi_{ps,j}\rangle = \delta_{ij} \tag{30}$$

By means of this transformation, all–electron observables can be mapped to physical variables obtained with the PP method with a considerably smaller computational effort, since the number of plane waves needed to describe each atom is drastically reduced compared to all–electron methods or even norm–conserving PP methods. For further details see Ref. [46].

2.3 COMPUTATIONAL DETAILS

All the calculations presented in this thesis (but for Chapter 7) have been carried out within the DFT framework as implemented in the VASP [43, 42]

and SIESTA-GREEN [35, 41] packages. In both calculation schemes SOC can be included in a self–consistent manner. The PBE exchange-correlation functional [27] was chosen within the GGA in every case. For bulk systems k–meshes of (13×13×13) were used. A (13×13×n_k) k–point mesh was used for slab calculations with and without SOC (n_k depending on the slab thickness) while exceptionally fine meshes of (65×65×1) had to be employed when including SOC to achieve convergence for non–centrosymmetric slab systems in Chapter 5 (see explanation in 5.4.5). The ultra–fine k–mesh calculations could only be carried out with the SIESTA-GREEN code due to computational limitations. The electronic temperature in the Fermi-Dirac distribution was set to k_BT =10 meV in all calculations.

Ionic relaxations of bulk and slab systems were calculated with Grimme's DFT-D2 [29] method in VASP, which includes vdW interactions by adding a semi-empirical dispersive potential to the energy functional. This method yields very good results for non–defective Bi_2Se_3 systems (see Chapter 3). The specific parameters used for the vdW potential are listed in Table 1. The atoms were allowed to relax until forces among them reached values smaller than 0.02 eV/Å. The convergence criterion for electronic self–consistent calculations with SIESTA was set to the difference in energy between the input and output density matrices $\rho(\boldsymbol{r})$ being below 1 meV for every matrix element. For VASP calculations, the stopping criterion for the self–consistent loop is that the input and output total free energy *and* the initial and final set of energy eigenvalues (band structure) differ both by less than 0.1 meV.

For VASP calculations, the plane wave cut–off for the basis set was chosen to be 340 eV. For SIESTA-GREEN, the atomic orbital basis was generated within a double ζ-polarised scheme with confinement energies of 100 meV. An ultrafine mesh cut–off of 1200 Ry. was employed for three–centre integrals, which is equivalent to a real space resolution below 0.05 $Å^3$.

3

BULK AND SURFACE PROPERTIES

3.1 INTRODUCTION

In this chapter we will describe the bulk properties of the Bi_2Se_3 family of compounds studied along the thesis, namely Bi_2Te_3, Sb_2Te_3, Bi_2Se_3 and Sb_2Se_3. The first three are known to be 3D strong topological insulators [7], while antimony selenide is usually predicted to be a trivial insulator, although the proper growth of this material in the rhombohedral phase remains an open challenge and, therefore, experimental confirmation of its non-topological nature is still to come. These materials, and particularly the Bi-based ones, have been studied since the 60s for their outstanding thermoelectric properties, and have aroused a great interest in the last decade after the prediction and later discovery of their topological properties. In particular, Bi_2Se_3 is considered the paradigm of 3D TIs, being the one with the largest band gap known to date ($\sim$ 300 meV). Along with Bi_2Te_3, it is one of the most studied TIs up to date (see Figure 1).

3.2 CRYSTAL STRUCTURE

This family of dichalcogenides obeys the formula X_2Y_3 with X=Bi, Sb and Y=Te, Se, and crystallises in the rhombohedral space group $R\bar{3}m$ (D^5_{3d}). The crystal structure is of the tetradymite type. In the following discussion we will refer to Bi_2Se_3 (X=Bi and Y=Se), but the description is general for the four compounds. The system can be described as a layered compound in which every atomic layer is hexagonally compact and is formed of only one chemical species. The most convenient building block of the crystal is called quintuple layer (QL) and is constituted of five consecutive atomic layers alternating Se and Bi ones, so that the sequence is Se1-Bi-Se2-Bi-Se1. The two Bi atoms occupy equivalent positions, while the Se atom in the middle of a QL is inequivalent to the external Seleniums, and the former is usually labelled as Se2 to distinguish it from the outer Se1 atoms. Along the (111) direction the system is similar to an face–centred cubic (*fcc*) crystal, showing hexagonal compact layers with a stacking pattern of the form ... AbCaB CaBcA BcAbC ... When expressing stacking sequences, we will use capital letters for Se atoms along the whole thesis for clarity, and small letters for Bi atoms. Therefore, the primitive unit cell contains only one QL, whereas the conventional hexagonal unit cell spans over three QLs (see Fig. 2). Each atom has six first nearest neighbours (n.n.), half on the upper atomic layer and the other half in the layer below, and another six next nearest neighbours (n.n.n.) in its own atomic layer. The interactions between adjacent layers are strong within a QL, while vdW forces dominate the Se1-Se1 interaction which binds together consecutive QLs. For this reason, a Se1-terminated (111) surface is the energetically most favourable surface of these systems. The whole crystal can be described by means of the in–plane and perpendicular lattice

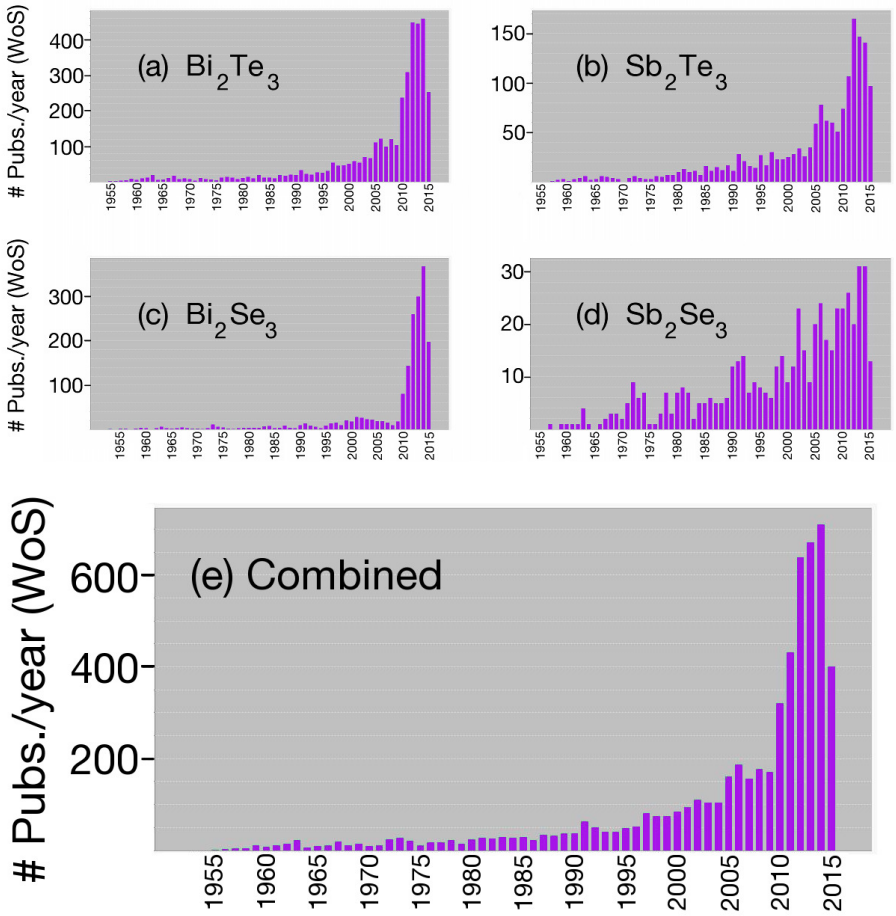

Figure 1: Number of publications per year referring to: (a) Bi_2Te_3, (b) Sb_2Te_3, (c) Bi_2Se_3, (d) Sb_2Se_3, and (e) any of the four. A huge increase for the four materials can be seen after 2009, when they were theoretically predicted to be 3D TIs (but for Sb_2Se_3). Sb_2Se_3 is by far the least mentioned of the four members for two main reasons: it has been predicted to be a trivial insulator and it has not been synthesised in the rhombohedral phase to confirm or deny this prediction. Data taken from Thomson Reuters' Web of Science database.

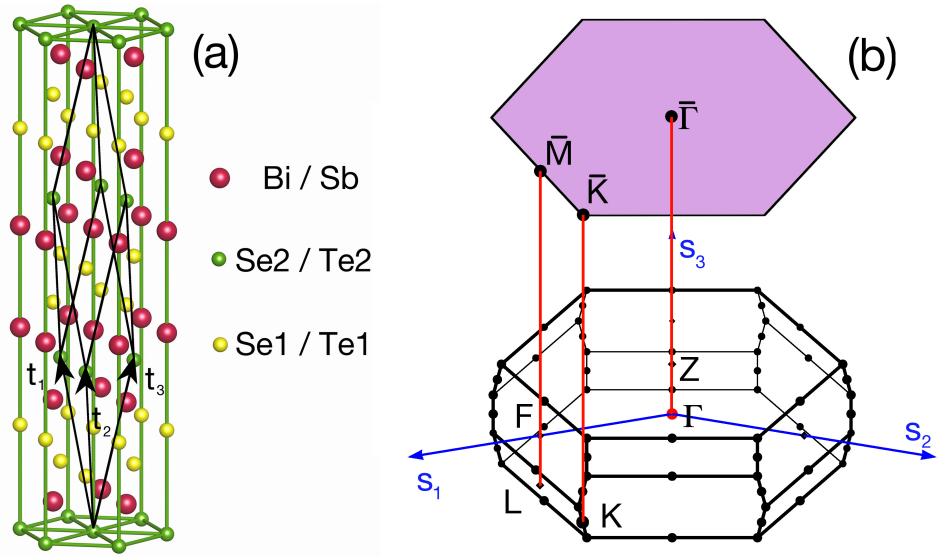

Figure 2: (a) Crystal structure of the Bi_2Se_3 family of compounds. The rhombohedral unit cell is shown in black lines, and the arrows indicate the lattice vectors. (b) First BZ. The reciprocal lattice vectors are depicted as blue arrows. Four inequivalent high symmetry points are marked: $\Gamma = (0,0,0)$, $F = (\pi,\pi,0)$, $L = (\pi,0,0)$ and $Z = (\pi,\pi,\pi)$. The hexagonal 2D first BZ of the (111) surface is additionally shown on top along with the bulk BZ projections.

parameters of the conventional hexagonal unit cell, a and c respectively, and the inner coordinates of the Bi and Se1 atoms with respect to the Se2 atom, μ and ν respectively. The lattice vectors $\boldsymbol{t}_{1,2,3}$ shown in Figure 2(a) are:

$$\begin{aligned} \boldsymbol{t}_1 &= (-a/2, -\sqrt{3}a/6, c/3) \quad ; \\ \boldsymbol{t}_2 &= (a/2, -\sqrt{3}a/6, c/3) \quad ; \\ \boldsymbol{t}_3 &= (0, \sqrt{3}a/3, c/3) \quad . \end{aligned} \tag{31}$$

and their corresponding reciprocal lattice vectors given by $\boldsymbol{s}_i \cdot \boldsymbol{t}_j = 2\pi\delta_{ij}$ and shown in Figure 2(b) will be:

$$\begin{aligned} \boldsymbol{s}_1 &= \frac{2\pi}{a}(-1, -\sqrt{3}/3, a/c) \quad ; \\ \boldsymbol{s}_2 &= \frac{2\pi}{a}(1, -\sqrt{3}/3, a/c) \quad ; \\ \boldsymbol{s}_3 &= \frac{2\pi}{a}(0, 2\sqrt{3}/3, a/c) \quad . \end{aligned} \tag{32}$$

With the Se2 atom in the origin, the positions of the Bi atoms will be $(0,0,\pm\mu c)$, and the Se1 positions will be given by $(0,0,\pm\nu c)$ in Cartesian coordinates. Note that the $R\bar{3}m$ space group is centrosymmetric, being the inversion centre precisely the Se2 atom. The system also exhibits three–fold rotation symmetry (C_3) and three vertical mirror planes. The experimental and calculated lattice parameters and inner coordinates for the bulk systems of the Bi_2Se_3 family of compounds are shown in Table 2.

As the interaction between adjacent QLs is of the vdW kind, it is important to include the vdW correction in the DFT calculations as described in 2.2.3. In Figure 3 the total energy for Bi_2Se_3 and Bi_2Te_3 is shown as a function

	Bi_2Te_3	Sb_2Te_3	Bi_2Se_3	Sb_2Se_3
a (Å)	4.40 (4.383)	4.25 (4.25)	4.17 (4.138)	4.04 (-)
c (Å)	30.5 (30.487)	30.9 (30.35)	28.4 (28.64)	28.7 (-)
μ	0.399 (0.400)	0.397 (0.400)	0.399 (0.399)	0.398 (-)
ν	0.211 (0.212)	0.213 (0.211)	0.211 (0.206)	0.214 (-)

Table 2: Calculated values of the lattice parameters and internal coordinates of the Bi_2Se_3 family of compounds. Relaxations were carried out with VASP with GGA+vdW. Values in parentheses correspond to experimental data from Ref.[47]. No experimental data was found for Sb_2Se_3 in the rhombohedral phase.

of the lattice parameters, which illustrates the importance of including vdW interactions for lattice relaxations. It is clear that without this correction to the energy the relaxed lattice parameters are further away from the experimental value. GGA overestimates a by ∼3% in both systems, and c by ∼4% in Bi_2Te_3. Furthermore, GGA without vdW predicts Bi_2Se_3 to be an unbound compound, as the total energy continuously decreases with increasing c –see Fig 3(a)–.

3.3 BAND STRUCTURES

In this section we show the electronic structure of the bulks of Bi_2Te_3, Sb_2Te_3, Bi_2Se_3 and Sb_2Se_3. The band dispersion diagrams for the four compound are depicted in Figure 4. The valence bands (in the range of ∼ -6 to 0 eV) are predominantly of the Se p–type while the conduction bands (in the range of 0 to ∼ 6 eV) are predominantly of the Bi p–character. The SOC drives the system into an inverted band structure, meaning that the orbital character of the valence and conduction bands are locally exchanged around the Γ point of the BZ. This band inversion is responsible for the topological character of these systems. Figure 5 shows a close-up of the bands around the Fermi level with and without SOC. In the latter case, the four systems show a direct band gap at the Γ point, being the character of the valence (conduction) band mainly Se (Bi) p_z. The SOC induces the inversion of the Se p_z and the Bi p_z bands around the Γ point, preserving the gap but changing the curvature of the valence (conduction) band to hole–(electron–)like. Therefore, these systems are narrow gap semiconductors with a negative gap according to the traditional classification. This is a key feature of all TRS protected TIs, such as quantum wells of HgTe/CdTe [5], InAs/GaSb [48] and Ge/GaAs [49], which belong to the 2D TI class, or Bi_xSb_{1-x} [8], $PbBi_2Te_4$ [50] or thallium based ternary chalcogenides (for instance $TlBiSe_2$ or $TlSbTe_2$) [51, 52], which are also 3D TIs. The calculated gaps for the Bi_2Se_3 family of compounds agree quite well with the experimentally observed ones. The comparison is shown in Table 3. Although DFT usually underestimates the size of the gap for semiconductors, the inverted nature of the electronic band structure and the strong influence of the SOC in the gap give rise to accurate bulk gaps without the need of hybrid functionals or GW calculations which involve extremely resource–demanding calculations. The experiments and *ab initio* calculations carried out by other groups show a wide range of values for

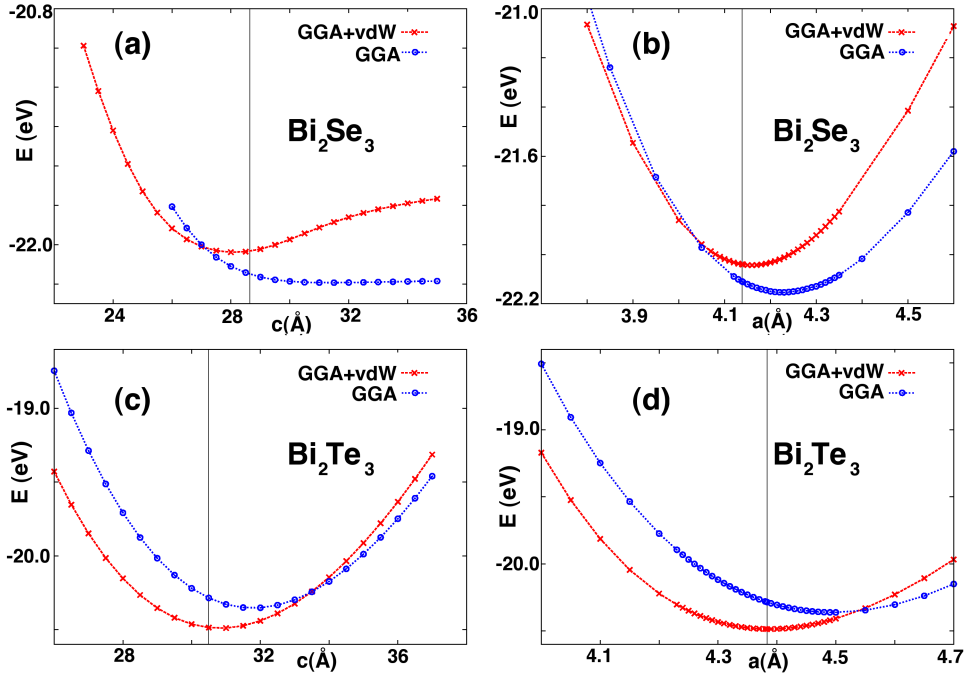

Figure 3: Total energy for Bi_2Se_3 –(a) and (b)– and Bi_2Te_3 –(c) and (d)– as a function of lattice parameters c –(a) and (c)– and a –(b) and (d)–. Lattice parameter a [c] was fixed to its experimental value in Figures (a) and (c) [(b) and (d)]. The vertical lines are the experimental lattice constants. The calculations carried out with (without) the vdW corrections correspond to the red (blue) lines. GGA without the vdW term predicts Bi_2Se_3 to be an unbound system in the (111) direction

Bi_2Te_3, Sb_2Te_3 and Bi_2Se_3. The values we obtained are well inside those ranges.

3.4 SURFACE STATES AND TOPOLOGICAL PROPERTIES

The Bi_2Se_3 family of compounds is probably the most extensively studied group of 3D TIs. Bi_2Te_3, Sb_2Te_3 and Bi_2Se_3 have been theoretically predicted and experimentally confirmed to be topologically non–trivial, while Sb_2Se_3 has been predicted to be a normal insulator [7], but experiments regarding its topological features remain unclear, partly because although it is predicted to crystallise in the rhombohedral phase isostructural to the other members of the family, at ambient pressure it has only been observed in an orthorhombic phase (*Pnma*) [53]. Moreover, recent DFT results from other groups predict a band structure for Sb_2Se_3 which shows the characteristic "M"–like curvature of band inversion around the Γ point, although its possible topological nature is unfortunately not analysed in their published work [54].

In particular, these materials belong to the $\mathbb{Z}_2$ topological class of TRS protected TIs. Schnyder *et al.* published an exhaustive classification (see Ref. [55]) of TIs, according to which 3D insulators that fulfil TRS but not particle–hole symmetry or chiral symmetry belong to the $\mathbb{Z}_2$ symmetry class. This means that topological invariant that characterises this class can only be 0 –for trivial insulators– or 1 –for what we will call TIs from now on, as

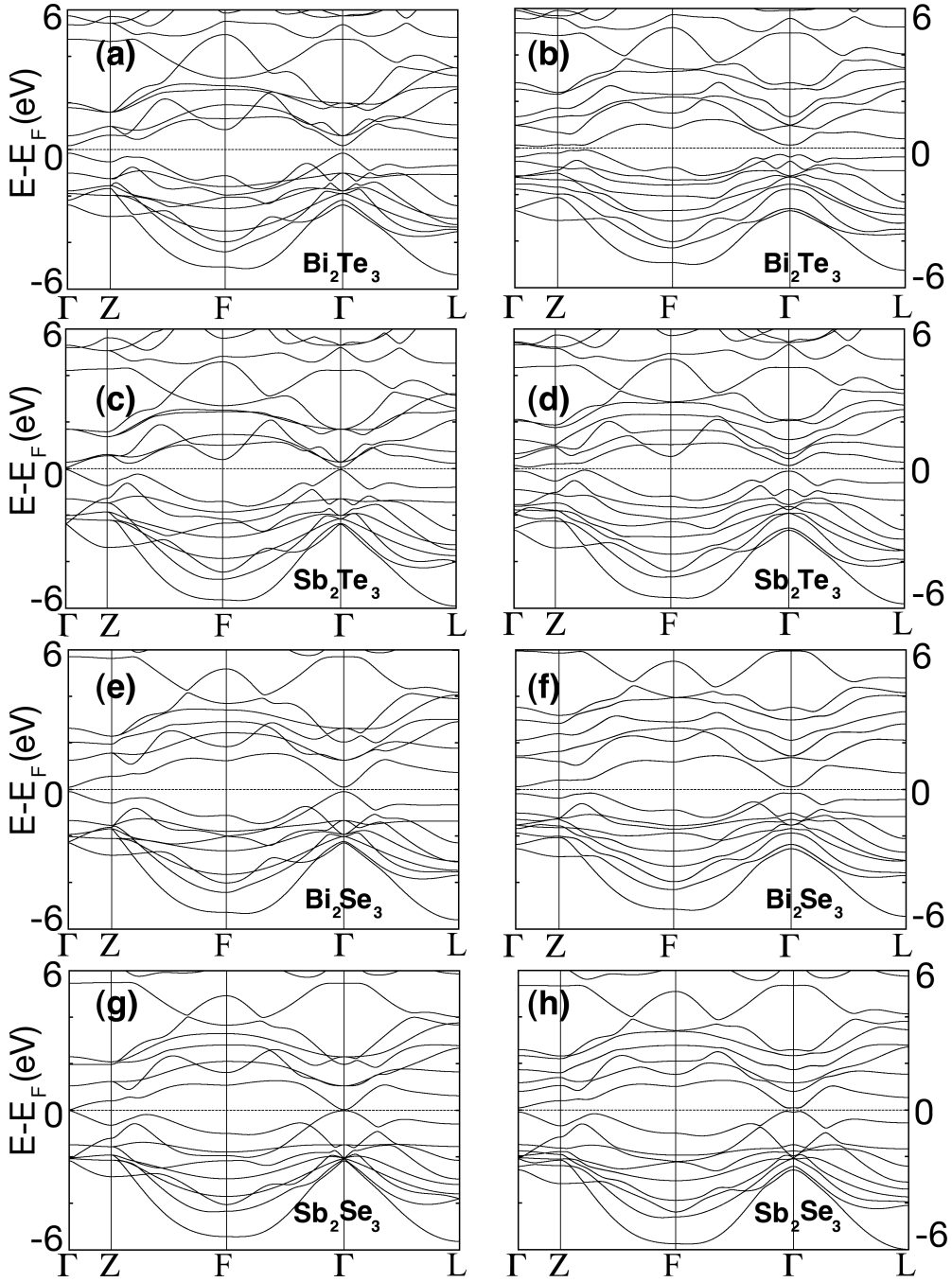

Figure 4: Band structure along high symmetry lines for the Bi_2Se_3 family of compounds without (first column) and with (second column) SOC. The Fermi level is indicated with a horizontal dashed line as a guide to the eye.

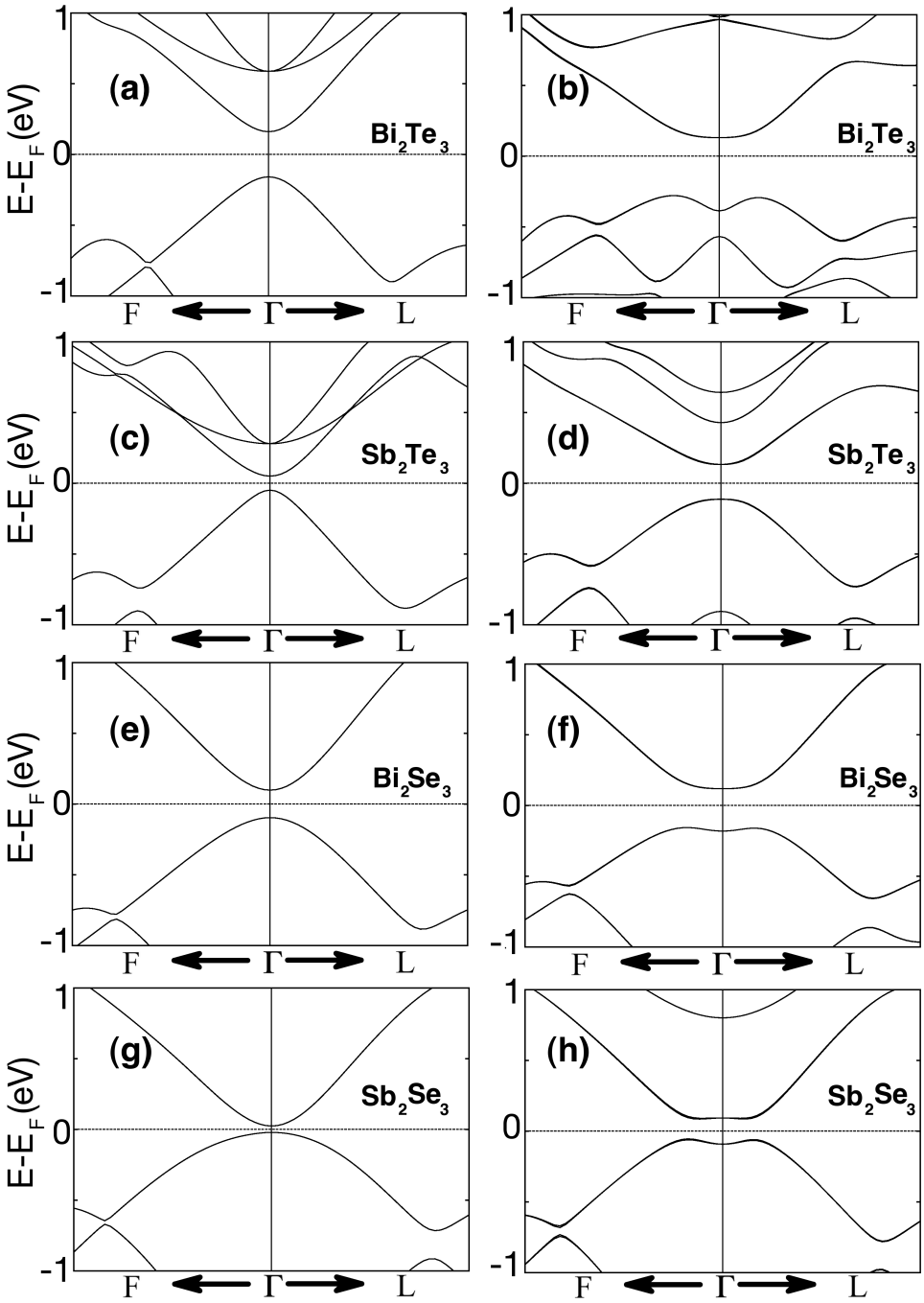

Figure 5: Close–up of the band structure around the Γ point for the Bi_2Se_3 family of compounds without (first column) and with (second column) SOC. The band inversion is already apparent in the change of curvature of the valence and conduction bands.

			This Work	
	Exp	DFT (other)	VASP	SIESTA
Bi_2Te_3	0.15[a], 0.16[b], 0.35[e], 0.17[h], 0.13[i,l], 0.16-0.20[j], 0.22[k]	0.10[α], 0.11[γ]	0.15	0.2
Sb_2Te_3	0.3[a] , 0.28[g], 0.21[l]	0.13 [α]	0.13	0.38
Bi_2Se_3	0.35[a], 0.2[c,m] , 0.3[d,f], 0.17[e]	0.26 [α], 0.21-0.31[β], 0.24[γ]	0.27	0.32
Sb_2Se_3	-	0.20[α]	0.14	0.23
	a Ref [60], *b* Ref [61], *c* Ref [62]	*α* Ref [54]		
	d Ref [63], *e* Ref [64], *f* Ref [65]	*β* Ref [66]		
	g Ref [67], *h* Ref [68], *i* Ref [69]	*γ* Ref [70]		
	j Ref [71], *k* Ref [72], *l* Ref [73]			
	m Ref [74]			

Table 3: Comparison of bulk band gap for several experimental and theoretical works for the Bi_2Se_3 family of compounds. Small discrepancies are found both theoretically and experimentally. Note that due to the band inversion, the valence bands acquire a letter "M" shape and the gap becomes indirect, particularly for Bi_2Te_3. This might explain the discrepancies with the experimental results.

opposed to normal insulators (NIs)–. There are several approaches to calculate this invariant [56, 57] that comprise integrating the Berry curvature over the BZ or counting the pairs of complex zeros of the Pfaffian of an antisymmetric matrix defined by the overlaps of time reversal [58][59]. Fortunately, the $R\bar{3}m$ space group has an inversion centre, and the calculation of the $\mathbb{Z}_2$ invariant for inversion–symmetric systems is reduced to computing the parity of the occupied bands at the time–reversal invariant momenta (TRIM) of the BZ. We will follow the approach of Fu and Kane described in Ref [58], and define δ_i as:

$$\delta_i = \prod_{m=1}^{N} \xi_{2m}(\Gamma_i) \tag{33}$$

where $\xi_{2m}(\Gamma_i) = \pm 1$ is the parity eigenvalue of the $2m$–th occupied band at the TRIM labelled by Γ_i, and 2N is the number of occupied bands. Because of TRS, at TRIM every band is degenerate with its Kramers partner and $\xi_{2m} = \xi_{2m-1}$, so the product only takes into account each Kramers pair once. With the above definition, the $\mathbb{Z}_2$ invariant ν_0 will be given by:

$$(-1)^{\nu_0} = \prod_{\Gamma_i} \delta_i \tag{34}$$

where the product is over all TRIM of the BZ.

In fact, by simple inspection of the band structures we can see that a band inversion can only occur at the Γ point. Therefore, since the system is topologically trivial without the SOC, it suffices to see if ν_0 changes sign when including the spin–orbit interaction. Tables 4 and 5 show the parities of the occupied bands (and the first unoccupied band) for the four systems without and with SOC respectively. The value of δ_Γ is shown in red in the righmost column. All four crystals are topologically trivial without including spin–orbit, and SOC induces several band inversions among the occupied bands. The only relevant inversion for our current purpose is the one between the conduction and valence bands (CB and VB respectively) which are of opposite parities. Close to the Γ point, the CB (VB) without SOC corresponds to a Bi or Sb (Se or Te) p_z band with positive (negative) parity eigenvalue. Turning on the SOC inverts the situation in the sense that the CB is now Se or Te p_z like and *vice versa*, while the band gap is preserved. Therefore we may conclude that SOC drives a topological band inversion that turns Bi_2Te_3, Sb_2Te_3, Bi_2Se_3 and Sb_2Se_3 into $\mathbb{Z}_2$ TRS protected 3D TIs. According to other theoretical calculations, Sb_2Se_3 is expected to remain a trivial insulator [7] even in the presence of SOC. This is usually attributed to the fact that the strength of the spin–orbit interaction is smaller in Sb_2Se_3 than in the rest of the Bi_2Se_3 family of compounds because of the smaller atomic number (Z) of its constituents (the atomic SOC scales roughly as Z^4). Nonetheless, our calculations predict such a small band gap without SOC that the inversion still takes place. Experimental verification has not been carried out to our knowledge confirming nor denying the topological character of Sb_2Se_3. Moreover, no experimental data is available for the rhombohedral phase of Sb_2Se_3, and only theoretical predictions of the crystal structure can be found. Very small variations in the lattice parameters and internal coordinates of this

Bi_2Te_3	+	−	+	−	+	+	−	−	−	+	+	−	−	−	;	+	(+)
Sb_2Te_3	+	−	+	−	+	+	−	−	−	+	+	−	−	−	;	+	(+)
Bi_2Se_3	+	−	+	−	+	−	+	−	−	+	+	−	−	−	;	+	(+)
Sb_2Se_3	+	−	+	−	+	−	−	−	+	+	+	−	−	−	;	+	(+)

Table 4: Parity in Γ of all 14 occupied bands ξ_m and first unoccupied band for the Bi_2Se_3 family of compounds (without SOC). The righmost column indicates the total parity (product) of all occupied bands.

Bi_2Te_3	+	−	+	−	+	−	+	+	−	+	−	−	−	+	;	−	(−)
Sb_2Te_3	+	−	+	−	+	+	−	+	−	+	−	−	−	+	;	−	(−)
Bi_2Se_3	+	−	+	−	+	−	+	−	−	+	+	−	−	+	;	−	(−)
Sb_2Se_3	+	+	−	−	+	−	+	−	+	−	+	−	−	+	;	−	(−)

Table 5: Parity in Γ of all 14 occupied Kramers pairs ξ_{2m} and first unoccupied band for the Bi_2Se_3 family of compounds (including SOC). The righmost column indicates the total parity (product) of all occupied bands.

compound can shift the valence and conduction bands and hence open or close the gap regardless of SOC [75]. Finally, a very recent theoretical work reports an inverted band structure for Sb_2Se_3 [54] in agreement with our calculations.

A non-zero ν_0 invariant of a system is revealed at the interface with any other system with ν_0=0 (for instance, vacuum). The bulk-to-boundary correspondence [21] states, in general, that at a boundary between two gapped systems with different values of a certain topological invariant N (N_1 and N_2 for systems 1 and 2 respectively), $|N_2 - N_1|$ interface states must exist [59]. For the $\mathbb{Z}_2$ topological class only one topologically protected interface (edge or surface) must arise, should the other material have a different value of the $\mathbb{Z}_2$ invariant (in this case ν_0). This statement can easily be checked in Bismuth dichalcogenides. Due to the weak nature of the inter-QL bonding, the (111) surface is chemically stable and we can construct slabs with an integer number of QLs in which a topologically protected surface state (TSS) will appear at each surface. Figure 6 shows the band dispersion of 1 to 10 QL slabs of Bi_2Se_3 in the surface BZ. A surface state appears that spans the whole bulk band gap, and is only present when SOC is included in the calculation. The TSS penetration depth is around 2 QLs, and despite its topological protection, a gap in the spectrum opens for slabs smaller than ∼4 QLs. This is due to hybridisation of the TSS belonging to opposite surfaces [76]. In fact, the penetration depth of the surface states all across the bulk band gap is precisely ∼2 QL as shown in Figure 7, so that surface-surface interaction takes place below twice this value. The TSS is linear above the Fermi level, although it acquires some mass when approaching the VB. This is clearly seen in the occupied surface states of Bi_2Se_3 displayed in Figure 6. Nevertheless, this surface state is usually called Dirac cone (DC) and the crossing point is called Dirac point (DP) accordingly. In Figure 8 the energy levels for all occupied and unoccupied states close to Fermi in the $\bar{\Gamma}$ point is displayed, showing again the aforementioned hybridisation gap. Note also that both DPs are pinned to the Fermi level, as there is no other state in their

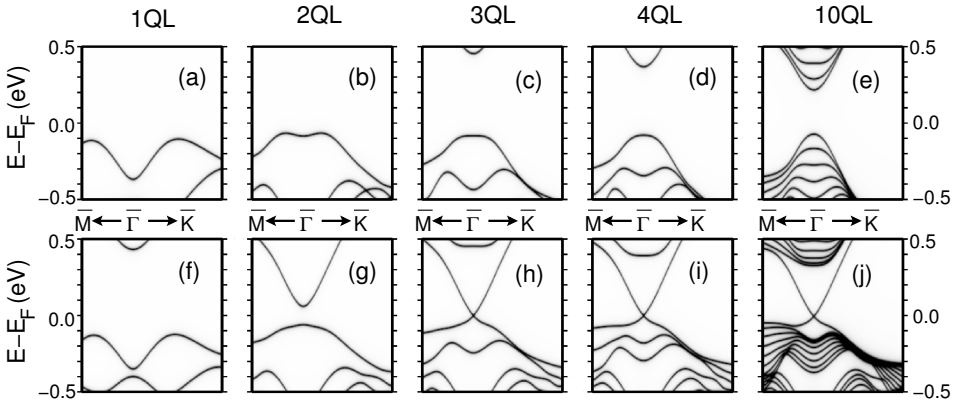

Figure 6: Band dispersion around the surface $\bar{\Gamma}$ point close to the Fermi level for Bi_2Se_3 slabs of different thicknesses without SOC –(a) to (e)– and with SOC –(f) to (j)–. The TSS is clearly only present when SOC is included. The hybridisation gap of the TSS is closed at ~ 4 QL.

vicinity and they are inside the bulk band gap. The quantum well behaviour of the states with the slab thickness [77, 78, 79] is also made patent in the figure.

The topological nature of the surface states of the Bi_2Se_3 family of compounds is also exhibited in their spin texture. The strong SOC present in these systems tightly couples the electron's spin to its angular momentum, and in the case of 3D TRS–protected TIs the TSSs show a circular skyrmion–like spin texture. This feature forbids backscattering of the electrons as long as TRS is preserved, and, as the surface states are topologically protected, backscattering is suppressed even in the presence of (non–magnetic) point defects or steps, as a flip of the movement direction must come with a flip of spin. In 2D TIs the electronic transport is expected to be completely ballistic, as the edge states are one–dimensional and only forwards– and backwards–moving electrons can exist within the bulk gap, so that the absence of backscattering implies the movement direction of electrons can not change. Figure 9 shows the spin texture of the TSS of a 6 QL thick Bi_2Se_3 slab. Close to the DP the spin lies in the xy plane, always perpendicular to $\boldsymbol{k}$. A small out–of–plane component S_z develops away from the $\bar{\Gamma}$–point which oscillates with three–fold symmetry, being 0 in the $\bar{\Gamma} - \bar{M}$ direction as dictated by mirror symmetry [80]. Recall that spin angular momentum is a pseudovector and at mirror planes only the component that is orthogonal to that plane can be non–zero. This symmetry constraint is also patent in the spin texture shown in the figure, in which the direction of the spin is perpendicular to the $\bar{\Gamma} - \bar{M}$ directions (which are vertical mirror planes of the system) precisely at those high–symmetry lines. The hole–like and electron–like surface state (HSS and ESS respectively) exhibit opposite in–plane helicity and also opposite S_z for every $\boldsymbol{k}$–point. The trigonal warping is also apparent in the top view of the HSS –Figure 9 (c)–, and vanishes close to the DP.

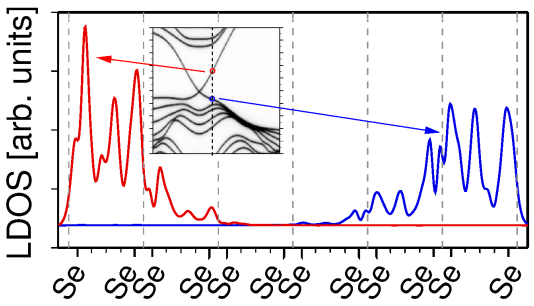

Figure 7: Surface state localisation for a 6 QL Bi_2Se_3 slab close to the $\bar{\Gamma}$ point (see inset for precise location) The TSSs are localised mostly within the 2 QLs closest to the surface. This agrees with the fact that a hybridisation gap opens for slabs smaller than 4 QLs. Note that the TSSs are doubly degenerate, and only one is shown for each surface for clarity. Vertical dashed lines indicate the position of the vdW gaps.

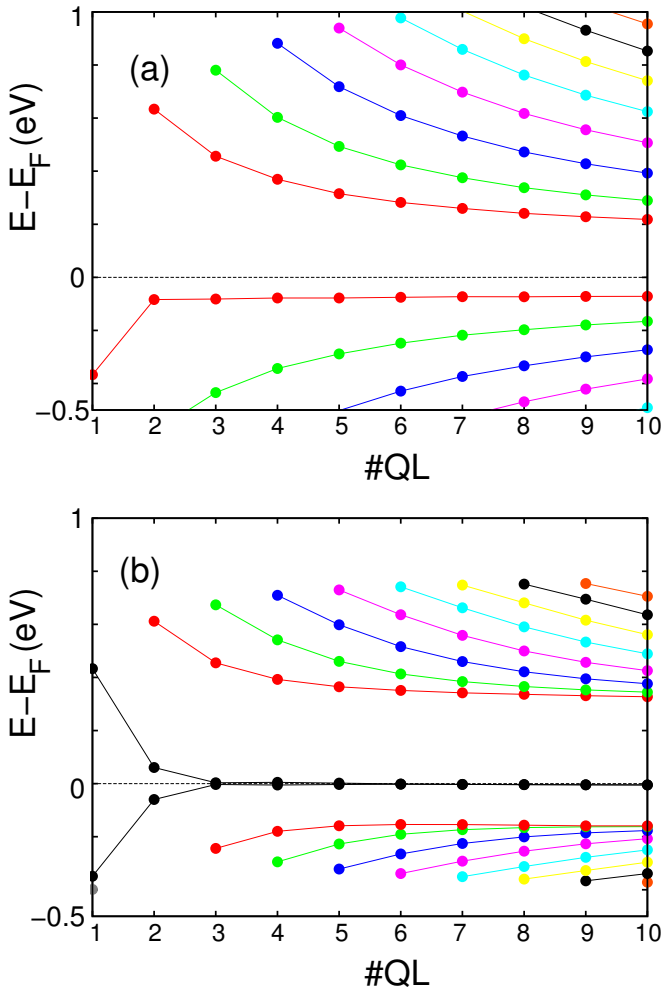

Figure 8: Energy levels in $\bar{\Gamma}$ point close to the Fermi level for Bi_2Se_3 slabs of different thicknesses (a) without SOC and (b) with SOC. The hybridisation gap of the TSS is closed at $\sim$ 4 QL. The levels approach the bulk levels in both cases.

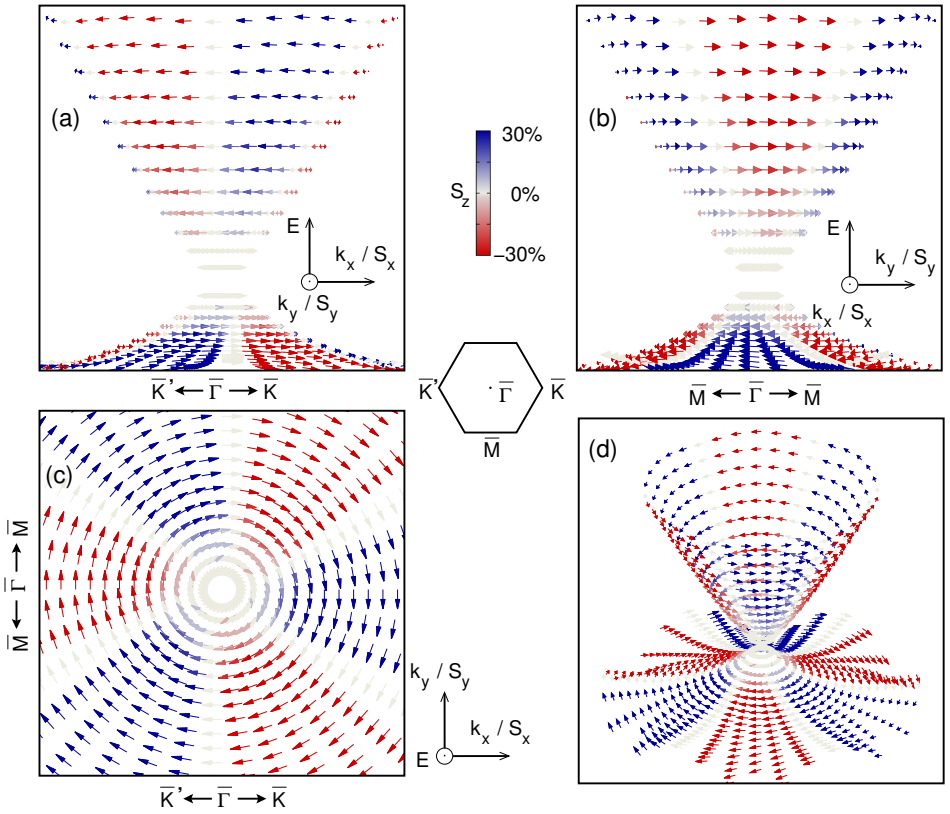

Figure 9: (a) Front view, (b) side view, (c) top view –of the HSS– and (d) perspective view of the spin texture of the DC. The calculation was made for a 6 QL Bi_2Se_3 slab. The x, y and z components of the spin are plotted as arrows, and the z component is additionally represented with the colour code shown in the inset. The value of S_z is depicted as the percentage of the modulus of $S = \sqrt{S_x^2 + S_y^2 + S_z^2}$. Spin–momentum lock is realised for the helical TSS. S_z presents a small modulation with three–fold symmetry, being 0 in the $\bar{\Gamma}$–$\bar{M}$ direction, as dictated by mirror symmetry along that line.

3.5 SUMMARY AND CONCLUSIONS

In this chapter we have shown the crystal structure and electronic band structure of bulk Bi_2Te_3, Sb_2Te_3, Bi_2Se_3 and Sb_2Se_3. The SOC induces a band inversion of the valence and conduction bands in all cases. This drives the systems into a topologically non–trivial phase protected by TRS, as shown in the band parity analysis. This phase is robust as long as the bulk gap is present, and its most clear manifestation, i.e. the linear surface states, have additionally been shown in thin films of Bi_2Se_3. For ultrathin slabs the TSSs at opposite surfaces hybridise, leading to a gap opening in the surface spectrum that can be tuned with the film thickness. Finally, the localisation and spin texture of the TSSs have been displayed, demonstrating the spin–momentum lock and the circular skyrmionic texture of such states.

4

TENSION AND TI/TI HETEROSTRUCTURES

4.1 INTRODUCTION AND MOTIVATION

A very wide variety of physical properties can be tuned by applying different kinds of strain. For instance, the piezoelectric effect was discovered more than a century ago and has been of fundamental importance in the development of many technologies and fields of Physics, among which atomic resolution microscopy is one of its greatest beneficiaries. In the last few years, a novel effect in the field of straintronics [81] has been predicted and later measured: a non–uniform strain field in graphene induces a gauge field that acts as a pseudomagnetic field [82, 83]. In this chapter we will study the role of uniaxial and biaxial tension on the Bi_2Se_3 family of compounds. Being the four compounds narrow gap semiconductors, small strain fields can strongly affect their electronic properties, and, consequently, their topological nature.

4.2 UNIAXIAL AND BIAXIAL TENSION

4.2.1 *Bulk*

To address the effects of biaxial tension, we first calculated the total energy of the Bi_2Se_3 family of compounds for different values of the lattice constants using GGA+vdW with the VASP code (all the other results shown in this chapter were obtained with the SIESTA-GREEN package). In this way, we obtain the relaxed geometry for a fixed value of the in–plane lattice parameter a. Figure 10 shows the total energy of Bi_2Te_3, Sb_2Te_3, Bi_2Se_3 and Sb_2Se_3 for different values of a as a function of the out–of–plane lattice constant c. For compressive in–plane biaxial strains ($a < a_{eq}$, being a_{eq} the equilibrium lattice constant), lattice parameter c tends to increase with respect to its equilibrium value, which agrees with the fact that these systems have a positive Poisson ratio [84].

In order to address the combined effects of out–of–plane uniaxial and in–plane biaxial tension, the phase diagram of the Bi_2Se_3 family of compounds was computed for several points in parameter space (a, c). For every pair of values of the lattice constants, we allowed the ionic positions to relax and we calculated the energy spectrum. In this way we can address the combined effect of uniaxial (along the c direction) and biaxial tension. The results are summarised in Figure 11 for the four compounds, and their universal behaviour is sketched in Figure 13 In the former, for a fixed value of a, points along vertical lines correspond to increases of $\sim 1.5\%$ of uniaxial strain, being the central point of each vertical line the relaxed value of c for the given amount of biaxial strain in that line. For the four systems, three distinct phases can be identified: a metallic phase, a topologically trivial insulating phase and a topologically non–trivial phase. The metallic phase is obtained for large in–plane biaxial strains in any direction. This is due

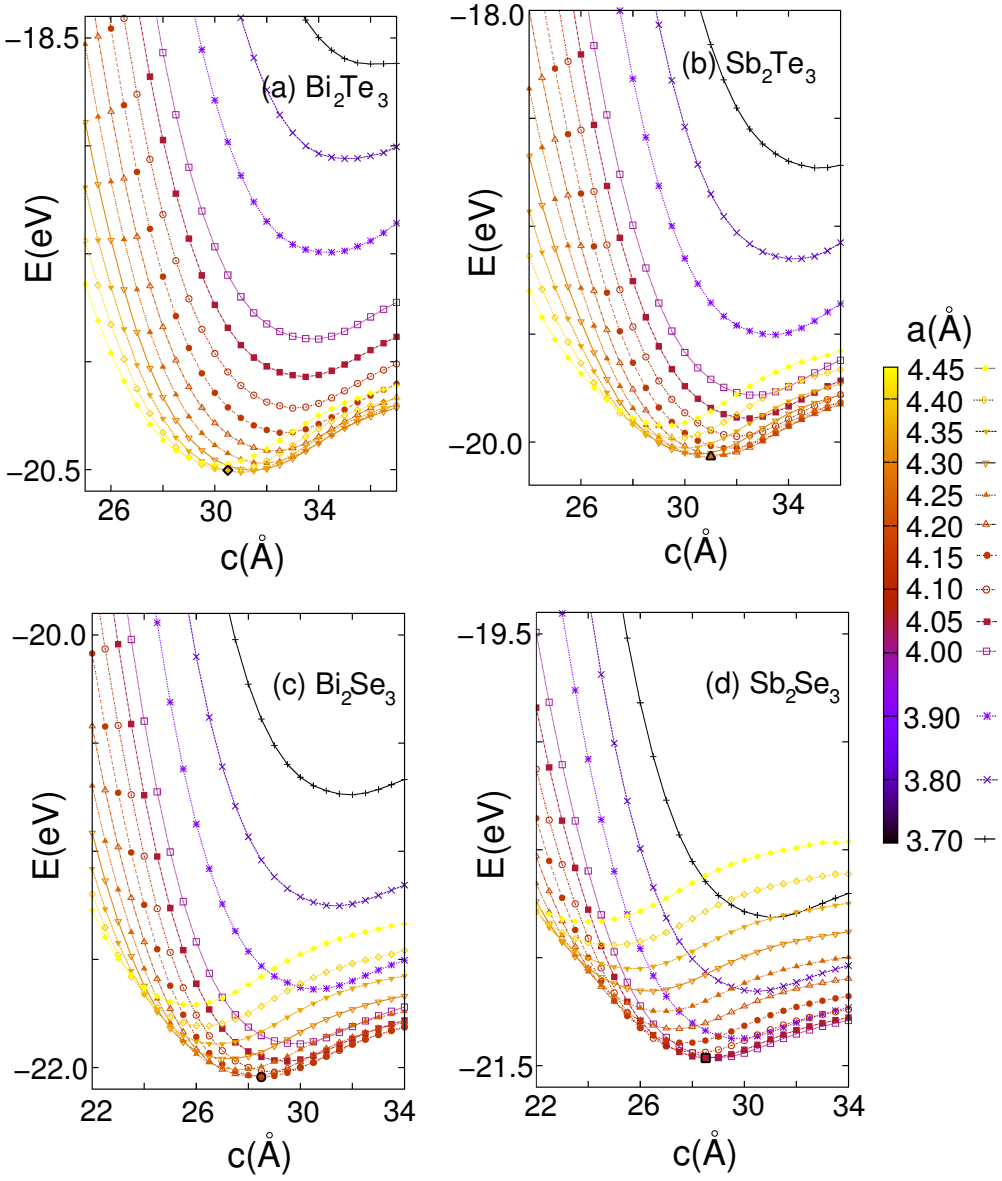

Figure 10: Total energy calculations using GGA+vdW in VASP for (a) Bi_2Te_3, (b) Sb_2Te_3, (c) Bi_2Se_3 and (d) Sb_2Se_3. Each curve shows the energy versus c for a fixed value of a (see legend at the right). Symbols marked in black indicate the equilibrium configuration.

to the fact that a high compressive in–plane strain enlarges the band width of the p_x and p_y orbitals in the valence band, and eventually they cross the Fermi level and the system becomes metallic. For high tensile in–plane biaxial strains, the conduction band undergoes a similar process, leading also to a metallic system. For moderate in–plain strains (below $\sim$ 10% in absolute value) the systems remain insulating. In this range, the topological behaviour of these systems is governed by the band inversion between the Se and Bi p_z bands, and a topological phase transition (TPT) can be induced by out–of–plane strain. Starting from an inverted phase, the compression of lattice parameter c enlarges the bandwidth of the p_z bands, which in turn makes the gap bigger at first, until eventually the gap becomes indirect, starts to decrease and at a certain large compressive out–of–plane strain the system becomes metallic again. On the other hand, tensile out–of–plane strain tends to diminish the gap until it closes when the energies of the Bi and Se p_z bands at the Γ point become equal. Further tensile strain in that direction reopens the gap, turning the system into a topologically trivial insulator. Figure 14 shows the behaviour of the gap with out–of–plane strain for Bi_2Se_3 at a=4.20 Å. The band gap closing and reopening is evident, due to the crossing between the Bi and Se p_z bands that are responsible for the topological structure of the Bi_2Se_3 family of compounds.

For a=a_{eq}, the critical uniaxial strain for Sb_2Se_3, Bi_2Se_3 Sb_2Te_3 and Bi_2Te_3 is 3%, 6%, 6% and 12% respectively, which in turn is related to the crystal structure *and* the strength of the SOC in each system, being largest in Bi_2Te_3, smallest in Sb_2Se_3 and intermediate in Bi_2Se_3 and Sb_2Te_3. Note that this values are given for zero biaxial in–plane strain, and the TPT will occur at different values of uniaxial strain for non–zero biaxial strains. Other studies have shown similar TPTs for Bi_2Se_3–like systems under purely uniaxial strain of 6–10% [85, 86, 87, 88, 89, 84, 90], which is in good agreement with out results. Nevertheless, no other study has shown the effects of combined uniaxial and biaxial strain to our knowledge. Moreover, as the four systems show a positive Poisson ratio, pure compressive biaxial strain induces an expansion in the c direction which can drive the system into the topologically trivial phase, but if no additional uniaxial strain is applied, we find that the four systems undergo a TI to metallic phase transition with both tensile and compressive biaxial strain. The phase diagram we provide can be useful for topological, band and orbital engineering of the Bi_2Se_3 family of compounds in the fields of straintronics and spintronics.

4.2.2 *Thin Films*

In the previous section we have seen how an in–plane compression decreases the band gap and can turn the system metallic with a large enough uniform strain field. Here we investigate the effect of pure biaxial in–plane strain along with low dimensional effects on thin films of Bi_2Se_3–like systems.

Our starting points are bulk calculations in which, for a fixed amount of biaxial strain, the lattice parameter c was allowed to fully relax along with the atomic coordinates, which corresponds to the minimum of each curve for fixed a in Figure 10 and to the thick lines in Figure 11. Then, slabs of 1, 2, 3, 4 and 6 QL thicknesses were built with the bulk positions and their

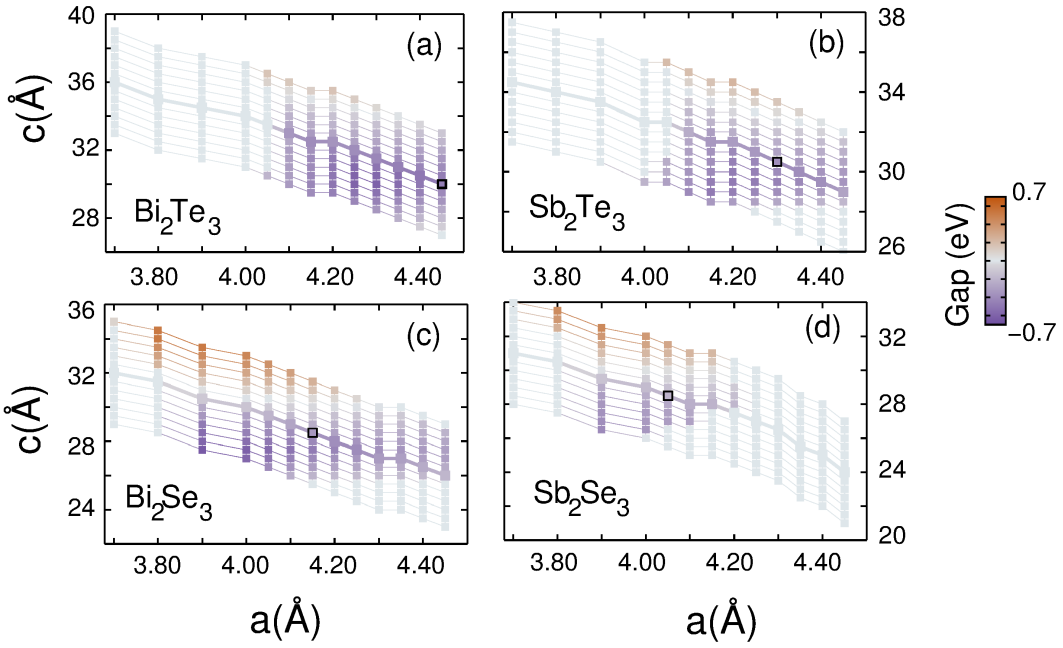

Figure 11: (a) Band gap (in colour code shown on the right) for Bi_2Te_3 for different values of lattice constants a and c. The ionic configurations were allowed to relax for every single calculation. Negative gaps indicate that the energy of Bi p_z orbital is lower than the Se p_z orbital, i.e., the system is topologically non–trivial. (b), (c) and (d) show equivalent diagrams for Sb_2Te_3, Bi_2Se_3 and Sb_2Se_3 respectively. These phase diagrams show the regions in phase space where the system is a trivial insulator (orange), a TI (purple) or a metal (light grey). The equilibrium position is marked with a black square and the thicker line corresponds to the relaxed c lattice parameter for a fixed value of a for each system.

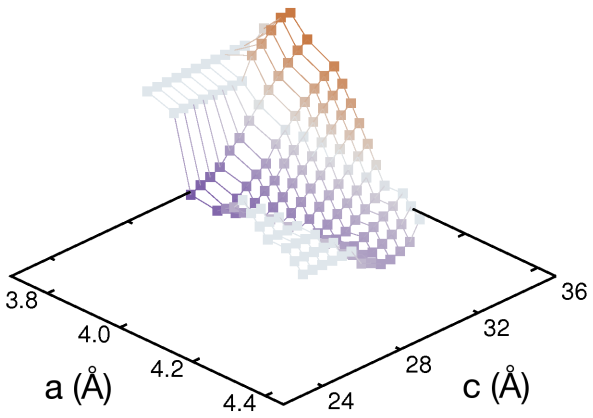

Figure 12: Phase diagram of Bi_2Se_3 as shown in Figure 11 (c) from a perspective view. The colour code for the gap is the same as in that Figure.

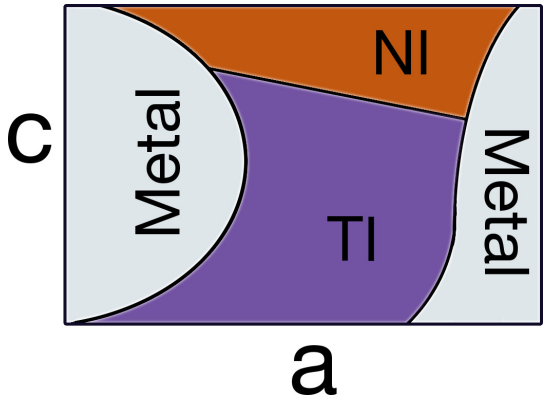

Figure 13: Schematic phase diagram for Bi_2Se_3–like systems in the (a, c) parameter space. For high tensile and compressive in–plane strain the system becomes metallic. Uniaxial strain applied in the out–of–plane direction triggers a TPT.

band dispersions were computed. The results are shown in Figures 15, 16, 17 and 18 for Bi_2Te_3, Sb_2Te_3, Bi_2Se_3 and Sb_2Se_3 respectively, in the range of lattice parameter a in which the systems are TIs (except Bi_2Te_3 and Sb_2Te_3 for the smallest value of a shown). Compressive biaxial strain drives the four systems into a metallic phase due to the shift in energy of the valence band maximum (see leftmost columns of Figures 15 and 16). On the other hand, at a critical tensile biaxial strain the bulk–like conduction band crosses the Fermi level and the system becomes metallic again (see for instance the rightmost column of Figure 18), so the behaviour with both compressive and tensile biaxial strain of thin films is in clear analogy with the bulk behaviour. Nevertheless, in the intermediate region the size of the bulk gap acquires larger values than that of the unstrained system, and therefore a smaller bulk contribution to the electron mobility is expected. The penetration depth of the TSS also varies with strain, and the closer in the phase diagram to the critical line the more QLs are needed to close the hybridisation gap (see for instance the 3 QL series of Bi_2Se_3 in Figure 17, in which compressive biaxial strain takes the system closer to the critical line in the phase diagram), in agreement with the results displayed in Ref [85]. The "M"–shaped feature in the valence around the $\bar{\Gamma}$ point becomes more pronounced with tensile biaxial strain. Therefore, the position of the DP can also be tuned, as a sharp enough "M"–shaped feature detaches the DP from the Fermi level (an example is the 6 QL series for Bi_2Se_3 in Figure 17). This induces n–type doping in the surface states and explains the shift in the DP observed in Ref. [90]. Moreover, a small decrease in the Fermi velocity with tensile strain is also apparent in the four systems. The table–like figures for the four systems are displayed so that they can be used for determining what kind of band dispersion is expected when a Bismuth dichalcogenide of a certain thickness is grown on a substrate with a particular lattice parameter. Strain can therefore turn the Bi_2Se_3 family of compounds insulating or metallic, and allows for engineering of the gap, the orbital character of the bands, the Fermi velocity, DP energy and thus also the doping of the TSSs.

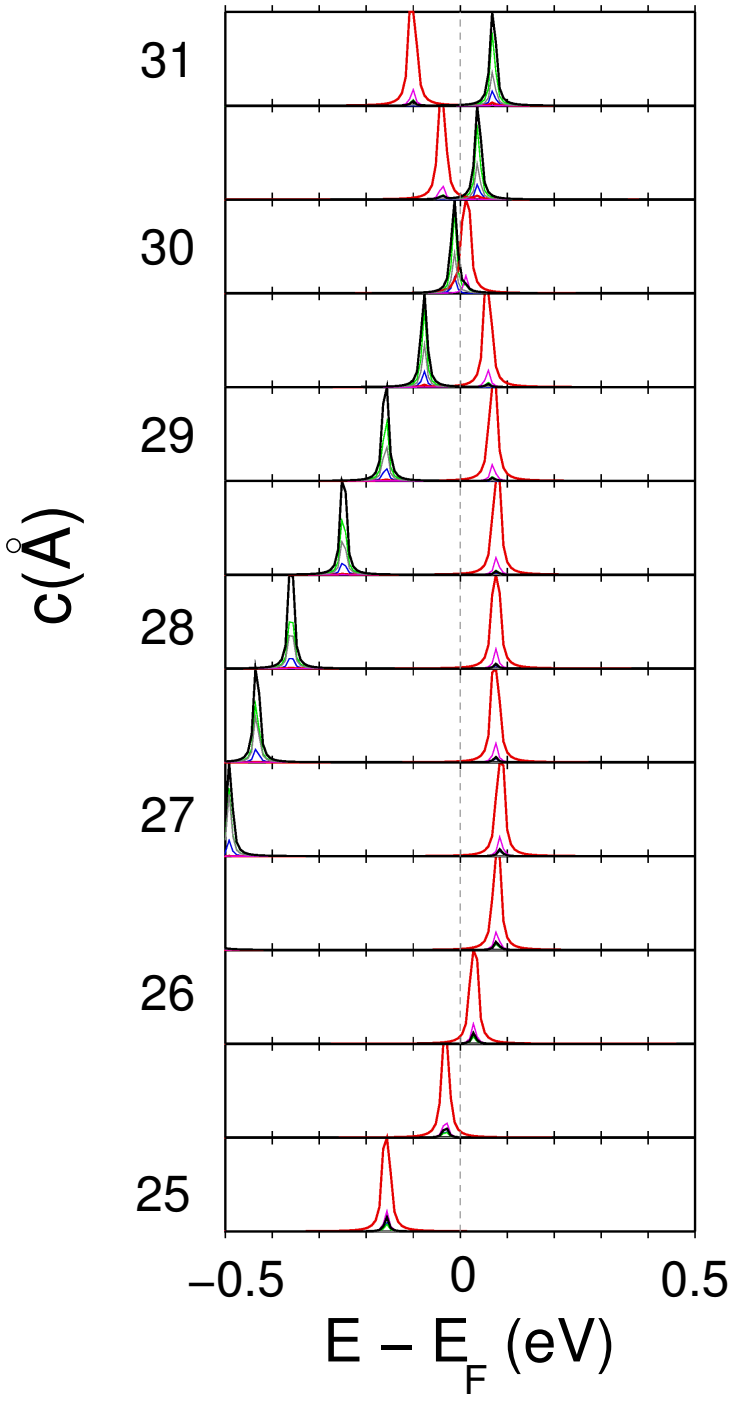

Figure 14: PDOS in the Γ point for bulk Bi_2Se_3 with lattice parameter a fixed to 4.20 Å and different values of c (left axis). The black and red lines show the contribution of Bi p_z and Se p_z orbitals respectively. The magenta and blue line indicate the Bi and Se s contributions, while the grey and green lines depict the Bi and Se $p_x + p_y$ weight. At $c \sim$30 Å the bulk band gap closes and the system undergoes a topological phase transition, so that for $c >$ (<) 30 Å the bands are *uninverted* (inverted) and the system is topologically trivial (non–trivial). The different behaviour of the Se and Bi p_z bands with uniaxial strain is apparent in the figure.

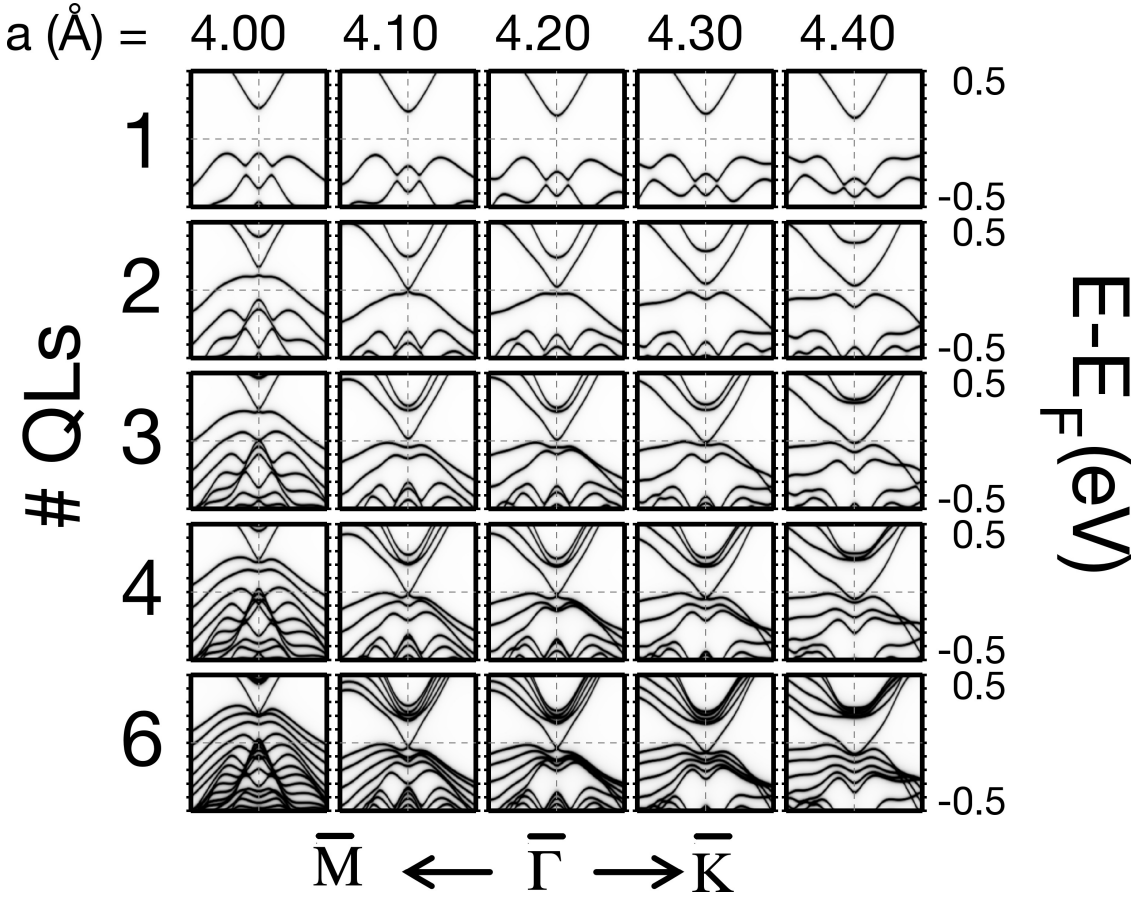

Figure 15: Band dispersion diagrams close to the $\bar{\Gamma}$ point along the $\bar{M}$–$\bar{\Gamma}$–$\bar{K}$ directions for Bi_2Te_3 slabs under biaxial strain. Each column corresponds to a fixed value of the in–plane lattice parameter labelled on top. The five rows correspond to different slab thicknesses: 1, 2, 3, 4 and 6 QLs from top to bottom. The horizontal dashed lines indicate the Fermi level, whereas the vertical dashed lines show the $\bar{\Gamma}$ point.

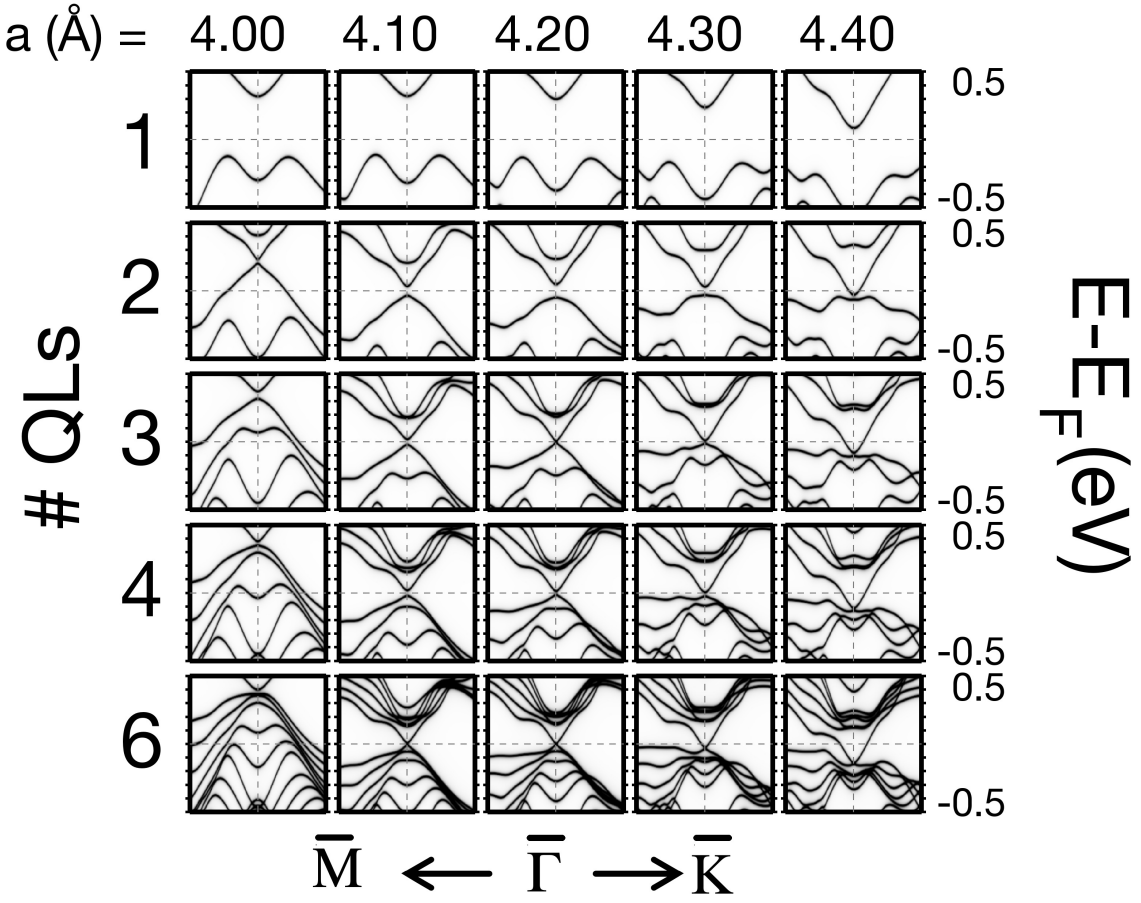

Figure 16: Same as Figure 15 for Sb_2Te_3.

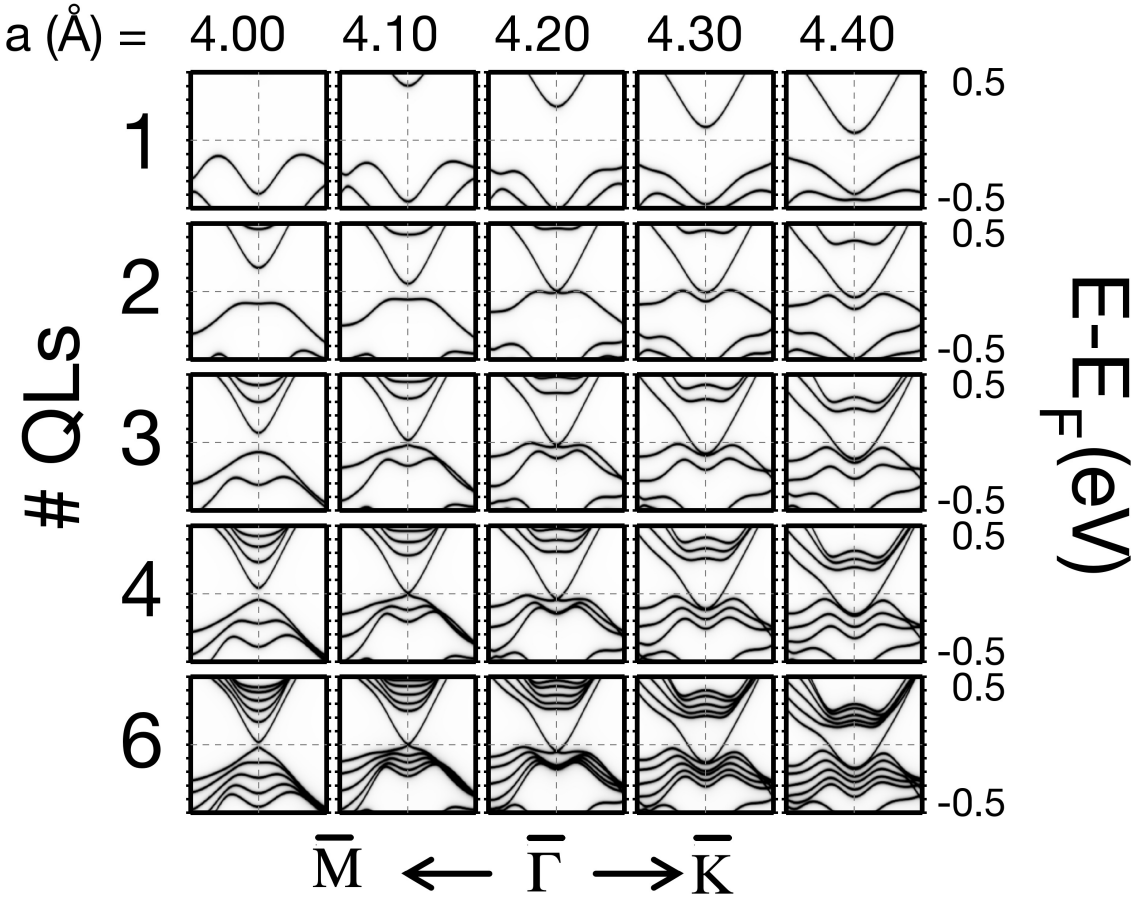

Figure 17: Same as Figure 15 for Bi_2Se_3.

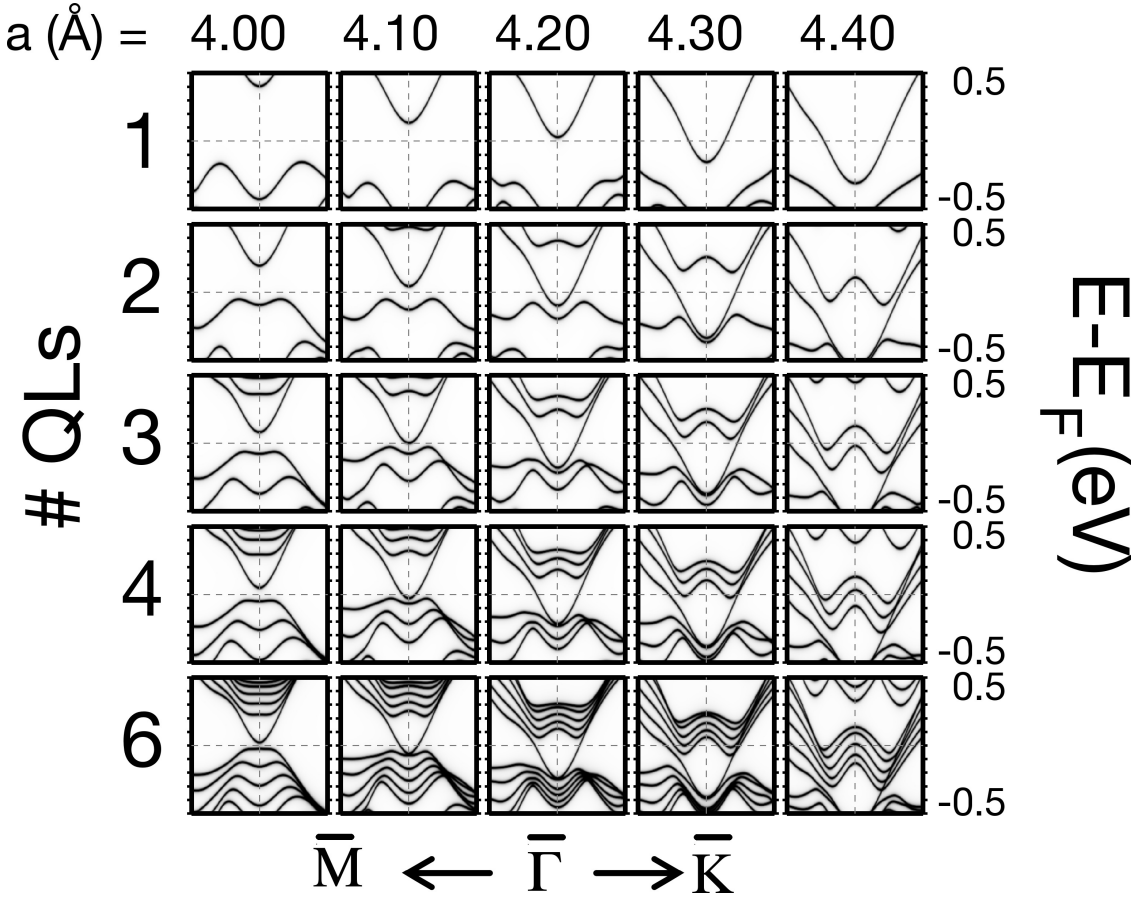

Figure 18: Same as Figure 15 for Sb_2Se_3.

	Bi	Sb	Te	Se
χ_P [91]	2.02	2.05	2.1	2.55
χ_A [92]	2.01	1.984	2.158	2.434

Table 6: Electronegativities of the four elements present in the Bi_2Se_3 family of compounds according to the Pauling scale (first row) and the Allen scale (second row). Bi and Sb present very similar values, whereas the difference between the electronegativities of Te and Se is significant in both scales.

4.3 TI/TI INTERFACES

When two distinct TIs are faced to one another, an interesting problem arises. If both materials belong to the same $\mathbb{Z}_2$ topological class, no interface state is guaranteed by the bulk–to–boundary correspondence, as the change in topological invariant is zero. Therefore, a surface state can be annihilated by placing another (topological) insulator on top, even if both bulk gaps align in a straddling gap configuration. Still, topologically trivial interface states may arise regardless of the topological invariants, as the topological protection only holds for surface or interface states within the bulk band gap region. In this Section we will study interfaces of Bi_2Te_3 and Sb_2Te_3 both in superlattices and in slab geometry. Among the four members of the Bi_2Se_3 family of compounds, we have chosen these two so that the difference in electronegativity (χ) between the A and B elements in the A_2B_3 compounds is as small as possible, in order to obtain a straddling gap at the heterojunction and minimise the band bending along the system. Table 6 shows the Pauling and Allen electronegativities (χ_P and χ_A) for Bi, Sb, Te and Se. The first two elements have an almost equal value of the electronegativity (in fact $\chi_P(\text{Bi}) < \chi_P(\text{Sb})$ while $\chi_A(\text{Bi}) > \chi_A(\text{Sb})$). On the other hand, Se and Te show a bigger difference in their χ values. Opposite doping for for Se- and Te-based materials is expected, and we have additionally calculated Bi_2Se_3/Bi_2Te_3 heterojunctions which exhibit a broken gap alignment, thus leading to a metallic phase where the $\mathbb{Z}_2$ is ill-defined and no topological interface states can exist.

4.3.1 *TI/TI heterojunctions*

In this subsection we will study Bi_2Te_3/Sb_2Te_3 interfaces in slab and superlattice geometries. We have chosen $Sb_2Te_3/Bi_2Te_3/Sb_2Te_3$ trilayers with equal number of QLs of Sb_2Te_3 at both sides so that inversion symmetry is preserved, making the analysis simpler, as both interfaces will be equivalent. We calculated m-Sb_2Te_3/n-Bi_2Te_3/m-Sb_2Te_3 trilayers, where m and n are the number of QLs of Sb_2Te_3 and Bi_2Te_3 respectively. In the superlattice geometry, due to periodic boundary conditions, the trilayer turns into a $2m$-Sb_2Te_3/n-Bi_2Te_3 structure repeated in the (111) direction. We still call it a m-Sb_2Te_3/n-Bi_2Te_3/m-Sb_2Te_3 superlattice to emphasise the centrosymmetric nature of the system. We fixed n=6, for which the surface–surface interaction in Bi_2Te_3 is negligible and a gapless DC develops at the surface (see Fig. 20(f)), while the number of Sb_2Te_3 QLs at both sides is varied from m=1 to 3. The AbCaB stacking sequence of the pristine subsystems is

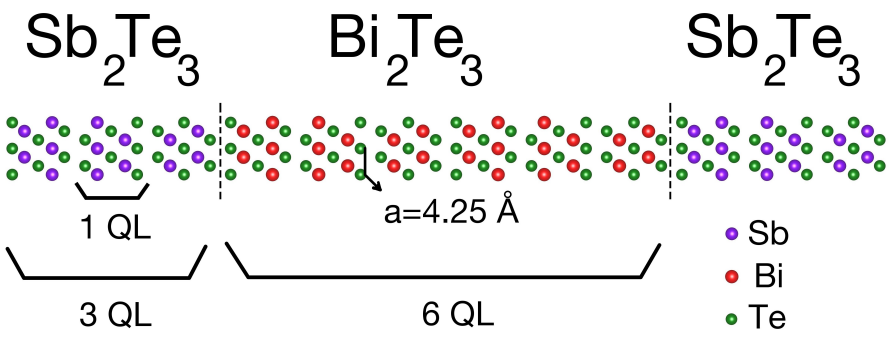

Figure 19: Geometry of the m-Sb_2Te_3/n-Bi_2Te_3/m-Sb_2Te_3 trilayer with m=3 and n=6. The in–plane lattice parameter a is fixed to that of Sb_2Te_3 under no strain. Interfaces are shown as dashed lines as a guide to the eye. The whole system follows the AbCaB stacking pattern analogous to an *fcc* (111) crystal, which ensures inversion symmetry is preserved. Superlattices are constructed by imposing periodic boundary conditions on this and similar trilayers, which will also preserve inversion symmetry.

preserved along the interfaces and in the superlattices in order to preserve inversion symmetry. The C_3 rotation axis and the three vertical mirror planes of the pristine systems are also preserved in the heterojunction. We fix the in–plane lattice vector a to that of Sb_2Te_3 in equilibrium, a_{eq} =4.25 Å and the c lattice parameter for each subsystem, (Sb_2Te_3 and Bi_2Te_3) is set to its relaxed value for a fixed to the aforementioned value, that is 30.9 Å for Sb_2Te_3 and 32.0 Å for Bi_2Te_3 (see Fig. 10). The ionic coordinates within each subsystem are fixed to their relaxed bulk values, and the vdW gap between Sb_2Te_3 and Bi_2Te_3 is taken as the average vdW gap between both subsystems. This setup could correspond to a 6 QL thick Bi_2Te_3 slab grown on a m–QL Sb_2Te_3 substrate, and another m–QL Sb_2Te_3 thin film grown on top of it. Figure 19 depicts the geometry for the m=3 case. According to the phase diagram calculated in Fig. 11, both the Sb_2Te_3 and Bi_2Te_3 subsystems show an inverted gap in the bulk. This means that the existence of an interface state is not guaranteed because the change in the $\mathbb{Z}_2$ invariant across the interface is zero, being both TIs.

4.3.1.1 *Electronic structure*

We start by analysing the electronic structure of the isolated subsystems, depicted in Figure 20. Bi_2Te_3 under small biaxial strain remains a TI, and so it develops surface states when truncated in the (111) direction. For a 6 QL slab (as shown in the Figure), surface–surface interaction is already negligible and the DCs are massless. In contrast with Bi_2Se_3 the DP of the Bi_2Te_3 surfaces is not at the Fermi level and lies below the valence band maximum. This is in agreement with previous results [7], and can be attributed to the bigger curvature of the valence band along the $\bar{\Gamma}$–$\bar{M}$ direction. Sb_2Te_3 in this system presents neither uniaxial nor biaxial strain, and it is therefore also in the topologically non–trivial phase. In Figure 20 the electronic structure of 1, 2, 3, 4 and 6 QL thick Sb_2Te_3 films is also shown. Antimony telluride presents a topological surface state being the DP at the Fermi level for 6 QLs. The penetration depth is $\sim$ 2 QLs, so that a gap opens in thin films of less

than 5 QLs due to surface–surface hybridisation. The band structures of the periodic superlattices and the trilayer slabs are shown in Figure 21 for m=1, 2 and 3. The former present a band gap of $\sim$ 0.1 eV, being the VB (CB) offset of $\sim$ 0.1 (0.05) eV between both subsystems, with the VB (CB) of Sb_2Te_3 lying at a higher energy. The small band staggering at the heterojunction can be attributed to the small deviation in the values of the electronegativity for Bi and Sb. The bulk–to–boundary correspondence predicts no topologically protected interface state at the junction, although trivial interface states could develop, but our results show that this is not the case. We therefore conclude that this Sb_2Te_3/Bi_2Te_3 is insulating with no interface states whatsoever, but will develop surface states when truncated. This is proved in the thin film geometry, where surface states than span the whole bulk band gap appear at both ends. The DP of these TSSs is pinned at the Fermi level irrespective of the thickness of the Sb_2Te_3 layers. In fact, even for the m=1 and 2 for which the thickness of the Sb_2Te_3 subsystem is below the penetration depth of the surface states, the spectrum still exhibits a semimetallic character, which corroborates the fact that unstrained Sb_2Te_3 is a TI even for ultrathin films, and supports the idea that the Sb_2Te_3-Bi_2Te_3 interface does not confine the TSS. The TSS localisation is shown in Figure 24 (a), for the three different slabs. The surface state is strongly confined in the Sb_2Te_3 subsystem, with a penetration depth of $\sim$ 2 QLs, although for the m=1 case the state is strongly localised at the surfacemost QL.

4.3.2 *NI/TI heterojunctions*

Now we will discuss the effect of applying uniaxial tensile strain to Sb_2Te_3 in the system presented in the previous section. The systems considered are again m-Sb_2Te_3/n-Bi_2Te_3/m-Sb_2Te_3 trilayers in either a slab geometry (thin film) or a superlattice. The in–plane lattice parameter is again fixed to a=4.25 Å and c is set to 32.0 Å for Bi_2Te_3 but now the Sb_2Te_3 subsystem is expanded to c=34.0 Å corresponding to a uniaxial strain of -10%. According to the phase diagram shown in Figure 11, Sb_2Te_3 will now be in a topologically trivial insulating phase, so that at the interface of Sb_2Te_3 and Bi_2Te_3 the topological $\mathbb{Z}_2$ invariant will increase from 0 to 1.The TPT can be induced by external uniaxial tensile strain as shown in the previous section, or, alternatively, by the chemical intercalation of zerovalent non–magnetic metals in the vdW gaps of Sb_2Te_3. This technique has already been experimentally demonstrated and developed by Koski *et al.* [93] in Bi_2Se_3, and we propose its application to effectively enhance the c lattice parameter of Sb_2Te_3 without disrupting the ionic or electronic structure.

4.3.2.1 *Electronic and spin structure*

The electronic structure of the different isolated constituents is shown in Figure 22. Sb_2Te_3 under such out–of–plane strain shows no band inversion in the bulk, and this is reflected in the thin film electronic structure. In contrast with the previously analysed systems, Sb_2Te_3 now shows no surface state since it is in the NI phase. The gap is of 0.4 eV for the 1 QL slab and decreases down to 0.2 eV for the 6 QL thin film. On the other hand, the 6 QL Bi_2Te_3 slab under purely biaxial strain is a TI which develops TSSs with

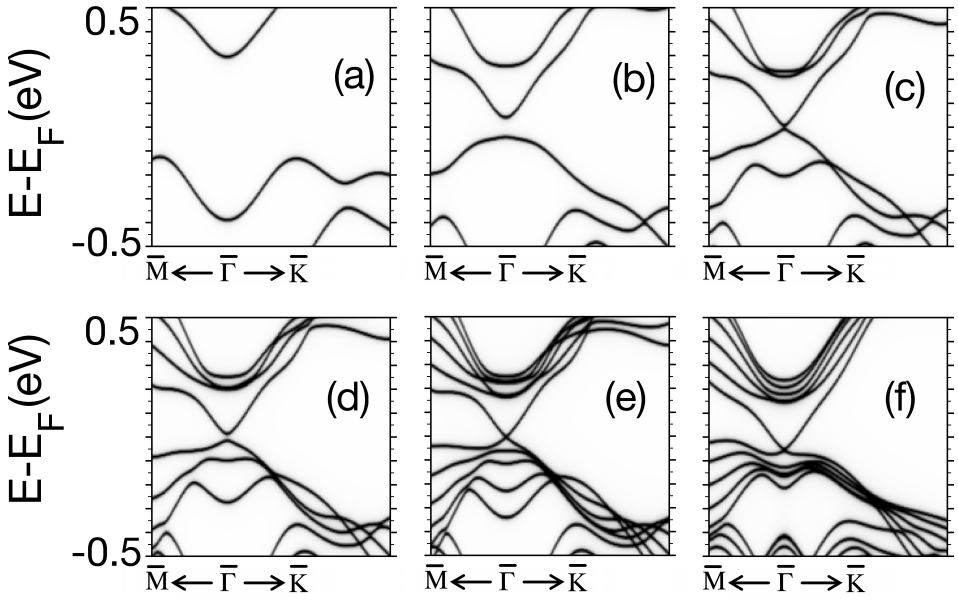

Figure 20: Band structure of the different isolated subsystems involved in the trilayers. (a), (b), (c), (d) and (e) show the band dispersion for Sb_2Te_3 slabs of 1, 2, 3, 4 and 6 QLs respectively. (f) corresponds to a 6 QL Bi_2Te_3 thin film under biaxial compressive strain so that its in–plane lattice parameter matches that of equilibrium Sb_2Te_3 (4.25 Å). All subsystems are TIs, although for thicknesses below $\sim$ 5 QL a gap opens in the TSSs due to surface–surface interaction.

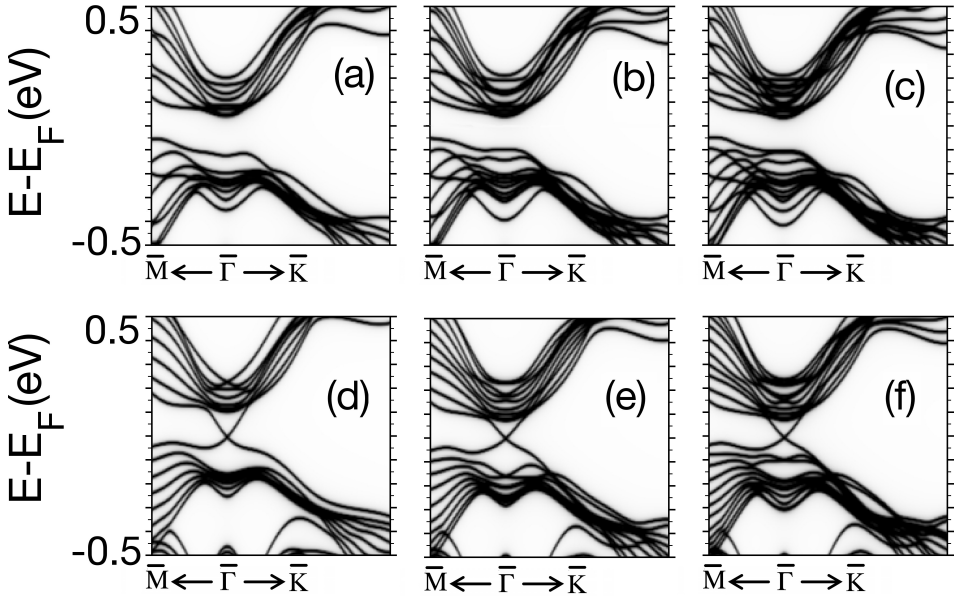

Figure 21: Band structure of the m-Sb_2Te_3/n-Bi_2Te_3/m-Sb_2Te_3 trilayers considered. (a), (b) and (c) show the band dispersion for the trilayers in a superlattice with n=6 and m = 1, 2, and 3 respectively. As all the constituents of the superlattice are topologically non–trivial, there are no interfaces between subsystems with different value of the $\mathbb{Z}_2$ topological invariant, and no interface state exists. (d), (e) and (f) correspond to slab geometries with n=6 and m = 1, 2, and 3 respectively. In these three cases a surface state develops irrespective of the number of Sb_2Te_3 layers, but no interface state is present.

no gap, and its DP lies below the Fermi level. When the two subsystems are brought together, the bulk–to–boundary correspondence dictates that topologically protected interface states must develop in the gap. The band structures of the junctions are shown in Figure 23.

For periodic boundary conditions, and in contrast to the trilayers analysed in subsection 4.3.1, a topologically protected interface state (TIS) also develops than spans the bulk band gap. In this case a hybridisation gap opens in the spectrum for thicknesses of the $2m$–Sb_2Te_3 layer below m=2 QLs (note that for m=2 the total thickness of the Sb_2Te_3 subsystem is 4QLs) since the two opposed interfaces are closer than twice the penetration depth of the TISs (see Figure 25). The TISs show no doping in contrast with the TSS of 6 QL Bi_2Te_3 –see Figure 22 (f)–.

For the trilayer slab configurations shown in subfigures (a) to (c), the system shows a common bulk gap of $\sim$ 0.15 eV and a gapless interface state with the DP at the Fermi level. This interface state is also undoped and develops irrespective of the thickness of the Sb_2Te_3 layers, but is surprisingly not strictly localised at the interface. Instead, the state at the gap is confined in the Sb_2Te_3 subsystem, with more weight at the interfacemost QL of Sb_2Te_3, but exceeding the expected $\sim$ 2 QL penetration depth of the TSSs in an isolated Bi_2Te_3 slab (see Figure 25). This is in agreement with previous results [94, 95] in which similar TISs with large penetration depths appear in NI/TI junctions localised in the NI.

We have also calculated the spin texture of the topological interface states at the heterojunction for the periodic superlattice systems. For thicknesses below 4 QLs of the NI subsystem (m=2), the interaction between both TIS at opposite interfaces is large, and both states are mixed and equally distributed at the two interfaces. As we have calculated inversion symmetric systems, the TIS will also be degenerate. In the spin texture some of the symmetries of the crystal (mirror symmetries along the $\bar{\Gamma}$-$\bar{M}$ directions, TRS) are not fulfiled by each of the individual TIS, but for the sum of both degenerate TIS. The hybridisation takes place around the $\bar{\Gamma}$ point, and far from it the modulation in S_z with three–fold symmetry of the non–hybridised topological helical states is recovered. Interestingly, close to the $\bar{\Gamma}$ point the S_z component dominates the texture, and is negative for both the electron–like interface state and the hole–like interface state of the interface state depicted, while it is positive at the other interface. For the m=3 superlattice, the spin texture was also calculated and is presented in Figure 26. There is no hybridisation between the TISs due to the larger interface–interface distance, and so even though both TIS are degenerate, they are completely decoupled. Therefore, no gap appears in the spectrum and all the symmetries of the crystal are fulfiled for each of the TIS, in contrast to the m=1 case. The expected value of the spin lies perpendicular to each of the mirror planes along the $\bar{\Gamma}$-$\bar{M}$ directions and the three–fold symmetric oscillation of S_z due to the trigonal warping is present all over the electronic state, being smaller close to the $\bar{\Gamma}$-$\bar{M}$ point. The skyrmionic spin texture of this system is in very close resemblance with the unhybridised topological surface states of Bi_2Te_3 or Sb_2Te_3.

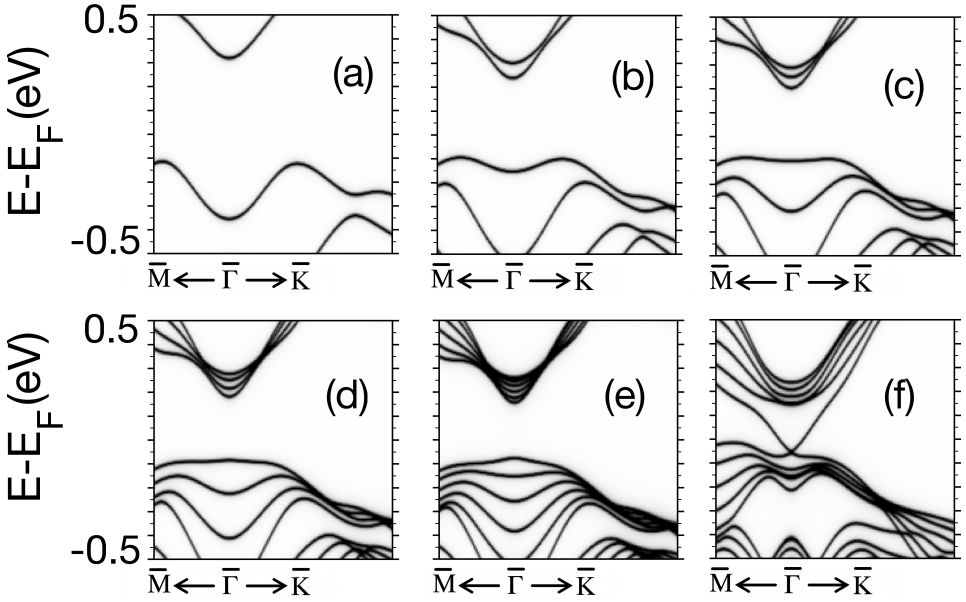

Figure 22: Band structure of the different isolated subsystems that form the trilayers. (a), (b), (c), (d) and (e) show the band dispersion for Sb_2Te_3 slabs of 1, 2, 3, 4 and 6 QLs respectively. Uniaxial tensile strain of $\sim 10\%$ has been applied in the five cases. (f) corresponds to a 6 QL Bi_2Te_3 thin film under biaxial compressive strain so that its in–plane lattice parameter matches that of equilibrium Sb_2Te_3 (4.25 Å). Sb_2Te_3 is clearly in the normal insulating phase, as no surface state develops for thicknesses as large as 6 QLs.

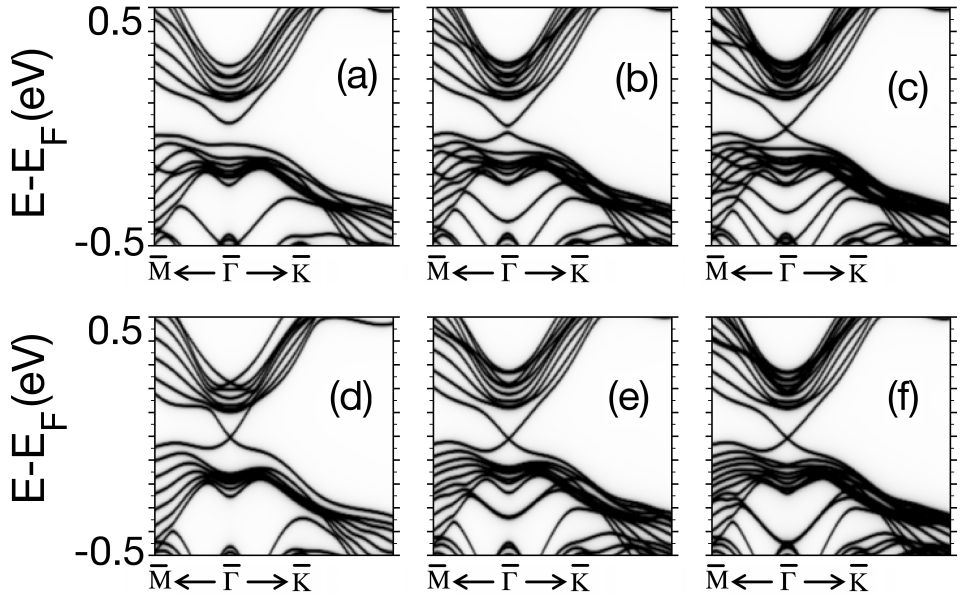

Figure 23: Band structure of the m-Sb_2Te_3/n-Bi_2Te_3/m-Sb_2Te_3 trilayers considered. (a), (b) and (c) show the band dispersion for the superlattices with n=6 and m = 1, 2, and 3 respectively. As the Sb_2Te_3 subsystem has been driven to the normal insulating phase by applying uniaxial tensile tension, topologically protected states localised at the interface appear, according to the bulk–to–boundary correspondence. A gap in the spectrum opens for m below ~ 2 due to interface–interface interaction (note that the total thickness of the Sb_2Te_3 subsystem is $2m$QLs in the superlattices) (d), (e) and (f) correspond to slab geometries with n=6 and m = 1, 2, and 3 respectively. In these three cases a surface state develops irrespective of the number of Sb_2Te_3 layers, but no interface state is present.

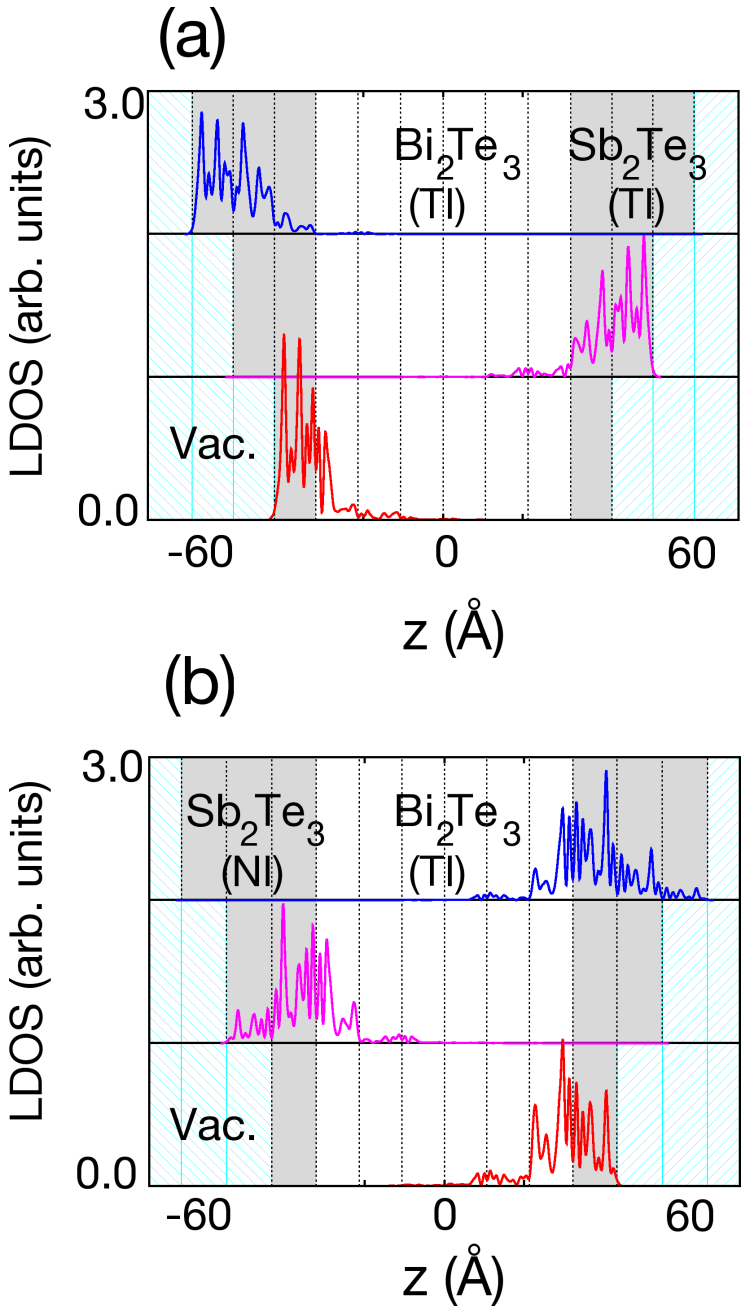

Figure 24: LDOS of the topological states in m-Sb_2Te_3/n-Bi_2Te_3/m-Sb_2Te_3 trilayer slabs for m=1 (red line at the bottom), m=2 (magenta line in the middle) and m=3 (blue line at the top). The LDOS was computed at $\boldsymbol{k}$=(5, 0) $\cdot 10^{-3}$Å^{-1}, along the $\bar{\Gamma}$–$\bar{K}$ direction and close to the $\bar{\Gamma}$ point for the electron–like TSSs. The trilayer is centred at the middle of the 6 QL Bi_2Te_3 layer. Vertical dashed lines depict the boundaries of each QL. The grey shaded region corresponds to the Sb_2Te_3 subsystem, while white regions belong to the Bi_2Te_3 subsystem and the vacuum is shaded with a cyan pattern. (a) shows the TI/TI/TI trilayer for which TSSs localise at the surfacemost QL of the Sb_2Te_3 which is in the topological insulating phase. In (b) the LDOS of the NI/TI/NI trilayer is shown. In this case TISs localise at both interfacial QLs, one in the Bi_2Te_3 subsystem and the other in the Sb_2Te_3 subsystem, being the latter in the NI phase. The extension of the TISs spans the whole trivial Sb_2Te_3 subsystem.

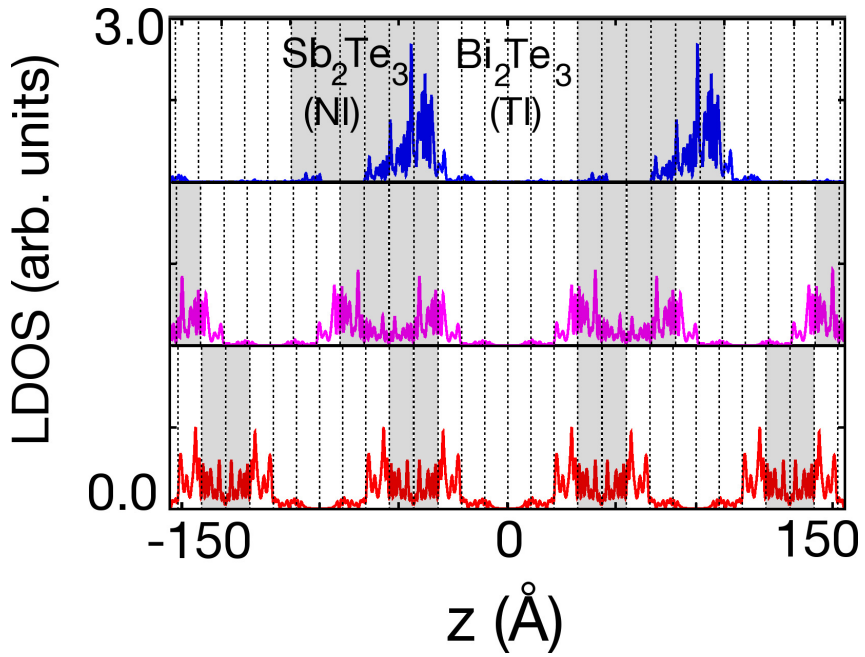

Figure 25: LDOS of the TISs in m-Sb_2Te_3/n-Bi_2Te_3/m-Sb_2Te_3 superlattices for m=1 (red line at the bottom), m=2 (magenta line in the middle) and m=3 (blue line at the top) –note that the total thickness of the Sb_2Te_3 subsystem is $2m$QLs–. The LDOS was computed at $\boldsymbol{k}$=(5, 0) $\cdot 10^{-3}$Å^{-1}, along the $\bar{\Gamma}$–$\bar{K}$ direction and close to the $\bar{\Gamma}$ point for the electron–like TISs. The system is centred at the middle of the 6 QL Bi_2Te_3 layer. Vertical dashed lines depict the boundaries of each QL. The grey shaded region corresponds to the Sb_2Te_3 subsystem, while white regions belong to the Bi_2Te_3 subsystem. TISs of NI/TI superlattices exhibit strong hybridisation with the opposite interface for thicknesses of the $2m$–Sb_2Te_3 layer below m=2 QLs, while for the m=3 QLs the TISs are already decoupled. All three TISs shown are degenerate due to inversion symmetry, and only one of the two–fold degenerate states is shown in each case.

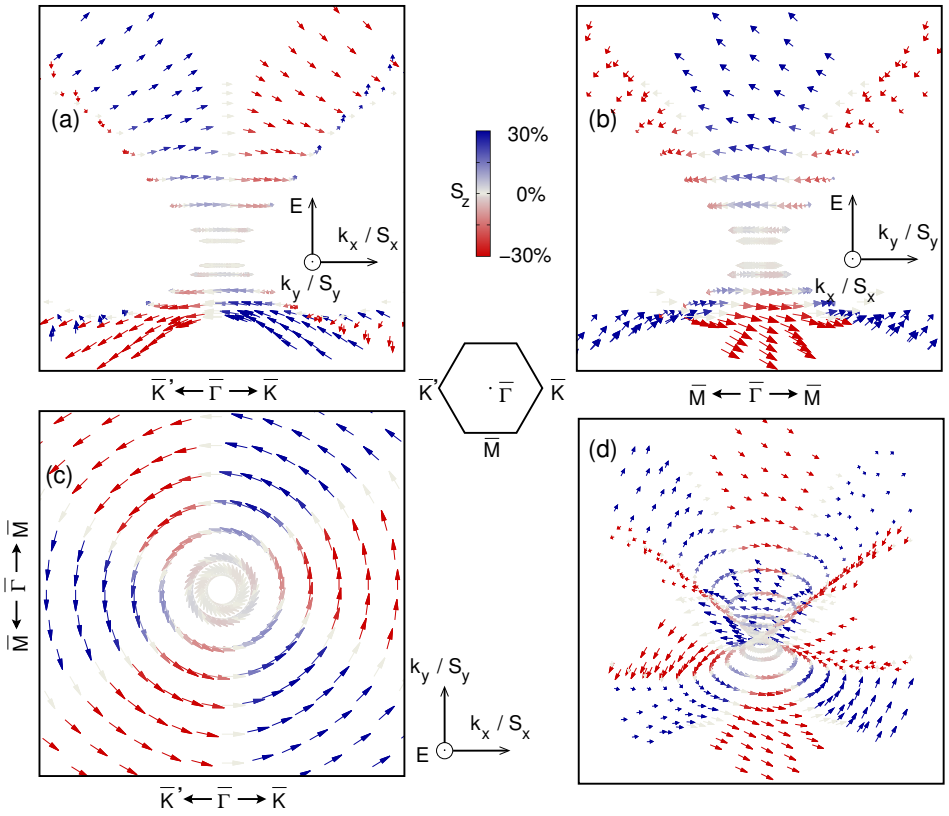

Figure 26: Spin texture of the TIS for m=3. Both TISs are decoupled, in contrast to the m= 1 and 2 cases. Mirror symmetry for each TIS individually is now fulfiled and the spin lies perpendicular to the mirror planes in the $\bar{\Gamma}$-$\bar{M}$ directions. Also, the value of S_z decreases close to the $\bar{\Gamma}$ point, and the trigonal symmetry of S_z is patent all across the DC.

4.4 SUMMARY AND CONCLUSIONS

In this chapter we have shown the combined effects of uniaxial and biaxial strain on Bi_2Te_3, Sb_2Te_3, Bi_2Se_3 and Sb_2Se_3, both in bulk and slab geometries. A phase diagram for the four systems was computed and analysed, demonstrating that topological phase transitions can occur for both kinds of strains. We showed how strain can engineer the DP energy, the Fermi velocity, the metallic character and the topology of the four compounds, thus offering a wide tunability regarding straintronics. We have also calculated the electronic and spin structure of $Sb_2Te_3/Bi_2Te_3/Sb_2Te_3$ trilayers, in which Sb_2Te_3 was driven into the topologically trivial insulating regime by applying uniaxial strain. For the TI/TI systems no trivial nor topological interface state is found, and the superlattice shows a straddling gap of ~ 0.1 eV. In the NI/TI heterojunctions, topologically protected interface states were found and characterised. Our results for the NI/TI heterojunctions indicate a way to avoid interactions of the topological states with undesired ambient impurities while preserving the bulk band gap of the system, and thus maintaining the topological protection of the states. Uniaxial strain on the Sb_2Te_3 subsystem can also turn the interface conducting channel on or off, which can also be of importance in the field of straintronics and spintronics.

5 STACKING DEFECTS

5.1 INTRODUCTION AND MOTIVATION

Defects have played a cornerstone role throughout history in material science. Today's uncountable electronic devices are only possible thanks to doped semiconductors, a wide variety of properties can be tuned by doping in the fields of optics, medicine or metallurgy (just to name some examples), and, more recently, a huge enhancement of graphene's Young modulus has been measured by introducing intrinsic defects [96].

The Bi_2Se_3 family of compounds presents a layered structure as described in Chapter 3, in which the inter–QL bonding is predominantly of the vdW kind, and therefore relatively weak. This already suggests that extended 2D defects are prone to be present when growing real samples of these materials. In fact, numerous experimental groups have reported the occurrence of stacking defects (SDs) in Bi_2Se_3 and Bi_2Te_3 systems [97, 98, 99, 100, 101, 102, 103]. In this chapter, we study the two most common types of SDs in Bismuth dichalcogenides, namely stacking faults (SFs) and basal twin domain boundaries (TBs). The chapter is structured as follows: First, we describe the atomic structure of a SF and a TB. Second, the defect formation energies for several defective configurations are calculated and compared. Then, the impact of these defects on the electronic properties and spin structure is addressed. In Section 5.4 periodic arrays of aligned TBs and SFs are investigated, while in Section 5.5 anti–parallel configurations are taken into consideration too.

5.2 GEOMETRY AND NOMENCLATURE

5.2.1 *Stacking Fault*

Stacking faults are one of the most common defects in layered structures, and are usually present in many *fcc* crystals. The ideal *fcc* stacking sequence along the (111) direction can be denoted by $ABCABC$. A SF between the third and fourth atomic layers (consecutive C and A respectively) in the structure would have a stacking sequence $AB\boldsymbol{CB}CA$. The fourth layer has moved from A to B, and the rest of the crystal follows the original ABC pattern.

The Bi_2Se_3 family of compounds shows an *fcc*–like stacking along the (111) direction. In these 3D TIs, a SF can occur at three unequivalent positions:

(i) between the two Se_1 layers,

(ii) between a Bi and a Se_1 atom, and

(iii) between a Bi and the Se_2 atom.

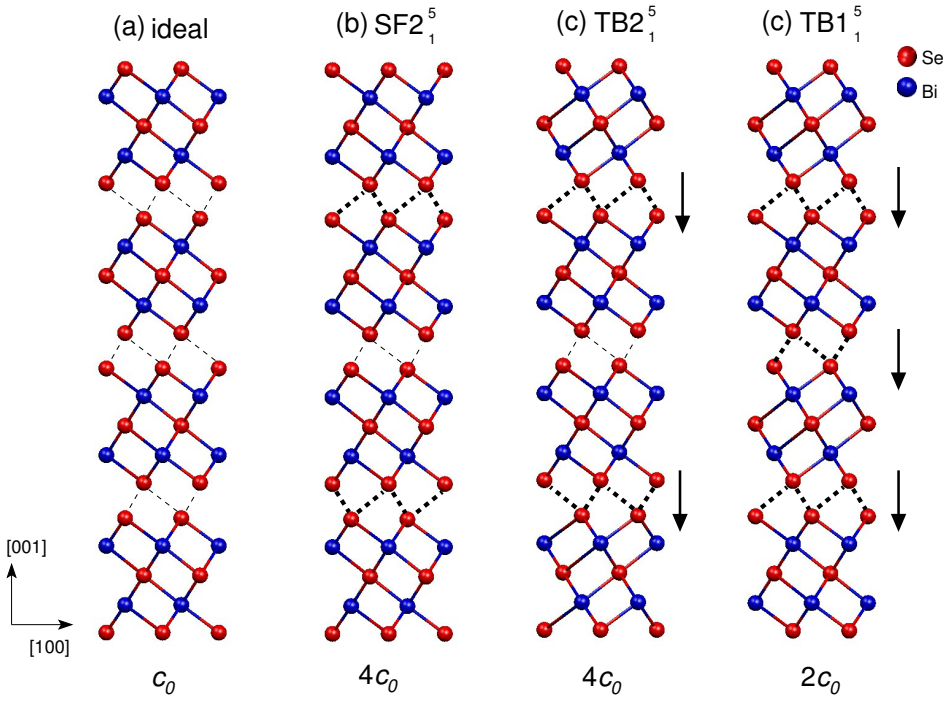

Figure 27: Crystal structure for some of the Bi_2Se_3 polytypes considered. Se (Bi) atoms are shown in red (blue). (a) Ideal, defect–free case. (b) $SF2_1^5$ structure with an inter–QL SF every two QLs (c) $TB2_1^5$ structure with an inter–QL TB every two QLs and (d) $TB1_1^5$ structure with an inter–QL TB every QL. Thin (tick) lines indicate inter–QL vdW bonds for an ideal (defective) stacking. The arrows at the right of the TB systems indicate the direction of the dipole moment associated to each TB (see text). Lattice parameter c is indicated below each case.

Note that (i) involves a rearrangement of vdW bonds between different QLs, while the other two affect stronger chemical bonds within the same QL. The corresponding stacking patterns are, explicitly

(i) $AbCa\boldsymbol{B}\ \boldsymbol{A}bCaB$

(ii) $AbC\boldsymbol{a}\boldsymbol{C}\ AbCaB$

(iii) $Ab\boldsymbol{C}\boldsymbol{b}C\ AbCaB$

Regarding symmetry, in a Bi_2Se_3–like system a single intra–QL SF –(ii) and (iii)– breaks inversion symmetry (IS), regardless of where it is localised, whereas an inter–QL SF –(i)– preserves it locally (and can preserve it globally if the SF is in the centre of the system), which is explicitly shown in Figure 27. The other symmetries of the crystal (C_3 rotation axis, 3 vertical mirror planes) are preserved by SFs.

Along this chapter several Bi_2Se_3–like systems with different arrangement of SDs will be studied. For SFs, we adopt the nomenclature SFn_i^j for Bi_2Se_3 and Bi_2Te_3 polytypes with a periodic arrangement of inter–QL SFs, where n is the inverse of the linear density of SFs in the z direction in units of the unit cell vector c_0, and the SF will be located between the j^{th} atomic layer in the i^{th} QL from the bottom surface and the $(j+1)^{th}$ atomic layer. For systems with a single SF there is no defect periodicity and n will not be written. For example, $SF3_2^5$ denotes a polytype with a inter–QL SF every 3

QLs in which the first SF will be located in between the second and third QLs (always starting from the bottom surface). SF_2^3 denotes a system with a single stacking fault located between the third (Se_2) and fourth (Bi) atomic layers in the 2^{nd} QL (which are the 13^{th} and 14^{th} atomic layers)

5.2.2 *Twin Boundary*

Twin boundaries are also widely present in layered crystals, particularly in those with low SF formation energy [104] and they are, in general, interfaces between twinned domains in a crystal. Here we will focus particularly on a basal twin domain boundary along the (111) direction of the Bi_2Se_3–like systems (TB for short), which is a junction of two domains with opposite stacking chiralities, one growing with an $ABCABC$ pattern and the other with an $ACBACB$ pattern. It can equivalently be described as a rotation of 180° along the z direction of one of the domains with respect to the ideal system. Unlike SFs that occur *between* two atomic layers, the position of a TB is better described by a single atomic layer in which the kink in the stacking pattern is located (see Figure 27).

The stacking sequences for the different possible TBs in a Bi_2Se_3–like system are

(ia) $AbCaB\ \dot{C}bAcB$

(ib) $AbCa\dot{B}\ AcBaC$

(iia) $AbC\dot{a}C\ BaCbA$

(iib) $Ab\dot{C}bA\ CbAcB$

(iic) $A\dot{b}AcB\ AcBaC$

where the atoms in red belong to one domain and the ones in blue to the opposite domain, and the dotted atom in purple belongs to both domains and represents the location of the kink. Note that, in contrast to SFs, there are two unequivalent possible inter–QL –(ia) and (ib)– and three intra–QL TB positions –(iia), (iib) and (iic)–. Local IS is broken for every case, whereas a horizontal mirror symmetry plane appears for case (iib).

For TBs we use an analogous nomenclature to the one for SFs. TBn_i^j will be a polytype with a TB every n QLs in which the first defect (kink) is at i QLs from the bottom surface in the j^{th} atomic layer (being j =1 the Se1 atom closest to the bottom surface).

5.3 METHODS

Apart from the usual slab geometries we additionally constructed true semi-infinite surfaces via Green's functions matching techniques , as described in Ref. [105] and as implemented in the SIESTA-GREEN package [35, 41], in order to obtain a precise description of each TSS and analyse its doping. Since most of the considered slabs are asymmetric, we could construct, from each calculation, an *up* and a *down* surface by retaining the matrix elements of either the upper or lower half of the slab and replacing the rest of elements

below or above by those of the bulk. The Fermi level E_F of the semi-infinite system was fixed to that obtained for the slab, while in the insulating bulk E_F was adjusted after comparing the on-site energies of the atoms at the centre of the slab versus those in the bulk. Self-consistency in the matching procedure was quantified by inspecting the maximum deviations among these energies after the bulk E_F alignment, to always find values below 10 meV. Nevertheless, the DP shifts derived from the semi-infinite surface calculations matched very closely (within 2 meV) those directly derived from the slab's band structure. This is because the bulk calculation, having periodic boundary conditions, cannot contribute to the polarisation field and hence, any spontaneous polarisation (SP) derived doping at the surface solely arises from the slab's Hamiltonian.

5.4 PARALLEL CONFIGURATIONS

5.4.1 *Energetics*

The SD formation energy ΔE_{SD} can be obtained as the difference between the total energy of a slab with a single SD minus that of the equivalent defect-free slab. We calculated the total energy of 6 QL thick (111) Bi_2Se_3 and Bi_2Te_3 slab (including SOC) systems in order to have the surface states decoupled. The results are shown in Figure 28 and listed in Table 7. We obtain a very good agreement between the VASP and SIESTA formalisms, finding that the biggest deviation below 4 meV/Å^2. Despite the different calculation schemes of the two *ab initio* procedures, the general agreement in the values and in the overall tendency demonstrates the good accuracy of the calculated energies.

As expected, SD formation energies that involve a rearrangement of vdW bonds (inter–QL SDs) are noticeably smaller than those that involve chemical bonds (intra–QL SDs), both for SFs as for TBs. A SF is surprisingly always more energetic than its corresponding TB. Besides, the smallest ΔE_{SD} is found for inter–QL TBs in Bi_2Te_3, and for this system the energy difference between placing the defect in an inter–QL or intra–QL position is larger than for Bi_2Se_3. [98] Note that the TB_1^2 and SF_1^1 defects give rise to the same crystal structure, while TB_1^1 can not exist (it is equivalent to the defect–free system). We have also checked that for the $TB1_1^5$ *polytype*, which for a 6 QL thick slab includes 5 inter–QL TBs, the formation energy is exactly (within our numerical accuracy) the sum of the energies of the individual TBs present in the system –TB_1^5, TB_2^5, TB_3^5, TB_4^5 and TB_5^5, being the first (second) system equivalent to the last (one before the last) system in this list due to inversion symmetry–. This means that for dipoles aligned in parallel the formation energy is essentially additive, as will be shown in the next sections.

5.4.2 *Charge and Potential*

The changes in the charge distributions induced by SDs and their associated potential are now analysed. A single SD perturbs the charge density locally, and its effect is negligible ≈ 1 QL away from the defect inside a slab. Figure 29

SD Bi_2Se_3	ΔE_{SD-SG}	ΔE_{SD-VP}	SD Bi_2Te_3	ΔE_{SD-SG}	ΔE_{SD-VP}
TB_1^2	19.04	18.70	TB_1^2	26.68	22.50
TB_1^3	8.20	7.10	TB_1^3	3.63	4.51
TB_1^4	17.51	17.79	TB_1^4	25.09	22.28
TB_1^5	2.21	2.77	TB_1^5	1.71	0.32
TB_2^1	2.23	2.82	TB_2^2	24.79	22.24
TB_2^2	17.42	18.01	TB_2^3	3.38	4.46
TB_2^3	7.87	7.20	TB_2^4	24.64	22.29
TB_2^4	17.39	18.00	TB_2^5	1.63	0.25
SF_1^1	19.04	18.70	SF_1^1	26.68	22.50
SF_1^2	29.72	26.37	SF_1^2	33.44	27.78
SF_1^3	27.87	25.84	SF_1^3	31.13	27.49
SF_1^4	19.37	20.18	SF_1^4	26.18	22.03
SF_1^5	9.91	7.77	SF_1^5	6.99	1.54
SF_2^1	19.39	19.99	SF_2^1	25.97	22.03
SF_2^2	27.85	25.90	SF_2^2	31.22	27.36
SF_2^3	27.83	25.73	SF_2^3	31.17	27.37
SF_2^4	20.69	20.09	SF_2^4	25.79	21.77
SF_2^5	9.99	7.71	SF_2^5	6.91	1.52

Table 7: SD formation energies, ΔE_{SD}, in meV/Å^2, for a SD, either a TB or a SF, placed at different locations in a 6 QLs thick Bi_2Se_3 (table on the right) and Bi_2Te_3 (table on the left) slab. We provide the SIESTA-GREEN derived energies (ΔE_{SD-SG}) in the second column, and those obtained from equivalent VASP calculations (ΔE_{SD-VP}) in the third column.

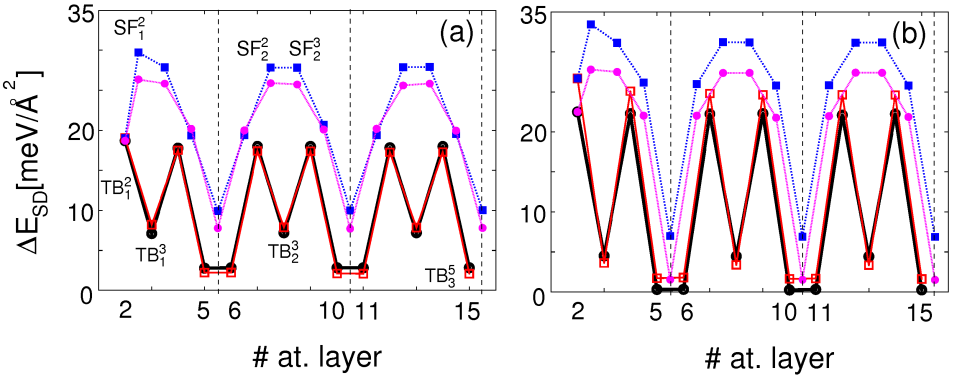

Figure 28: (a) Defect Formation Energy of SDs in different positions in a Bi_2Se_3 6 QL thick slab. The horizontal axis is the atomic layer at which the defect is located, being 1 the first atomic layer. Vertical dashed lines indicate the vdW gaps. Solid (dotted) lines with empty (filled) symbols correspond to TBs (SFs), while circles (squares) correspond to energies obtained with SIESTA-GREEN (VASP). Some of the systems are labelled according to the nomenclature (see text) for guidance. (b) Same as (a) for Bi_2Te_3.

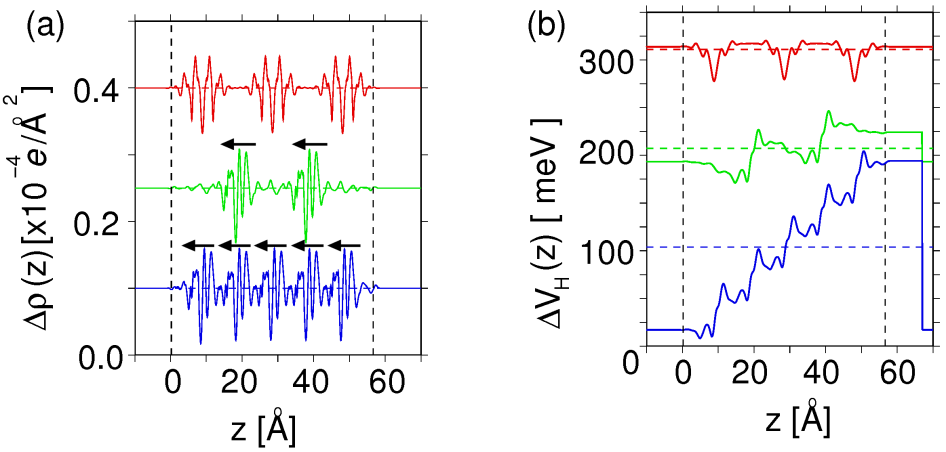

Figure 29: (a) Charge density profiles, $\Delta\rho(z)$, averaged over the 2D unit cell for a 6 QL thick Bi_2Se_3 slab after subtracting the defect free contribution. (b) Same as (a) but for the associated Hartree potential, $\Delta V_H(z)$. Red, green and blue lines correspond to defective structures $SF2_1^5$, $TB2_2^5$ and $TB1_1^5$ respectively. The z origin is located at the bottom surfaces. Vertical dashed lines indicate the two surfaces of the slab. Arrows in (a) show the direction of the dipole moment associated to the TBs. The drop in the potential at the vacuum seen in (b) is proportional to the total dipole moment of the system.

shows the 2D averaged charge density and potential profiles along the (111) direction, $\Delta\rho(z)$ and $\Delta V_H(z)$ respectively, for several SD arrangements in a 6 QL slab of Bi_2Se_3. The corresponding defect–free profile is subtracted in each case for clarity –recall that pristine Bi_2Se_3 and Bi_2Te_3 are centrosymmetric and therefore ideal slabs present no net electric dipole moment (DM)–. Inter-QL SFs produce a symmetric $\Delta\rho(z)$ and $\Delta V_H(z)$ perturbation, in contrast to intra–QL SFs and all TBs. Therefore, there is no DM for the former, while the latter do present a non-zero DM. The Mulliken charge analysis of a single SF and TB is presented in Figure 30(b), which is reminiscent of the charge density profiles in Figures 29 and 30(a). In the inter–QL TB case charge is rearranged with respect to the non-defective case among the atoms of the QLs at both sides of the defect. In the left QL, the Se and Bi atoms closest to the TB acquire a small amount of charge at the cost of the next inner Se, while in the QL at the right the interfacial Se donates charge to its closest Bi. On the other hand, in an inter–QL SF the Se-Bi-Se atoms at each side of the SD lose, gain and lose the same amount of charge respectively, leading to a highly symmetric electronic configuration. The difference in both charge rearrangements can be understood in terms of their symmetries: in the inter–QL SF inversion symmetry is preserved, in contrast to the inter–QL TB case (see insets in Figure 30). Figure 29 also shows clearly how the effect of single dipoles is cumulative and that the potential at both surfaces of the slab is determined by the internal dipoles. Thus, a doping of the surface states is expected for SD arrangements with non–zero DM.

5.4.3 *Dielectric properties*

Next, we examine the dielectric properties of Bi_2Se_3 systems with periodic arrangements of inter–QL TBs, which have been shown to be the most com-

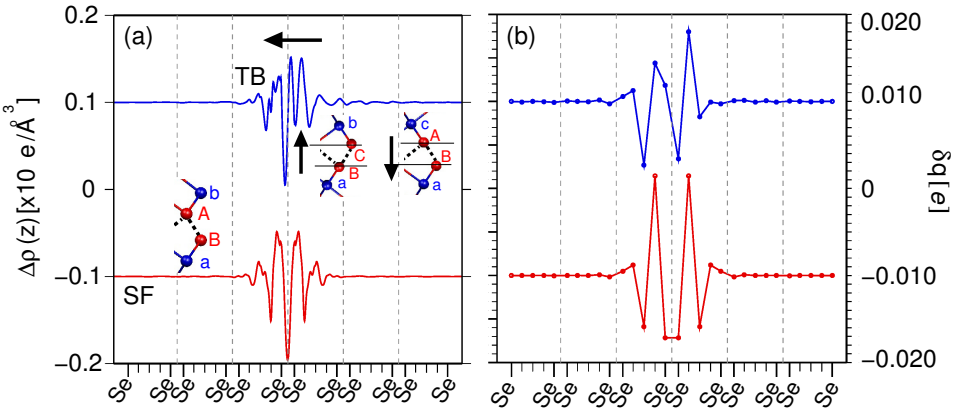

Figure 30: (a) Charge density profiles $\Delta\rho(z)$ averaged over the 2D unit cell for an inter–QL TB (blue line) and an inter–QL SF (red line). The asymmetry of the TB can be seen, in contrast to the symmetry in the charge rearrangement of the SF. Van der Waals gaps are marked with dashed lines for guidance. The insets show the local atomic configuration around each SD. The arrow indicates the direction of the electric dipole moment generated by the two possible inter–QL TB configurations, TB_1^5 and TB_2^1. (b) Atomic Mulliken populations for the cases depicted in (a) and after subtracting those of the defect–free slab. Data is shifted both in (a) and (b) for clarity.

mon type of SDs due to their low formation energy. In order to obtain the macroscopic relative permittivity of Bi_2Se_3 from DFT calculations, we can express the slab's dipole moment per unit area, m, for a slab with a spontaneous DM, in terms of the total polarisation P in the dielectric as:

$$m(t) = m_s + P\,t \tag{35}$$

where m_s is a surface localised contribution that accounts for the polar character of the slab, and t is the slab thickness. For Bi_2Se_3-like systems, m_s is zero due to their non-polar character. Assuming the dielectric is homogeneous in the z direction, the polarisation P can be written as:

$$P = P_S + P_E = P_S + \epsilon_0 \chi_e E_{int} \tag{36}$$

where P_S corresponds to the spontaneous polarisation of the system (i.e. the polarisation of the slab at zero internal field $P_S = P(E_{int} = 0)$), P_E is the induced polarisation due to the internal electric field E_{int} and ϵ_0 and χ_e are the vacuum permittivity and the system's electrical susceptibility respectively (we are therefore assuming implicitly a linear dielectric response of the system, and $\chi_e = \epsilon_r - 1$ with ϵ_r the system's relative permittivity). Continuity of the normal component of the displacement vector across any of the system's surfaces yields:

$$\epsilon_0 \epsilon_r E_{int} + P_S = \epsilon_0 E_{ext} \tag{37}$$

where E_{ext} is an applied external electric field and we have assumed zero surface charge.

Thus, even if $E_{ext} = 0$, a finite value of P_S will be associated to a non-vanishing internal field E_{int} inside the slab.

Combining Eqs. 36 and 37 we arrive at a general expression for the total polarisation which does not depend on the macroscopically averaged field E_{int}:

$$P = \frac{P_S}{\epsilon_r} + \frac{\chi_e}{\epsilon_r}\epsilon_0 E_{ext} \tag{38}$$

Comparison of Eq. 36 versus 38 clearly establishes that the SP defined at zero internal field and that defined at zero external field differ by a $1/\epsilon_r$ factor [106]. It also follows that if $P_S \neq 0$, the E_{ext} contribution in the second term above should not be identified with the induced polarisation $P_E = \epsilon_0 \chi_e E_{int}$.

Finally, inserting Eq. 38 in 35 we arrive at our desired expression for $m(t)$:

$$m = m_s + (P_S + \chi_e \epsilon_0 E_{ext})\ \frac{t}{\epsilon_r} \tag{39}$$

This equation allows us to derive expressions for the relative permittivity and the spontaneous polarisation in terms of variables that can be directly obtained via DFT calculations.

5.4.3.1 *Relative Permittivity*

Taking the partial derivative with respect to t in Eq. 39, we have:

$$\epsilon_r = \frac{\epsilon_0 E_{ext} - P_S}{\epsilon_0 E_{ext} - \partial m/\partial t} \tag{40}$$

For defect-free Bi_2Se_3 slabs $P_S = 0$, and the relative permittivity can be calculated as follows:

$$\epsilon_r = \frac{\epsilon_0 E_{ext}}{\epsilon_0 E_{ext} - \frac{\partial m}{\partial t}} \tag{41}$$

In Figure 31 we show the dependence of m with t for Bi_2Se_3 slabs 4-8 QLs thick under the presence of electric fields of 0.05 and 0.1 V/Å. The calculations were performed either fixing the ionic positions or allowing them to relax in the presence of the electric field (not shown), and we switched off SOC in order to avoid surface charges. The resulting high frequency and static permittivities, $\epsilon_r(\infty)$ and $\epsilon_r(0)$ respectively, are given in Table 8. For testing purposes, we alternatively calculated $\epsilon_r(\infty)$ with the VASP code using the Berry-phase approach [107]. As seen in the table, both approaches yield static permittivities in good agreement with the experimental ones. However, a large discrepancy was found for the static case. Although its origin is unclear to us, we just note the atypically large difference between the experimental $\epsilon_r(0)$ and $\epsilon_r(\infty)$ permittivity values.

5.4.3.2 *Spontaneous Polarisation and Doping Charges*

In analogy with ferro-electric materials [112], the existence of sizeable internal dipoles at the TBs yields a spontaneous polarisation, P_S, along the (111) direction. The continuity of the displacement vector, $\vec{D}$, across any of

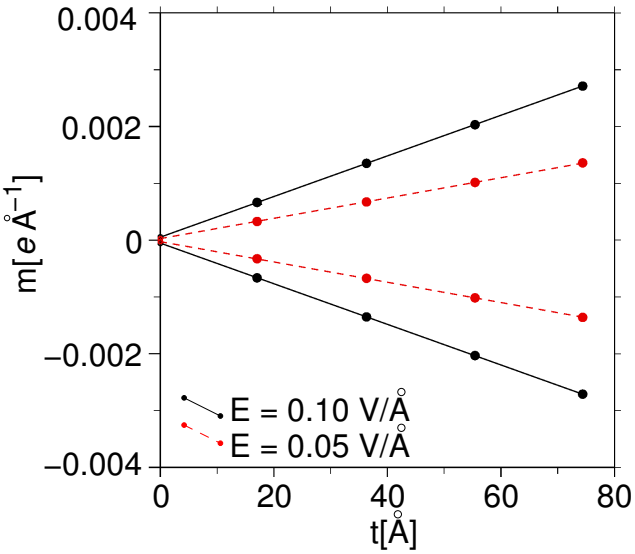

Figure 31: Slab's dipole moment per unit area, m, vs. slab thickness, t for ideal (non-defective) Bi_2Se_3 systems. Symbols correspond to the computed values of m, while lines are linear fits to the data points from which $\epsilon_r(\infty)$ is deduced. Solid (dashed) lines corresponds to calculations with E_{ext}= 0.1 (0.05) V/Å.

	This work	Experimental
$\epsilon_r(\infty)$	24.55 (25.2)	24.6[a], 25.4[a], 29.0[b], 29.2[c]
$\epsilon_r(0)$	29.92 (27.9)	113[d]

a Ref [108] *c* Ref [109]
b Ref [110] *d* Ref [111]

Table 8: Calculated and experimental values for the high (ion-clamped) and low frequency permittivities. Values in the second column were obtained from SIESTA slab calculations, while the permittivities obtained from the Berry phase approach employing the VASP code are given in parentheses.

the two slab's surfaces dictates that, $(\Delta\vec{D})\cdot\vec{u}_n = -(\epsilon\vec{E}_{int}+\vec{P}_S)\cdot\vec{u}_n = \sigma$, where $\vec{E}_{int}$ is the macroscopic field inside the TI (generally denoted as the depolarisation field if E_{ext}=0), σ is the surface charge density allocated at the TSSs and $\vec{u}_n$ is a unitary vector normal to the surface that points out of the film. In the large thickness limit the depolarisation field will vanish and, thus, a direct equivalence between the SP and the TSS doping is expected: $-\vec{P}_S\cdot\vec{u}_n = \sigma$. [107] Physically, this means that *bound* charges appearing at the surfaces of Bi_2Se_3 slabs containing SDs are fully compensated by the *free* TSS charge. For finite films, however, the surface charge distribution causes a finite depolarisation field that softens the SP discontinuity or, in other words, leaves the SP partially uncompensated. As a result, P_S represents an *upper* limit to the TSS doping σ –which will depend on the slab thickness. Once the relative permittivity is known, the spontaneous polarisation of a given system may be calculated by setting E_{ext} to 0 in Eq. 39:

$$m = m_s + \frac{P_S}{\epsilon_r}t = m_s + \frac{P_c}{\epsilon_r}t + m_{TB}N_{TB} \tag{42}$$

where P_c is the net polarisation in the defect–free regions, N_{TB} the number of TBs in the slab and m_{TB} the dipole moment per unit area associated to a single TB. Figure 33(a) shows the dipole moments per unit area as a function of slab thickness for the $TB1_1^5$, $TB2_1^5$ and $TB2_2^5$, and $TB3_1^5$, $TB3_2^5$ and $TB3_3^5$ polytypes. For the system with the highest density of defects, $TB1_1^5$, a TB is present every QL with parallelly aligned DMs and $m(t)$ shows an almost perfect linear behaviour. For the other cases, an abrupt descent (increase in absolute value) of the dipole moment appears every time a TB is included in the system, which justifies the existence of a m_{TB} associated to a single TB, while the slope in the non-defective region is small but positive ($P_c \approx 0.2\ 10^{12} e/\text{cm}^2$). The average value of m_{TB} is found to be $\langle m_{TB}\rangle$=3.8×$10^{-4} e/\text{Å}$ with deviations below 5% among all the studied *polytypes*, which indicates that interactions among inter–QL TBs are negligible. The bulk SP may now be estimated as: $P_S = 2\epsilon_r(m_{TB}/c)$ where c is the repeat vector of each *polytype*, which using the theoretically derived value of $\epsilon_r = 24.55$ yields P_S values of 9.6, 4.6, 3.0 and 2.3 $e\times10^{12}/\text{cm}^2$ for the TB1, TB2, TB3 and TB4 cases respectively. Notably, they correspond to substantial doping charges of the same order ($10^{12} e/\text{cm}^2$) as those measured for graphene on SiC *polytypes*, [113] or oxide interfaces ($10^{12}-10^{14} e/\text{cm}^2$) and even larger than those in doped semiconductors ($10^{10}-10^{12} e/\text{cm}^2$).

5.4.3.3 *Surface doping*

Here we present band structure calculations for *polytypes* of Bi_2Se_3 with periodic arrangements of inter–QL TBs, where the self-doping of the TSSs is patent. In Figure 32 we display the electronic structure around the DP for the top and bottom surfaces of structures $TB2_1^5$ (a-b) and $TB1_1^5$ (c-d). Clear shifts in the DPs with respect to the Fermi level can be observed in all of them, with the peculiarity that the sign of the doping can be tuned by inverting the orientation of the TB; top surfaces (a) and (c) present p–type doping while bottom surfaces (b) and (d) present n–type doping. The shifts are sensibly larger for the TB1, confirming that the density of TBs is a key ingredient in the doping mechanism. Remarkably, SFs induce almost

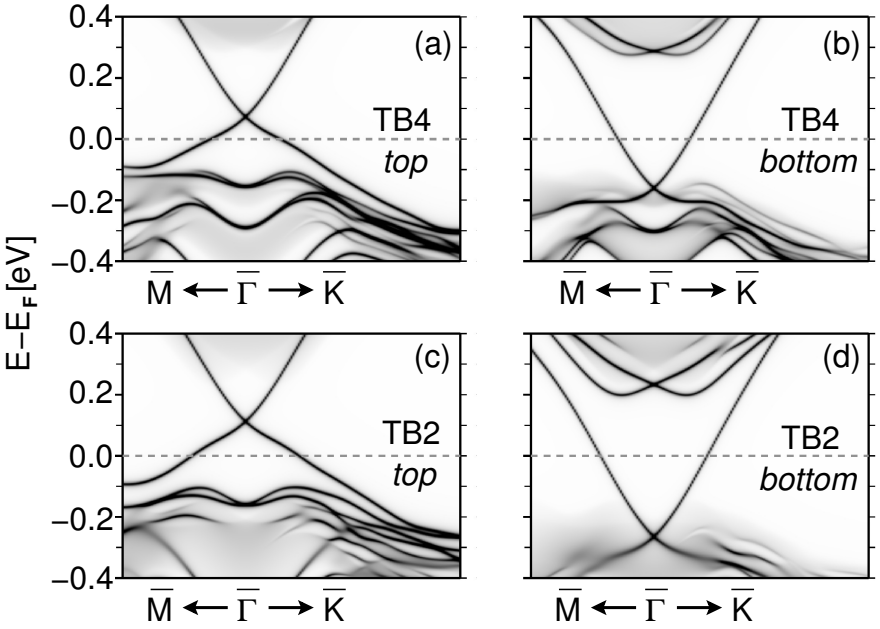

Figure 32: Electronic band structure for Bi_2Se_3 semi–infinite surfaces (a) $TB2_1^5$–top, (b) $TB2_1^5$–bottom, (c) $TB1_1^5$–top and (d) $TB1_1^5$–bottom. The maps are obtained from the k–resolved DOS projected on the 3 QLs closest to the surface. An 8 QL thick slab was employed in all cases to construct the surface, so that 4 (7) TBs are included in the TB2 (TB1) case. As a TB is not symmetric in z, the top and bottom surfaces give raise to dopings of opposite sign (see Figure 27), with the left (right) column showing p-(n-)doped TSSs. Due to the smaller group velocity of the TSS in the valence band region, the DP shifts are smaller for p-doped surfaces.

negligible DP shifts of less than 10 meV due to their very small DM. The quantitative evaluation of the doping charges in the TSSs is not, as it may seem, a trivial task, and is detailed in subsection 5.4.5 below.

A summary of the dopings for all the bottom and top surfaces with inter–QL defects is presented in Figure 33(b), and compared with the dipole moment per unit area dependence on the slab thickness and defect periodicity in (a). The TSS charge (left axis) or, equivalently, the DP shifts in energy (right axis in non–linear scale) is plotted as a function of the slab thickness t. The first observation is that all bottom (top) surfaces show clear n–(p–)type doping, as dictated by the direction of the spontaneous polarisation. Next, doping levels increase with t and approach a limiting value, which is precisely the SP associated to each *polytype* (indicated by horizontal lines on the right in the figure). At the largest thickness we considered (10 QLs), the dopings reach up to 60% of this limit (5.4 and -5.9 $e \times 10^{12}/\mathrm{cm}^2$for the maximum hole and electron concentrations respectively), while we estimate by extrapolation that almost full compensation of the SP is reached at ~ 18 QLs. In addition, there is a clear resemblance between these curves and the $m(t)$ ones in Figure 33(a), specially the ladder type behaviour of TB2 and TB3. Again, sudden jumps in the doping are seen whenever a defective QL is added to the slab, whereas if the additional QL is non–defective, it tends to screen the SP causing a slight decrease in the surface doping. We may therefore conclude that the doping can be tuned via the actual number of TBs and its density N_{TB}/c, as well as by the proximity of the first TB to the surface.

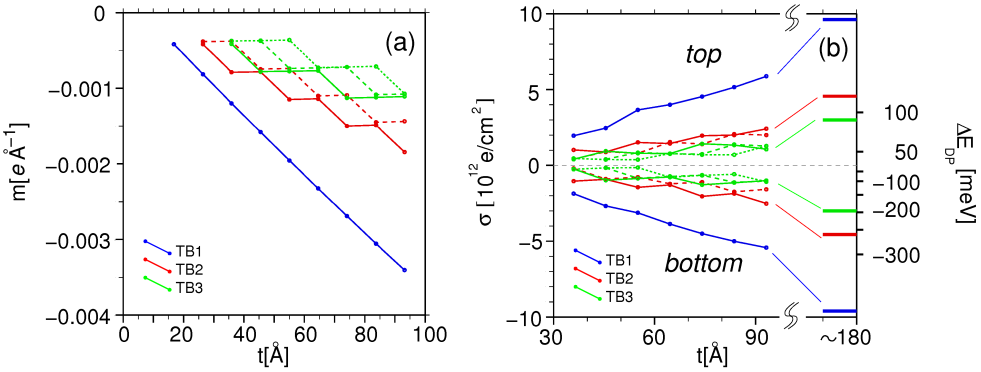

Figure 33: (a) Dipole moments per unit area, m, for Bi_2Se_3 slabs with different TB arrangements as a function of the slab thickness, t. Blue, red, and green lines correspond to best fits to the data points (circles) for structures TB1, TB2, and TB3, respectively, according to eq. 42. For the last two we used solid, dashed, and dotted lines after grouping the slabs according to the location of the TB closest to the uppermost QL. SOC was not included in these calculations in order to remove the TSS and hence obtain an insulating (dielectric) slab. (b) Doping charge (left axis) and DP shifts in the TSS (right axis) for the top and bottom surfaces constructed from the same slabs as in (a), again as a function of t. Horizontal lines at the right show the limiting charges for each *polytype* derived from their bulk SPs.

Note that in the reported doped surfaces all the DMs generated by TBs are aligned in parallel, and, hence, accumulate. Indeed, surfaces and slabs with anti–parallel configurations show no net SP due to the cancellation of the DMs, and thus, the value of the doping at the TSSs vanishes. Nevertheless, the anti–parallel TB arrangement results energetically less favourable than the parallel one, as will be shown in Section 5.5, where this other kind of systems will be analysed in more detail.

5.4.3.4 *Effects of Relaxation*

We also calculated the SP of defected Bi_2Se_3 slabs allowing the atoms to fully relax. As a result the distance between adjacent QLs increased up to 2.4 Å (being 2.25 Å in ideal slabs) in order to better screen the SD dipoles. This is in perfect agreement with previous calculations [114] Nevertheless, the calculated P_S values differ by less than 10% from the *unrelaxed* results and, as shown in Fig. 34, the linear relationship with the SD density is preserved.

5.4.4 *Surface State Characterisation*

We present below a detailed electronic and spin characterisation of the TSS in our Bi_2Se_3 systems which, when compared to previous studies, confirms the correct performance of the calculation scheme described in Section 5.3. The study also serves to determine to what extent the TBs perturb the TSS properties.

First we address the penetration depth of the TSS into the substrate by examining its LDOS profile along the slab normal and calculated close to $\bar{\Gamma}$. In Figure 35 we compare the TSS-LDOS profiles for the upper (occupied) and lower (empty) surfaces for a faulted and unfaulted 6 QL thick film. Recall

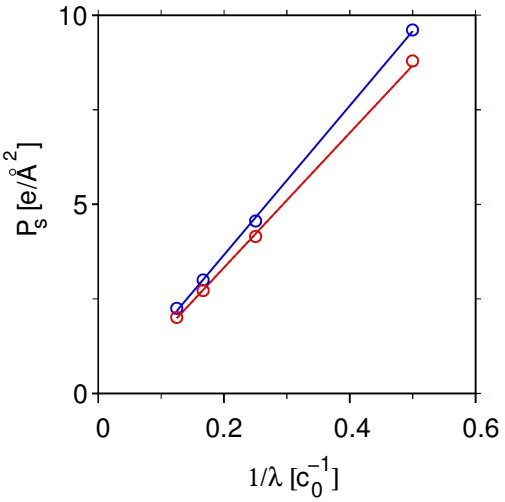

Figure 34: Spontaneous polarisation of different Bi_2Se_3 *polytypes* calculated from the slope of m vs. t. Only *polytypes* with inter–QL TBs are considered. λ is the periodicity of the twin defect in each system, and is expressed in terms of the lattice vector c_0 of the *polytype*. The red points correspond to the values of P^s obtained for fully relaxed slabs for each *polytype*, while blue points correspond to the partially relaxed calculations described in the main text. Fitting the data to a linear function $P = a/\lambda + P_0$ we obtain a = 17.8 and 19.7 e/c_0 and P_0 =-0.23 and -0.28 e/Å^2 for the fully and partially relaxed cases respectively.

that even for the ideal case the upper and lower TSSs are not symmetric due to the particular dispersion relation where electron-hole symmetry is not fulfiled (see below). The plots show that the TSSs are strongly localised within the first two QLs in all cases, and that their spatial profiles are not altered by the SDs.

Next we examine the TSS spin texture close to $\bar{\Gamma}$ by calculating the in- and out-of-plane spin components, S_{xy} and S_z respectively, of the DC's states. The results are displayed in Fig. 36. The 3–fold symmetric modulation of S_z, vanishing along the $\bar{\Gamma} - \bar{M}$ directions and alternating maximum positive and negative values along $\bar{\Gamma} - \bar{K}$ and $\bar{\Gamma} - \bar{K}'$ respectively, shows that the spin is locked to crystal momentum [80, 115, 116, 117]. Again, the spin texture is essentially skyrmion–like, indicating that the surface state remains topologically protected.

5.4.5 *k-sampling and doping estimations*

The k-convergence in the faulted Bi_2Se_3 slabs was found to be extremely slow due to the highly dispersive character of the DC and the fact that, across the gap, it covers only around 16% of the total BZ . In Figure 37(a) we present the density of states projected on the TSS as a function of the k-sampling employed in the self-consistent calculations. For a finite small broadening of 5 meV the expected square-root-like behaviour above E_F (see dashed line) is not even reproduced with a k-point sampling as dense as (100×100), while typical meshes of around (10×10) yield an unrealistically large peak at $\bar{\Gamma}$. Recall that the dispersion relation is linear only in the vicinity of the Γ point. For a SD free slab the impact of a poorly sampled BZ

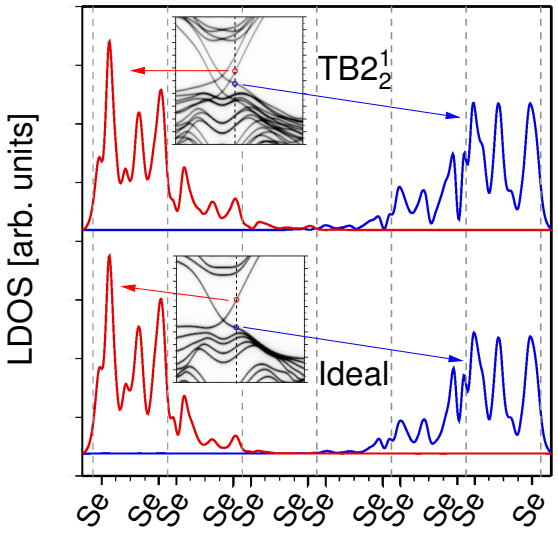

Figure 35: LDOS for the TSSs in an ideal slab and a TB2$^1_2$ slab calculated at $k = 0.05$ Å^{-1} in the $\bar{\Gamma} - \bar{K}$ direction (vertical dashed line in the insets). The unoccupied (occupied) TSS at the lower (upper) surface of the slab is coloured in red (blue). The TB2 case is shifted for clarity. Note that the TSSs shown in the figure are not at the same energy. The penetration depth in both cases is ∼2 QLs, which is in accordance with the fact that a gap opens for slabs with thicknesses below 4 QLs. The spatial profile of the TSS is preserved in the presence of SDs. the state for which the LDOS is shown in each case. Blue and red arrows indicate the surface within each state is localised.

should not affect the location of the DP since charge neutrality will pin it precisely at E_F as long as the DP lies in the bulk band gap. However, when estimating the DP shift in faulted slabs together with its associated doping charge, large errors may be expected. Fortunately, integrating the DOS to obtain these charges presents a better k-convergence. After extensive tests, we fixed the k-supercell to a (65×65) in all calculations since it already yields well-converged values, as can be seen in Fig. 37(b). We recall that any source of asymmetry between the upper and lower surfaces of the slab, not necessarily a SD but, for instance, an external electric field, will require as well dense k-meshes for a proper estimation of the DP energy.

Once the DP is accurately determined, the calculation of the charge acquired or released by the TSS is not, as it may seem, a trivial issue. As shown in the insets of Fig. 37(b), for large n-dopings $\lesssim -50$ meV (purple TSS in the inset) the DP falls below the VBM and therefore, numerical integration of the PDOS would include additional contributions from the VB. To elude this problem, we derive the TSS charge by employing an analytical expression as shown next. On the other hand, p-doped surface states (orange TSS) do not pose this problem and the hole concentration in these cases has been calculated by numerical integration of the PDOS obtained with DFT –in fact, the curvature of the hole-like band is strongly dependent on the position of the DP and thus, the same analytical expression cannot be used for different p-dopings.

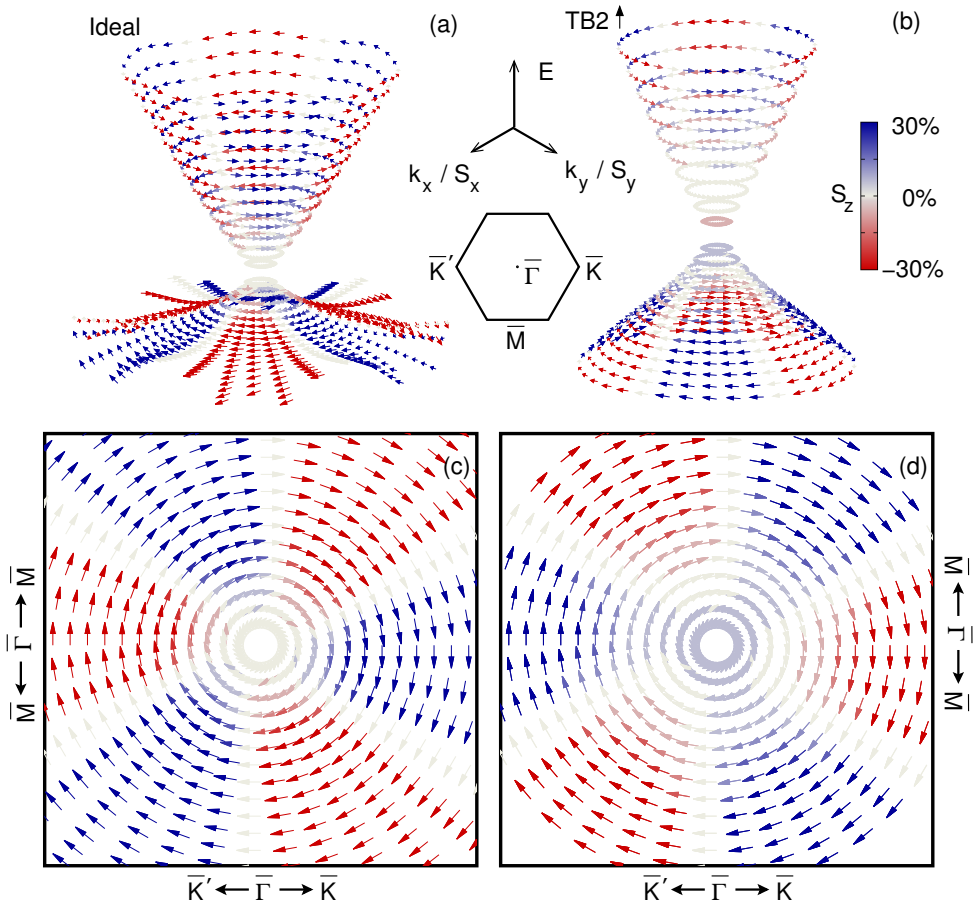

Figure 36: (a) and (b): Spin texture of the DC in an ideal surface and a p-doped TSS respectively. The x and y components of the spin are plotted as arrows, while the z component is represented with the col or code. Spin-momentum lock is realised for the helical TSSs, even with defects present in the system. The value of S_z is represented as the percentage of the modulus of $S = \sqrt{S_x^2 + S_y^2 + S_z^2}$. S_z presents a small modulation with three-fold symmetry, being 0 in the $\bar{\Gamma} - \bar{M}$ direction as required by mirror symmetry. The energy difference between the DP and the VBM is greater in (b), which reduces the hexagonal warping effect that is caused by hybridisation of the TSSs with the VB. (c) and (d) show a top view of the DC below the DP (hole-like band) for the same two systems.

	Region	
	1	2
m_i^* (m_e)	-0.18	0.26
v_{Fi} (10^5m/s)	-0.77	3.36
E_i (meV)	-61.0	3.4
σ_i (10^{12}e/cm)	3.39	-6.46

Table 9: Fitted values for the dispersion relation in the two different regions. m_e is the electron mass. σ_i were obtained by imposing $\sigma(0) = 0$ and continuity of $\sigma(E)$.

5.4.5.1 *Analytical Model*

As shown in Figure 38, we fit the TSS dispersion relation of an ideal slab to a continuously differentiable quadratic two piecewise function, assuming the band dispersion is isotropic close to the $\bar{\Gamma}$ point:

$$E(k) = \begin{cases} \frac{\hbar^2 k^2}{2m_1^*} + \hbar v_{F1} k + E_1, & k < k_c \\ \\ \frac{\hbar^2 k^2}{2m_2^*} + \hbar v_{F2} k + E_2, & k \geq k_c \end{cases} \tag{43}$$

where v_{Fi} and m_i^* are the Fermi velocity and the effective mass in region i respectively and $k_c = -0.047$ Å^{-1} is the boundary between the two regions. This fit is only valid for energies higher than -125 meV. The optimised parameter values are given in table 9 while the goodness of the fit can be visually checked in Fig. 38.

The corresponding DOS, $D(E)$, is therefore:

$$D(E) = \begin{cases} A_1 \left| \frac{1}{\sqrt{1 + \frac{2}{B_1}(E - E_1)}} - 1 \right|, & E < E_c \\ A_2 \left| \frac{1}{\sqrt{1 + \frac{2}{B_2}(E - E_2)}} - 1 \right|, & E \geq E_c \end{cases} \tag{44}$$

where $E_c = E(k_c) = -61.5$ meV, $A_i = \frac{m_i^*}{2\pi\hbar^2}$ and $B_i = m_i^* v_{Fi}^2$.

Finally, the resulting carrier density $\sigma(E)$ will be:

$$\sigma(E) = \int_0^E D(E')dE' \tag{45}$$

, yielding:

$$\sigma(E) = \begin{cases} A_1 [\sqrt{B_1(B_1 + 2(E - E_1)} - E] - \sigma_1, & E < E_c \\ A_2 [\sqrt{B_2(B_2 + 2(E - E_2)} - E] - \sigma_2, & E \geq E_c \end{cases} \tag{46}$$

where σ_i are integration constants given in Table 9.

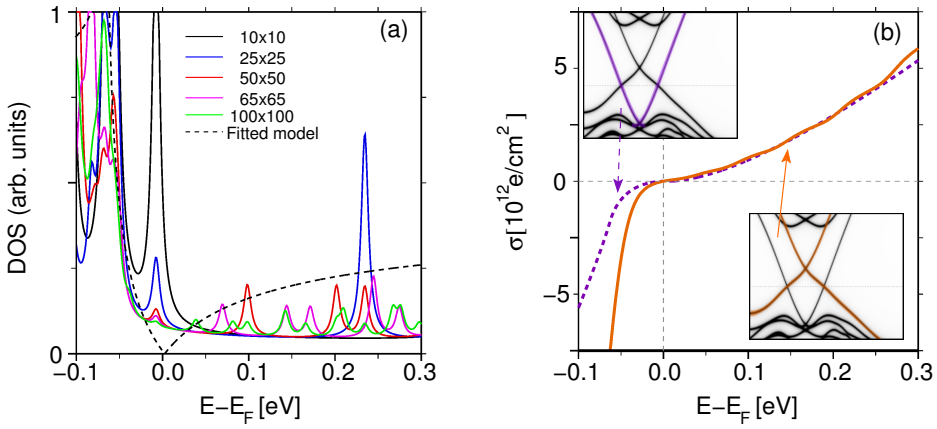

Figure 37: (a) DOS around the DP for an ideal 6 QL slab. The solid black, blue, red, magenta and green lines correspond to DOS obtained with increasingly denser k-point meshes (see legend) and using a broadening of 5 meV in all cases. The dashed black line shows the DOS derived from the fitted model (see text). As the DC occupies a small portion of the whole BZ, even dense meshes of (100x100) k-points do not reproduce the square-root-like behaviour of the DOS expected for the TSSs. (b) Surface charge density σ of the TSSs with respect to energy. The orange, solid line shows the value obtained directly from the SIESTA-GREEN calculation, and the purple, dashed line the σ obtained from the fitted model. The former was used to obtain the value of the surface charge density for $p-$doped TSSs and the latter was used for $n-$doped TSSs (see text). The mismatch between the model and the numerically calculated σ is originated by the additional contribution of the electrons in the VB below $\sim$ -50 meV, which are avoided with the model.

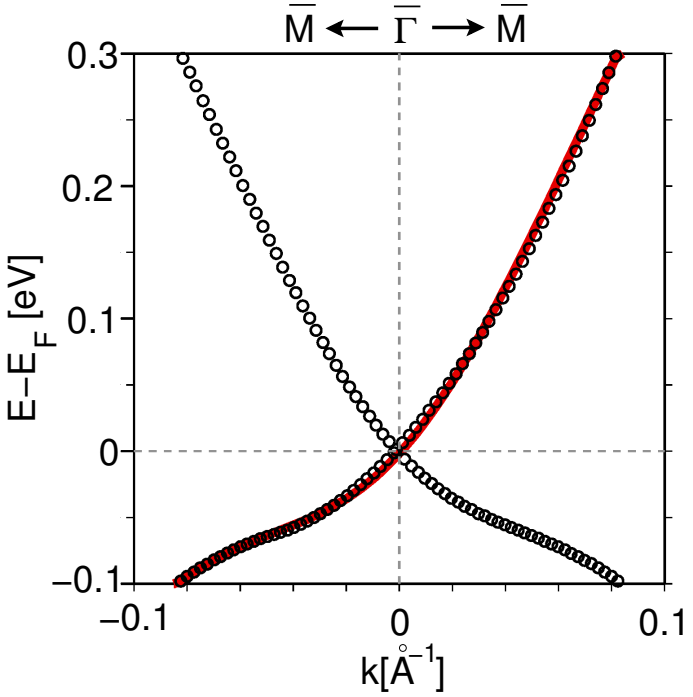

Figure 38: Dispersion relation of the TSS along the $\bar{\Gamma} - \bar{M}$ direction of an ideal 6 QL slab. The red line is the fitted $E(k)$.

5.5 ANTI–PARALLEL CONFIGURATIONS

The systems which exhibit self-doping due to their spontaneous polarisation shown in the previous section have their DMs aligned in parallel. Here we will study the defect formation energy and electronic structure of faulted Bi_2Se_3 systems in which the inter–QL TBs are in an anti–parallel configuration. We start by considering a 6 QL Bi_2Se_3 slab with different number of inter–QL TBs (N_{TB}=2, 4 and 5) to explore any interactions among them. Furthermore, TBs may be oriented so that their dipoles point either towards the bottom or the top surface of the slab (see Figure 39). In Table 10 we give the average TB formation energy for the different configurations considered. Overall, the smallest $\langle \Delta E_{SD} \rangle$ values are obtained for those slabs where all TBs are aligned parallel to each other, with only a slight increase as N_{TB} increases (configurations $[00++0]$ and $[00--0]$ versus $[+++++]$, see Figure 39 for the notation scheme), indicating that inter-TB interactions are small. On the other hand, the presence of anti–aligned TBs consistently leads to larger average formation energies by around $\sim$0.1 meV/Å^2. Notably, from the slab's dipole moment per unit area (also given in the table), it is clear that aligned TBs accumulate their dipole moments while those anti–aligned tend to cancel (last four rows in the table). The slight increase in $\langle \Delta E_{SD} \rangle$ for the $[00++0]$ and $[+++++]$ cases with respect to $[00--0]$, being the three of them parallel TB configurations, can be explained by the distance of the dipoles to the surface. An increase of the formation energy of a TB is seen as the defect is placed closer to a surface, as seen in Figure 28. The $[+++++]$ case clearly presents twins closer to the surface than $[00--0]$. But, although not apparent with the chosen notation, $[00++0]$ also presents a smaller distance of the last $+$ dipole to the top surface, as the centre of the dipole itself is not between the two uppermost QLs, but is slightly shifted

TB conf.							$\langle \Delta E_{SD} \rangle$	m
[	0	0	−	−	0	]	2.15	2.6
[	0	0	+	+	0	]	2.18	-2.6
[	+	+	+	+	+	]	2.20	-14.3
[	−	−	0	+	+	]	2.23	0.0
[	+	+	0	−	−	]	2.28	0.0
[	0	0	−	+	0	]	2.30	-0.1
[	+	−	+	−	+	]	2.30	-0.3
[	−	+	−	+	−	]	2.30	-0.3

Table 10: Average TB formation energies, $\langle \Delta E_{SD} \rangle$, in meV/Å^2, and total slab's dipole moment per unit area, m, in 10^{-4} e/Å, obtained for a 6 QL thick Bi_2Se_3 slab with different inter–QL TB configurations as indicated in the first column –see Figure 39 for the notation scheme–. All tabulated values have been obtained with the SIESTA formalism.

towards the top surface (see also Figure 39, where the topmost kink in the stacking sequence for the (a) and (b) cases is at different distances from the top surface). Therefore, despite the small energy difference between aligned and anti–aligned TB configurations, we may conclude that the polytypes discussed in the previous section of this chapter are the most stable, as the formation energy increases with every anti–parallel pair of TBs.

With the notation scheme depicted in Figure 39, we can define the inversion operation $\mathbb{I}$ as:

(i) reversing the order of the configuration

(ii) flipping the sign of the components, leaving the zeroes unchanged

We can check that for the inversion–symmetric cases listed in Table 10, applying $\mathbb{I}$ returns the same configuration, i.e. $\mathbb{I}[--0++] = [--0++]$.

In the last section, we showed how aligned TBs induce opposite doping at opposite surfaces of a slab, but looking at the whole, spin–textured band structure, and regardless of the localisation of the states, the effect of aligned TBs can also be viewed as a Rashba–like splitting of the DCs. As inversion symmetry is broken, the spin degeneracy is lifted and the DCs shift laterally in momentum space while preserving TRS. The overall result is an effective electric field perpendicular to the surface that gives rise to opposite doping for opposite surfaces. We will now study the effect of TB arrangements which do *not* break inversion symmetry, and, therefore, no splitting of the DCs should occur, so both surfaces of the slab should be equivalent being related precisely by $\mathbb{I}$.

For this purpose, we construct Bi_2Se_3 slabs of different thicknesses in which each half of the system has opposite dipoles to the other half. The two unequivalent configurations we consider have the forms $[-...--0++...+]$ and $[+...++0--...-]$ where the 0 in the middle is only present in QLs with an even number of QLs. We will refer to them as Pm and Nm systems respectively, where m will be the thickness of the slab in QLs. The presence of inversion symmetry is evident from the notation and the definition of $\mathbb{I}$, and already dictates that the total dipole moment of the system must be

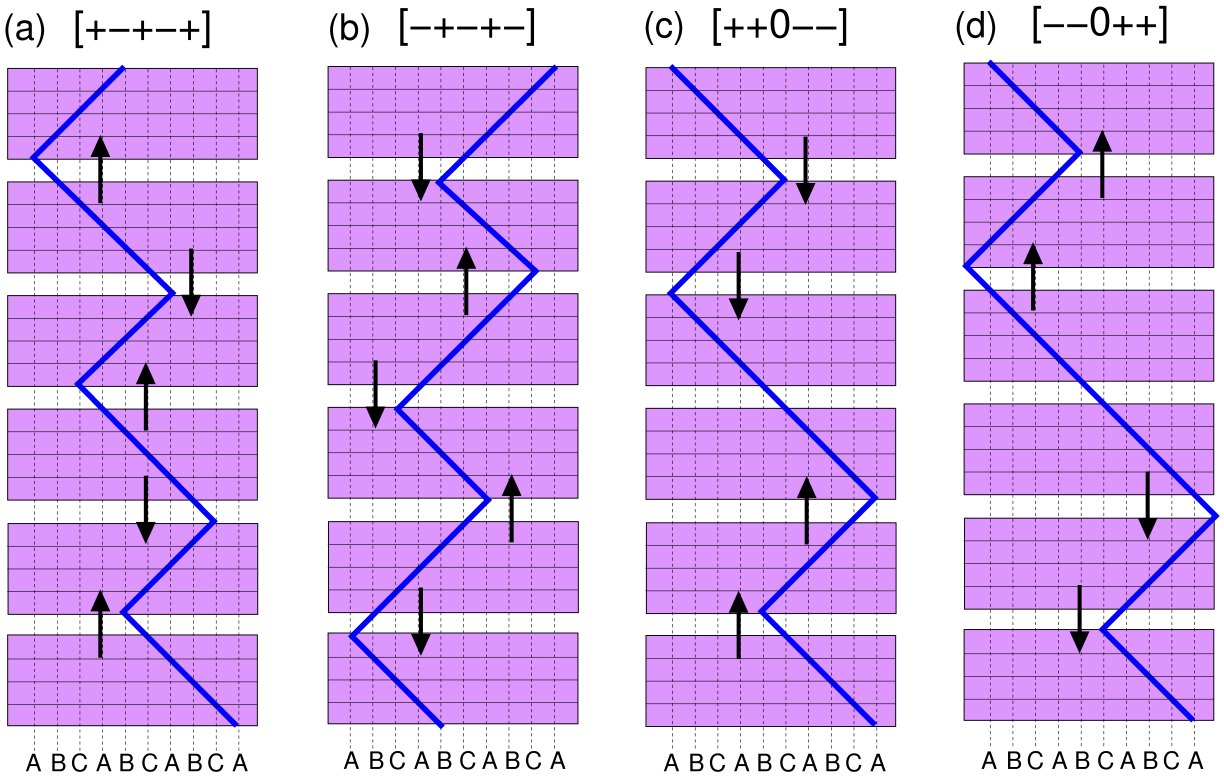

Figure 39: TB notation scheme for a 6 QL slab for different TB arrangements: (a)$[+-+-+]$, (b) $[-+-+-]$, (c) $[++0--]$ and (d) $[--0++]$. QLs are sketched by filled rectangles, thick blue lines follow the QL stacking sequence for each configuration (indicated by the horizontal dashed lines) and arrows point along each TB's dipole moment. from bottom to top, we denote by $+$ and $-$ the TB dipole moments pointing upwards and downwards, respectively, while 0 corresponds to the absence of a TB. Note that configurations (a) and (b) are equivalent (its the same system rotated by 180°), while (c) and (d) are not.

exactly zero. The defect formation energy for such configurations are listed in table 11. All of them are consistently slightly larger than their aligned counterparts. These systems present two distinct regions with opposite spontaneous polarisations, leading to the formation of a ferroelectric 180° domain wall in the centre of each slab. This domain wall is of the head–to–head or the tail–to–tail kind for the Nm or Pm systems respectively.

The average DFE for the Pm systems is 2.23 meV/Å^2, and 2.24 for the Nm systems. For all the TBs aligned in parallel, the same calculation leads to an average value of 2.20 meV/Å^2, so the domain wall formation energy can be estimated to be ~ 0.02 meV/Å^2. Although the energy differences shown here are smaller than our numerical precision they are still meaningful, given the fact that the total energy differences for the slabs are of the order of several meV, but are then divided by the area of the slab and the number of defects to obtain the above values.

5.5.1 *Charge and Potential*

The changes in charge rearrangement and their associated potential are now analysed and compared to the parallel TB cases. The dipoles generated by the inter–QL TBs in one half of the sample compensate those of the other half. Figure 40 shows the 2D averaged charge density and potential profiles along the (111) direction, $\Delta\rho(z)$ and $\Delta V_H(z)$ respectively, for the $P7$, and $N7$ systems together with $T7$ for comparison. In the first two cases the dipoles accumulate towards the centre of the slab, generating a two–dimensional electron gas (2DEG) or a two–dimensional hole gas (2HEG) for the Nm and Pm cases respectively. In the large thickness limit, the charge in the boundary between the two domains with opposite polarisations should be equal to $\sigma = \pm 2|P_s|$.

5.5.2 *Band structure*

The electronic band structure of the Pm and Nm systems is shown in Figure 42 for m=3–7 QLs. A positive (negative) shift in energy of the TSSs with respect to the bulk subbands is obtained for the Pm (Nm) configurations which increases with the thickness of the slabs. The Fermi level is still pinned at the DP as long as the latter remains in the bulk band gap, so no net doping arises. Instead, a bulk subband coming from the unoccupied (occupied) is lifted (brought down) in energy and localised at the domain wall for the Pm (Nm) cases. That subband is strongly localised at the domain wall, and it extends over $\sim$3 QLs in total, the one of the domain wall itself and the two adjacent QLs (see Figure 43). Another important result is that, as the size (number of dipoles) increases, the hole–like surface state (HSS) for the Pm systems becomes more linear. This is due to a decrease in the interaction with the VB, since the energy difference between the VBM and the DP becomes larger with increasing thickness. As a consequence, the hexagonal warping effect of the HSS also diminishes. If the number of anti–parallel defects (which for these polytypes grows linearly with the thickness of the slab) is large enough to induce a band bending bigger than the VBM (CBM) energy, the conduction band (valence band) crosses the Fermi level and the

System	defect formation energy (DFE)	N_{TB}	$\langle \Delta E_{SD} \rangle$
P3	4.43	2	2.21
P4	4.46	2	2.23
P5	8.95	4	2.24
P6	8.90	4	2.23
P7	13.37	6	2.23
P8	13.31	6	2.22
P9	17.78	8	2.22
N3	4.45	2	2.22
N4	4.44	2	2.22
N5	8.92	4	2.23
N6	9.12	4	2.28
N7	13.47	6	2.25
N8	13.55	6	2.26
N9	17.86	8	2.23
T3	4.40	2	2.20
T4	6.61	3	2.20
T5	8.80	4	2.20
T6	11.00	5	2.20
T7	13.18	6	2.20
T8	15.37	7	2.20
T9	17.53	8	2.19

Table 11: DFE in meV/Å^2, number of twin boundaries N_{TB} and average TB formation energies, $\langle \Delta E_{SD} \rangle$, in meV/Å^2. obtained for 3-9 QL thick Bi_2Se_3 slabs with inversion–symmetric TB arrangements Pm and Nm (see main text) and for all TBs aligned in parallel (Tm cases). All tabulated values have been obtained with the SIESTA formalism.

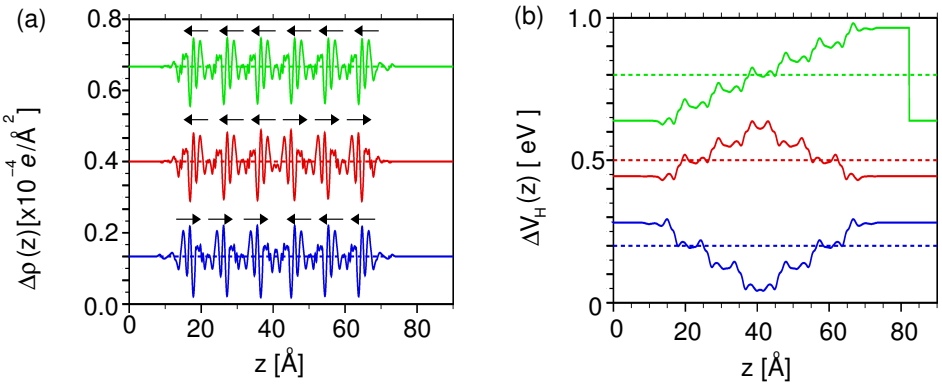

Figure 40: (a) Charge density profiles, $\Delta\rho(z)$, averaged over the 2D unit cell for a 7 QL thick Bi_2Se_3 slab after subtracting the defect free contribution. (b) Same as (a) but for the associated Hartree potential, $\Delta V_H(z)$. Green, red and blue lines correspond to defective structures $T7$, $N7$ and $P7$ respectively. Arrows in (a) show the direction of the dipole moment associated to the TBs. The drop in the potential at the vacuum seen in (b) is proportional to the total dipole moment of the system, and therefore is zero for the inversion–symmetric cases $N7$ and $P7$. The inversion symmetry is evident in the Hartree potential profiles.

system becomes metallic for the Nm (Pm) systems. In such situation, the domain wall at the centre of the slab becomes charged and a 2HEG or 2DEG localises for the Nm and Pm cases respectively, and the TSSs acquire (half) the opposite charge, keeping the system electrically balanced.

5.6 SUMMARY AND CONCLUSIONS

In the first part of this chapter we have shown the effect of two main kinds of stacking defects in Bi_2Se_3 systems, namely SFs and TBs. Being both more energetically favourable if they affect the vdW bonds, the former are less probable and preserve inversion symmetry, while the latter are more stable and generate an electric dipole. Our results can explain at least part of the TSS doping observed in many experiments, as TBs are ubiquitous in the literature on real samples of the Bi_2Se_3 family of compounds. Moreover, a periodic arrangements of TBs can be used to tune the sign and magnitude of the doping of the TSS. We have also shown the electronic and spin texture of the doped TSSs, and proved that they remain topologically protected.

In the last section we have investigated inversion–symmetric Bi_2Se_3 slabs that exhibit equivalent surfaces, as opposed to the parallel alignments of TBs described in the previous Section. In a system with inversion symmetry Krammers' degeneracy holds and consequently no Rashba splitting of the TSSs is seen. Moreover, the TSSs remain undoped as long as the DP stays within the bulk gap. A shift in the energy of the DCs is obtained with respect to the bulk subbands. The magnitude of the shift is determined by the number of TBs, whereas the sign of the shift is opposite for head–to–head and tail–to–tail configurations (Pm and Nm systems respectively). At the boundary between the two ferroelectric domains with opposite polarisation a domain wall appears at the cost of $\sim$0.02 meV/Å^2, and for thick enough slabs a 2DEG or 2HEG localises.

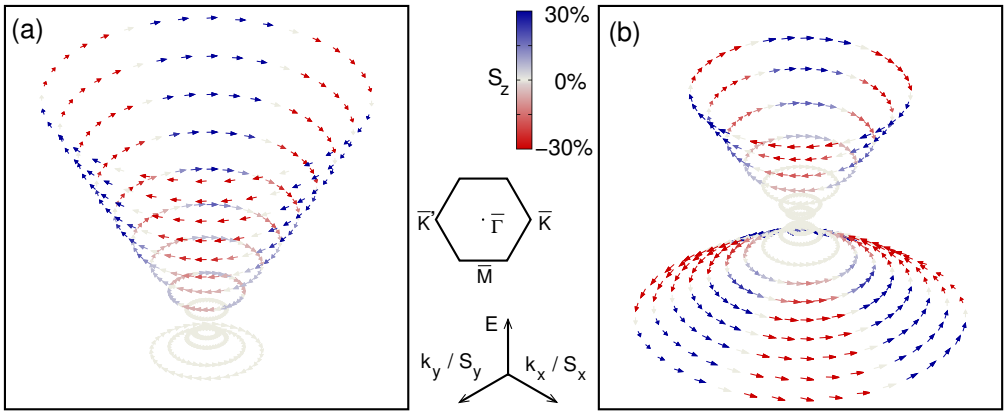

Figure 41: Spin–texture of the TSSs for the $N7$ –(a)– and $P7$ systems –(b)–. The x and y components of the spin are plotted as arrows, while the z component is represented with the colour code shown between (a) and (b). The value of S_z is represented as the percentage of the modulus of $S = \sqrt{S_x^2 + S_y^2 + S_z^2}$. Spin–momentum locking is preserved as well as its three-fold symmetry. Moreover, no small S_z component develops close to the $\bar{\Gamma}$ point, in contrast to Tm systems shown in the previous section. The distance in energy from the DP to the VBM in the $P7$ slab is larger than in the pristine surface, leading to a decrease in the hexagonal warping effect (see Figure 9).

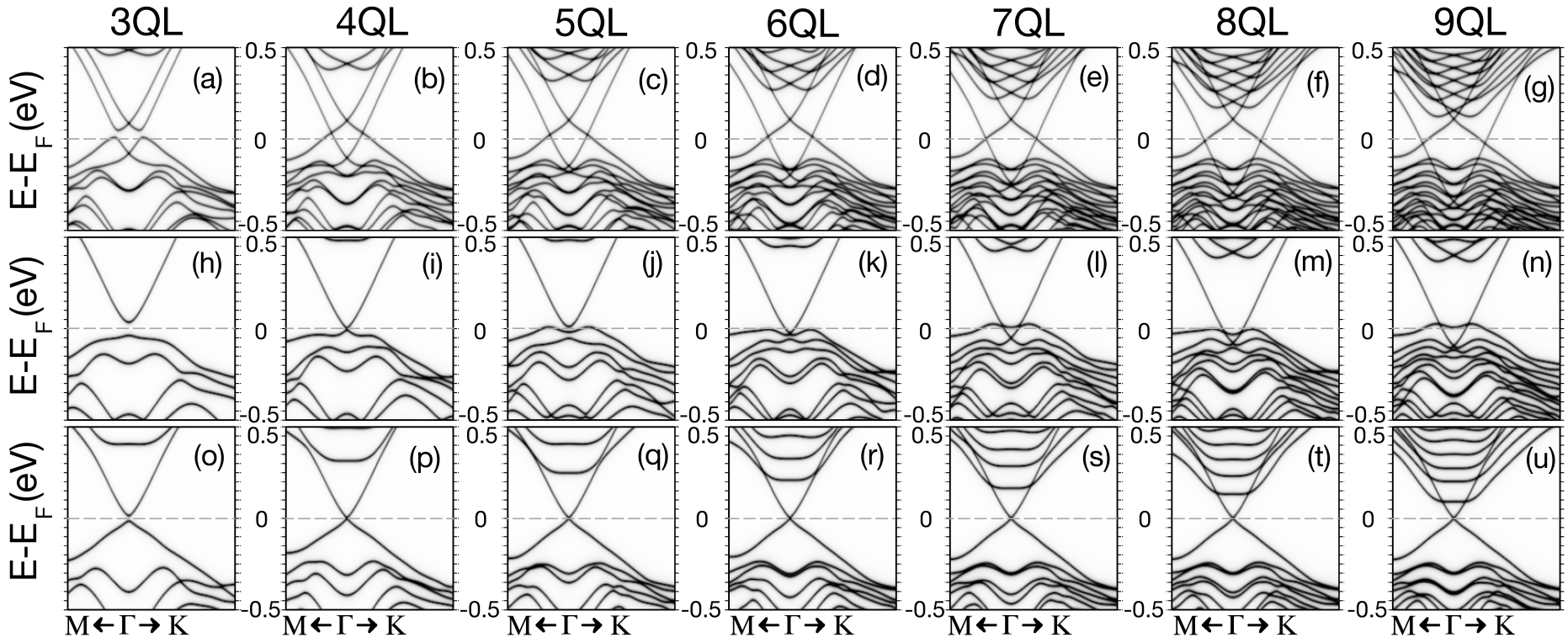

Figure 42: Band structures close to the $\bar{\Gamma}$ point for Tm, Nm and Pm (first, second and third row respectively). Columns 1 to 7 correspond to increasing slab thicknesses from 3 to 9 QLs. Nm (Pm) systems show no Rashba splitting of the TSSs, in contrast to the Tm cases. Nevertheless, the DCs are shifted upwards (downwards) in energy with respect to the bulk subbands for the Pm (Nm) configurations. Slabs of 3 QLs show a gap in the TSSs due to surface-surface interaction in the 3 cases. The DP of the Nm systems is below the VBM for m>4, and for the special case $N5$ the DP coincides with VBM and a small gap opens in the DC due to hybridisation. The Fermi level is shown as a grey dashed line as a guide to the eye.

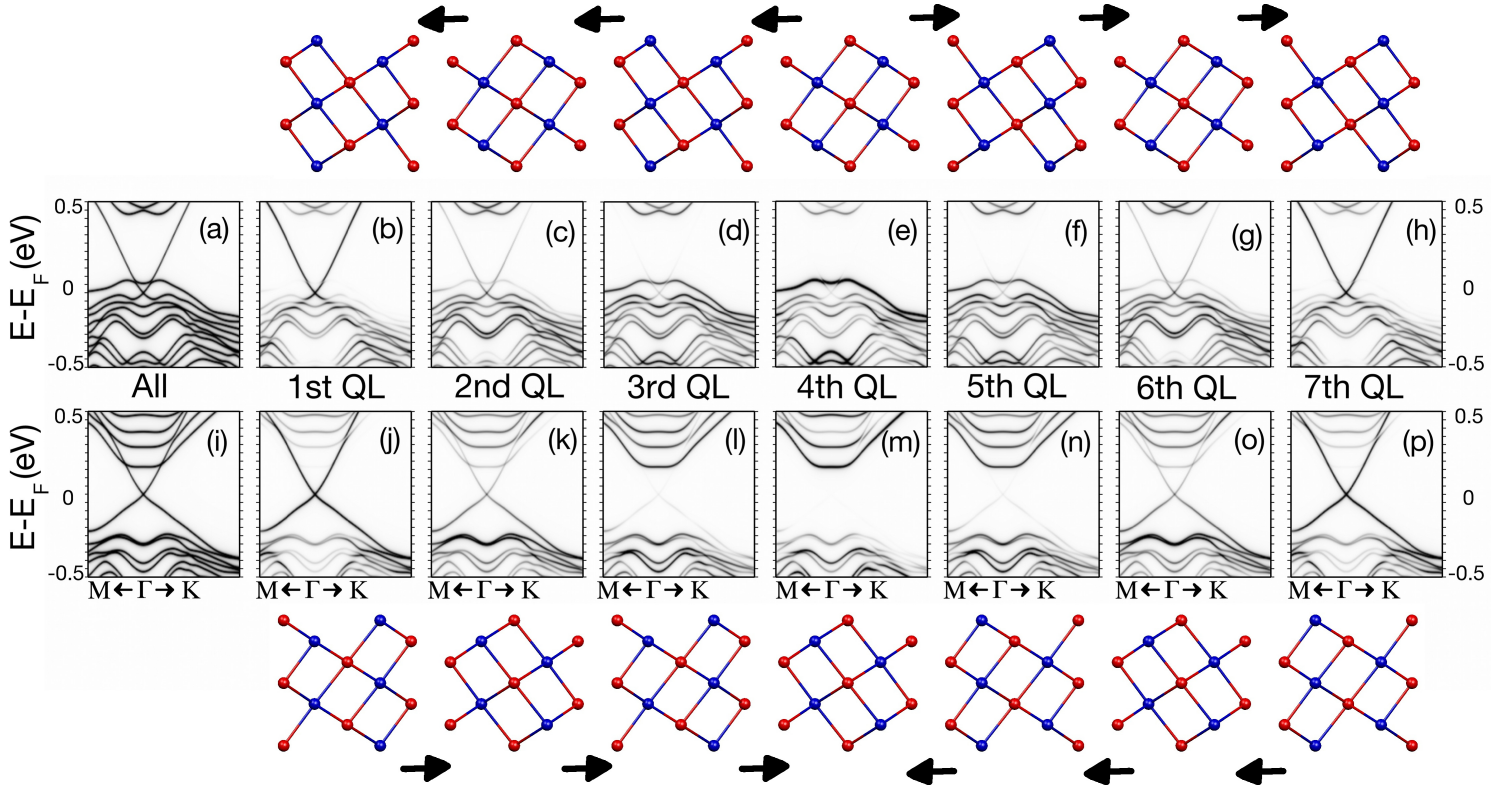

Figure 43: Projected band structure for the $N7$ and $P7$ systems (first and second row respectively). The surface QLs for $N7$ [$P7$] are shown in (b) and (h) [(j) and (p)], while the projection of the electronic states on the innermost QL at the centre of the slab is depicted in (e) [(m)]. A strong enhancement of the uppermost VB (lowermost CB) can be seen precisely at the domain wall in the $N7$ ($P7$) TB configuration. In the $N7$ case, the band bending is sufficiently large to turn the system metallic, and a 2HEG localises at the domain wall, while each TSS acquires half the electric charge missing at the centre of the slab. In the $P7$ system, the band bending is not large enough to make the lowermost CB cross the Fermi level and thus no charge is accumulated in the TSSs The crystal structure of the $N7$ ($P7$) is showed above (below) its projected band structures. Thick black arrows indicate the direction of the dipole moment generated by each TB.

6

METALLIC IMPURITIES AND OVERLAYERS

6.1 INTRODUCTION AND MOTIVATION

In this chapter we will study the role of magnetic impurities, namely Cr substitutional defects, as well as thin metallic overlayers of Cr and Au in contact with Bi_2Se_3 thin films. On the one hand, Au is a heavy atom with a large SOC, so that a SOC enhancement proximity effect may occur at the Au–Bi_2Se_3 interface. Gold shows no magnetic behaviour, thus TRS is preserved in an Au–Bi_2Se_3 system, but its electronic properties, and, consequently, its transport and optical properties, may be altered. On the other hand, magnetic atoms such as Cr break the topological protection of the surface states in Bi_2Se_3, as the system will no longer exhibit TRS. This lifts the Kramers degeneracy and destroys the topological protection of the DCs, but does not necessarily make them vanish. Indeed, the presence of an exchange field in the TI discloses novel spin related phenomena directly derived from the combination of topology and magnetism. For example, ferromagnetic order within a TI might open a gap at the DP eventually leading to the realisation of a novel insulating phase, the QAHE [20].

There are three different ways to spontaneously break time reversal invariance in TIs, either by conventional doping with magnetic elements, by proximity to a magnetic film at a TI-magnetic interface [118, 119] or by an external magnetic field. In this chapter we will study the first two mechanisms, while the effects of external fields will be addressed in Chapter 7.

6.2 CR SUBSTITUTIONAL DEFECTS

The effect of the magnetic doping of $3d$ transition metals in the Bi_2Se_3 family of compounds has been extensively investigate both theoretically and experimentally. It has been shown that the interaction with the magnetic impurities modifies the electronic and magnetic ground state of the 3D TIs. However, the changes of the ground state are not universal since they critically depend on the specific magnetic atoms, occupation sites of the magnetic impurities, [120] and experimental conditions [121, 122, 123, 124, 125, 126]. Cr-doped Bi_2Se_3 is a prototype magnetic TI, and several works have reported magnetically induced effects in this system [125, 127, 120, 128, 129, 130]. First-principles calculations found that substitutional Cr, which is energetically more favourable than interstitial Cr, preserves the insulating character in the bulk and that Cr-doped Bi_2Se_3 is likely to be ferromagnetic [131, 126]. However, evidence from the experimental observations is so far inconclusive [125, 120, 130, 132, 133, 134]. Ferro– [120] and antiferromagnetism [130] have been reported and recently the coexistence of both ferro- and antiferromagnetic Cr defects in high quality epitaxial thin films has been observed [135].

6.2.1 *Cr Substitutional Defects in Bi_2Se_3 Bulk*

To study the effect of Cr substitutional impurities as well as the magnetic interaction among the Cr dopants, we employed a 3×3×1 supercell for the bulk in which n_{subst} atoms are replaced by Cr atoms. The total energy of such systems E_{Tot} is compared to that of the pristine 3×3×1 Bi_2Se_3 bulk E_0 and the atomic energies to calculate the substitutional formation energy E_{subst}:

$$E_{subst} = E_{Tot} - E_0 - n_{subst} \cdot E_{\mathrm{Cr}} + n_{subst} \cdot E_{\mathrm{Y}} \tag{47}$$

where E_{Cr} is the atomic energy of a Cr atom and E_{Y} is the atomic energy of the substituted element Y (Bi or Se). For n_{subst}=1, 2, Se–substitution was consistently found to be an endothermic process, resulting in formation energies of +0.6 to +1.8 eV per Se substitution, depending on the precise location of the impurity, being more energetic the Se2 substitution. On the contrary, replacing Bi atoms by Cr impurities yields values of $E_{subst} \sim$ -0.5 eV per Bi substitution, in agreement with previous studies [131, 126]. Therefore, we will restrict the following analysis to Bi–substitutional Cr impurities, since Se–substitutions are not energetically favourable.

Next, we explore the effect of diluted Cr impurities in the bulk electronic structure. For this purpose we employed the 3×3×1 supercell scheme explained above with one Cr impurity (x=0.11) and we allowed the neighbouring Se atoms to relax. The Cr-Se1 distance decreases from 2.97 Å in the unrelaxed case to 2.54 Å after the relaxation, and the Cr-Se2 distance is 3.04 Å in the unrelaxed case and 2.74 Å in the relaxed system. The Se atoms surrounding the Cr impurity form a distorted octahedral structure, and the Cr dopants show a predominant divalent character. This is in agreement with experimental x-ray spectroscopy results [132] which report a ∼ 0.36 Å decrease in the Cr-Se bonds. Figure 44 shows the band dispersion for $Bi_{1.89}Cr_{0.11}Se_3$ in the unrelaxed and relaxed geometries. For the former, the energy difference between the lowest Bi_2Se_3 conduction band and highest Bi_2Se_3 valence band is reduced to 0.25 eV (being of 0.32 eV in the pristine Bi_2Se_3 bulk), while Cr states appear in the Bi_2Se_3 gap decreasing the total gap to 0.11 eV. For the latter, the relaxation enhances the hybridisation of the Cr *d* and the Se *p* bands, inducing a charge rearrangement that populates part of the Cr states and shifts the rest higher in energy. Furthermore, the bulk band gap diminishes down to 0.075 eV and the system is still insulating, in agreement with previous theoretical results [126]. An orbital analysis of the CB and VB in the Γ point reveals that the former (latter) is predominantly of the Se (Bi) p_z type, therefore the bands remain inverted upon Cr–dopings of 11%. As the bulk gap is inverted due to SOC, substituting Bi by a much lighter element like Cr drastically reduces the strength of the SOC, giving rise to a decrease of the inverted gap. The relaxation reduces the Cr-Se bond length, which in turn increases the bandwidth of the valence bands and further reduces the gap. A Dresselhaus–like splitting of the valence bands is also apparent in the band dispersion diagrams due to the lack of inversion symmetry in the systems, being the effect more pronounced for the relaxed geometry. The magnetic moment of the Cr dopants is of 3.4 (4.1) μ_B for the relaxed (unrelaxed) geometries, where μ_B is the Bohr mag-

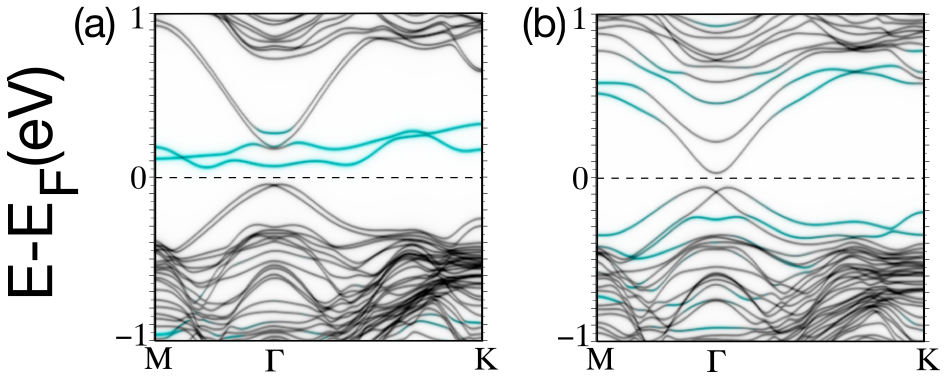

Figure 44: Band structure of $Bi_{1.89}Cr_{0.11}Se_3$ bulk with x=0.11 (a) unrelaxed and (b) relaxed. The projection on the Cr atoms is shown in cyan. The gap is reduced in both cases.

Cr conf.	J (meV)	d(Cr-Cr) (Å)
β	29.2	4.14
γ	13.5	4.46
δ	20.9	6.08
ϵ	5.9	7.17
ζ	7.0	7.36

Table 12: Magnetic coupling strength of the different Cr impurities configurations in a 3×3×1 supercell of Bi_2Se_3 with n_{subst}=2. The Cr configuration for each case corresponds to a Cr impurity in Bi–site α and another Cr in the Bi–site given in the first column (see Figure 45 for the site notation). The coupling is estimated as $J = (E_{AF} - E_{FM})/2$, being E_{AF} (E_{FM}) the total energy of the system with the Cr atoms coupled antiferromagnetically (ferromagnetically). Magnetic interactions show a non–monotonic FM behaviour with the Cr-Cr distance (third column).

neton, in close agreement with experimental results [132], and confirming the predominant divalent character of the Cr impurities in Bi_2Se_3.

We additionally examined the magnetic coupling between Cr impurities in the aforementioned 3×3×1 bulk supercell. Different impurity arrangements were explored with n_{susbt}=2, for which the $Bi_{2-x}Cr_xSe_3$ compound has a Cr doping concentration of x=0.22. The total energy was computed in ferromagnetic (FM) and antiferromagnetic (AF) configurations for different Cr arrangements (see Figure 45 for the Cr arrangement notation), and the results are displayed in Table 12. A FM configuration is more stable for all the Cr configurations studied. The magnetic coupling strength shows an overall non–monotonic behaviour with the Cr-Cr distance, and also depends on the relative orientation of the Cr impurities within the crystal. The band inversion close to the Γ point enhances the matrix elements of the spin operator between the valence and conduction bands, giving rise to a large van Vleck–type spin susceptibility and thus a long range FM order [136, 137] that has recently been observed for the first time in Vanadium doped Sb_2Te_3 systems [138].

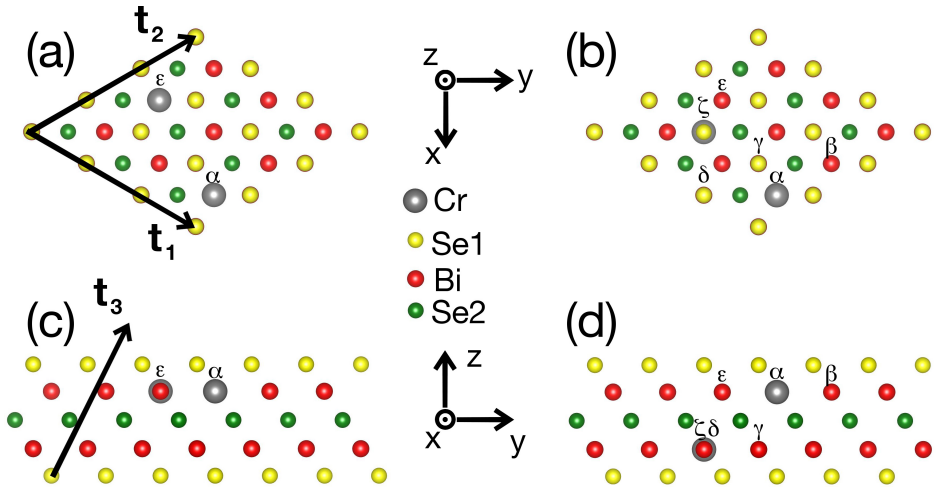

Figure 45: For all the cases we studied one of the Cr dopants is placed at Bi–site α, so the impurity arrangement is well described by the position of the second Cr atom (β, γ, δ, ϵ and ζ) as indicated in (b) and (d). Top –(a)– and side view –(c)– of the 3×3×1 supercell with two Cr substitutions being the impurity configuration ϵ and the Cr–Cr distance 7.17 Å. The in–plane lattice vectors $\boldsymbol{t}_1$ and $\boldsymbol{t}_2$ are indicated as arrows in (a) and the out of plane lattice vector $\boldsymbol{t}_3$ is depicted in (c). (b) and (d) show the ζ impurity configuration, with a Cr-Cr distance of 7.36 Å. Note that in the γ, δ and ζ cases the two Cr atoms lie on different atomic planes, while in the β and ϵ arrangements the Cr impurities are coplanar.

6.2.2 *Cr–doped Bi_2Se_3 Thin Films*

We additionally explored the effect of Cr impurities in thin films of Bi_2Se_3. We investigated 2 and 4 QLs thick slabs in a 3×3 in–plane supercell configuration with two Cr impurities in the surfacemost QL. For both slabs thicknesses, two different Cr arrangements, ϵ and ζ, were considered (see Figure 45). First, we studied the electronic structure of the aforementioned Cr-doped Bi_2Se_3 thin films. The band dispersion diagrams for the 2 and 4 QL thick films are shown in Figures 46 and 47 respectively. Surface states are present in the four cases displayed, indicating that the band inversion of the bulk–like bands of the slabs is maintained upon Cr dopings of 22% in the surfacemost QL. In the 2 QL slabs a hybridisation gap opens due to surface–surface interaction, since the penetration depth of the surface states is precisely 2 QLs, and the system is an insulator. In addition, the surface state that localises closest to the Cr–doped QL is higher in energy than that of the opposite surface, and shows a small gap in its DC–like dispersion due to the presence of the Cr–induced exchange field along the z direction. For the two impurities in the ϵ arrangement, both surface states at opposite surfaces show a similar effective mass, while for the two Cr impurities in the ζ arrangement the surface state closer to the Cr dopants acquires more mass than its counterpart at the opposite surface. Both 2 QL thin films exhibit a large Rashba splitting due to the lack of inversion symmetry in the system. In the 4 QL slabs no hybridisation gap is present, indicating that the surface states maintain their penetration depth upon Cr doping. The surface state furthest from the Cr dopants exhibits a DC–like dispersion very similar to that of a pristine Bi_2Se_3 surface, indicating that the exchange field induced

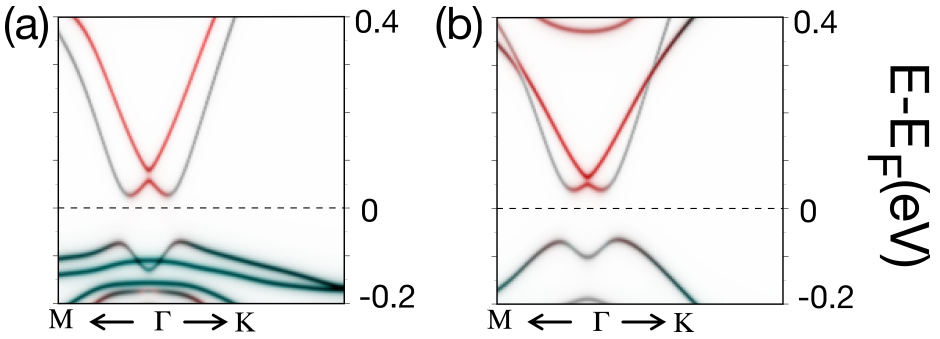

Figure 46: Band structure of Bi_2Se_3 2 QL thin films with 2 Cr dopants in a 3×3 supercell being the impurity arrangement (a) ϵ –both Cr dopants in the same atomic layer– and (b) ζ –Cr dopants in different atomic layers–. The projection on the Cr atoms is shown in cyan while the red bands are the projection of the states on the QL that hosts the Cr dopants.

by the Cr impurities is local and negligible 3 QLs away. Besides this, a clear analogy with the 2 QL thin films can be established. A small gap opens in the spectrum of the surface state closest to the Cr impurities. This surface state lies ~ 0.12 eV higher in energy than that of the opposite surface, and for the two Cr impurities in the ζ arrangement the surface state under the influence of the exchange field acquires some mass.

Next, we calculate the magnetic coupling between Cr atoms in these thin film geometries and the influence of the surface state on the magnetic configuration of the Cr atoms. The magnetic coupling strength J is estimated as in the previous subsection (see caption in Table 12). We obtain values of J=5.3 and 2.5 meV for Cr-Cr distances of 7.17 (ϵ) and 7.36 Å (ζ) respectively, regardless of the film thickness. Note that both values are positive indicating FM coupling. As in the 2 QL thick films the Fermi level lies in the gap, the origin of the magnetic exchange coupling can not be of the Ruderman-Kittel-Kasuya-Yosida (RKKY) type, since this only occurs in metallic systems. Therefore, the exchange mechanism between Cr impurities must be of the van Vleck–type for the 2 QL Cr–doped Bi_2Se_3 thin films. Since the estimated value of J is not modified for 4 QL thin films, our results suggest that the van Vleck–type magnetism is predominant over the RKKY interaction, even though the Fermi level crosses the surface states. This is in close agreement with the experimental results shown in Ref. [139] for 5 QL $Cr_{0.22}(Bi_xSb_{1-x})_{1.78}Te_3$ thin films.

The Cr impurities in Bi_2Se_3 thin films show a van Vleck–like ferromagnetism, similar to that of bulk Cr–doped Bi_2Se_3, that in turn induces a gap in the surface states. The presence of the Cr dopants influences the dispersion relation of the surface states in two significant points: the mass of the DCs varies with the precise location of the Cr atoms and a gap opens in the surface spectrum. Our results predict that Cr–doped Bi_2Se_3 thin films of 2 QLs could host a QAHE phase, and thicker films ($\gtrsim$ 4 QLs) can also host the QAHE phase by tuning the chemical potential to be in the surface state gap induced by the exchange field of the Cr impurities.

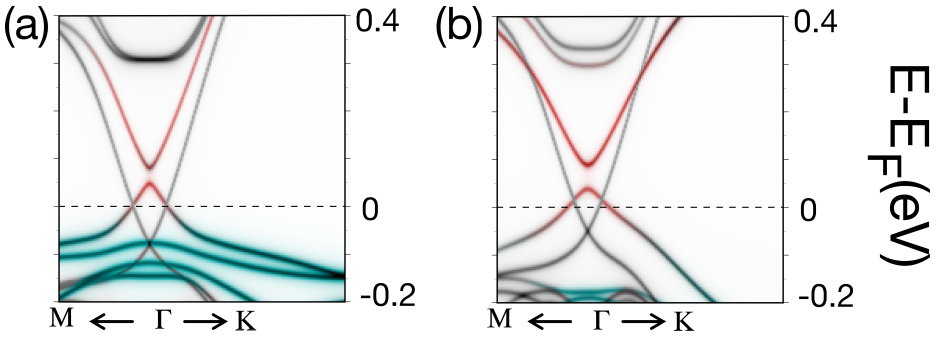

Figure 47: Band structure of Bi_2Se_3 4 QL thin films with 2 Cr dopants in a 3×3 supercell being the impurity arrangement (a) ϵ –both Cr dopants in the same atomic layer– and (b) ζ –Cr dopants in different atomic layers–. The projection on the Cr atoms is shown in cyan while the red bands are the projection of the states on the QL that hosts the Cr dopants.

6.3 ATOM THIN METALLIC OVERLAYERS

6.3.1 *Cr*

We investigated the Cr thin film deposition on the (111) surface of Bi_2Se_3. Although TRS is broken, surface states may arise and can host non–trivial interesting phases and may reveal a magnetoelectric effect [17, 18]. Recent experimental results for very dilute concentrations of Cr adatoms ($\sim$ 9% monolayer (ML)) [140] report the absence of long–range out–of–plane FM order, thus the surface states exhibit no gap. Here we discuss the effects of much more concentrated Cr overlayers (1, 2 and 3 MLs) on the 3D TRS–protected TI Bi_2Se_3.

The bulk lattice constant of body–centred cubic (*bcc*) Cr is a_{Cr} =2.91 Å. Bulk Cr is an antiferromagnetic material that exhibits a spin density wave almost commensurate with the lattice along the (100) direction below its Néel temperature T_N =311 K. For the (111) surface the in–plane lattice parameter will be $\sqrt{2}a_{Cr}$ =4.12 Å, which gives a small lattice mismatch of 0.5% with the in–plane lattice parameter of Bi_2Se_3. The *bcc* (111) surface fulfils C_3 symmetry and follows an ABC stacking pattern similar to that of the Bi_2Se_3 family of compounds. Therefore, Cr is expected to grow commensurately on top of the (111) surface of Bi_2Se_3. In order to investigate the effects of Cr overlayers, we employed a 4 QL Bi_2Se_3 slab and we allowed the Cr atomic layers on top to relax for Cr adsorptions of 1, 2 and 3 MLs. Three possible different adsorption sites for the interfacemost Cr layer were considered in each case: the *fcc* and hexagonal close–packed (*hcp*) hollow sites (on top of the uppermost Se2 and Bi atoms respectively), and the on–top site (on top of the uppermost Se1 atomic layer). The ground state geometries (along with the magnetic ground state) are depicted in Figure 48, and the values of the Cr atomic positions are given in Table 13. For 1 and 2 MLs of Cr, the first Cr atomic layer is more stable at the hollow *fcc* site (on top of the Se2 atom at the centre of the QL), in agreement with to previous results on dilute Cr adatoms on Bi_2Se_3 [140], and lies almost co–planar with the last Se1 atomic layer due to the small atomic radius of Cr and the relatively large Se1-Se1 distance in the xy plane. On the other hand, for the 3 ML case the first Cr layer moves to the *hcp* hollow site (on top of the Bi atom) and

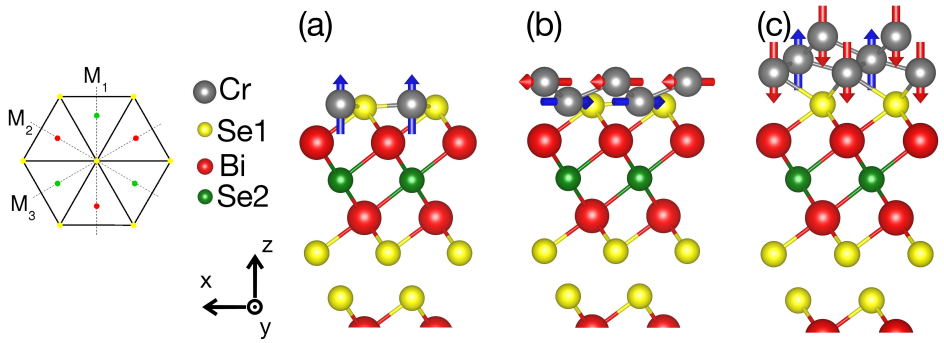

Figure 48: Relaxed atomic positions for a Bi_2Se_3 (111) surface with Cr coverages of 1, 2 and 3 MLs –(a), (b) and (c) respectively–. The first Cr layer is almost coplanar with the last Se1 atomic layer for 1 and 2 ML coverages, while for 3 MLs the Cr detaches from the Bi_2Se_3 slab. The Cr layers follow the ABC stacking sequence but the order is reversed in the 3 ML case with respect to the Bi_2Se_3 stacking. The ground state magnetic configuration for each system is indicated with arrows. The diagram on the left depicts the top view of the pristine Bi_2Se_3 slab with dashed lines indicating the mirror planes of the surface.

	Cr1 (Cr1-Se)	Cr2 (Cr2-Cr1)	Cr3 (Cr3-Cr2)
1 ML	0.16 (2.39)	- (-)	- (-)
2 ML	0.19 (2.40)	1.18 (2.59)	- (-)
3 ML	1.54 (2.84)	2.19 (2.48)	3.31 (2.64)

Table 13: Heights in Å of the Cr layers with the last Se1 atomic layer at the origin for the relaxed geometries of 1, 2 and 3 ML coverages. Cr1, Cr2 and Cr3 correspond to the first, second and third Cr atomic layer from the surfacemost Se1 respectively. The values in parentheses indicate the distance between atoms in contiguous atomic layers.

the whole Cr trilayer detaches form the Bi_2Se_3 slab, probably due to the formation of stronger bonds within the Cr layers. Recall that the *bcc* (111) surface is very open. In fact, out of the 8 n.n. of each atom, 6 lie on the first atomic layer above and below it, but the remaining 2 n.n. lie *three* layers above and below.

The adsorption energy E_{ads} of the Cr on Bi_2Se_3 is estimated as:

$$E_{ads} = E_{Tot} - E_{Bi_2Se_3} - E_{Cr} \tag{48}$$

where E_{Tot} is the total energy of the Cr-Bi_2Se_3 system, $E_{Bi_2Se_3}$ is the energy of the 4 QL Bi_2Se_3 slab employed as a substrate, and E_{Cr} is the energy of the isolated Cr subsystem in the same geometry acquired when deposited on top of Bi_2Se_3. We obtained values of -1.4, -0.9 and -0.9 for 1, 2 and 3 ML adsorptions respectively, indicating a strong bonding of the Cr overlayers in contact with Bi_2Se_3.

Cr-Bi_2Se_3 systems exhibit strong magnetism according to our calculations. The Cr coverage is a layer-by-layer ferrimagnet, being the atoms in the same atomic layer coupled ferromagnetically, while the inter-layer coupling is antiferromagnetic. Table 14 shows the calculated magnetic moments (MMs) along the easy magnetisation axis of each system for the 1, 2 and 3 Cr-Bi_2Se_3 slabs. A magnetic moment of 3–4 μ_B per Cr atom is found in the three cases,

	Cr1	Cr2	Cr3	Tot
1 ML	4.333	-	-	4.028
2 ML	-3.113	4.157	-	1.390
3 ML	-3.704	3.601	-4.231	-4.263

Table 14: Magnetic moments of the Cr layers in Bohr magnetons for 1, 2 and 3 ML coverages. Cr1 (Cr3) corresponds to the interfacemost (furthest from the interface) Cr layer. The rightmost column shows the total magnetisation of the whole Cr-Bi_2Se_3 system for each case. The Cr overlayers grow as a layer–by–layer ferrimagnet with in–plane FM coupling.

close to the Hund rule value for isolated Cr atoms, being always larger for the Cr plane furthest from the interface. The ferrimagnetic coupling between Cr layers is evident form the alternating signs in the values of the table. For 1 and 2 ML Cr films there is an appreciable induced magnetic moment ($\sim$ 0.2 μ_B) in the Se and Bi topmost layers, oppositely aligned to the adsorbed Cr magnetic moment.

The preferential orientation of the Cr magnetisation vector is obtained by comparing the total energies of the in–plane ($\mathcal{M}_x$, $\mathcal{M}_y$) and out–of–plane ($\mathcal{M}_z$) orientations of the Cr magnetisation $\boldsymbol{\mathcal{M}}$. The easy magnetisation axis is perpendicular to the (111) surface for 1 and 3 ML coverages, with a crystalline magnetic anisotropy energy (MAE) of $\sim$ 25 and 5 meV respectively. For the Bi_2Se_3 slab with 2 adsorbed Cr MLs the easy magnetisation axis is along the in–plane direction. We can not determine its precise direction in the xy plane within our numerical accuracy, but the perpendicular MAE is of $\sim$ 35 meV. Therefore, a double spin–reorientation transition takes places as the number of adsorbed Cr layers increases stepwise from 1 to 3 MLs. In Ref. [141] a similar transition is studied in Co atoms on Bi_2Se_3, revealing a spin–reorientation transition with increasing concentration of the adsorbed Co in a much more dilute regime ($\sim$ 1 to 8% ML of adatoms).

The magnetic behaviour of Cr adsorbed on Bi_2Se_3 can be understood in terms of the electronic structure. The Cr d orbitals hybridise with the Bi_2Se_3 p orbitals, which gives rise to the magnetic character of the system. Figure 49 shows the spin–resolved DOS for the Cr trilayer adsorbed on Bi_2Se_3. The strong pd hybridisation drives the Cr states close to the Fermi level, confined in an energy region $\approx$ 2 eV below E_F. Moreover, a large energy splitting of about 4.5 eV between the spin-majority states and the spin-minority states is obtained and, for each Cr atomic layer, the spin–majority Cr states are fully occupied while the minority-spin channel is almost unoccupied. This explains the large value of the magnetic moment of the Cr layers, close to the Hund rule value. The spin–resolved DOS for the 1 and 2 ML cases show an analogous behaviour (not shown).

Next, we examine the effects of the Cr adsorbed layers on the electronic structure. Figure 50 shows the band dispersion diagrams for the three aforementioned Cr coverages. The DC of the free surface at the bottom of the slab exhibits an n–doping, being the shift of the DP of -0.4, -0.25 and -0.3 eV for the 1, 2 and 3 ML systems respectively. A gap is opened in the surface state of the 1 and 3 ML cases, for which the magnetisation lies in the z direction. The gap is of 90 and 30 meV respectively, being larger for the 1 ML system

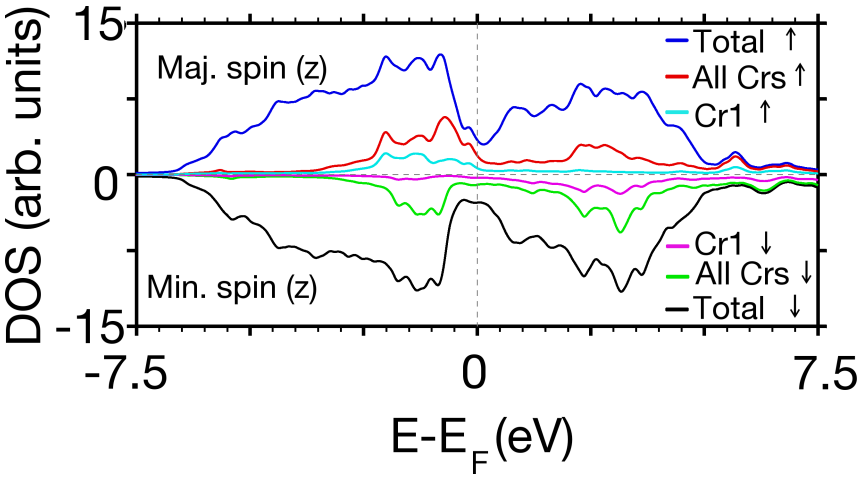

Figure 49: Spin–resolved DOS for the Cr trilayer adhered to Bi_2Se_3. The blue (black) line shows the majority (minority) spin total DOS, while the red (line) corresponds to the DOS projected on the whole Cr trilayer for the majority (minority) spin bands and the cyan (magenta) indicates the DOS projected on the interface–most Cr layer for the majority (minority) spin. Magnetism is patent from the difference in the majority and minority curves. Two Cr bands can be identified: one $\sim$ 1.5 eV below E_F with a bandwidth of $\sim$ 2.5 eV with a net majority spin, and another band at $\sim$ 2 eV above the Fermi level of similar bandwidth with a net minority spin.

in which the MM of the interfacial layer is larger and the Cr-Se distance is smaller. In both cases the DC acquires mass and becomes parabolic, being the Fermi level precisely in the surface gap for the 3 ML case.

On the contrary, the surface state is gapless for a Cr coverage of 2 MLs. As the magnetisation vector of the Cr lies in the x direction for this system, topological protection of the surface states is lost due to TRS breaking. Nevertheless, mirror symmetry M_1 (perpendicular to the x axis, see Figure 48) is preserved (recall that $\boldsymbol{\mathcal{M}}$ transforms as a pseudo–vector under reflection symmetry) and thus the DC shows no gap [142]. An analogous case is presented in Subsection 7.5.2.1 in the next chapter, where TRS is explicitly violated in a TI by means of an external magnetic field, but no gap opens unless other symmetry (in that case inversion symmetry) is additionally broken. In the 2 ML Cr-Bi_2Se_3 slab no shift in momentum space of the DP is observed. Instead, the dispersion relation of the surface state becomes highly anisotropic. The bands along the K_2–Γ and -K_2–Γ high symmetry lines are equal since they are related by the only surviving mirror symmetry M_1, and the asymmetry is maximum along the M_1–Γ and -M_1–Γ directions –see also Figure 52 (a) and (b)–.

Finally, we study the behaviour of the spin texture of the surface states in the presence of adsorbed Cr layers. Figures 51, 52 and 53 show the expected value of the spin all over the surface state for the 1, 2 and 3 ML Cr-Bi_2Se_3 systems described above. The adsorption of magnetic layers induces an effective magnetic field along the magnetisation direction. For 1 and 3 Cr ML coverages the magnetic moment lies along the z direction, and this induces a global S_z component in the vicinity of the $\bar{\Gamma}$ point which is opposite for the upper –electron–like surface state (ESS)– and lower –HSS– part of the

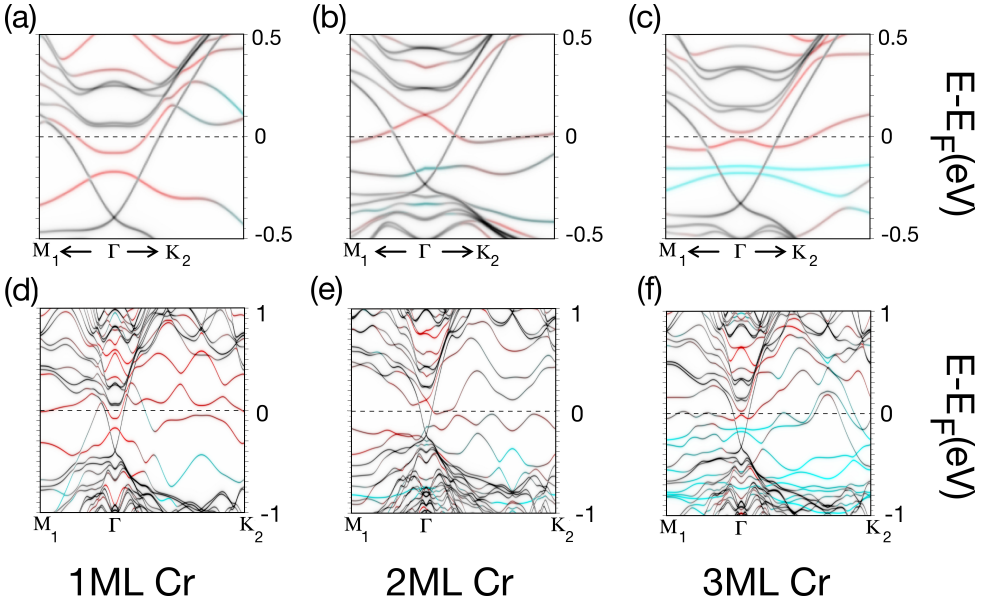

Figure 50: Band structure close to the $\bar{\Gamma}$ point of Cr overlayers on a 4 QL Bi_2Se_3 slab for 1, 2 and 3 MLs coverage – (a), (b) and (c) respectively–. The projection on the Cr atoms is shown in cyan while the red bands are the projection of the states on the QL closest to the overlayers. The remaining black bands correspond to the three QLs furthest from the Cr, among which the DC of a pristine Bi_2Se_3 (111) surface can be seen in all cases. Cr induces an n–doping of Bi_2Se_3 (see the position of the pristine DC). A gap is opened in the surface state closest to the Cr atoms for the 1 and 3 ML cases, since the topological protection is destroyed and all the mirror symmetries are broken. The DC acquires mass but remains localised at the surface. For the 2 ML case the magnetisation of the Cr lies in the x direction and, although the TRS protection is lifted, the gap remains closed since mirror symmetry M_1 is still fulfiled. The bands in a larger energy window along the complete $\bar{M}_1$–$\bar{\Gamma}$–$\bar{K}_2$ high symmetry lines are shown in (d), (e) and (f) for the 1, 2 and 3 ML Cr thicknesses respectively.

DC. The sign of this S_z component is equal –opposite– to that of the net magnetisation of the Cr subsystem in the HSS –ESS–. We have also checked that reversing the sign of the magnetisation in the Cr layers reverses the sign of the S_z component in the surface state with no additional net energy cost. Away from the surface $\bar{\Gamma}$ point the value of S_z gradually decreases, the spin tends to lie in the xy plane and the three-fold symmetric oscillation of S_z due to the trigonal warping dominates the texture for high k in both the ESS and the HSS. This spin texture evidences the competition between the magnetisation $\mathcal{M}_z$, which tends to align the spin along the z direction, and SOC, which tends to orientate the spin in the xy plane and perpendicular to crystal momentum $\boldsymbol{k}$. The spin vector field is of the circular meron kind according to its topological classification. As all mirror symmetries are broken, no nodal lines with S_z=0 exist, in contrast with the spin texture of pristine Bi_2Se_3. The rupture of TRS is also evident, since for a given point in reciprocal space $\boldsymbol{k}$ with spin σ, no state exists at $-\boldsymbol{k}$ with $-\sigma$.

For 2 ML Cr coverage, the skyrmionic character prevails, analogous to that of TSSs. Nevertheless, since the magnetisation lies in the x direction, of the three mirror symmetries of pristine Bi_2Se_3 only M_1 remains and therefore only the nodal line along the M_1–Γ direction persists. Along this vertical mirror plane the components of the spin that are orthogonal to such mirror plane (S_y and S_z) are zero, which is seen in Figure 52 (a) and (b). A three–fold oscillation of the S_z component is also patent all over the DC. The large anisotropy induced by the proximity of the Cr bilayer is most apparent along the $\bar{M}_1$–$\bar{\Gamma}$–$\bar{K}_2$ high symmetry lines as shown in (b). Due to the anisotropic character of the effective mass, constant energy contours are no longer circular, but present an elliptical shape. Note that the spin texture presented in Fig. 52 is presented for various constant $|\boldsymbol{k}|$ circles that do not correspond to constant energy lines. The total value of the spin in the surface state of the 2 Cr ML on Bi_2Se_3 yields zero at every energy, indicating that neither the ESS nor the HSS are spin polarised.

We have investigated the adsorption of 1, 2 and 3 MLs of Cr on Bi_2Se_3. The system undergoes a double spin reorientation transition as the Cr coverage increases stepwise, from out–of–plane to in–plane and out–of–plane magnetisation. This subsequently induces a gap opening, closing and reopening in the surface state of Bi_2Se_3, which comes along with a circular meron to skyrmion to circular meron transition of the surface state spin–texture. For 1 and 3 ML Cr coverages the spin lies predominantly in the z direction close to the $\bar{\Gamma}$ point, and is opposite for ESS and HSSs, so a spin–flip of the conducting electrons can be achieved by fine–tuning the chemical potential of such systems. This effect could be of great use in the field of spintronics.

6.3.2 *Au*

Gold is a heavy metallic element (Z=89). It is one of the few noble metals, i.e. its d–bands are completely filled. It is also non–magnetic, so golden impurities preserve TRS, in contrast with Cr, and the topological protection of the TSS would remain as long as there is still a gap. Nevertheless, the mass of its nucleus is very large, giving rise to a strong SOC, which can lead to a

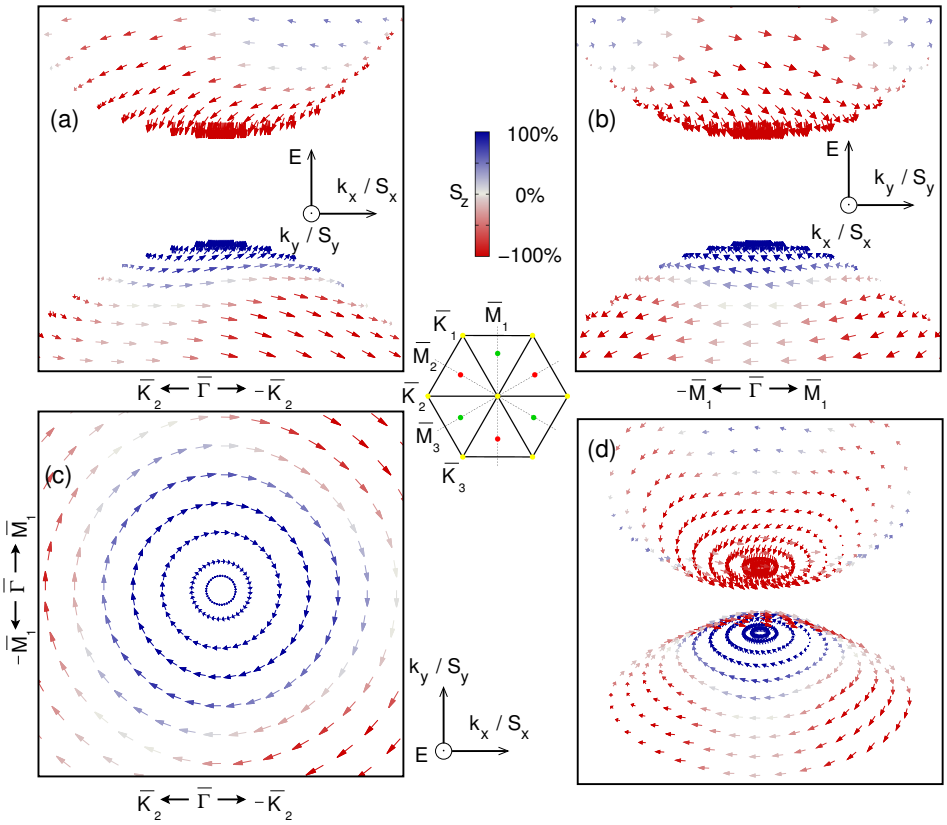

Figure 51: Spin texture of the surface state in the 1 ML Cr/Bi_2Se_3 system. A gap is opened in the surface state due to breaking of TRS *and* all the mirror symmetries of the pristine Bi_2Se_3 surface. The magnetisation of the Cr layer lies in the z direction, and thus the spin texture acquires a large S_z component close to the $\bar{\Gamma}$ point. Further away from the centre of the BZ the S_z component decreases and the oscillation in S_z with trigonal symmetry is recovered. Note that no mirror symmetries are fulfiled, nor is TRS. The spin vector field is of the circular meron type.

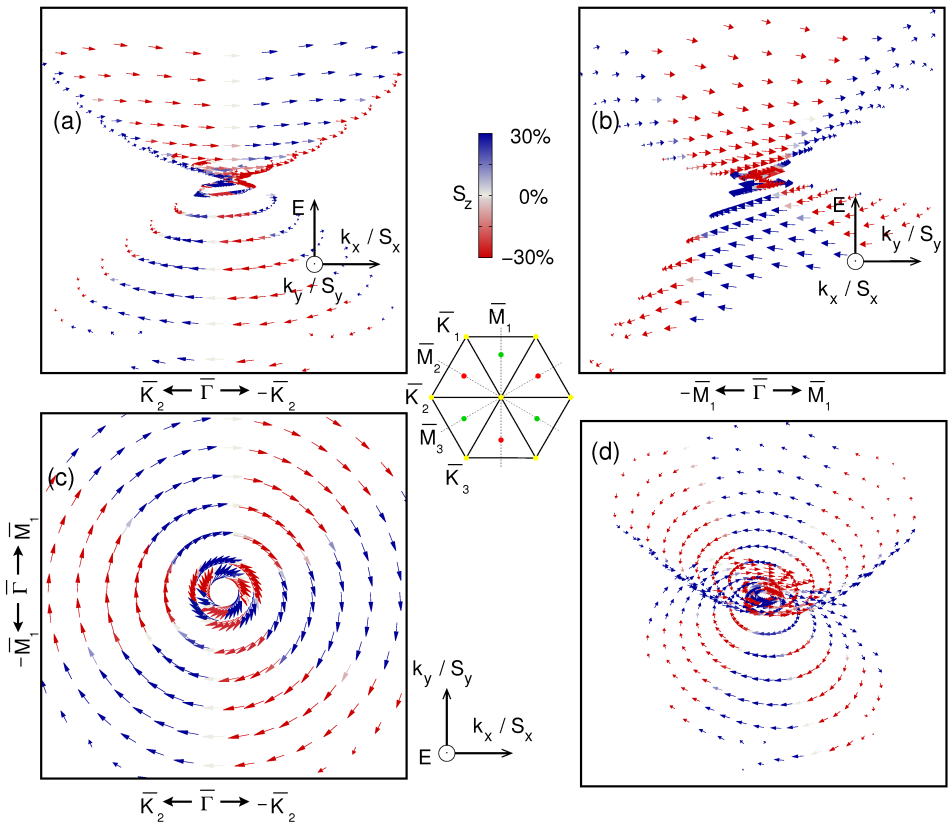

Figure 52: Spin texture of the surface state in 2 ML Cr/Bi_2Se_3 system. No gap is opened in the surface state despite the loss of topological protection since the M_1 mirror symmetry is preserved. The spin–texture is skyrmion–like, although a the DC is highly anisotropic. As the M_1 symmetry is preserved, the spin lies perpendicular to the mirror plane.

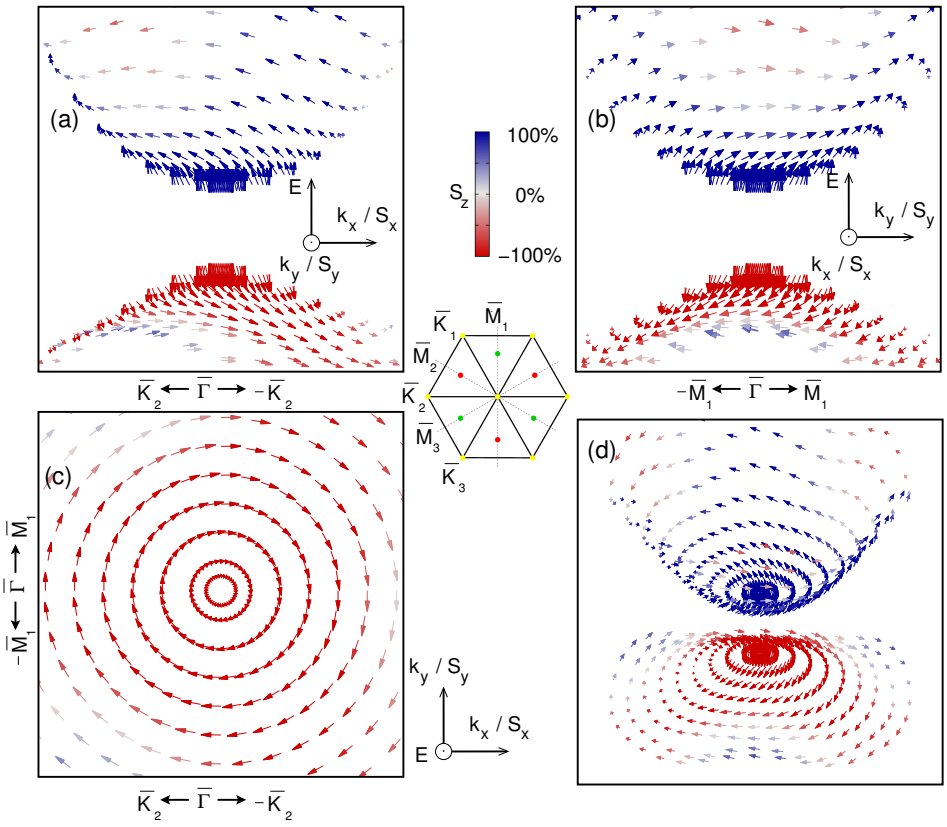

Figure 53: Spin texture of the 3 ML Cr/Bi_2Se_3 system. A gap is opened in the surface state due to breaking of TRS *and* all the mirror symmetries of the pristine Bi_2Se_3 surface.

stronger topological protection of the TSSs. The effect of gold adsorption on Bi_2Se_3 thin films is addressed in the current subsection.

Bulk gold exhibits an *fcc* crystal structure of lattice parameter a_{Au}=4.08 Å. The (111) surface follows the ABC stacking pattern of Bi_2Se_3–like systems, while the in–plane lattice parameter for that surface is $a_{Au}/\sqrt{2}$=2.88 Å, much smaller than the in–plane lattice parameter of Bi_2Se_3. We employed 4 QL thick Bi_2Se_3 slabs in which 1, 2 and 3 MLs of gold were placed on top. The Au atoms were allowed to relax, and the relaxed ionic configurations are displayed in Figure 54 for adsorptions of 1, 2 and 3 MLs. The Au atomic radius is larger than that of Cr, and for the former the interfacemost overlayer is no longer coplanar with the top Se. Instead, gold grows following the ABC stacking sequence of the Bi_2Se_3 substrate with a distance between atomic layers of $\sim$ 1.5 Å (see Table 15). The resulting Au–Au distances are close to those in bulk Au.

The effects of Au adsorption in the electronic and spin structure of Bi_2Se_3 are displayed in Figure 55 for 1, 2 and 3 MLs Au coverages. The DC hybridises with the d bands of the gold subsystem away from the surface $\bar{\Gamma}$ point. In close resemblance with the adsorption of Cr layers, Au induces an n–doping of the TSS at the bottom pristine surface of Bi_2Se_3. The shift in energy of the DP is of -0.3, -0.35 and -0.35 eV for 1, 2 and 3 MLs of Au respectively. The interfacial DC also exhibits doping. For the 1 Au ML system the surface state is p–doped and hybridises with the conduction bands. In the 2 ML case the TSS shows slightly higher n–doping than the TSS at the opposite surface,

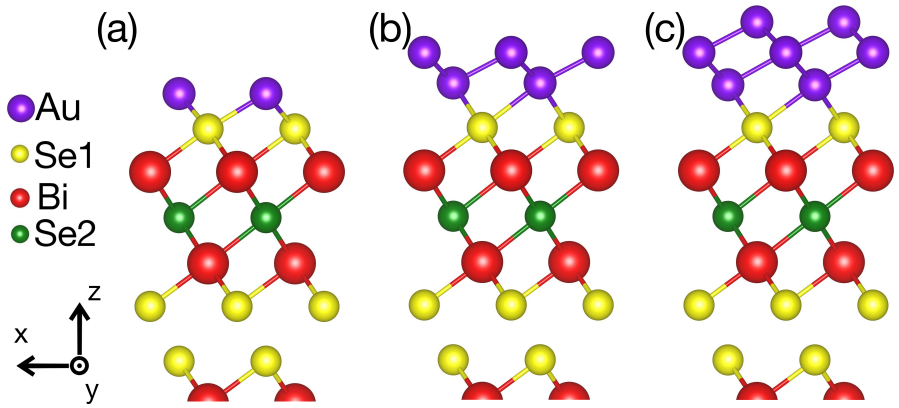

Figure 54: Relaxed atomic positions for a Bi_2Se_3 (111) surface with Au coverages of 1, 2 and 3 MLs –(a), (b) and (c) respectively–. The Au layers follow the ABC stacking sequence.

	Au1 (Au1-Se)	Au2 (Au2-Au1)	Au3 (Au3-Au2)
1 ML	1.45 (2.80)	- (-)	- (-)
2 ML	1.83 (3.00)	3.08 (2.70)	- (-)
3 ML	1.76 (2.96)	3.09 (2.74)	4.34 (2.70)

Table 15: Heights in Å of the Au layers with the last Se1 atomic layer at the origin for the relaxed geometries of 1, 2 and 3 ML coverages. Au1, Au2 and Au3 correspond to the first, second and third Au atomic layer from the Se1 respectively. The values in parentheses indicate the distance between atoms in contiguous atomic layers

being the DP at $\sim$ -0.5 eV. For a 3 Au ML coverage the interfacial DP lies $\sim$ 0.05 eV below the Fermi level and very close to the conduction band.

Regarding the spin texture of the surface states, the skyrmion character of the pristine Bi_2Se_3 surfaces prevails and only minor changes due to the Au adsorption can be appreciated, as shown in Figure 56 for 2 and 3 Au ML coverages. As the Au/Bi_2Se_3 systems preserve both TRS and the three mirror symmetries of the Bi_2Se_3 crystal, the helicity of the surface states remains robust and the spin lies perpendicular to the vertical mirror planes in the $\bar{\Gamma}$–$\bar{M}$ lines. The whole spin vector field exhibits the three–fold symmetric modulation of S_z due to the trigonal warping already patent in clean Bi_2Se_3 surfaces. Nevertheless, close to the $\bar{\Gamma}$ point a net z component arises due to hybridisation of the surface state with the valence (conduction) band in the 2 (3) Au ML system.

6.4 SUMMARY AND CONCLUSIONS

In this chapter we have shown the effects of magnetic Cr impurities on the Bi_2Se_3 bulk, which our calculations predict to take Bi–substitutional sites. The magnetic coupling between Cr dopants is of the van Vleck–type in the bulk showing a FM configuration with the exchange coupling depending on the precise impurity configuration. Moreover, the bulk band gap is strongly reduced due to a decrease in the SOC strength and the hybridisation of the Cr atoms with Se. We have also shown that in thin films the FM configura-

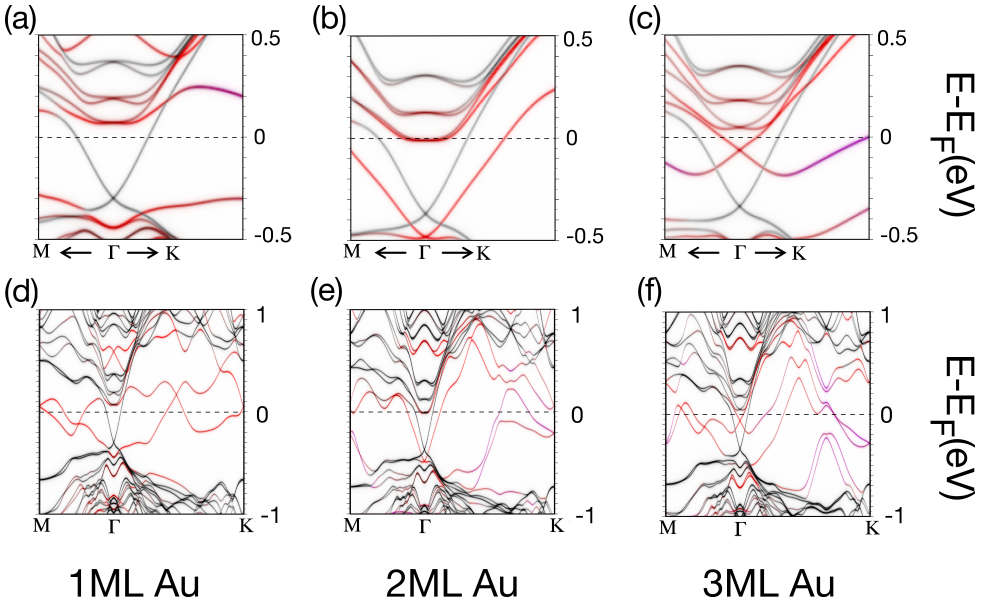

Figure 55: Band structure of Au overlayers on a 4 QL Bi_2Se_3 slab for 1, 2 and 3 MLs coverage – (a), (b) and (c) respectively–. The projection on the Au atoms is shown in purple while the red bands are the projection of the states on the QL closest to the overlayers. The remaining black bands correspond to the three QLs furthest from the Au, among which the DC of a pristine Bi_2Se_3 (111) surface can be seen in all cases. Au induces an n–doping of Bi_2Se_3 (see the position of the pristine DC).

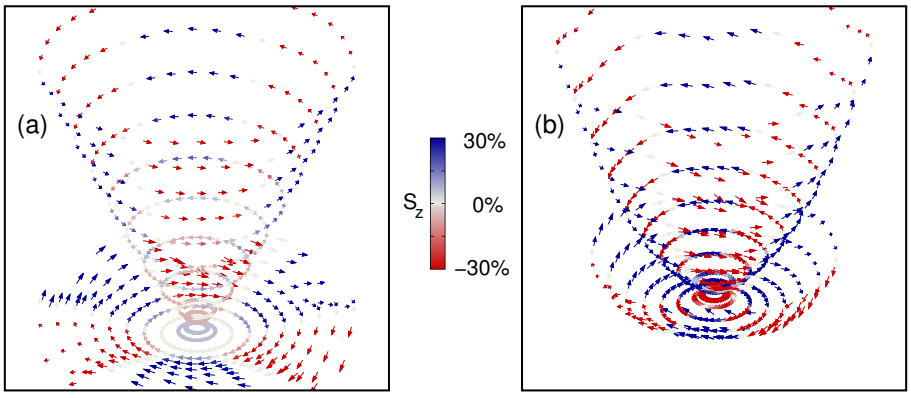

Figure 56: Spin texture of the surface state in the 2 –(a) and (c)– and 3 –(b) and (d)–ML Au/Bi_2Se_3 systems. The DCs remain gapless upon Au adsorption. The skyrmion structure with a trigonal warping of the pristine Bi_2Se_3 TSSs is also maintained, and the mirror symmetry along the $\bar{\Gamma}$–$\bar{M}$ high symmetry lines is also patent.

tion of the Cr impurities is also more favourable than the AF one, and our results suggest that the underlying exchange coupling mechanism is also the van Vleck–type magnetism. Cr-dopants open a gap in the surface spectrum that can host QAHE states, and the effective mass of the surface states varies with different dopant configurations. The atom thin Cr film induces a gap opening, closing and reopening as the thickness of the adsorbed Cr layer increases stepwise from 1 to 3 MLs. The gap is opened due to an exchange field perpendicular to the surface, which breaks TRS and all the mirror symmetries of the pristine surface and induces a net z component in the spin texture of the surface states. For 2 MLs the magnetisation lies along the surface plane in the x direction, breaking TRS but preserving one of the mirror symmetries. Thus, no gap opens, but the dispersion relation becomes highly anisotropic. In addition, for 1 and 3 Cr ML coverages the ESS and HSS show opposite S_z, so that the spin of the conducting electrons can be flipped by tuning the chemical potential from the electron–like state to the hole–like state and *vice versa*. Finally, we have investigated the Au adsorption on Bi_2Se_3 showing that the doping of the surface states is also modulated, whereas the spin texture remains robust in the gap region.

7

BHZ HAMILTONIAN AND AC SPIN SOURCES

7.1 INTRODUCTION AND MOTIVATION

In this chapter we will present an analytical approach to TIs that complements the *ab initio* techniques described and used in other chapters. We will discuss the effects of a magnetic field on time-reversal symmetric TIs, focusing on the edge states in terms of localisation and spin polarisation. Our starting point will be the BHZ Hamiltonian developed in 2006 by Bernevig, Hughes and Zhang that has served as the preferred toy model for TRS–protected TIs. The effect of an external magnetic field will be taken into account via the minimal coupling, and, taking advantage of its impact on the edge states, an alternate current (AC) spin source will be proposed at the end of the chapter. A pure spin current source may be of great interest in the development of spintronic devices [143, 144, 145].

7.2 THE BHZ MODEL

In 2006, Bernevig, Hughes and Zhang (BHZ) [5] developed a simple analytical model that captures the main physics of TIs. It describes two dimensional systems and fulfils TRS, and for the non–trivial case a QSHE phase appears. Based on the $k \cdot p$ approach of Kane [146] for semiconductors, they derived a simpler (4×4) Hamiltonian for 2D TIs which reads:

$$\begin{aligned} H(\boldsymbol{k}) &= \begin{pmatrix} h(\boldsymbol{k}) & 0 \\ 0 & h^*(-\boldsymbol{k}) \end{pmatrix}; \\ h(\boldsymbol{k}) &= \begin{pmatrix} \widetilde{C} + \widetilde{M} - (\widetilde{B} + \widetilde{D})k^2 & \widetilde{A}k_- \\ \widetilde{A}k_+ & \widetilde{C} - \widetilde{M} + (\widetilde{B} - \widetilde{D})k^2 \end{pmatrix} \end{aligned} \tag{49}$$

where the quantities with a tilde are material specific parameters, $k^2 = k_x^2 + k_y^2$ is the modulus of the crystal momentum $\boldsymbol{k}$ and $k_\pm = k_x \pm i k_y$. The basis states of the BHZ Hamiltonian are denoted by ($|E, +1/2\rangle$, $|H, +3/2\rangle$, $|E, -1/2\rangle$, $|H, -3/2\rangle$), where E (H) stands for states derived from electron-like (hole-like) bands and the number in the ket gives m_j, the projection of the total angular momentum on the z-axis. It is easy to see that $h(\boldsymbol{k})$ describes only spin–up electrons and its complex–conjugate $h^*(\boldsymbol{-k})$ spin–down electrons, and in this simple model there is no interaction between both spin species. The list of systems that are described by this Hamiltonian includes quantum wells (QWs) of HgTe/CdTe [5], InAs/GaSb/AlSb [48] and Ge/GaAs [49], which have recently been reported to be 2D TIs.

$h(\boldsymbol{k})$ can be written in a more compact way by making use of the Pauli matrices $\boldsymbol{\sigma}$: [11]

$$\begin{aligned} h(\boldsymbol{k}) &= \epsilon(\boldsymbol{k})\mathbb{1}_2 + \boldsymbol{d}(\boldsymbol{k}) \cdot \boldsymbol{\sigma}, \qquad \epsilon(\boldsymbol{k}) = \widetilde{C} - \widetilde{D}k^2, \\ \boldsymbol{d}(\boldsymbol{k}) &= [\widetilde{A}k_x, \widetilde{A}k_y, M(\boldsymbol{k})], \quad M(\boldsymbol{k}) = \widetilde{M} - \widetilde{B}k^2 \end{aligned} \tag{50}$$

where $\mathbb{1}_2$ is the identity matrix of order 2.

The BHZ model fulfils TRS by construction and inversion symmetry, as $H_{BHZ}(\boldsymbol{k}) = -H_{BHZ}(-\boldsymbol{k})$. Thus, the eigenstates form Kramers pairs due to TRS, so that for any given state $|\boldsymbol{k}, \sigma\rangle$ a time reversed state $|-\boldsymbol{k}, -\sigma\rangle$ exists with the same energy and opposite momentum and spin, and inversion symmetry dictates that they are spin–degenerate, as for $|\boldsymbol{k}, \sigma\rangle$, the inverted state $|-\boldsymbol{k}, \sigma\rangle$ exists at the same energy.

7.2.1 *Eigenstates of original BHZ model*

The BHZ Hamiltonian can be solved by blocks, as each spin–block is decoupled from the other. The energy spectrum is therefore spin–degenerate, and can be obtained by diagonalising H_{BHZ}:

$$E_{\pm} = \epsilon(\boldsymbol{k}) \pm \sqrt{M^2(\boldsymbol{k}) + \widetilde{A}^2(k_x^2 + k_y^2)} \tag{51}$$

and the eigenstates for each spin–block are of the form:

$$\Psi = \begin{pmatrix} c_A \\ c_B \end{pmatrix} e^{i(k_x x + k_y y)} \tag{52}$$

being the unnormalised coefficients

$$\begin{aligned} c_A^{\uparrow} &= M(\boldsymbol{k}) \pm \sqrt{M^2(\boldsymbol{k}) + \widetilde{A}^2(k_x^2 + k_y^2)} = c_A^{\downarrow}; \\ c_B^{\uparrow} &= \widetilde{A}(k_x + ik_y) = c_B^{\downarrow}(-\boldsymbol{k})^* \end{aligned} \tag{53}$$

It is easy to see that at the Γ point (k=0) there is a gap of size equal to $2\widetilde{M}$. The sign of $\widetilde{M}/\widetilde{B}$ determines whether the system is a trivial insulator ($\widetilde{M}/\widetilde{B} > 0$), a TI ($< 0$) or a semimetal ($= 0$). $\widetilde{C}$ gives the Fermi level position, $\widetilde{D}$ accounts for any source of electron-hole asymmetry, $\widetilde{B}$ describes the quadratic dispersion of the conduction and valence bands to lowest order in k, and $\widetilde{A}$ couples electrons and holes of the same spin species.

7.2.2 *Edge States*

We can find solutions to H_{BHZ} that correspond to edge states by making k_x imaginary in Equation 52. Substituting $k_x \to \frac{i}{\lambda}$ and solving Equation 51 for λ yields:

$$\lambda_{\pm}^{-2} = k_y^2 + F \pm \sqrt{F^2 + \frac{[(E - \widetilde{C})^2 - \widetilde{M}^2]}{\widetilde{B}^2 - \widetilde{D}^2}} \tag{54}$$

with

$$F = \frac{\widetilde{A}^2 - 2[\widetilde{M}\widetilde{B} + \widetilde{D}(E - \widetilde{C})]}{2(\widetilde{B}^2 - \widetilde{D}^2)} \tag{55}$$

The complete derivation can be found in Refs. [147] and [148], where it is stated that in the large thickness limit, real solutions of λ always exist as long as:

$$\frac{A^2}{\widetilde{B}^2 - \widetilde{D}^2} > 4\frac{\widetilde{M}}{\widetilde{B}} > 0 \tag{56}$$

and that, for small k_y, the dispersion is linear and the penetration depth is roughly $\sim \frac{\widetilde{A}}{\widetilde{M}}$.

7.3 BHZ WITH A MAGNETIC FIELD

An external magnetic field $\boldsymbol{B}$ is now included via the minimal coupling of the momentum to the electromagnetic field. The Zeeman term is neglected for the moment in the following analysis and will be included in the tight–binding model in Section 7.4. For a homogeneous $\boldsymbol{B} = B \cdot \boldsymbol{u}_z$ in the z direction, we choose the vector potential $\boldsymbol{A}$ in the Landau gauge:

$$\boldsymbol{A} = \begin{pmatrix} 0 \\ Bx \\ 0 \end{pmatrix} \tag{57}$$

and to take into account broken translational invariance in the x direction along with a non-zero vector potential we make the following substitutions in Eq. 49:

$$k_x \to -i\partial_x; k_y \to k_y - b_B x \tag{58}$$

where $b_B = \frac{eB}{\hbar}$ is the square of the inverse magnetic length associated to the magnetic field B. For a lattice model (see below), this substitution remains valid as long as the lattice spacing is much smaller than the magnetic length, *i.e.* $a_0 << \frac{1}{\sqrt{b_B}}$.

The upper spin–block Hamiltonian results in

$$h(\boldsymbol{k}) = \begin{pmatrix} (\widetilde{C} + \widetilde{M}) - (\widetilde{B} + \widetilde{D})[(k_y - b_B x)^2 - \partial_x^2] & i\widetilde{A}(k_y + b_B x - \partial_x) \\ -i\widetilde{A}(-k_y + b_B x + \partial_x) & (\widetilde{C} - \widetilde{M}) + (\widetilde{B} - \widetilde{D})[(k_y - b_B x)^2 - \partial_x^2] \end{pmatrix} \tag{59}$$

We now define the ladder operators a and $a^\dagger$,

$$\begin{aligned} a = \frac{1}{\sqrt{2}}(q + \partial_q); \quad a^\dagger = \frac{1}{\sqrt{2}}(q - \partial_q); \\ q = \sqrt{b_B}\, x - \frac{1}{\sqrt{b_B}}\, k_y; \quad [a, a^\dagger] = 1 \end{aligned} \tag{60}$$

by means of which expression 59 can be rewritten as:

$$h(\boldsymbol{k}) = \begin{pmatrix} (\widetilde{C} + \widetilde{M}) + 2b_B(\widetilde{B} + \widetilde{D})(a^\dagger a + \frac{1}{2}) & i\widetilde{A}\sqrt{2b_B}a \\ -i\widetilde{A}\sqrt{2b_B}a^\dagger & (\widetilde{C} - \widetilde{M}) + 2b_B(\widetilde{B} - \widetilde{D})(a^\dagger a + \frac{1}{2}) \end{pmatrix} \tag{61}$$

Analogously, the bottom spin–block Hamiltonian reads:

$$h^*(-\boldsymbol{k}) = \begin{pmatrix} (\widetilde{C} + \widetilde{M}) + 2b_B(\widetilde{B} + \widetilde{D})(a^\dagger a + \frac{1}{2}) & -i\widetilde{A}\sqrt{2b_B}a^\dagger \\ i\widetilde{A}\sqrt{2b_B}a & (\widetilde{C} - \widetilde{M}) + 2b_B(\widetilde{B} - \widetilde{D})(a^\dagger a + \frac{1}{2}) \end{pmatrix} \tag{62}$$

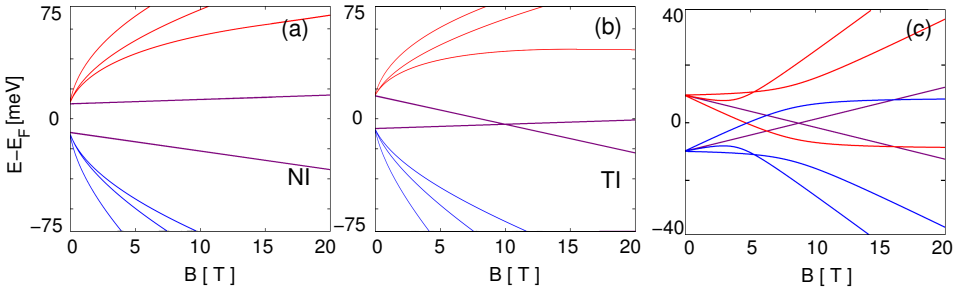

Figure 57: Evolution of the BHZ model eigenstates in a perpendicular magnetic field. (a) and (b) show QW systems of HgTe/CdTe of 55 and 75 Å respectively. Red (blue) lines represent hole–(electron–)like states, and the zero–modes are coloured in purple. The parameters used in (a) and (b) are given in table 17 in rows 1 and 3, while for (c) the parameters were chosen *ad hoc* for illustrative purposes so that a bulk band gap closing of the n=1 modes takes place. Parameters in (c): $\widetilde{B}$=-75; $\widetilde{M}$=-0.01; $\widetilde{D}$=0; $\widetilde{A}$=0.25.

7.3.1 *Eigenstates under a Magnetic Field*

The above Hamiltonian can be solved by blocks using the following ansatz for the general solution:

$$\begin{aligned} h(\boldsymbol{k})\,|\Psi^{\uparrow}\rangle &= h(\boldsymbol{k}) \begin{pmatrix} |n\rangle \\ \gamma_{\pm}^{\uparrow}(n)\,|n-1\rangle \end{pmatrix} = E_{\pm}^{\uparrow}(n) \begin{pmatrix} |n\rangle \\ \gamma_{\pm}^{\uparrow}(n)\,|n-1\rangle \end{pmatrix} \\ h^{*}(-\boldsymbol{k})\,|\Psi^{\downarrow}\rangle &= h^{*}(-\boldsymbol{k}) \begin{pmatrix} \gamma_{\pm}^{\downarrow}(n)\,|n-1\rangle \\ |n\rangle \end{pmatrix} = E_{\pm}^{\downarrow}(n) \begin{pmatrix} \gamma_{\pm}^{\downarrow}(n)\,|n-1\rangle \\ |n\rangle \end{pmatrix} \end{aligned} \tag{63}$$

yielding

$$\gamma_{\pm}^{\sigma}(n) = \frac{1}{i\widetilde{A}\sqrt{2b_B\cdot n}}\left(b_B(2\widetilde{B}n+\sigma\widetilde{D}) - \widetilde{M} \pm \sqrt{b_B^2(2\widetilde{B}n+\sigma\widetilde{D}-\widetilde{M})^2 + 2\widetilde{A}^2 b_B\cdot n}\right) \tag{64}$$

and

$$E_{\pm}^{\sigma} = \widetilde{C} - b_B(\sigma\widetilde{B}+2\widetilde{D}n) \pm \sqrt{b_B^2(2\widetilde{B}n+\sigma\widetilde{D}-\widetilde{M})^2 + 2\widetilde{A}^2 b_B\cdot n} \tag{65}$$

for $n > 0$. The plus (minus) sign in front of the square root corresponds to electron–(hole–)like states, and $\sigma = \uparrow, \downarrow$ is the spin of the corresponding eigenstate.

The n=0 case must be studied separately, for which we get the following two solutions:

$$\begin{aligned} h(\boldsymbol{k})\,|\Psi_0^{\uparrow}\rangle &= h(\boldsymbol{k}) \begin{pmatrix} |0\rangle \\ 0 \end{pmatrix} = E_0^{\uparrow} \begin{pmatrix} |0\rangle \\ 0 \end{pmatrix}; \\ h^{*}(-\boldsymbol{k})\,|\Psi_0^{\downarrow}\rangle &= h^{*}(-\boldsymbol{k}) \begin{pmatrix} 0 \\ |0\rangle \end{pmatrix} = E_0^{\downarrow} \begin{pmatrix} 0 \\ |0\rangle \end{pmatrix}; \\ E_0^{\sigma} &= \widetilde{C} + b_B\widetilde{D} + \sigma(\widetilde{M} - b_B\widetilde{B}) \end{aligned} \tag{66}$$

which are usually called zero–modes. Their evolution with the magnetic field is strictly linear, in contrast with the general $E^{\sigma}(n)$. Fan plots of the energy (Landau–like) levels are shown in Fig. 57 for the trivial ($\widetilde{M}/\widetilde{B} > 0$) and topological ($\widetilde{M}/\widetilde{B} < 0$) phases –(a) and (b) in the figure respectively– . Interestingly, for the topological regime a bulk band gap closing of the zero–modes appears for a magnetic field of

$$E_0^{\uparrow}(b_B = b_B^{crit}) = E_0^{\downarrow}(b_B = b_B^{crit}) \Longrightarrow b_B^{crit} = \frac{\widetilde{M}}{\widetilde{B}} \tag{67}$$

Above this critical magnetic field, the inverted electron–like valence band and hole–like conduction band undergo an 'un-inversion', so that after the band crossing the system is no longer in the inverted band regime. Note that this result is independent of $\widetilde{C}$, $\widetilde{D}$ and $\widetilde{A}$. Other bulk band gap closings may also appear for $n \neq 0$ levels as shown in Fig. 57(c). The values of the critical magnetic field for QWs of HgTe/CdTe, InAs/GaSb/AlSb and Ge/GaAs are shown in table 16.

7.3.2 *Other terms*

A more realistic description can be achieved by adding the effects of the bulk inversion asymmetry (BIA) and structure inversion asymmetry (SIA), which are non negligible in real samples of the known 2D TIs [48, 149]. The former arises in any non-centrosymmetric spin-orbit coupled system and introduces a Dresselhaus–like term in the Hamiltonian, while the latter accounts for asymmetries such as external electric fields or unequal surface terminations in a slab, and enters as a Rashba–like term. In the BHZ model, and up to first order in k (there are no second order terms), the BIA term reads:

$$H_{BIA} = \begin{pmatrix} 0 & 0 & \Delta_e k_+ & -\Delta_0 \\ 0 & 0 & \Delta_0 & \Delta_h k_- \\ \Delta_e k_- & \Delta_0 & 0 & 0 \\ -\Delta_0 & \Delta_h k_+ & 0 & 0 \end{pmatrix} \tag{68}$$

and the SIA term has the form:

$$H_{SIA} = \begin{pmatrix} 0 & 0 & i\xi k_- & 0 \\ 0 & 0 & 0 & 0 \\ -i\xi^* k_+ & 0 & 0 & 0 \\ 0 & 0 & 0 & 0 \end{pmatrix} \tag{69}$$

Finding an analytical solution of the full Hamiltonian $H_{BHZ} + H_{BIA} + H_{SIA}$ becomes now a non–trivial issue that is beyond the scope of this work. Instead, we will show a solution for $H_{BHZ} + H_{BIA}$ taking into account in H_{BIA} only the terms with lowest order in k (the full Hamiltonian with the BIA and SIA terms will be solved numerically in the next section of this chapter). We thus have:

$$H_{BIA}^0 = \Delta_0 \begin{pmatrix} 0 & 0 & 0 & -1 \\ 0 & 0 & 1 & 0 \\ 0 & 1 & 0 & 0 \\ -1 & 0 & 0 & 0 \end{pmatrix} \tag{70}$$

	HgTe/CdTe (70 Å)	InAs/GaSb/AlSb	Ge/GaAs
B^{crit}(T)	9.6	8.3	668

Table 16: Critical magnetic field in Teslas for different 2D TIs. The material specific parameters used are listed in table 17.

	d	$\widetilde{D}$	$\widetilde{M}$	$\widetilde{B}$	$\widetilde{A}$	Δ_0	Δ_e	Δ_h	g_E	g_H
HgTe/CdTe	55	-30.6	$9{\cdot}10^{-3}$	-48.0	3.87	$1.8{\cdot}10^{-3}$	-	-	-	-
HgTe/CdTe	61	-37.8	$-1.5{\cdot}10^{-4}$	-55.3	3.78	$1.7{\cdot}10^{-3}$	-	-	-	-
HgTe/CdTe	70	-51.2	-0.01	-68.6	3.65	$1.6{\cdot}10^{-3}$	-	-	22.7	-1.21
InAs/GaSb/AlSb	19	-30	$-5{\cdot}10^{-3}$	-40	0.3	$2{\cdot}10^{-4}$	$6.6{\cdot}10^{-4}$	$6{\cdot}10^{-4}$	-8	-3
Ge/GaAs	18	-0.115	$-3.28{\cdot}10^{-3}$	-0.323	0.0285	-	-	-	-	-

Table 17: Values of the material dependent parameters in the BHZ Hamiltonian for several semiconductor QWs of different thicknesses d. The value of d is given in Å, $\widetilde{M}$ and Δ_0 in eV, $\widetilde{A}$, Δ_e and Δ_h in $eV{\cdot}$Å and $\widetilde{B}$ and $\widetilde{D}$ in $eV{\cdot}$Å^2. g_E and g_H are the electron and hole g–factors respectively (dimensionless). For HgTe/CdTe QWs, the tilded parameters were taken from Ref. [11], the BIA and SIA related parameters from Ref. [149] and the effective g–factors from Ref. [148]. The InAs/GaSb/AlSb QW parameters were taken form Ref. [150](in the Supplemental Material), and those of Ge/GaAs QWs form Ref. [151](in the Supplemental Material).

so that now electrons are coupled to holes of opposite spin and the full Hamiltonian can not be solved by blocks. The general solution will have the form:

$$|\Psi_n\rangle = \begin{pmatrix} |n\rangle \\ f_{\pm}^{1}(n)\,|n-1\rangle \\ f_{\pm}^{2}(n)\,|n-1\rangle \\ f_{\pm}^{3}(n)\,|n\rangle \end{pmatrix} \tag{71}$$

for $n \neq 0$, and the zero-modes will be of the form:

$$[H_{BHZ} + H_{BIA}^{0}] \begin{pmatrix} f_{\pm}^{0}\,|0\rangle \\ 0 \\ 0 \\ |0\rangle \end{pmatrix} = E_{\pm}^{0} \begin{pmatrix} f_{\pm}^{0}\,|0\rangle \\ 0 \\ 0 \\ |0\rangle \end{pmatrix} \tag{72}$$

yielding:

$$f_{\pm}^{0} = \frac{\widetilde{B} b_B - \widetilde{M}}{\Delta_0} \pm \frac{1}{\Delta_0}\sqrt{(\widetilde{B} b_B - \widetilde{M})^2 + \Delta_0^2} \tag{73}$$

and

$$E_{\pm}^{0} = \widetilde{C} - \widetilde{D} b_B \pm \sqrt{(\widetilde{B} b_B - \widetilde{M})^2 + 4\Delta_0^2} \tag{74}$$

The additional term $4\Delta_0^2$ prevents the zero–modes from being degenerate at $b_B = b_B^{crit}$ or any other value of the magnetic field, effectively turning the crossing of the levels into an anti–crossing (see Figure 60).

7.4 TIGHT–BINDING REGULARISATION

7.4.1 *Lattice regularisation*

In order to gain some insight into the states of the full Hamiltonian and with the main purpose of solving the electronic structure of a realistic sample of an experimentally available 2D TI that could be used as an AC spin source, we now regularise the continuum BHZ Hamiltonian on a lattice following Ref. [11]. Note that all the interesting physics will occur near the Γ point of the BZ at low energies, where the BHZ description is valid. Therefore, the replacement remains valid in the same energy–momentum window in which H_{BHZ} is valid. In order to regularise the BHZ Hamiltonian over a lattice, we first write the BHZ Hamiltonian as:

$$H_{BHZ}(k) = (\widetilde{C} + \widetilde{D}k^2)\mathbb{1}_4 + (\widetilde{M} - \widetilde{B}k^2)\beta + \widetilde{A}(k_x\alpha_x + k_y\alpha_y) \tag{75}$$

where β and α_i are 4×4 representations of Dirac matrices:

$$\beta = \sigma_0 \otimes \tau_3 = \begin{pmatrix} 1 & 0 & 0 & 0 \\ 0 & -1 & 0 & 0 \\ 0 & 0 & 1 & 0 \\ 0 & 0 & 0 & -1 \end{pmatrix} \tag{76}$$

$$\alpha_x = \sigma_3 \otimes \tau_1 = \begin{pmatrix} 0 & 1 & 0 & 0 \\ 1 & 0 & 0 & 0 \\ 0 & 0 & 0 & -1 \\ 0 & 0 & -1 & 0 \end{pmatrix} \tag{77}$$

$$\alpha_y = -\sigma_0 \otimes \tau_2 = \begin{pmatrix} 0 & i & 0 & 0 \\ -i & 0 & 0 & 0 \\ 0 & 0 & 0 & i \\ 0 & 0 & -i & 0 \end{pmatrix} \tag{78}$$

Here the σ_i's describe spin degrees of freedom and the τ_i's the orbital degrees of freedom.

Discretising the above Hamiltonian in a lattice with lattice spacing a_0 leads to [11]:

$$\begin{aligned} H_{BHZ}(k) = &\left(\widetilde{C} + \frac{2}{a_0^2}\widetilde{D}(2 - \cos k_x a_0 - \cos k_y a_0)\right)\mathbb{1}_4 + \\ &+\left(\widetilde{M} - \frac{2}{a_0^2}\widetilde{B}(2 - \cos k_x a_0 - \cos k_y a_0)\right)\beta + \\ &+\frac{1}{a_0}\widetilde{A}(\alpha_x \sin k_x a_0 + \alpha_y \sin k_y a_0) \end{aligned} \tag{79}$$

For small k, where the original BHZ model is valid (recall that it is derived within the $k \cdot p$ approximation), the discretised Hamiltonian is equivalent to the continuum BHZ Hamiltonian. The lattice spacing will be set to $a_0 = 1$ hereafter with no loss of generality. We will focus on systems with translational invariance in the y direction but (possible) broken translational invariance in the x direction, so that edges can be taken into account. In order to write down a tight-binding model for an infinite stripe we make the following substitutions:

$$\begin{aligned} 2\ \sin k_x &\to i\sum_j c_{j+1}^\dagger c_j + h.c. \\ 2\ \cos k_x &\to \sum_j c_{j+1}^\dagger c_j + h.c. \end{aligned} \tag{80}$$

where the summation is over the lattice sites and $c_j^\dagger$ and c_j are the fermionic creation and annihilation operators on site j respectively.

With these substitutions we arrive at a tight–binding Hamiltonian with an on–site term with the form:

$$H_0^{onsite} = \left(\widetilde{C} - 2\widetilde{D}(2 - \cos k_y)\right)\mathbb{1}_4 + \left(\widetilde{M} - 2\widetilde{B}(2 - \cos k_y)\right)\beta + \alpha_y \widetilde{A}\sin k_y \tag{81}$$

and a hopping term between neighbouring sites in the x direction that reads:

$$T_j \equiv t_{j+1,j} = -\widetilde{D}\mathbb{1}_4 + \widetilde{B}\beta + i/2\widetilde{A}\alpha_x \tag{82}$$

For the magnetic translation group, the magnetic field enters the Hamiltonian as an additional site–dependent phase in the hopping parameters [152, 153]. Choosing the Landau gauge with $\boldsymbol{A} = Bx\hat{\boldsymbol{u}}_y$ we get the hopping along the y direction to be renormalised by $e^{(i2\pi j_x \Phi/\Phi_0)}$ where j_x is the j-th site in the x direction, $\Phi = Ba_0^2$ is the magnetic flux in a unit cell and $\Phi_0 = \frac{h}{e}$ is the magnetic flux quantum. For infinite systems in the y direction, and in this Landau gauge, this is equivalent to substituting $[k_y]$ with $[k_y + \pi\frac{\Phi}{\Phi_0}(2j_x - L_x + 1)]$ for every $H_0^{onsite}(j_x)$ (now site–dependent).

7.4.2 *Final Hamiltonian*

Other terms can now be easily added to the Hamiltonian. A potential gradient along the x direction would enter as a site–dependent on–site diagonal term, and can address the effect of gating the sample. The Zeeman term for a perpendicular magnetic field is addressed with a constant on–site term of the form:

$$H_{Zee} = \mu_B b_B \frac{\hbar}{e}\begin{pmatrix} g_E & 0 & 0 & 0 \\ 0 & g_H & 0 & 0 \\ 0 & 0 & -g_E & 0 \\ 0 & 0 & 0 & -g_H \end{pmatrix}; \tag{83}$$

where μ_B is the Bohr magneton and g_E and g_H the effective electron and hole g–factors respectively. The BIA and SIA terms presented in Eqs. 68-69 are regularised analogously to the aforementioned H_{BHZ}, so that the full

regularised Hamiltonian that includes the effects of the magnetic field, BIA and SIA reads:

$$
\begin{aligned}
H^{onsite}(j_x) = \Big(\widetilde{C} - 2\widetilde{D}(2-\cos[k_y-q])\Big)\mathbb{1}_4 + \Big(\widetilde{M} - 2\widetilde{B}(2-\cos[k_y-q])\Big)\beta + \\
\sin[k_y-q]\Big(\widetilde{A}\alpha_y + \Delta_e\gamma_x + \Delta_h\delta_x - \xi\gamma_y\Big) + H_0^{BIA} + H_{Zee} + V(j_x); \\
T_j \equiv t_{j+1,j} = -\widetilde{D}\mathbb{1}_4 + \widetilde{B}\beta + \frac{i}{2}(\widetilde{A}\alpha_x + \Delta_e\gamma_y + \Delta_h\delta_y - \xi\gamma_x); \\
\gamma_x = \begin{pmatrix} 0 & 0 & 1 & 0 \\ 0 & 0 & 0 & 0 \\ 1 & 0 & 0 & 0 \\ 0 & 0 & 0 & 0 \end{pmatrix}; \delta_x = \begin{pmatrix} 0 & 0 & 0 & 0 \\ 0 & 0 & 0 & 1 \\ 0 & 0 & 0 & 0 \\ 0 & 1 & 0 & 0 \end{pmatrix}; \\
\gamma_y = \begin{pmatrix} 0 & 0 & i & 0 \\ 0 & 0 & 0 & 0 \\ -i & 0 & 0 & 0 \\ 0 & 0 & 0 & 0 \end{pmatrix}; \delta_y = \begin{pmatrix} 0 & 0 & 0 & 0 \\ 0 & 0 & 0 & -i \\ 0 & 0 & 0 & 0 \\ 0 & i & 0 & 0 \end{pmatrix}
\end{aligned}
\tag{84}
$$

where $q = \pi\frac{\Phi}{\Phi_0}(2j_x - L_x + 1)$ and $V(j_x)$ is the site dependent external electrostatic potential.

Now that we have a full realistic Hamiltonian, we can accurately describe QWs of 2D TIs subject to a magnetic field and/or potential gradient or gating.

7.5 AC SPIN SOURCE

In this section we will propose an AC current source based on 2D TIs and mesoscopic capacitors acting as single–particle sources. The device generates an AC current in the GHz range that can be tuned from a pure AC spin–current to a pure AC electrical current. Since a realistic Hamiltonian for 2D TIs has been developed in the previous section, we will calculate the band structure of such a device built with different experimentally observed 2D TIs in order to give realistic values for the operating gate voltages and magnetic fields.

7.5.1 *Time Reversal invariant source*

The proposed source is sketched in Figure 58. The device consists of two single–particle sources provided by mesoscopic capacitors that are attached to opposite sides of a 2D TI strip. A mesoscopic capacitor is nothing but a quantum dot tunnel–coupled to the sample. A time driven top gate, $U(t)$ shifts the potential in the dot above and below the Fermi level in a periodic manner, pumping counterpropagating electrons (holes) into the edge states of the sample every time the energy level of the degenerate Kramers pair in the dot is shifted above (below) E_F. Thus, a single mesoscopic capacitor generates a spin-polarised AC charge current in contacts L and R in the figure. In this setup no magnetic field is required for the generation of an AC spin current.

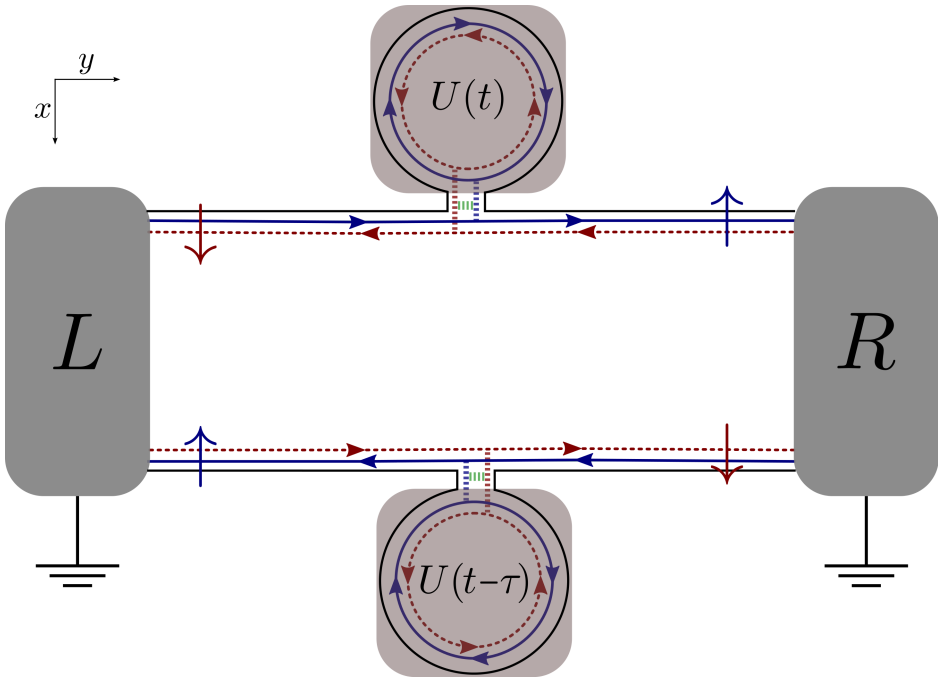

Figure 58: Proposed AC spin current source in the TI regime. Two mesoscopic capacitors are attached to a two-dimensional TI. If they are operated in phase ($\tau = 0$), they both emit electrons and holes at equal times resulting in a pure and equal AC *charge* current in the two contacts (R/L). A delay, τ, can synchronise electron and hole emission on the different edges. This results in a pure AC *spin* current of opposite sign in the different contacts. The arrows indicate the expectation value of the spin for an electron.

We consider two identical capacitors that work with a time delay τ in the periodic top gate potential. If the capacitors are operated in phase (τ=0), the charge current at each of the contacts (L/R) is twice the charge pumped by a single capacitor, while the spin current is cancelled since there is a channel of each spin entering each contact. If the capacitors are operated in antiphase, the electron emission of one capacitor is synchronised with a hole emission in the other capacitor, cancelling the charge current. Regarding spin, an electron of a given spin species and a hole of opposite spin species contribute equally to the spin current, resulting in a purely AC spin current that is opposite in each contact. We can study the currents quantitatively using the scattering approach [154]. For sufficiently separated edges there is no scattering among any of the four channels that connect contacts L and R –the critical separation below which edge states of opposite edges interact is given by twice the penetration depth of the edge states, given by $\sim \frac{\widetilde{A}}{\widetilde{M}}$–. The total charge current will therefore be the sum of the currents generated at each capacitor.

The dot levels can be driven in an oscillating manner above and below E_F by a step–like top gate potential with the amplitude given by the dot level spacing Δ_D and the frequency $2\pi/\mathcal{T}$. This kind of driving potential has been successfully used in several experiments in the GHz range [155, 156].

Thus, the capacitor at the upper edge will emit a periodic charge current of period $\mathcal{T}$ that can be written as follows [157]:

$$I^c(t) = \begin{cases} \frac{e}{\tau_D} e^{-t/\tau_D} & \text{for } 0 \leq t < \mathcal{T}/2, \\ -\frac{e}{\tau_D} e^{-(t-\mathcal{T}/2)/\tau_D} & \text{for } \mathcal{T}/2 \leq t < \mathcal{T} \end{cases} \tag{85}$$

where $\tau_D = h/(D\Delta_D)$ is the dwell time, being D the transmission probability through the quantum point contact (QPC), and $e < 0$ is the electron charge. For the case where $\tau_D \ll \mathcal{T}/2$, one electron and one hole is emitted in each cycle. The charge current emitted by the capacitor located at the lower edge is given by $I^c(t-\tau)$.

The spin current in a given channel α is proportional to the charge current $I^s_\alpha(t) = \langle J_z \rangle_\alpha I^c_\alpha / e$ since the dispersion is linear. Therefore, the quantised emission of a single electron or hole into channel α is accompanied by the quantised emission of total angular momentum in units of $\langle J_z \rangle_\alpha$. If we operate the two capacitors with a time shift of τ, the currents in the right and left contacts will be:

$$\begin{aligned} I^c_R(t) &= I^c_L(t) = I^c(t) + I^c(t-\tau), \\ I^s_R(t) &= -I^s_L(t) = \frac{\hbar}{e}\left[I^c(t) - I^c(t-\tau)\right], \end{aligned} \tag{86}$$

where the subscript R/L denotes the contact (right/left) and we made use of the fact that $\langle J_z \rangle_\alpha = \pm\hbar$ for the edge channels.

Figure 59 shows the charge and spin currents entering the right contact. For $\tau = 0$, each capacitor emits a single electron at time $t = 0$ and a single hole at $t = \mathcal{T}/2$. In this situation the charge current acquires its maximum possible value and the spin current vanishes. For finite τ, the upper capacitor emits an electron at time $t = 0$ which contributes positively to both charge and spin current, whereas the lower capacitor emits an electron at time $t = \tau$ which contributes positively to the charge but negatively to the spin current. The opposite holds for the holes and for the spin current in the left contact. Finally, when $\tau = \mathcal{T}/2$, the electron of the upper capacitor and the hole of the lower capacitor are synchronised. The charge current is zero while the spin current is maximised. Thus, controlling the time shift allows us to tune from a pure charge to a pure spin current. Conveniently, mesoscopic capacitors are usually operated in the GHz range, where experimental detection of AC spin currents has been reported recently [144].

7.5.1.1 *Note on spin–current*

In spin–orbit coupled systems, and in particular in the 2D BHZ Hamiltonian, the projection of the electron spin on the z axis, m_s is not generally a good quantum number. Instead, the projection of the *total* angular momentum, m_j, is a good quantum number for the basis states and therefore does not depend on the specific material or the sample geometry. This means that our device is truly a total angular momentum source. The electron spin in z is only a good quantum number for the states $|H, \pm 3/2\rangle$ for which $m_j = 3/2$ and $m_s = 1/2$. Nevertheless, we can estimate the spin polarisation of the $|E, \pm 1/2\rangle$ states based on Ref. [158], which gives an expectation value of

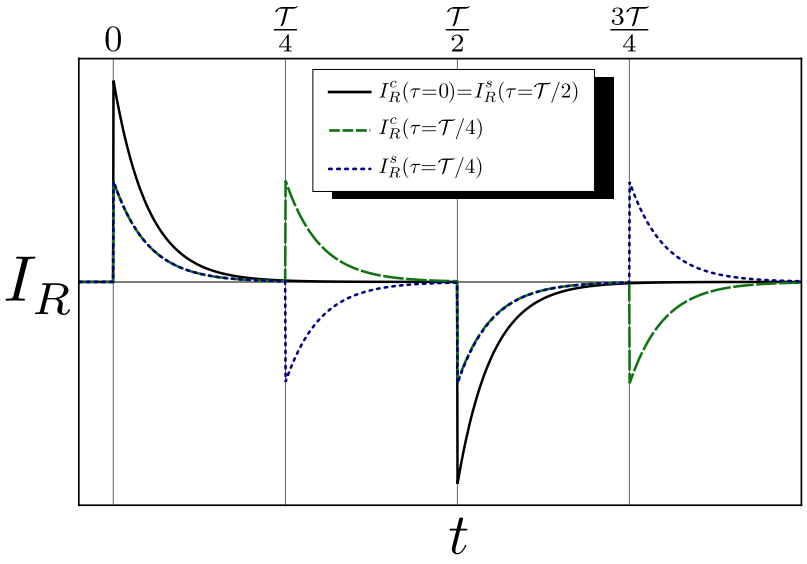

Figure 59: Charge and spin current ($e = \hbar = 1$) emitted by the source into the right contact. Black (solid) line shows the pure charge current for synchronous operation which is equal to the pure spin current for $\tau = \mathcal{T}/2$. The green (broken) line shows the charge current, the blue (dashed) line the spin current, for a finite delay. Changing τ moves the peaks and dips centred around τ and $\mathcal{T}/2 + \tau$, going from a pure charge ($\tau = 0$) to a pure spin current ($\tau = \mathcal{T}/2$). Note that an equal (opposite) charge (spin)current enters the left contact.

$\langle S_z \rangle = \langle E, \pm 1/2 | \, S_z \, | E, \pm 1/2 \rangle$ of $\pm 0.73\hbar/2$ for a 70 Å QW of HgTe/CdTe, with a small dependence on the QW width, and similar values are expected for the other materials studied in this chapter. Therefore, for all basis states $\langle S_z \rangle$ and m_j have the same sign, and the currents associated to these two quantities are proportional to each other (and quantitatively similar). This justifies the notion of spin–current even though the proposed source is discussed in terms of total angular momentum current, which is sample and material dependent in contrast with electron–spin current.

7.5.2 *Quantum Hall source*

7.5.2.1 *Evolution of edge states in a magnetic field*

We now solve numerically the regularised BHZ Hamiltonian taking into consideration a perpendicular magnetic field, and the effects of the BIA and SIA terms. We can distinguish three different regimes:

(i) TRS protected TI

(ii) Broken TRS intermediate state

(iii) Quantum Hall state

An increasing perpendicular magnetic field drives the system from regime (i) to (ii) and finally (iii). For small B, the degeneracy of the original Kramers pairs (which are not so in the presence of B) is lifted, and the edge states are shifted laterally in momentum space, being the shift opposite for both edges. Nevertheless, the spin flavour of these edge states remains practically the

same as for the TI regime. A small gap opens where edge states belonging to the same edge cross, as they are no longer protected by TRS. The gap is induced by the BIA and SIA terms, which couple states with opposite spins –see insets in Figures 61(b) and 62(b)– .

Further increasing the magnetic field gradually couples the edge states via the bulk states and flattens the spectrum around the Γ point, forming Landau levels. In the topologically non–trivial regime, the spin up states give rise to a hole–like Landau level that is above a corresponding electron–like spin down state due to the intrinsic band inversion (see the fan plots in Figures 57 and 60). Above the critical magnetic field given by $b_B^{crit} = \frac{\widetilde{M}}{\widetilde{B}}$ the aforementioned levels undergo an *uninversion*, meaning that the hole–like spin up level remains below the electron–like spin down one. This regime can be identified as a QHE state –(iii)–, in which all the electron–like Landau levels are above the hole–like Landau levels, and close to E_F they alternate in the sign of $\langle J_z \rangle$. Figures 61 and 62 show the expected value of the total angular momentum J along the z axis, $\langle J_z \rangle$, along with the spatial localisation of the states at the various stages described above for an InAs/GaSb/AlSb QW of 19 Å and a HgTe/CdTe QW of 70 Å respectively. The first, second and third column in each figure correspond to regimes (i), (ii) and (iii) respectively. The parameters used for the calculations are taken from Refs. [11, 148, 149, 150] and are listed in table 17.

7.5.2.2 *The QH source*

The fabrication of QPCs still represents a considerable experimental challenge in TIs, so we propose an additional setup which requires a constant magnetic field by which the TI is tuned into the QHE regime. For this setup, all the building blocks are presently available, since the QPCs can be provided by top gates that locally charge the filling factor in the sample. The proposed source is sketched in Figure 63. The system is subject to a perpendicular magnetic field above the critical value of $B^{crit} = \frac{\hbar \widetilde{M}}{e\widetilde{B}}$ –see Figures 61(c) and 62 (c)–. A bottom gate can be used to shift the band structure relative to E_F, and a split gate can shift the energy levels up in one half of the sample and down in the other half, as experimentally demonstrated in Ref [159]. This is easily included in the Hamiltonian as positive on–site potential in one half of the sample and negative in the other half. The resulting band structure is shown in 64. There are four states at E_f, two of which are localised in the edges and two in the middle of the system. The former propagate right while the latter propagate right. For the upper edge state $\langle J_z \rangle_u = 3\hbar/2$ and for the lower edge $\langle J_z \rangle_u = -\hbar/2$. In contrast to the TRS invariant source described before, in this setup all the channels connected to the mesoscopic capacitors propagate to the right, so that $I_L^c = I_L^s = 0$. The charge current in the right contact is still given by Equation 86, and the spin current will now be:

$$I_R^s(t) = \frac{\hbar}{e}\left[\frac{3}{2}I^c(t) - \frac{1}{2}I^c(t-\tau)\right], \tag{87}$$

This means that for $\tau = 0$ a spin current of I^c is emitted, so that a pure charge current can no longer be generated by the system. Nevertheless, a pure spin current of $2I^c$ is still achieved for $\tau = \mathcal{T}/2$.

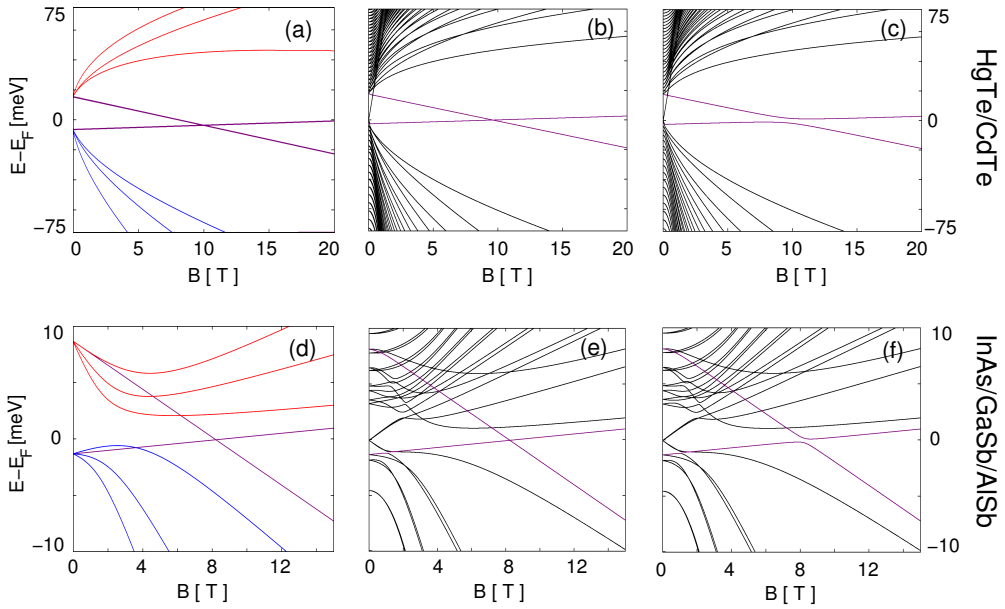

Figure 60: Fan plots for a 70 Å QW of HgTe/CdTe –first row, (a) to (c)– and a 19 Å QW of InAs/GaSb –second row, (d) to (f)–. The first column shows the analytical evolution of the eigenstates, while the second and third columns show the evolution of the states at the Γ point of the BHZ model regularised on a finite lattice with two edges. The BIA and SIA were only included in the calculation displayed in the third column. The zero–modes (in purple) are well reproduced by the lattice–regularised model, being the critical magnetic field B^{crit} the same in the analytical and numerical solutions. The electron–like and hole–like n=1 states are also well described. In the lattice model the edge states are also visible at small values of the magnetic field, as well as several additional states that appear due to confinement of the bulk states. Still, the physics at low energies is well reproduced by the regularised version of the Hamiltonian. The BIA and SIA terms turn the crossing in (b) and (e) into an anticrossing in (c) and (f) respectively, while the rest of the states remain almost identical to the inversion–symmetric case (recall that here we only display the eigenstates in the highly symmetric Γ point).

7.6 SUMMARY AND CONCLUSIONS

In this chapter we have studied the 2D BHZ model that describes TRS–protected two dimensional TIs, which is a realisation of the QSHE. We have addressed the impact of several additional terms such as BIA, SIA, the coupling to a magnetic field via the Peierls substitution, the Zeeman term and a potential gradient along the sample. A lattice regularisation of the model was carried out in order to obtain numerical solutions for finite size systems. This allowed us to study the evolution of the electronic band structure (including the edge states) in the presence of a magnetic field. In the last section two similar AC spin–current sources were proposed, one that preserves TRS and works in the absence of a magnetic field but requires the fabrication of a QPC in a 2D TI (which remains an experimental challenge up to date), and another that can be built with experimentally available building blocks but only works with a perpendicular magnetic field. Band structure calculations, along with spin texture and state localisation, are shown for the two proposed sources, using parameter values that correspond to real systems

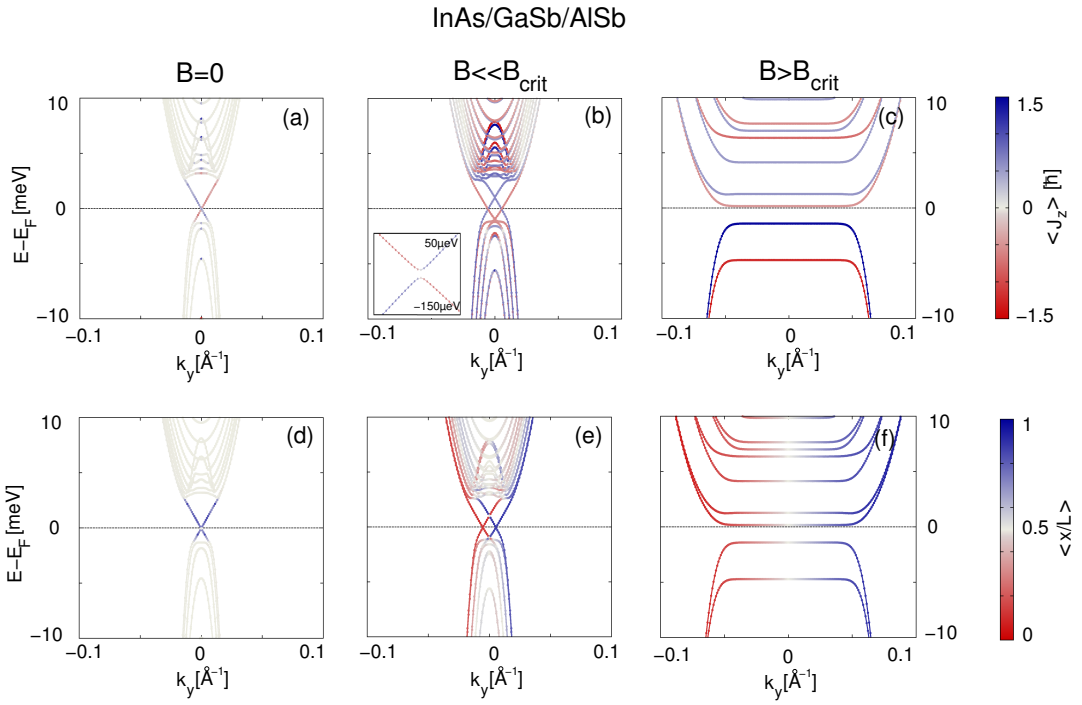

Figure 61: Band structure of a 19 Å InAs/GaSb QW calculated within the tight–binding regularised BHZ model. From left to right, the magnetic field is 0 –(a) and (d)–, 1.24 –(b) and (e)– and 9.5 Tesla –(c) and (f)–. The colour code in the first (second) row shows the expected value of $\langle J_z \rangle$ ($\langle x \rangle$). At zero magnetic field –(a) and (d)– both edge states are degenerate, and only one is shown. For small magnetic fields the edge states shift in opposite directions in momentum space. As TRS is broken, the inversion asymmetry terms open a gap in the spectrum of the edge states –see inset in (b)–. For magnetic fields higher than B^{crit} the bands undergo an *uninversion* and the system is in a QHE phase. In (c) and (f) the Landau levels are already formed, characterised by a flat spectrum in the bulk, high dispersion and strong localisation in the edges and spin polarisation of the eigenstates.

such as Ge/GaAs, HgTe/CdTe and InAs/GaSb/AlSb QWs. For the last two, the proposed QHE spin–source can be built with current-day technology and a magnetic field of the order of 10 Tesla. Such an AC spin–source may be greatly useful in the promising field of spintronics.

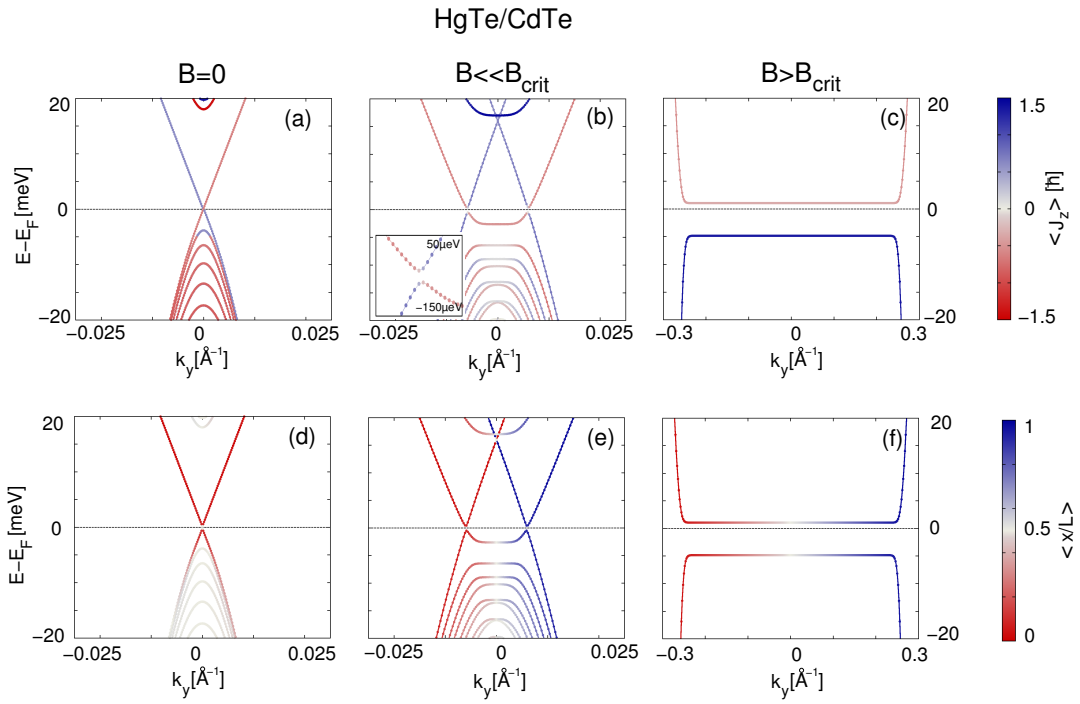

Figure 62: Same as Figure 61 for a 70 Å HgTe/CdTe QW calculated within the tight–binding regularised BHZ model. From left to right, the magnetic field is 0 –(a) and (d)–, 0.94 –(b) and (e)– and 12.0 Tesla –(c) and (f)–.

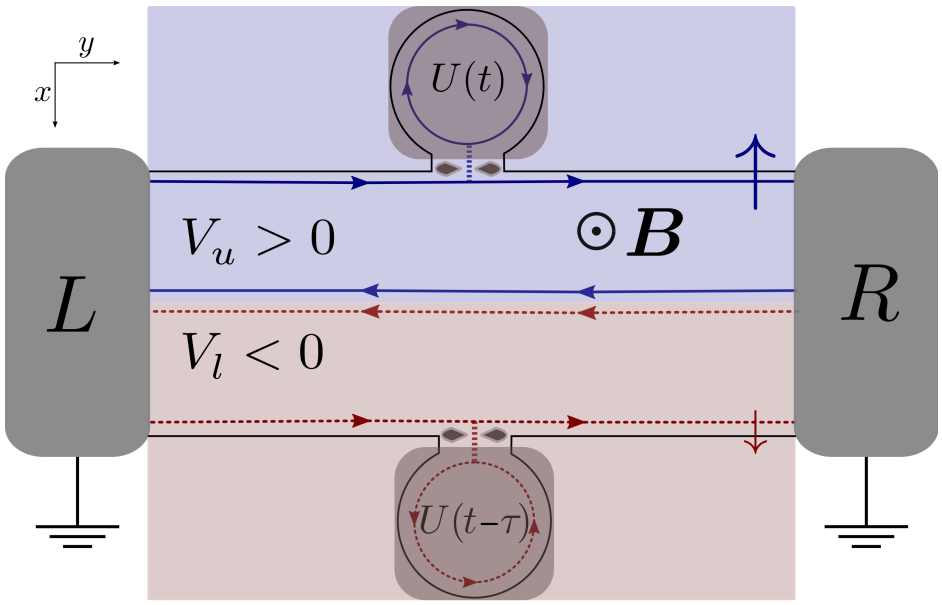

Figure 63: Proposed AC spin current source in the QHE regime. A strong magnetic field is used to produce Landau levels. Using a split gate (V_u and V_l, blue and red shading), the upper half is tuned into a regime where one edge state with $\langle J_z \rangle_u = 3\hbar/2$ (blue, solid) propagates clockwise, while in the lower half an edge state with $\langle J_z \rangle_l = -\hbar/2$ (red, dashed) propagates counter–clockwise. The leftmoving states are localised in the middle of the sample, which ensures the absence of backscattering.

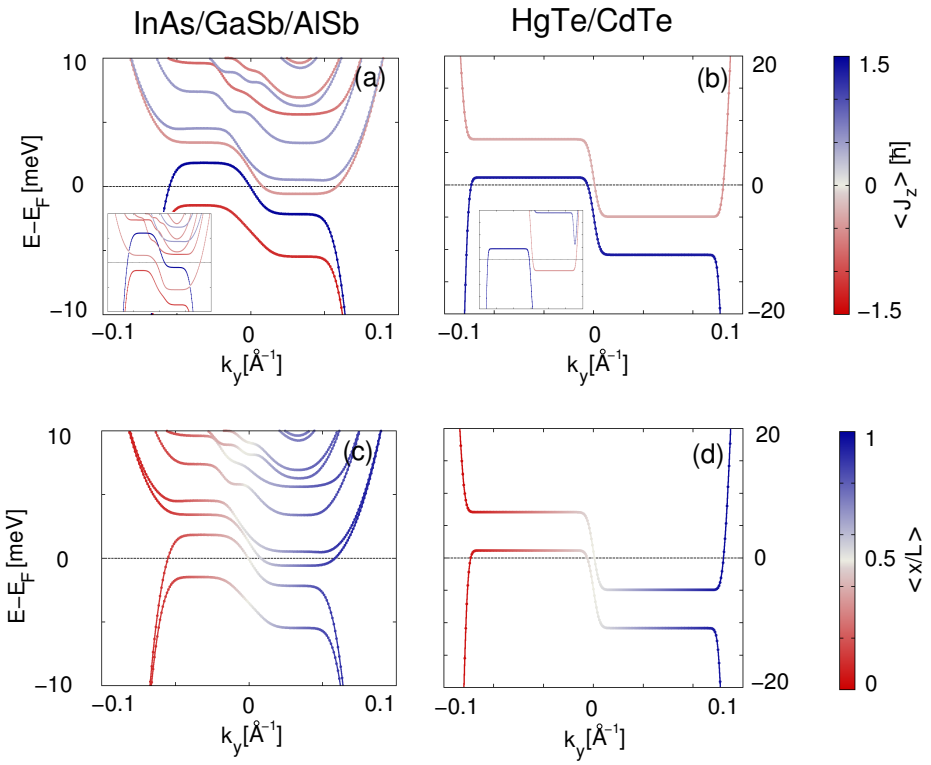

Figure 64: Electronic band structure of a 19 Å InAs/GaSb/AlSb QW –(a) and (c)– and a 70 Å HgTe/CdTe QW –(b) and (d)– subject to a supercritical perpendicular magnetic field and a split gate. In this regime these 2D TIs would operate as the proposed AC spin current source sketched in Figure 63 and described in the main text. The colour code in the first (second) row shows the expected value of $\langle J_z \rangle$ ($\langle x \rangle$). The values of the magnetic field B and split gate voltages V_u and V_l are 9.5 Tesla, +3.25 mV, -0.75 mV for the InAs/GaSb/AlSb system and 12.0 Tesla, +5 mV, -5 mV for the HgTe/CdTe system respectively. Figures (c) and (d) show clearly that two edge states cross the Fermi level (and other two states localised in the centre of the sample), and their expected value of $\langle J_z \rangle$ is $+3\hbar/2$ and $-\hbar/2$ as seen in (a) and (b). The insets show the corresponding band structure including the Zeeman splitting for the same magnetic fields and V_u= +5 mV (+8.0 mV), V_l= -2 mV (-21 mV) for the InAs/GaSb/AlSb (HgTe/CdTe) systems.

8

SUMMARY AND CONCLUSIONS

8.1 (ENG) SUMMARY AND CONCLUSIONS

Topological insulators are a novel ordered phase of matter defined by a topological invariant instead of an order parameter. In particular, time–reversal symmetry protected topological insulators are defined by $\mathbb{Z}_2$ topological invariant and the physical mechanism responsible for their non–trivial topology is usually the spin–orbit coupling. This phase occurs in a variety of 3D materials and 2D heterostructures, and is characterised by an insulating bulk and metallic boundaries when in contact with any other trivial insulating phase, including vacuum. Therefore, low dimensional systems and heterostructures where surfaces and interfaces dominate the most significant physical properties are particularly relevant to disclose distinct and unusual characteristics of this new quantum phase of matter.

In this thesis we have studied low dimensional effects in 2D and 3D time–reversal symmetry protected topological insulators from different perspectives. On the one hand, we have investigated two–dimensional systems of the 3D topological insulating Bismuth dichalcogenides Bi_2Te_3, Sb_2Te_3, Bi_2Se_3 and Sb_2Se_3 by means of realistic *ab initio* calculations. In particular, we have studied thin films and heterostructures of these materials under different intrinsic and extrinsic perturbations and external fields, such as strain fields, stacking defects or magnetic impurities. On the other hand, we investigated 2D topological insulating heterostructures under external magnetic fields based on a phenomenological model, and proposed topological insulator–based devices that produce pure AC spin currents.

The main conclusions of this work are summarised below.

3. Bulk and surface properties of Bi_2Te_3, Sb_2Te_3, Bi_2Se_3, and Sb_2Se_3 based on *ab initio* calculations. We describe the bulk band dispersion diagrams and their topological characterisation. (111) surfaces show the well–known Dirac cone–like topologically protected surface states. The spin texture of the surface states is presented and classified as a circular skyrmion in reciprocal space. The spin is locked perpendicular to the crystal momentum and the helical character of the states is patent from the texture, while a three–fold symmetric oscillation of the S_z component is observed away from the centre of the Brillouin zone. In ultrathin films a gap opens in the surface spectrum due to surface–surface hybridisation, which can be tuned with the slab thickness.

4. Tension and TI/TI Heterostructures. We obtained the phase diagrams of the bulk Bi_2Se_3 family of compounds depending on uniaxial and biaxial strain. Tensile uniaxial strain drives the four systems into a normal insulating phase, while biaxial strain (both compressive and tensile) drives them into a metallic phase. The band (un)inversion in the Γ point as a function of uniaxial strain is analysed in terms of the Bi and Se p_z bands. Compressive and tensile biaxial strains larger than $\sim 10\%$ drive Bismuth dichalcogenide thin films into a metallic phase as in the bulk systems. For intermediate strains

the size of the gap in the topological phase can additionally be enhanced or reduced in this way. The Fermi velocity of the topologically protected states is reduced with tensile biaxial strain, while their penetration depth is enhanced with this kind of strain. Tensile biaxial strain can also empty the valence band and n–dope the topological surface states since the M–shaped feature of the valence band close to the surface $\bar{\Gamma}$ point becomes more pronounced with such strain. We provide table–like band dispersions for thin films of different thicknesses for the four compounds under biaxial strain as reference tables for experimentalists when growing one of these systems on a substrate. We characterise two topologically distinct Sb_2Te_3/Bi_2Te_3 heterojunctions, one in which both subsystems are TIs and another in which Sb_2Te_3 has been driven into a normal insulating (NI) regime by applying uniaxial tensile strain. In the TI–TI heterostructure with open Sb_2Te_3 surfaces, topological surface states are confined in the Sb_2Te_3 subsystem regardless of the Sb_2Te_3 thickness. In NI–TI superlattices the bulk–to–boundary correspondence is probed with a system different from vacuum that provides topologically protected interface states. These states in Sb_2Te_3/Bi_2Te_3 heterojunctions are topologically protected and, additionally, physically protected from adsorption of impurities, and can be created and annihilated by means of uniaxial strain.

5. Stacking Defects. Energy, symmetry and charge analysis of stacking faults and twin domain boundaries. Twin domain boundaries at vdW gaps exhibit the lowest formation energy among the studied stacking defects. They break inversion symmetry and preserve time–reversal symmetry, thus inducing a surface charge doping. Twin defects generate a spontaneous polarisation in the bulk that is correlated to the surface doping. We obtain the low frequency and ion–clamped relative permittivities of Bi_2Se_3 through first principles calculations, and the surface doping is obtained for several twinned slabs of different defect densities and thicknesses, showing that higher twin densities induce larger electron or hole surface dopings. We show that by inducing twin domain boundaries in a controlled way, thin films with tailored two–dimensional electron and hole gases can be fabricated. An analytical model for the pristine Bi_2Se_3 surface states is additionally derived and fitted to the DFT results. In addition, we show inversion–symmetric polytypes of Bi_2Se_3 with twin defects that can induce the formation of 2DEG and 2HEG in ferroelectric domain walls are also proposed, which can also serve to tune the position of the DP within the gap, diminishing the interaction with the valence bands and inducing a truly linear dispersion of the surface DCs without any charge doping.

6. Metallic Impurities and Overlayers. Cr impurities are energetically favourable at Bi–substitutional positions and exhibit long range ferromagnetic order in bulk Bi_2Se_3. The exchange coupling among Cr dopants is non–monotonic with the Cr–Cr distance and depends on the particular arrangement of the Cr atoms. Cr–doped thin films exhibit a gap in the surface state due to Cr–induced ferromagnetism. The effect is local and while the 2 QLs thin films remain insulating, for 4 QLs there is only a local gap in the surface state closest to the Cr impurities. Therefore, Cr–doped Bi_2Se_3 thin films can host the QAHE phase. The adsorption of one, two and three monolayers of Cr on the (111) Bi_2Se_3 surface triggers a double spin reorientation transition of the Cr overlayer that induces in the surface states a gap

opening, closing and reopening for coverages of 1, 2 and 3 Cr monolayers respectively. This in turn modifies the spin texture of the states, being of the circular meron kind for one and three Cr monolayer coverages and of the skyrmion kind for two Cr monolayers. Furthermore, the 2 Cr ML–Bi_2Se_3 thin films exhibit a highly anisotropic surface state dispersion relation around the Dirac point. The adsorption of Au, on the contrary, maintains the skyrmion character of the DCs regardless of the Au layer thickness, and induces a charge doping in the topological surface states.

7. BHZ Hamiltonian and AC Spin Sources. We describe the analytical BHZ model for 2D TIs including the effect of an external magnetic field and several additional terms (BIA, SIA, Zeeman). The model is regularised on a lattice in order to account for low dimensional effects at the edges. For small magnetic fields, the edge states are displaced laterally in momentum space, and at a critical magnetic field the bulk bands uninvert and the system is driven into a quantum Hall effect phase. In the former regime no gap is opened in the spectrum of the edge states unless an additional inversion–symmetry breaking perturbation is included. Two different AC spin current sources are proposed: one that requires no external magnetic field and another that requires experimentally available current–day technology and works under magnetic fields of less than 10 T. The electronic and spin structure of the latter is calculated employing realistic parameters for HgTe/CdTe and InAs/GaSb/AlSb quantum wells.

The present work displays several ways to tune a wide range of properties of the topological surface and interface states of time–reversal–invariant TIs, including charge doping, spin texture, Fermi velocity and effective mass. The effects of external magnetic fields or uniform strain fields are also discussed and explained, and we make various experimental proposals (surface doping due to twin boundaries, switchable topological interfaces states in Sb_2Te_3/Bi_2Te_3 heterojunctions, AC spin current sources) which can be of great interest from both a theoretical and an experimental point of view and may be of use in the rapidly emerging fields of straintronics and spintronics.

8.2 (ESP) RESUMEN Y CONCLUSIONES

Los aislantes topológicos son una nueva fase ordenada de la materia caracterizada por un invariante topológico, en lugar de por un parámetro de orden. En particular, los aislantes topológicos protegidos por simetría de inversión temporal se caracterizan por un invariante topológico del tipo $\mathbb{Z}_2$, y el origen físico de su topología no trivial es habitualmente el acoplo espín–órbita. Esta fase cuántica de la materia se da en diversos materiales tridimensionales y heteroestructuras bidimensionales, y está caracterizada por un volumen (superficie) aislante con superficies (bordes) metálicos al entrar en contacto con cualquier otro material aislante topológicamente trivial (incluído el vacío). Por lo tanto, es en sistemas de baja dimensionalidad y heteroestructuras, en las que las propiedades físicas más significativas están determinadas por sus superficies e intercaras, donde se manifiestan las inusuales características propias de esta nueva fase cuántica de la materia.

En esta tesis hemos estudiado efectos de baja dimensionalidad en aislantes topológicos 2D y 3D desde diversas perspectivas. Por un lado hemos investigado mediante cálculos *ab initio* sistemas bidimensionales de los dicalcogenuros de Bismuto Bi_2Te_3, Sb_2Te_3, Bi_2Se_3 y Sb_2Se_3, conocidos por ser aislantes topológicos tridimensionales. En concreto, hemos estudiado láminas delgadas y heteroestructuras de dichos materiales bajo distintas perturbaciones intrínsecas y extrínsecas, tales como tensiones, fallas de apilamiento o impurezas magnéticas. Por otro lado, hemos investigado el efecto de un campo magnético externo en heteroestructuras de aislantes topológicos bidimensionales basándonos en un modelo analítico fenomenológico, y hemos propuesto cómo generar corrientes alternas de espín a partir de dispositivos de aislantes topológicos.

Las principales conclusiones de este trabajo se resumen a continuación:

3. Propiedades de volumen y superficies de Bi_2Te_3, Sb_2Te_3, Bi_2Se_3, y Sb_2Se_3 a partir de cálculos *ab initio*. Se describen los diagramas de bandas y su caracterización topológica. Las superficies (111) muestran los conocidos estados de superficie topológicamente protegidos de tipo cono de Dirac. Presentamos la textura de espín de dichos estados, clasificándola como un *skyrmión* circular en el espacio recíproco. El momento de espín está anclado perpendicularmente al momento cristalino y el carácter helicoidal se hace patente en la textura de espín, mientras que se observa una oscilación con simetría trigonal en la componente S_z lejos del centro de la zona de Brillouin. En láminas ultradelgadas se abre un gap en el espectro de estados de superficie debido a la hibridación entre las superficies opuestas, y este gap depende del grosor de la lámina.

4. Tensión y heteroestructuras TI/TI. Obtenemos los diagramas de fase de los compuestos de la familia del Bi_2Se_3 en función de la deformación uniaxial y biaxial. Los cuatro compuestos se vuelven aislantes triviales mediante deformaciones uniaxiales extensivas, mientras que una deformación biaxial (tanto extensiva como compresiva) los lleva a una fase metálica. Analizamos la (des)inversión de las bandas p_z del Bi y Se en el punto Γ en función de la deformación uniaxial. Las láminas delgadas de estos dicalcogenuros de Bismuto también se vuelven metálicas para deformaciones biaxiales extensivas o compresivas de un $\sim 10\%$, al igual que los sistemas en volumen. Para deformaciones intermedias el tamaño del gap puede hacerse aumentar o disminuir de manera controlada en la fase topológica. La deformación biaxial extensiva reduce la velocidad de Fermi de los estados de superficie topológicamente protegidos, mientras que la longitud de penetración aumenta con dicha deformación. Otro efecto de este tipo de deformación es que la banda de valencia con forma de M alrededor de Γ se hace más pronunciada, llegando a vacíarse parcialmente y dopando con electrones los estados de superficie topológicos. Mostramos tablas de diagramas de dispersión de láminas delgadas de los cuatro compuestos bajo varias deformaciones biaxiales como tablas de referencia para grupos experimentales a la hora de crecer estas láminas en distintos sustratos. Caracterizamos dos heterouniones Sb_2Te_3/Bi_2Te_3 topológicamente distintas, una en la que ambos subsistemas son aislantes topológicos y otra en la que se ha comprimido uniaxialmente el Sb_2Te_3 hasta llevarlo a una fase aislante trivial. En la heteroestructura TI–TI con superficies de Sb_2Te_3 abiertas los estados de superficie se hallan confinados en el subsistema Sb_2Te_3 independientemente del grosor de éste. En superredes del tipo NI–TI se in-

vestiga la correspondencia volumen–frontera con un sistema trivial distinto al vacío, lo que da lugar a estados de intercara topológicamente protegidos. Estos estados están protegidos topológicamente y físicamente frente a impurezas, y pueden ser creados y destruidos por medio de una deformación uniaxial.

5. Defectos de Apilamiento. Análisis energético, de simetría y de carga de fallas de apilamiento y fronteras de dominios gemelos. De todos los defectos estudiados, las fronteras de dominios gemelos (*twin domain boundaries*) localizadas en los espaciados de vdW son las que presentan una energía menor. Éstas rompen la simetría de inversión espacial manteniendo la simetría de inversión temporal, induciendo por tanto una acumulación de carga superficial. Las fronteras de dominios gemelos generan una polarización espontánea en el seno del material que se relaciona con la carga superficial inducida. Obtenemos las permitividades estática y dinámica del Bi_2Se_3 mediante cálculos de primeros principios, y calculamos el valor del dopaje de los estados de superficie para diversas láminas delgadas de distintas densidades de defectos y grosores, mostrando que una mayor densidad de fronteras de dominios gemelos induce una carga superficial mayor, tanto de electrones como de huecos. Controlando la generación de fronteras de dominios gemelos se pueden fabricar láminas delgadas que alberguen gases bidimensionales de electrones y huecos con la carga deseada. También derivamos un modelo analítico para los estados de superficie ideales del Bi_2Se_3 y lo ajustamos a los resultados obtenidos con DFT. Además, proponemos una serie de politipos de Bi_2Se_3 con fronteras de dominios gemelos que mantienen la simetría de inversión global, y que pueden albergar gases bidimensionales de electrones o huecos en paredes de dominio ferroeléctricas. Estos politipos también pueden ser utilizados para situar el punto de Dirac a la energía deseada dentro del gap, lo que permite disminuir la interacción con las bandas de valencia y así conseguir una dispersión realmente lineal sin inducir cargas en la superficie.

6. Impurezas y Recubrimientos metálicos. Las impurezas de Cr son energéticamente favorables en posiciones sustitucionales de Bi, y muestran orden ferromagnético de largo alcance en el volumen de Bi_2Se_3. El canje entre las impurezas no es monótono frente a la distancia entre ellas, y depende de la disposición de los átomos de cromo en el cristal. Las láminas delgadas de Bi_2Se_3 dopadas con Cr sólo muestran un gap en el estado de superficie debido al magnetismo inducido por el Cr. Este efecto es local, y, mientras que las láminas de 2 QLs de grosor son aislantes, las de 4 QLs muestran un gap *local* en los estados de la superficie más cercana a las impurezas. Por lo tanto, las láminas delgadas de Bi_2Se_3 dopadas con Cr pueden albergar la fase QAHE. El recubrimiento de la superficie (111) de Bi_2Se_3 con una, dos y tres monocapas de Cr induce una doble transición de reorientación de espín en la capa de Cr, que a su vez abre, cierra y vuelve a abrir el gap en el estado de superficie para recubrimientos de 1, 2 y 3 monocapas respectivamente. Esta doble transición de espín también origina una doble transición en la textura de espín del estado de superficie, que pasa a ser del tipo *merón* circular para recubrimientos de Cr de 1 y 3 monocapas, y del tipo *skyrmión* circular para 2 monocapas de Cr. Además, la dispersión del estado de superficie en láminas delgadas de Bi_2Se_3 con 2 monocapas de Cr es altamente anisotrópica alrededor del punto de Dirac. Por el contrario, el recubrimiento con Au mantiene el carácter *skyrmiónico* del cono de Dirac

independientemente del grosor de dicho recubrimiento, e induce un dopaje en los estados de superficie.

7. Hamiltoniano BHZ y fuentes AC de espín. Se describe el modelo analítico BHZ para aislantes topológicos bidimensionales, incluyendo los efectos de un campo magnético perpendicular y varios términos adicionales (BIA, SIA, Zeeman). Se regulariza el modelo sobre una red discreta para poder tratar los efectos de baja dimensionalidad de los bordes. Para campos magnéticos pequeños, los estados de borde se desplazan lateralmente en el espacio recíproco, y para un cierto campo magnético crítico las bandas volúmicas se desinvierten y el sistema pasa a una fase de efecto Hall cuántico. En el primero de estos regímenes no se abre un gap en los estados de borde hasta que no se rompe adicionalmente la simetría de inversión. Se proponen dos dispositivos generadores de una corriente AC puramente de espín: uno que no requiere de un campo magnético externo y otro que puede ser fabricado con la tecnología actualmente disponible y funciona bajo campos magnéticos menores a 10 T. Calculamos la estructura electrónica y de espín de este último dispositivo con parámetros realistas de pozos cuánticos de HgTe/CdTe e InAs/GaSb/AlSb.

Este trabajo muestra varias formas de modificar, controlar y ajustar diversas propiedades físicas de los estados topológicos de superficie e intercara de aislantes topológicos protegidos por simetría de inversión temporal, entre las que se incluyen la carga, la textura de espín, la velocidad de Fermi o la masa efectiva. También investigamos y explicamos los efectos de campos magnéticos y de deformación, y hacemos varias propuestas experimentales (dopaje superficial de carga con fronteras de dominios gemelos, estados de intercara topológicos conmutables en intercaras de Sb_2Te_3/Bi_2Te_3, generadores de corriente AC de espín) que pueden ser de gran interés tanto desde un punto de vista teórico como experimental, y pueden resultar de utilidad en campos emergentes como la *tensiónica* y la *espintrónica*.

BIBLIOGRAPHY

[1] V. L. Ginzburg and L. D. Landau. *Zh. Eksp. Teor. Fiz.*, 20:1064, 1950. (Cited on page 1.)

[2] K. v. Klitzing, G. Dorda, and M. Pepper. New Method for High-Accuracy Determination of the Fine-Structure Constant Based on Quantized Hall Resistance. *Phys. Rev. Lett.*, 45:494–497, Aug 1980. (Cited on page 1.)

[3] D. J. Thouless, M. Kohmoto, M. P. Nightingale, and M. den Nijs. Quantized Hall Conductance in a Two-Dimensional Periodic Potential. *Phys. Rev. Lett.*, 49:405–408, Aug 1982. (Cited on page 1.)

[4] C. L. Kane and E. J. Mele. Quantum Spin Hall Effect in Graphene. *Phys. Rev. Lett.*, 95:226801, Nov 2005. (Cited on page 2.)

[5] B. Andrei Bernevig, Taylor L. Hughes, and Shou-Cheng Zhang. Quantum Spin Hall Effect and Topological Phase Transition in HgTe Quantum Wells. *Science*, 314(5806):1757–1761, 2006. (Cited on pages 2, 18, and 93.)

[6] M. König, S. Wiedmann, C. Brüne, A. Roth, H. Buhmann, L. W. Molenkamp, X.-L. Qi, and S.-C. Zhang. Quantum Spin Hall Insulator State in HgTe Quantum Wells. *Science*, 318(5851):766, 2007. (Cited on page 2.)

[7] Haijun Zhang, Chao-Xing Liu, Xiao-Liang Qi, Xi Dai, Zhong Fang, and Shou-Cheng Zhang. Topological insulators in Bi_2Se_3, Bi_2Te_3 and Sb_2Te_3 with a single Dirac cone on the surface. *Nature Physics*, 5(6): 438–442, 2009. (Cited on pages 2, 15, 19, 23, and 40.)

[8] David Hsieh, Dong Qian, Lewis Wray, YuQi Xia, Yew San Hor, R. J. Cava, and M. Zahid Hasan. A topological Dirac insulator in a quantum spin Hall phase. *Nature*, 452(7190):970–974, 2008. (Cited on pages 2 and 18.)

[9] Y. Xia, Dong Qian, David Hsieh, L. Wray, A. Pal, Hsin Lin, Arun Bansil, D. H. Y. S. Grauer, Y. S. Hor, R. J. Cava, et al. Observation of a large-gap topological-insulator class with a single Dirac cone on the surface. *Nature Physics*, 5(6):398–402, 2009. (Cited on page 2.)

[10] Liang Fu. Topological Crystalline Insulators. *Phys. Rev. Lett.*, 106: 106802, Mar 2011. (Cited on page 2.)

[11] Xiao-Liang Qi and Shou-Cheng Zhang. Topological insulators and superconductors. *Rev. Mod. Phys.*, 83:1057–1110, Oct 2011. (Cited on pages 2, 93, 98, 99, 100, and 106.)

[12] Hongming Weng, Chen Fang, Zhong Fang, B. Andrei Bernevig, and Xi Dai. Weyl Semimetal Phase in Noncentrosymmetric Transition-Metal Monophosphides. *Phys. Rev. X*, 5:011029, Mar 2015. (Cited on page 2.)

[13] Zheng Wang, Yidong Chong, J. D. Joannopoulos, and Marin Soljačić. Observation of unidirectional backscattering-immune topological electromagnetic states. *Nature*, 461(7265):772–775, 2009. (Cited on page 2.)

[14] B. Seradjeh, J. E. Moore, and M. Franz. Exciton Condensation and Charge Fractionalization in a Topological Insulator Film. *Phys. Rev. Lett.*, 103:066402, Aug 2009. (Cited on page 3.)

[15] Liang Fu and C. L. Kane. Superconducting Proximity Effect and Majorana Fermions at the Surface of a Topological Insulator. *Phys. Rev. Lett.*, 100:096407, Mar 2008. (Cited on page 3.)

[16] Anindya Das, Yuval Ronen, Yonatan Most, Yuval Oreg, Moty Heiblum, and Hadas Shtrikman. Zero-bias peaks and splitting in an Al-InAs nanowire topological superconductor as a signature of Majorana fermions. *Nature Physics*, 8(12):887–895, 2012. (Cited on page 3.)

[17] Xiao-Liang Qi, Taylor L. Hughes, and Shou-Cheng Zhang. Topological field theory of time-reversal invariant insulators. *Phys. Rev. B*, 78: 195424, Nov 2008. (Cited on pages 3 and 80.)

[18] Andrew M. Essin, Joel E. Moore, and David Vanderbilt. Magnetoelectric Polarizability and Axion Electrodynamics in Crystalline Insulators. *Phys. Rev. Lett.*, 102:146805, Apr 2009. (Cited on pages 3 and 80.)

[19] Rui Yu, Wei Zhang, Hai-Jun Zhang, Shou-Cheng Zhang, Xi Dai, and Zhong Fang. Quantized anomalous Hall effect in magnetic topological insulators. *Science*, 329(5987):61–64, 2010. (Cited on page 3.)

[20] Cui-Zu Chang, Jinsong Zhang, Xiao Feng, Jie Shen, Zuocheng Zhang, Minghua Guo, Kang Li, Yunbo Ou, Pang Wei, Li-Li Wang, et al. Experimental observation of the quantum anomalous Hall effect in a magnetic topological insulator. *Science*, 340(6129):167–170, 2013. (Cited on pages 3 and 75.)

[21] M Zahid Hasan and Charles L Kane. Colloquium: topological insulators. *Reviews of Modern Physics*, 82(4):3045, 2010. (Cited on pages 3 and 24.)

[22] Max Born and Robert Oppenheimer. Zur quantentheorie der molekeln. *Annalen der Physik*, 389(20):457–484, 1927. (Cited on page 6.)

[23] J. C. Slater. The Theory of Complex Spectra. *Phys. Rev.*, 34:1293–1322, Nov 1929. (Cited on page 6.)

[24] D. M. Ceperley and B. J. Alder. Ground State of the Electron Gas by a Stochastic Method. *Phys. Rev. Lett.*, 45:566–569, Aug 1980. (Cited on page 8.)

[25] J. P. Perdew and Alex Zunger. Self-interaction correction to density-functional approximations for many-electron systems. *Phys. Rev. B*, 23:5048–5079, May 1981. (Cited on page 8.)

[26] Chengteh Lee, Weitao Yang, and Robert G. Parr. Development of the Colle-Salvetti correlation-energy formula into a functional of the electron density. *Phys. Rev. B*, 37:785–789, Jan 1988. (Cited on page 8.)

[27] John P. Perdew, Kieron Burke, and Matthias Ernzerhof. Generalized Gradient Approximation Made Simple. *Phys. Rev. Lett.*, 77:3865–3868, Oct 1996. (Cited on pages 8, 9, and 14.)

[28] John P. Perdew, Stefan Kurth, Aleš Zupan, and Peter Blaha. Accurate Density Functional with Correct Formal Properties: A Step Beyond the Generalized Gradient Approximation. *Phys. Rev. Lett.*, 82:2544–2547, Mar 1999. (Cited on page 8.)

[29] S. Grimme. Semiempirical GGA-type density functional constructed with a long-range dispersion correction. *Journal of computational chemistry*, 27(15):1787–1799, 2006. (Cited on pages 9 and 14.)

[30] F. Ortmann, F. Bechstedt, and W. G. Schmidt. Semiempirical van der Waals correction to the density functional description of solids and molecular structures. *Phys. Rev. B*, 73:205101, May 2006. (Cited on page 9.)

[31] N. Troullier and José Luís Martins. Efficient pseudopotentials for plane-wave calculations. *Phys. Rev. B*, 43:1993–2006, Jan 1991. (Cited on page 10.)

[32] D. R. Hamann, M. Schlüter, and C. Chiang. Norm-Conserving Pseudopotentials. *Phys. Rev. Lett.*, 43:1494–1497, Nov 1979. (Cited on page 10.)

[33] G. P. Kerker. Non-singular atomic pseudopotentials for solid state applications. *Journal of Physics C: Solid State Physics*, 13(9):L189, 1980. (Cited on page 10.)

[34] David Vanderbilt. Optimally smooth norm-conserving pseudopotentials. *Phys. Rev. B*, 32:8412–8415, Dec 1985. (Cited on page 10.)

[35] José M Soler, Emilio Artacho, Julian D Gale, Alberto García, Javier Junquera, Pablo Ordejón, and Daniel Sánchez-Portal. The SIESTA method for *ab initio* order-N materials simulation. *Journal of Physics: Condensed Matter*, 14(11):2745, 2002. (Cited on pages 10, 12, 13, 14, and 51.)

[36] R. Cuadrado and J. I. Cerdá. Fully relativistic pseudopotential formalism under an atomic orbital basis: spin-orbit splittings and magnetic anisotropies. *Journal of Physics: Condensed Matter*, 24(8):086005, 2012. (Cited on pages 10, 11, and 12.)

[37] David Vanderbilt. Soft self-consistent pseudopotentials in a generalized eigenvalue formalism. *Phys. Rev. B*, 41:7892–7895, Apr 1990. (Cited on page 10.)

[38] R. J. Elliott. Theory of the Effect of Spin-Orbit Coupling on Magnetic Resonance in Some Semiconductors. *Phys. Rev.*, 96:266–279, Oct 1954. (Cited on page 10.)

[39] Yoon-Suk Kim, Kerstin Hummer, and Georg Kresse. Accurate band structures and effective masses for InP, InAs, and InSb using hybrid functionals. *Phys. Rev. B*, 80:035203, Jul 2009. (Cited on page 11.)

[40] L. A. Hemstreet, C. Y. Fong, and J. S. Nelson. First-principles calculations of spin-orbit splittings in solids using nonlocal separable pseudopotentials. *Phys. Rev. B*, 47:4238–4243, Feb 1993. (Cited on page 11.)

[41] J. I. Cerdá, M. A. Van Hove, P. Sautet, and M. Salmeron. Efficient method for the simulation of STM images. I. Generalized Green-function formalism. *Phys. Rev. B*, 56:15885–15899, Dec 1997. (Cited on pages 12, 14, and 51.)

[42] G. Kresse and J. Hafner. *ab initio* molecular dynamics for open-shell transition metals. *Phys. Rev. B*, 48:13115–13118, Nov 1993. (Cited on page 13.)

[43] G. Kresse and J. Furthmüller. Efficiency of *ab-initio* total energy calculations for metals and semiconductors using a plane-wave basis set. *Computational Materials Science*, 6(1):15–50, 1996. (Cited on page 13.)

[44] P. E. Blöchl. Projector augmented-wave method. *Phys. Rev. B*, 50: 17953–17979, Dec 1994. (Cited on page 13.)

[45] G. Kresse and D. Joubert. From ultrasoft pseudopotentials to the projector augmented-wave method. *Phys. Rev. B*, 59:1758–1775, Jan 1999. (Cited on page 13.)

[46] Carsten Rostgaard. The projector augmented-wave method. *arXiv preprint:0910.1921*, 2009. (Cited on page 13.)

[47] Ralph Walter Graystone Wyckoff. *Crystal structures*, volume 2. New York: Wiley, 1964. (Cited on page 18.)

[48] Chaoxing Liu, Taylor L. Hughes, Xiao-Liang Qi, Kang Wang, and Shou-Cheng Zhang. Quantum Spin Hall Effect in Inverted Type-II Semiconductors. *Phys. Rev. Lett.*, 100:236601, Jun 2008. (Cited on pages 18, 93, and 97.)

[49] Ivan Knez, Rui-Rui Du, and Gerard Sullivan. Evidence for Helical Edge Modes in Inverted InAs/GaSb Quantum Wells. *Phys. Rev. Lett.*, 107:136603, Sep 2011. (Cited on pages 18 and 93.)

[50] K. Kuroda, H. Miyahara, M. Ye, S. V. Eremeev, Yu. M. Koroteev, E. E. Krasovskii, E. V. Chulkov, S. Hiramoto, C. Moriyoshi, Y. Kuroiwa, K. Miyamoto, T. Okuda, M. Arita, K. Shimada, H. Namatame, M. Taniguchi, Y. Ueda, and A. Kimura. Experimental Verification of $PbBi_2Te_4$ as a 3D Topological Insulator. *Phys. Rev. Lett.*, 108:206803, May 2012. (Cited on page 18.)

[51] Binghai Yan, Chao-Xing Liu, Hai-Jun Zhang, Chi-Yung Yam, Xiao-Liang Qi, Thomas Frauenheim, and Shou-Cheng Zhang. Theoretical prediction of topological insulators in thallium-based III-V-VI_2 ternary chalcogenides. *EPL (Europhysics Letters)*, 90(3):37002, 2010. (Cited on page 18.)

[52] Y. L. Chen, Z. K. Liu, J. G. Analytis, J.-H. Chu, H. J. Zhang, B. H. Yan, S.-K. Mo, R. G. Moore, D. H. Lu, I. R. Fisher, S. C. Zhang, Z. Hussain, and Z.-X. Shen. Single Dirac Cone Topological Surface State and Unusual Thermoelectric Property of Compounds from a New Topological Insulator Family. *Phys. Rev. Lett.*, 105:266401, Dec 2010. (Cited on page 18.)

[53] Ilias Efthimiopoulos, Jiaming Zhang, Melvin Kucway, Changyong Park, Rodney C. Ewing, and Yuejian Wang. Sb_2Se_3 under pressure. *Scientific reports*, 3, 2013. (Cited on page 19.)

[54] Byungki Ryu, Min-Wook Oh, Bong-Seo Kim, Ji Eun Lee, Sung-Jae Joo, Bok-Ki Min, HeeWoong Lee, and Sudong Park. Prediction of Band Structure of Bi_2Te_3-related Binary and Ternary Thermoelectric Materials. *arXiv preprint:1506.01592*, 2015. (Cited on pages 19, 22, and 24.)

[55] Andreas P. Schnyder, Shinsei Ryu, Akira Furusaki, and Andreas W. W. Ludwig. Classification of topological insulators and superconductors in three spatial dimensions. *Phys. Rev. B*, 78:195125, Nov 2008. (Cited on page 19.)

[56] Liang Fu, C. L. Kane, and E. J. Mele. Topological Insulators in Three Dimensions. *Phys. Rev. Lett.*, 98:106803, Mar 2007. (Cited on page 23.)

[57] Rahul Roy. Topological phases and the quantum spin Hall effect in three dimensions. *Phys. Rev. B*, 79:195322, May 2009. (Cited on page 23.)

[58] C. L. Kane and E. J. Mele. Z_2 Topological Order and the Quantum Spin Hall Effect. *Phys. Rev. Lett.*, 95:146802, Sep 2005. (Cited on page 23.)

[59] C. L. Kane and E. J. Mele. Z_2 Topological Order and the Quantum Spin Hall Effect. *Phys. Rev. Lett.*, 95:146802, Sep 2005. (Cited on pages 23 and 24.)

[60] J. Black, E. M. Conwell, L. Seigle, and C. W. Spencer. Electrical and optical properties of some $M_2^{V-B}N_3^{VI-B}$ semiconductors. *Journal of Physics and Chemistry of Solids*, 2(3):240–251, 1957. (Cited on page 22.)

[61] B. M. Goltsman, V. A. Kudinov, and I. A. Smirnov. Semiconductor thermoelectric materials on the basis of Bi_2Te_3, 1972. (Cited on page 22.)

[62] Davidenko V. A. *J. Phys. (USSR)*, 4:170, 1941. (Cited on page 22.)

[63] Konorov P. P. *Zh. Tekh. Fiz.*, 26:394, 1956. (Cited on page 22.)

[64] G. R. Hyde, H. A. Beale, I. L. Spain, and J. A. Woollam. Electronic properties of Bi_2Se_3 crystals. *Journal of Physics and Chemistry of Solids*, 35(12):1719–1728, 1974. (Cited on page 22.)

[65] J. G. Checkelsky, Y. S. Hor, R. J. Cava, and N. P. Ong. Bulk Band Gap and Surface State Conduction Observed in Voltage-Tuned Crystals of the Topological Insulator Bi_2Se_3. *Phys. Rev. Lett.*, 106:196801, May 2011. (Cited on page 22.)

[66] I. A. Nechaev, R. C. Hatch, M. Bianchi, D. Guan, C. Friedrich, I. Aguilera, J. L. Mi, B. B. Iversen, S. Blügel, Ph. Hofmann, and E. V. Chulkov. Evidence for a direct band gap in the topological insulator Bi_2Se_3 from theory and experiment. *Phys. Rev. B*, 87:121111, Mar 2013. (Cited on page 22.)

[67] Landolt-Börnstein. *Numerical Data and Functional Relationships in Science and Technology*, volume New Series, Group III Vol. 17. O. Madelung, M. Schulz, and H. Weiss. Springer, New York, 1938. (Cited on page 22.)

[68] Che-Yu Li, A. L. Ruoff, and C. W. Spencer. Effect of Pressure on the Energy Gap of Bi_2Te_3. *Journal of Applied Physics*, 32(9):1733–1735, 1961. (Cited on page 22.)

[69] I. G. Austin. The Optical Properties of Bismuth Telluride. *Proceedings of the Physical Society*, 72(4):545, 1958. (Cited on page 22.)

[70] S. K. Mishra, S. Satpathy, and O. Jepsen. Electronic structure and thermoelectric properties of bismuth telluride and bismuth selenide. *Journal of Physics: Condensed Matter*, 9(2):461, 1997. (Cited on page 22.)

[71] C. B. Satterthwaite and R. W. Ure. Electrical and Thermal Properties of Bi_2Te_3. *Phys. Rev.*, 108:1164–1170, Dec 1957. (Cited on page 22.)

[72] G. A. Thomas, D. H. Rapkine, R. B. Van Dover, L. F. Mattheiss, W. A. Sunder, L. F. Schneemeyer, and J. V. Waszczak. Large electronic-density increase on cooling a layered metal: Doped Bi_2Te_3. *Phys. Rev. B*, 46:1553–1556, Jul 1992. (Cited on page 22.)

[73] R. Sehr and L. R. Testardi. The optical properties of p-type Bi_2Te_3-Sb_2Te_3 alloys between 2–15 microns. *Journal of Physics and Chemistry of Solids*, 23(9):1219–1224, 1962. (Cited on page 22.)

[74] E. Mooser and W. B. Pearson. New Semiconducting Compounds. *Phys. Rev.*, 101:492–493, Jan 1956. (Cited on page 22.)

[75] Zhiyong Zhu, Yingchun Cheng, and Udo Schwingenschlögl. Band inversion mechanism in topological insulators: A guideline for materials design. *Phys. Rev. B*, 85:235401, Jun 2012. (Cited on page 24.)

[76] Yi Zhang, Ke He, Cui-Zu Chang, Can-Li Song, Li-Li Wang, Xi Chen, Jin-Feng Jia, Zhong Fang, Xi Dai, Wen-Yu Shan, et al. Crossover of the three-dimensional topological insulator Bi_2Se_3 to the two-dimensional limit. *Nature Physics*, 6(8):584–588, 2010. (Cited on page 24.)

[77] Z.-H. Zhu, G. Levy, B. Ludbrook, C. N. Veenstra, J. A. Rosen, R. Comin, D. Wong, P. Dosanjh, A. Ubaldini, P. Syers, N. P. Butch, J. Paglione, I. S. Elfimov, and A. Damascelli. Rashba Spin-Splitting Control at the Surface of the Topological Insulator Bi_2Se_3. *Phys. Rev. Lett.*, 107:186405, Oct 2011. (Cited on page 25.)

[78] J. L. Pérez-Díaz and M. C. Muñoz. Quantum-well states in metallic-thin-film overlayers. *Phys. Rev. B*, 53:13583–13593, May 1996. (Cited on page 25.)

[79] J. L. Pérez-Díaz and M. C. Muñoz. Symmetry dependence of quantum-well states in thin metallic overlayers. *Journal of Magnetism and Magnetic Materials*, 156:165 – 166, 1996. (Cited on page 25.)

[80] Susmita Basak, Hsin Lin, L. A. Wray, S.-Y. Xu, L. Fu, M. Z. Hasan, and A. Bansil. Spin texture on the warped Dirac-cone surface states in topological insulators. *Phys. Rev. B*, 84:121401, Sep 2011. (Cited on pages 25 and 61.)

[81] Kuntal Roy, Supriyo Bandyopadhyay, and Jayasimha Atulasimha. Hybrid spintronics and straintronics: A magnetic technology for ultra low energy computing and signal processing. *Applied Physics Letters*, 99 (6):063108, 2011. (Cited on page 29.)

[82] María A. H. Vozmediano, M. I. Katsnelson, and Francisco Guinea. Gauge fields in graphene. *Physics Reports*, 496(4):109–148, 2010. (Cited on page 29.)

[83] F. Guinea, M. I. Katsnelson, and A. K. Geim. Energy gaps and a zero-field quantum Hall effect in graphene by strain engineering. *Nature Physics*, 6(1):30–33, 2010. (Cited on page 29.)

[84] Wenliang Liu, Xiangyang Peng, Chao Tang, Lizhong Sun, Kaiwang Zhang, and Jianxin Zhong. Anisotropic interactions and strain-induced topological phase transition in Sb_2Se_3 and Bi_2Se_3. *Phys. Rev. B*, 84:245105, Dec 2011. (Cited on pages 29 and 31.)

[85] Y. Liu, Y. Y. Li, S. Rajput, D. Gilks, L. Lari, P. L. Galindo, M. Weinert, V. K. Lazarov, and L. Li. Tuning Dirac states by strain in the topological insulator Bi_2Se_3. *Nature Physics*, 10(4):294–299, 2014. (Cited on pages 31 and 33.)

[86] Steve M. Young, Sugata Chowdhury, Eric J. Walter, Eugene J. Mele, Charles L. Kane, and Andrew M. Rappe. Theoretical investigation of the evolution of the topological phase of Bi_2Se_3 under mechanical strain. *Phys. Rev. B*, 84:085106, Aug 2011. (Cited on page 31.)

[87] Xin Luo, Michael B. Sullivan, and Su Ying Quek. First-principles investigations of the atomic, electronic, and thermoelectric properties

of equilibrium and strained Bi_2Se_3 and Bi_2Te_3 including van der Waals interactions. *Phys. Rev. B*, 86:184111, Nov 2012. (Cited on page 31.)

[88] Y. V. Lysogorskiy, A. G. Kijamov, O. V. Nedopekin, and D. A. Tayurskii. Ab initio studying of topological insulator Bi_2Se_3 under the stress. *Journal of Physics: Conference Series*, 394(1):012022, 2012. (Cited on page 31.)

[89] Junwei Liu, Yong Xu, Jian Wu, Bing-Lin Gu, S. B. Zhang, and Wenhui Duan. Manipulating topological phase transition by strain. *Acta Crystallographica Section C*, 70(2):118–122, Feb 2014. (Cited on page 31.)

[90] L. Zhao, Junwei Liu, Peizhe Tang, and Wenhui Duan. Design of strain-engineered quantum tunneling devices for topological surface states. *Applied Physics Letters*, 100(13):131602, 2012. (Cited on pages 31 and 33.)

[91] Linus Pauling. The nature of the chemical bond. IV. the energy of single bonds and the relative electronegativity of atoms. *Journal of the American Chemical Society*, 54(9):3570–3582, 1932. (Cited on page 39.)

[92] Leland C. Allen. Electronegativity is the average one-electron energy of the valence-shell electrons in ground-state free atoms. *Journal of the American Chemical Society*, 111(25):9003–9014, 1989. (Cited on page 39.)

[93] Kristie J. Koski, Colin D. Wessells, Bryan W. Reed, Judy J. Cha, Desheng Kong, and Yi Cui. Chemical Intercalation of Zerovalent Metals into 2D Layered Bi_2Se_3 Nanoribbons. *Journal of the American Chemical Society*, 134(33):13773–13779, 2012. (Cited on page 41.)

[94] Qianfan Zhang, Zhiyong Zhang, Zhiyong Zhu, Udo Schwingenschlögl, and Yi Cui. Exotic Topological Insulator States and Topological Phase Transitions in Sb_2Se_3–Bi_2Se_3 Heterostructures. *ACS nano*, 6(3):2345–2352, 2012. (Cited on page 43.)

[95] V. N. Men'shov, V. V. Tugushev, T. V. Menshchikova, S. V. Eremeev, P. M. Echenique, and E. V. Chulkov. Modelling near-surface bound electron states in a 3D topological insulator: analytical and numerical approaches. *Journal of Physics: Condensed Matter*, 26(48):485003, 2014. (Cited on page 43.)

[96] Guillermo López-Polín, Cristina Gómez-Navarro, Vincenzo Parente, Francisco Guinea, Mikhail I. Katsnelson, Francesc Pérez-Murano, and Julio Gómez-Herrero. Increasing the elastic modulus of graphene by controlled defect creation. *Nature Physics*, 11(1):26–31, 2015. (Cited on page 49.)

[97] D. L. Medlin and N. Y. C. Yang. Interfacial Step Structure at a (0001) Basal Twin in Bi_2Te_3. *Journal of electronic materials*, 41(6):1456–1464, 2012. (Cited on page 49.)

[98] D. L. Medlin, Q. M. Ramasse, C. D. Spataru, and N. Y. C. Yang. Structure of the (0001) basal twin boundary in Bi_2Te_3. *Journal of Applied Physics*, 108(4):043517–043517, 2010. (Cited on pages 49 and 52.)

[99] H. D. Li, Z. Y. Wang, X. Kan, X. Guo, H. T. He, Z. Wang, J. N. Wang, T. L. Wong, N. Wang, and M. H. Xie. The van der Waals epitaxy of Bi_2Se_3 on the vicinal Si (111) surface: an approach for preparing high-quality thin films of a topological insulator. *New Journal of Physics*, 12(10):103038, 2010. (Cited on page 49.)

[100] Bhakti Jariwala and D. V. Shah. Stacking fault in Bi_2Te_3 and Sb_2Te_3 single crystals. *Journal of Crystal Growth*, 318(1):1179–1183, 2011. (Cited on page 49.)

[101] Xie Mao-Hai, Guo Xin, Xu Zhong-Jie, and Ho Wing-Kin. Molecular-beam epitaxy of topological insulator Bi_2Se_3 (111) and (221) thin films. *Chinese Physics B*, 22(6):068101, 2013. (Cited on page 49.)

[102] Ho Sun Shin, Seong Gi Jeon, Jin Yu, Yong-Sung Kim, Hyun Min Park, and Jae Yong Song. Twin-driven thermoelectric figure-of-merit enhancement of Bi_2Te_3 nanowires. *Nanoscale*, 6(11):6158–6165, 2014. (Cited on page 49.)

[103] N. V. Tarakina, S. Schreyeck, M. Luysberg, S. Grauer, C. Schumacher, G. Karczewski, K. Brunner, C. Gould, H. Buhmann, R. E. Dunin-Borkowski, and L. W. Molenkamp. Suppressing Twin Formation in Bi_2Se_3 Thin Films. *Advanced Materials Interfaces*, 1(5):1400134, 2014. (Cited on page 49.)

[104] J. A. Venables. The electron microscopy of deformation twinning. *Journal of Physics and Chemistry of Solids*, 25(7):685 – 692, 1964. (Cited on page 51.)

[105] E. T. R. Rossen, C. F. J. Flipse, and J. I. Cerdá. Lowest order in inelastic tunneling approximation: Efficient scheme for simulation of inelastic electron tunneling data. *Phys. Rev. B*, 87:235412, Jun 2013. (Cited on page 51.)

[106] L. Fu, E. Yaschenko, L. Resca, and R. Resta. Hartree-Fock studies of surface properties of $BaTiO_3$. *Phys. Rev. B*, 60:2697–2703, Jul 1999. (Cited on page 56.)

[107] R. D. King-Smith and David Vanderbilt. Theory of polarization of crystalline solids. *Phys. Rev. B*, 47:1651–1654, Jan 1993. (Cited on pages 56 and 58.)

[108] M. Stordeur, K. K. Ketavong, A. Priemuth, H. Sobotta, and V. Riede. Optical and Electrical Investigations of n-Type Bi_2Se_3 Single Crystals. *Physica Status Solidi (b)*, 169(2):505–514, 1992. (Cited on page 57.)

[109] H. Gobrecht, S. Seeck, and T. Klose. Der Einfluß der freien Ladungsträger auf die optischen Konstanten des Bi_2Se_3 im Wellenlängengebiet von 2 bis 23 μm. *Zeitschrift für Physik*, 190(4):427–443, 1966. (Cited on page 57.)

[110] L. Tichý and J. Horák. Nonparabolicity of the conduction band and anisotropy of the electron effective mass in Bi_2Se_3 single crystals. *Phys. Rev. B*, 19:1126–1131, Jan 1979. (Cited on page 57.)

[111] W. Richter and C. R. Becker. A Raman and far-infrared investigation of phonons in the rhombohedral V_2-VI_3 compounds Bi_2Te_3, Bi_2Se_3, Sb_2Te_3 and $Bi_2(Te_{1-x}Se_x)_3$ $(0 < x < 1)$, $(Bi_{1-y}Sb_y)_2Te_3$ $(0 < y < 1)$. *Physica Status Solidi (b)*, 84(2):619–628, 1977. (Cited on page 57.)

[112] Nicola A. Hill. Why Are There so Few Magnetic Ferroelectrics? *Journal of Physical Chemistry B*, 104(29):6694–6709, 2000. (Cited on page 56.)

[113] Samir Mammadov, Jürgen Ristein, Roland J. Koch, Markus Ostler, Christian Raidel, Martina Wanke, Remigijus Vasiliauskas, Rositza Yakimova, and Thomas Seyller. Polarization doping of graphene on silicon carbide. *2D Materials*, 1(3):035003, 2014. (Cited on page 58.)

[114] L. Seixas, L. B. Abdalla, T. M. Schmidt, A. Fazzio, and R. H. Miwa. Topological states ruled by stacking faults in Bi_2Se_3 and Bi_2Te_3. *Journal of Applied Physics*, 113(2):023705–023705–4, 2013. (Cited on page 60.)

[115] Chao-Xing Liu, Xiao-Liang Qi, HaiJun Zhang, Xi Dai, Zhong Fang, and Shou-Cheng Zhang. Model Hamiltonian for topological insulators. *Phys. Rev. B*, 82:045122, Jul 2010. (Cited on page 61.)

[116] K. Kuroda, M. Arita, K. Miyamoto, M. Ye, J. Jiang, A. Kimura, E. E. Krasovskii, E. V. Chulkov, H. Iwasawa, T. Okuda, K. Shimada, Y. Ueda, H. Namatame, and M. Taniguchi. Hexagonally Deformed Fermi Surface of the 3D Topological Insulator Bi_2Se_3. *Phys. Rev. Lett.*, 105:076802, Aug 2010. (Cited on page 61.)

[117] Zhanybek Alpichshev, J. G. Analytis, J.-H. Chu, I. R. Fisher, Y. L. Chen, Z. X. Shen, A. Fang, and A. Kapitulnik. STM Imaging of Electronic Waves on the Surface of Bi_2Se_3: Topologically Protected Surface States and Hexagonal Warping Effects. *Phys. Rev. Lett.*, 104: 016401, Jan 2010. (Cited on page 61.)

[118] Wei Qin and Zhenyu Zhang. Persistent Ferromagnetism and Topological Phase Transition at the Interface of a Superconductor and a Topological Insulator. *Phys. Rev. Lett.*, 113:266806, Dec 2014. (Cited on page 75.)

[119] Wenqing Liu, Liang He, Yongbing Xu, Koichi Murata, Mehmet C. Onbasli, Murong Lang, Nick J. Maltby, Shunpu Li, Xuefeng Wang, Caroline A. Ross, Peter Bencok, Gerrit van der Laan, Rong Zhang, and Kang. L. Wang. Enhancing Magnetic Ordering in Cr-Doped Bi_2Se_3 Using High-T_C Ferrimagnetic Insulator. *Nano Letters*, 15(1):764–769, 2015. (Cited on page 75.)

[120] P. P. J. Haazen, J.-B. Laloë, T. J. Nummy, H. J. M. Swagten, P. Jarillo-Herrero, D. Heiman, and J. S. Moodera. Ferromagnetism in thin-film Cr-doped topological insulator Bi_2Se_3. *Applied Physics Letters*, 100 (8):082404, 2012. (Cited on page 75.)

[121] Xufeng Kou, Yabin Fan, Murong Lang, Pramey Upadhyaya, and Kang L. Wang. Magnetic topological insulators and quantum anomalous hall effect. *Solid State Communications*, 215–216:34 – 53, 2015. (Cited on page 75.)

[122] Cui-Zu Chang, Peng Wei, and Jagadeesh S. Moodera. Breaking time reversal symmetry in topological insulators. *MRS Bulletin*, 39:867–872, 10 2014. (Cited on page 75.)

[123] J. S. Dyck, Č. Drašar, P. Lošt'ák, and C. Uher. Low-temperature ferromagnetic properties of the diluted magnetic semiconductor $Sb_{2-x}Cr_xTe_3$. *Phys. Rev. B*, 71:115214, Mar 2005. (Cited on page 75.)

[124] Y. S. Hor, P. Roushan, H. Beidenkopf, J. Seo, D. Qu, J. G. Checkelsky, L. A. Wray, D. Hsieh, Y. Xia, S.-Y. Xu, D. Qian, M. Z. Hasan, N. P. Ong, A. Yazdani, and R. J. Cava. Development of ferromagnetism in the doped topological insulator $Bi_{2-x}Mn_xTe_3$. *Phys. Rev. B*, 81: 195203, May 2010. (Cited on page 75.)

[125] Y. L. Chen, J.-H. Chu, J. G. Analytis, Z. K. Liu, K. Igarashi, H.-H. Kuo, X. L. Qi, S. K. Mo, R. G. Moore, D. H. Lu, M. Hashimoto, T. Sasagawa, S. C. Zhang, I. R. Fisher, Z. Hussain, and Z. X. Shen. Massive Dirac Fermion on the Surface of a Magnetically Doped Topological Insulator. *Science*, 329(5992):659–662, 2010. (Cited on page 75.)

[126] Jian-Min Zhang, Wenguang Zhu, Ying Zhang, Di Xiao, and Yugui Yao. Tailoring Magnetic Doping in the Topological Insulator Bi_2Se_3. *Phys. Rev. Lett.*, 109:266405, Dec 2012. (Cited on pages 75 and 76.)

[127] Judy J. Cha, James R. Williams, Desheng Kong, Stefan Meister, Hailin Peng, Andrew J. Bestwick, Patrick Gallagher, David Goldhaber-Gordon, and Yi Cui. Magnetic Doping and Kondo Effect in Bi_2Se_3 Nanoribbons. *Nano Letters*, 10(3):1076–1081, 2010. (Cited on page 75.)

[128] Cui-Zu Chang, Peizhe Tang, Yi-Lin Wang, Xiao Feng, Kang Li, Zuocheng Zhang, Yayu Wang, Li-Li Wang, Xi Chen, Chaoxing Liu, Wenhui Duan, Ke He, Xu-Cun Ma, and Qi-Kun Xue. Chemical-Potential-Dependent Gap Opening at the Dirac Surface States of Bi_2Se_3 Induced by Aggregated Substitutional Cr Atoms. *Phys. Rev. Lett.*, 112:056801, Feb 2014. (Cited on page 75.)

[129] Judy J. Cha, Martin Claassen, Desheng Kong, Seung Sae Hong, Kristie J. Koski, Xiao-Liang Qi, and Yi Cui. Effects of Magnetic Doping on Weak Antilocalization in Narrow Bi_2Se_3 Nanoribbons. *Nano Letters*, 12(8):4355–4359, 2012. (Cited on page 75.)

[130] Y. H. Choi, N. H. Jo, K. J. Lee, J. B. Yoon, C. Y. You, and M. H. Jung. Transport and magnetic properties of Cr-, fe-, cu-doped topological insulators. *Journal of Applied Physics*, 109(7):07E312, 2011. (Cited on page 75.)

[131] Jian-Min Zhang, Wenmei Ming, Zhigao Huang, Gui-Bin Liu, Xufeng Kou, Yabin Fan, Kang L. Wang, and Yugui Yao. Stability, electronic, and magnetic properties of the magnetically doped topological insulators Bi_2Se_3, Bi_2Te_3, and Sb_2Te_3. *Phys. Rev. B*, 88:235131, Dec 2013. (Cited on pages 75 and 76.)

[132] A. I. Figueroa, G. van der Laan, L. J. Collins-McIntyre, S.-L. Zhang, A. A. Baker, S. E. Harrison, P. Schönherr, G. Cibin, and T. Hesjedal. Magnetic Cr doping of Bi_2Se_3: Evidence for divalent Cr from x-ray spectroscopy. *Phys. Rev. B*, 90:134402, Oct 2014. (Cited on pages 75, 76, and 77.)

[133] X. F. Kou, W. J. Jiang, M. R. Lang, F. X. Xiu, L. He, Y. Wang, Y. Wang, X. X. Yu, A. V. Fedorov, P. Zhang, and K. L. Wang. Magnetically doped semiconducting topological insulators. *Journal of Applied Physics*, 112(6):063912, 2012. (Cited on page 75.)

[134] Xufeng Kou, Liang He, Murong Lang, Yabin Fan, Kin Wong, Ying Jiang, Tianxiao Nie, Wanjun Jiang, Pramey Upadhyaya, Zhikun Xing, Yong Wang, Faxian Xiu, Robert N. Schwartz, and Kang L. Wang. Manipulating Surface-Related Ferromagnetism in Modulation-Doped Topological Insulators. *Nano Letters*, 13(10):4587–4593, 2013. (Cited on page 75.)

[135] Wenqing Liu, Damien West, Liang He, Yongbing Xu, Jun Liu, Kejie Wang, Yong Wang, Gerrit van der Laan, Rong Zhang, Shengbai Zhang, and Kang. L. Wang. Atomic-Scale Magnetism of Cr-Doped Bi_2Se_3 Thin Film Topological Insulators. *ACS Nano*, 9(10):10237–10243, 2015. (Cited on page 75.)

[136] John Hasbrouck Van Vleck. The theory of electric and magnetic susceptibilities. 1932. (Cited on page 77.)

[137] Rui Yu, Wei Zhang, Hai-Jun Zhang, Shou-Cheng Zhang, Xi Dai, and Zhong Fang. Quantized Anomalous Hall Effect in Magnetic Topological Insulators. *Science*, 329(5987):61–64, 2010. (Cited on page 77.)

[138] Mingda Li, Cui-Zu Chang, Lijun Wu, Jing Tao, Weiwei Zhao, Moses H. W. Chan, Jagadeesh S. Moodera, Ju Li, and Yimei Zhu. Experimental Verification of the Van Vleck Nature of Long-Range Ferromagnetic Order in the Vanadium-Doped Three-Dimensional Topological Insulator Sb_2Te_3. *Phys. Rev. Lett.*, 114:146802, Apr 2015. (Cited on page 77.)

[139] Cui-Zu Chang, Jinsong Zhang, Minhao Liu, Zuocheng Zhang, Xiao Feng, Kang Li, Li-Li Wang, Xi Chen, Xi Dai, Zhong Fang, Xiao-Liang Qi, Shou-Cheng Zhang, Yayu Wang, Ke He, Xu-Cun Ma, and Qi-Kun Xue. Thin Films of Magnetically Doped Topological Insulator with Carrier-Independent Long-Range Ferromagnetic Order. *Advanced Materials*, 25(7):1065–1070, 2013. (Cited on page 79.)

[140] Eryin Wang, Peizhe Tang, Guoliang Wan, Alexei V. Fedorov, Ireneusz Miotkowski, Yong P. Chen, Wenhui Duan, and Shuyun Zhou. Robust

Gapless Surface State and Rashba-Splitting Bands upon Surface Deposition of Magnetic Cr on Bi_2Se_3. *Nano Letters*, 15(3):2031–2036, 2015. (Cited on page 80.)

[141] T. Eelbo, M. Sikora, G. Bihlmayer, M. Dobrzański, A. Kozłowski, I. Miotkowski, and R. Wiesendanger. Co atoms on Bi_2Se_3 revealing a coverage dependent spin reorientation transition. *New Journal of Physics*, 15(11):113026, 2013. (Cited on page 82.)

[142] Xin Liu, Hsiu-Chuan Hsu, and Chao-Xing Liu. In-Plane Magnetization-Induced Quantum Anomalous Hall Effect. *Phys. Rev. Lett.*, 111:086802, Aug 2013. (Cited on page 83.)

[143] Igor Žutić, Jaroslav Fabian, and S. Das Sarma. Spintronics: Fundamentals and applications. *Rev. Mod. Phys.*, 76:323–410, Apr 2004. (Cited on page 93.)

[144] C. Hahn, G. de Loubens, M. Viret, O. Klein, V. V. Naletov, and J. Ben Youssef. Detection of Microwave Spin Pumping Using the Inverse Spin Hall Effect. *Phys. Rev. Lett.*, 111:217204, Nov 2013. (Cited on pages 93 and 104.)

[145] Yanxia Xing, Zhong-liu Yang, Qing-feng Sun, and Jian Wang. Coherent single-spin source based on topological insulators. *Phys. Rev. B*, 90:075435, Aug 2014. (Cited on page 93.)

[146] Evan O. Kane. Band structure of indium antimonide. *Journal of Physics and Chemistry of Solids*, 1(4):249–261, 1957. (Cited on page 93.)

[147] B. Zhou, H.-Z. Lu, R.-L. Chu, S.-Q. Shen, and Q. Niu. Finite Size Effects on Helical Edge States in a Quantum Spin-Hall System. *Phys. Rev. Lett.*, 101:246807, Dec 2008. (Cited on page 94.)

[148] Markus König, Hartmut Buhmann, Laurens W. Molenkamp, Taylor Hughes, Chao-Xing Liu, Xiao-Liang Qi, and Shou-Cheng Zhang. The Quantum Spin Hall Effect: Theory and Experiment. *Journal of the Physical Society of Japan*, 77(3):031007, 2008. (Cited on pages 94, 98, and 106.)

[149] D. G. Rothe, R. W. Reinthaler, C. X. Liu, L. W. Molenkamp, S. C. Zhang, and E. M. Hankiewicz. Fingerprint of different spin–orbit terms for spin transport in HgTe quantum wells. *New Journal of Physics*, 12 (6):065012, 2010. (Cited on pages 97, 98, and 106.)

[150] Qing-Ze Wang, Xin Liu, Hai-Jun Zhang, Nitin Samarth, Shou-Cheng Zhang, and Chao-Xing Liu. Quantum Anomalous Hall Effect in Magnetically Doped InAs/GaSb Quantum Wells. *Phys. Rev. Lett.*, 113: 147201, Sep 2014. (Cited on pages 98 and 106.)

[151] Dong Zhang, Wenkai Lou, Maosheng Miao, Shou-cheng Zhang, and Kai Chang. Interface-Induced Topological Insulator Transition in GaAs/Ge/GaAs Quantum Wells. *Phys. Rev. Lett.*, 111:156402, Oct 2013. (Cited on page 98.)

[152] J. Zak. Magnetic Translation Group. *Phys. Rev.*, 134:A1602–A1606, Jun 1964. (Cited on page 101.)

[153] J. Zak. Magnetic Translation Group. II. Irreducible Representations. *Phys. Rev.*, 134:A1607–A1611, Jun 1964. (Cited on page 101.)

[154] M. V. Moskalets. *Scattering matrix approach to non-stationary quantum transport*. Imperial College Press, 2012. (Cited on page 103.)

[155] A. Mahé, F. D. Parmentier, E. Bocquillon, J.-M. Berroir, D. C. Glattli, T. Kontos, B. Plaçais, G. Fève, A. Cavanna, and Y. Jin. Current correlations of an on-demand single-electron emitter. *Phys. Rev. B*, 82:201309, Nov 2010. (Cited on page 103.)

[156] F. D. Parmentier, E. Bocquillon, J.-M. Berroir, D. C. Glattli, B. Plaçais, G. Fève, M. Albert, C. Flindt, and M. Büttiker. Current noise spectrum of a single-particle emitter: Theory and experiment. *Phys. Rev. B*, 85:165438, Apr 2012. (Cited on page 103.)

[157] J. Keeling, I. Klich, and L. S. Levitov. Minimal Excitation States of Electrons in One-Dimensional Wires. *Phys. Rev. Lett.*, 97:116403, Sep 2006. (Cited on page 104.)

[158] A. Pfeuffer-Jeschke. *Ph. D. Thesis*. Physikalisches Institut, Universität Würzburg, 2000. (Cited on page 104.)

[159] C. Brüne, A. Roth, H. Buhmann, E. M. Hankiewicz, L. W. Molenkamp, J. Maciejko, X.-L. Qi, and S.-C. Zhang. Spin polarization of the quantum spin Hall edge states. *Nat Phys*, 8(6):485–490, Jun 2012. (Cited on page 106.)

PUBLICATIONS

Relevant publications:

Tunable Dirac Electron and Hole Self-Doping of Topological Insulators Induced by Stacking Defects, Hugo Aramberri, Jorge I. Cerdá and M. Carmen Muñoz, *Nano Letters*, 15: 3840–3844, May 2015.

Ab initio study of the relationship between spontaneous polarization and p-type doping in quasi-freestanding graphene on H-passivated SiC surfaces, Jagoda Sławińska, Hugo Aramberri, M. Carmen Muñoz and Jorge I. Cerdá, *Carbon* 93: 88–104, November 2015.

Proposal for an ac spin current source, Patrick P. Hofer, Hugo Aramberri, Christoph Schenke and Pierre A. L. Delplace, *Euro Physics Letters* 107: 27003, July 2014.